Determining the influence of polymer architecture on the transfection efficiency of cationic polymers

Thomas George Floyd

A thesis submitted in partial fulfilment of the requirements for the degree of

Doctor of Philosophy in Chemistry

Department of Chemistry

University of Warwick

June 2021

Table of Contents

List of Figures

List of Tables

List of Schemes

Abbreviations

4-VBC	4-Vinylbenzyl Chloride
4-VBI	4-Vinylbenzyl Iodide
AAV	Adeno-Associated Virus
AFM	Atomic Force Microscopy
ANOVA	Analysis of Variance
AV	Adenovirus
BA	Butyl Acrylate
BMA	Butyl Methacrylate
bPEI	Branched Poly(ethylenimine)
BzMA	Benzyl Methacrylate
$CDCl_3$	Deuterated Chloroform
CMV	Cytomegalovirus
Cp	Cloud Point
CROP	Cationic Ring Opening Polymerisation
CTA	Chain Transfer Agent
Đ	Dispersity
D_2O	Deuterated Water
DAPI	4′,6-diamidino-2-phenylindole
DCM	Dichloromethane
DCTB	trans-2-[3-(4-tert-Butylphenyl)-2-methyl-2-propenylidene]malononitrile
DLS	Dynamic Light Scattering
DMAEMA	2-(Dimethylamino)ethyl methacrylate
DMEM	Dulbecco's Modified Eagle Media

DMF	Dimethylformamide
DNA	Deoxyribonucleic acid
DP	Degree of Polymerisation
EGFP	Enhanced Green Fluorescent Protein
EthBr	Ethidium Bromide
EtOx	2-Ethyl 2-Oxazoline
FDA	Food and Drug Administration
GAG	Glycosaminoglycans
GFP	Green Fluorescent Protein
H_2O	Water
HCl	Hydrochloric Acid
HEK293T	Human Embryonic Kidney
HEPES	4-(2-hydroxyethyl)-1-piperazineethanesulfonic acid
HSAB	Hard-Soft Acid-Base
HSV	Herpes Simplex Virus
I_2	Iodine
kbp	Kilo Base Pairs
kDa	Kilo Daltons
k_i	Rate of Initiation
KOH	Potassium Hydroxide
k_p	Rate of Propagation
LCST	Lower Critical Solution Temperature
lPEI	Linear Poly(ethylenimine)
LS	Light Scattering

MALDI-TOF	Matrix Assisted Laser Ionisation/Desorption Time of Flight
MALLS	Multi Angle Laser Light Scattering
MeOD	Deuterated Methanol
MeOx	2-Methyl 2-Oxazoline
MeTos	Methyl p-toluenesulfonate
M_n	Number Average Molecular Weight
mRNA	messenger ribonucleic acid
M_w	Weight Average Molecular Weight
MWCO	Molecular Weight Cut-off
N_2	Nitrogen Gas
Na_2CO_3	Sodium Carbonate
NaCl	Sodium Chloride
NaI	Sodium Iodide
NaOH	Sodium Hydroxide
NMR	Nuclear Magnetic Resonance
Opti-MEM	Optimised Minimal Essential Medium
P(Ox-co-EI)	Poly(2-oxazoline-co-ethylenimine)
p(r)	pair distance distribution
PAMAM	Poly(amidoamine)
PAPATC	3-((((1-carboxyethyl)thio)carbonothioyl)thio)propanoic acid
PBS	Phosphate Buffered Solution
PDi	Polydispersity Index
pDNA	Plasmid DNA
pDNA	Plasmid DNA

PEG	Poly(ethylene glycol)
PEI	Poly(ethylenimine)
PEtOx	Poly(2-ethyl-2-oxazoline)
PLL	Poly(L-lysine)
PMMA	Poly(methyl methacrylate)
POx	Poly(2-oxazoline)
PVP	Poly(vinylpyridine)
RAFT	Reversible Addition-Fragmentation Chain Transfer
RDRP	Reversible-Deactivation Radical Polymerisation
RI	Refractive Index
RNA	Ribonucleic Acid
rpm	Revolutions Per Minute
RV	Retrovirus
SANS	Small-angle Neutron Scattering
SARS CoV-2	Severe acute respiratory syndrome coronavirus 2
SAXS	Small-angle X-Ray Scattering
SEC	Size Exclusion Chromatography
siRNA	Short Interfering Ribonucleic Acid
SLD	Scattering Length Density
Sty	Styrene
TEM	Transmission Electron Microscopy
TFA	Trifluoroacetic Acid
UV-vis	Ultra-Violet
VA-044	2,2'-azobis[2-(2-imidazolin-2-yl)propane]dihydrochloride

VA-086	2,2'-Azobis[2-methyl-N-(2-hydroxyethyl)propionamide]
VS	Viscometry
XTT	2,3-bis-(2-methoxy-4-nitro-5-sulfophenyl)-2H-tetrazolium-5-carboxanilide

Acknowledgements

First and foremost, I would like to thank my supervisor Professor Sébastien Perrier. Thank you for allowing me to join your group as a master's student and then taking me back for a PhD. Your guidance and support over the last few years has been invaluable and I have very much enjoyed working with you, even though I still get a little queasy at the sight of Verveine du Velay. Thank you for allowing me the freedom to explore all the weird side projects, for taking the time to chat when things got overwhelming, and for pushing me to be a better researcher.

From supervising me as a master's student to guiding me from afar during my PhD, I would like to thank Dr Matthias Hartlieb. I feel very fortunate to have had your help throughout the last five and a half years. From showing me how to correctly label my lab book, to teaching me how to write a paper and everything in between, you have made a large impact on me and the scientist I am today.

There are several people who have had a large influence on how I have grown as a scientist. I would like to especially thank Professor Peter Scott, Dr Christopher Kay, Dr Helen Wilcock, Professor Rachel O'Reilly, and Professor Markus Wilhelmsson. All of you have shaped me some way into the researcher I am today, and I will be forever grateful to you all for taking me into your research groups and supporting my development.

At the start of my PhD, I could confidently say that I was not a biologist, but through the patience and generosity of Dr Alexia Hapeshi, Dr Raoul Peltier, Ji-Inn Song, and Dr Carlos Sanchez-Cano I have developed into something vaguely resembling a competent one. Without your contributions and guidance, I would not have been able to complete half the work I did, so thank you!

Since I first joined the Perrier group in 2015 it has been an incredibly friendly and welcoming environment, through all the changes this has remained constant and I feel incredibly privileged to have been a part of this group. Special thanks go to Dr Fannie Burgevin, Dr Robert Richardson and Satu Häkkinen who I have shared this experience with in full. I will always fondly remember our time together in San Diego, especially at the bars. Thank you to all the members of the Perrier group past and present, your friendship and support has made my time here infinitely more enjoyable. In no particular order, thank you to Agnes Kuroki, Alexander Cook, Andrew Kerr, Andrew Lunn, Cathy Cheng, Edward Mansfield, Guillaume Moriceau, Hannah Burnage, Jeaniffer Yap, Jiajia

Li, Jie Yang, Joji Tanaka, Julia Rho, Magda Przybyla, Maria Kariuki, Pratik Gurnani, Qiao Song, Ramon Garcia Maset, Sean Ellacott, Sophie Cooper, Sophie Hill, Sophie Laroque, Stephen Hall, Taki Zhang, Vito Kontrimas, Ximo Sanchis-Martinez, and Xiujun Cao.

I would further like to thank everyone who has worked on floor 2, I don't think I have ever managed to walk from one end to the other without stopping for a chat with one of you. In particular, I would like to thank Dr Daniel Lester, Dr Rachel Hand, Lucas Al-Shok, and Chris Atkins, you have all been great friends during my time here.

I feel incredibly privileged to have spent the last four years living with some of my closest friends. Thank you to Dr George Saunders and Georgia Wood. Since coming to university, Apple Way was the first place I have lived to truly feel like a home and it is thanks to the two of you. I would also like to thank Shaun Morris for allowing me to stay with you for the last year, providing me with cheap rent and endless chats about football.

Thank you to Jungyeon Kim for all your support and encouragement over the last two years, especially during the final few months whilst I have been writing my thesis. You have made me a much better, less miserable person, and I am incredibly grateful to have you in my life.

Finally, I would like to thank my family who have been incredibly supportive over the last few years. You have instilled a work ethic and drive in me that has enabled me to see this project through to completion. Thank you for everything.

Declaration

Experimental work contained within this thesis is original research carried out by the author, unless otherwise stated, in the Department of Chemistry at the University of Warwick, between October 2017 and May 2021. No material contained has been submitted for any other degree, or at any other institution.

Results from other authors are referenced in the usual manner.

The work presented was carried out by the author with the following exceptions:

Chapter 2: Aqueous SEC was performed by Anne C. Lehnen (Institute of Chemistry, University of Potsdam)

Chapter 2: AFM micrographs were obtained by Satu Häkkinen (Department of Chemistry, University of Warwick)

Chapter 2: SANS measurements were performed and analysed by Dr Stephen C. L. Hall (Department of Chemistry, University of Warwick)

Chapter 3: TEM micrographs were obtained by Dr Alexia Hapeshi (Warwick Medical School, University of Warwick)

Chapter 3: The aggregation study was carried out by Dr Alexia Hapeshi and Ji-Inn Song under the direction of the author (Warwick Medical School, University of Warwick)

Chapter 3: Flow cytometry data was obtained by Ji-Inn Song (Warwick Medical School, University of Warwick)

Chapter 4: TEM micrographs were obtained by Dr Alexia Hapeshi (Warwick Medical School, University of Warwick)

Chapter 4: SAXS measurements were performed by Dr Steven Huband and analysed by Dr Stephen C. L. Hall (Department of Chemistry, University of Warwick)

Signed:_____ Date:_____

Thomas George Floyd

1 Introduction

1.1 Gene Therapy

Gene therapy is an approach to medicine where exogenous DNA is used as a treatment to target specific diseases, ideally in a single dose.[1, 2] Many diseases are caused by faults in our genetic code such as cystic fibrosis, cancer, hemophilia, or cardiovascular disease, to name a few. Replacement, or repair, of the faulty genetic sequence will lead to a permanent treatment for the targeted disease. Gene therapy encompasses a range of approaches to treating diseases, all based around our genetic code. The three main approaches are as follows.

- Replacement of a mutated gene with a functioning copy
- Inactivating a mutated gene
- Introducing a new gene encoding for therapeutic proteins

The potential of gene therapy has been discussed for the last 50 years since the ability to manipulate DNA and RNA *in vitro* and understand their structure.[3] However, until recently, very few therapies obtained regulatory approval. Their development has been hampered by disappointing clinical trial results showing little efficacy and unexpected toxicities, which unfortunately led to the death of a patient in 1999.[4] The following decades focused on improving the safety and further understanding the fundamental science behind the transfection vectors and biological pathways, until, in 2017, the US food and drug administration (FDA) approved the first *in vivo* gene therapy, Luxturna®.[5] Used in the treatment of Leber's congenital amaurosis, a rare inherited eye disease that causes visual impairment, Luxturna® is an adeno-associated virus (AAV) modified with a genetic sequence for the enzyme RPE65.[6] Expression of this enzyme helps to substantially restore vision; however, it is not a cure for the disease.

Since Luxturna's® approval more gene therapies have been approved by the US and European regulatory agencies. The treatments, however, are expensive and there are still issues with toxicity prevalent in clinical trials. Whilst they are not considered gene therapies, several mRNA vaccines have received approval in light of the recent SARS-CoV-2 pandemic. mRNA vaccines use our cellular processes to synthesise a protein found on a virus, encoded for by the mRNA.[7] Once transcribed, the protein molecules can trigger an adaptive immune response, teaching the body how to recognise and destroy foreign pathogens.[8]

Introducing exogenous nucleic acids into the body is not a straightforward process and there are many extra- and intra-cellular barriers to successful transfection. Therefore, it is

rare that the nucleic acid will be introduced to the body alone. Usually, it is packaged within a vector to facilitate cellular uptake and prevent enzymatic degradation.

1.1.1 Viral and Non-Viral Vectors

Whilst the delivery of "naked" nucleotides has been achieved using techniques such as electroporation or a gene gun, it is favoured to use a vector to complex the nucleotide and transport it to the site of interest.[9, 10] The use of vectors provides protection to the nucleotide cargo within and facilitates cellular uptake. There are two classes of vectors used in the delivery of nucleic acids, viral and non-viral. Each as their specific advantages and disadvantages, but to be a successful vector, they must satisfy several criteria.

- Possess the ability to transfect large therapeutic genes.
- Have a high transfection efficiency and stable expression.
- Provide the ability for long-term storage.
- Targeting of specific cells.
- Avoid random insertion of the gene into the host genome.

1.1.1.1 Viral Vectors

Viral vectors are modified viruses that deliver their cargo into the cell.[11, 12] This technique takes advantage of the inherent ability of viruses to be taken up by cells and propagate and offers the highest efficiency of transfection. Removal of virulent genes within the virus renders their replication inactive, but still retaining the ability to infect cells. This in combination of the addition of a therapeutic gene into the viral genome allows for safe and efficient gene therapy.

Commonly used viruses in the delivery of genetic material include adenoviruses (AV), adeno-associated viruses (AAV), herpes simplex viruses (HSV), and retroviruses (RV). Viral vectors are by far the most used vector for nucleic acid delivery, and considerable research and clinical trials have studied their application. As of 2017, over 2500 clinical trials have been undertaken in gene therapy, with modified viruses accounting for over 67 % of vectors used.[13]

However, whilst modified viruses are the most common and efficient transfection vectors, they come with a set of limitations that has driven research into alternative directions.[14, 15] Perhaps most prominent is the risk of an immune response caused by the introduction of the virus. This can reduce the efficiency of the transfection and furthermore, the generation of antibodies could prevent further doses being effective. The space within the virus to carry nucleic acids is also limited, restricting the size of the nucleic acid that can

be carried within. This further restricts the virus in the ability to carry multiple genes, limiting the diseases that can be treated. Furthermore, there are logistical challenges in the production of viruses on a large scale and their long-term storage.[16]

1.1.1.2 Non-Viral Vectors

Attempting to overcome the shortcomings of viral vectors, research into alternative vectors, not based on viruses, has been carried out.[17] Non-viral vectors are based on cationic lipids or polymers that can bind anionic nucleic acid via electrostatically interactions and condense it into lipoplexes or polyplexes, respectively (**Figure 1.1**) In principle, non-viral vectors can address many of the problems posed by viral vectors. They tend to cause a lower immune response, can effectively package larger strands of nucleic acids, are easier to synthesise, and patients do not tend to have pre-existing immunity. However, for all their benefits, non-viral vectors suffer from a significantly lower transfection efficiency than viral vectors. This so far has limited their clinical use and has been the major focus of research into these systems.[17, 18]

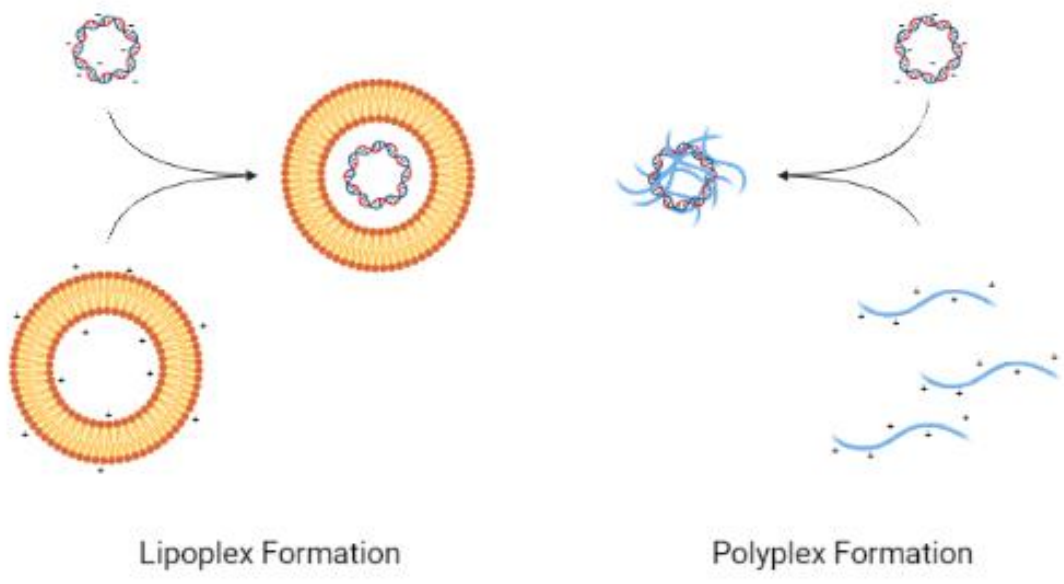

Figure 1.1 Cartoon illustration of lipoplex (left) and polyplex (right) formation.

Lipid vectors are much more prevalent in the literature and clinic than polymer-based vectors.[19, 20] Liposomes have been established as a delivery vehicle for small-molecule drugs,[21] and by formulating liposomes with cationic-containing lipids they are able to encapsulate nucleic acids. The first liposome-based transfection was reported in 1980

where the kidney cells of monkeys were transfected with SV40 DNA.[22] Since then, considerable research on the formulation of liposomes has been carried out to push the limits of their transfection capabilities, such as modifications to the structure of the cationic lipid or including helper lipids to aid in stability and cellular uptake (**Figure 1.2a**). Limitations in the use of liposomes include poor transfection efficiency caused by clearance of the particle or low stability in the presence of proteins. Furthermore, the generation of an inflammatory response towards certain liposomes has hindered their use.[23, 24]

Cationic polymers are less prevalent than liposomes in non-viral gene delivery, but their use is becoming more common (**Figure 1.2b**).[10, 25, 26] Polymers offer a high degree of structural variability and are straightforward to synthesised. Electrostatic complexation between cationic polymers and anionic nucleic acids results in the formation of vesicles or particles, condensed to a size smaller than that of the free nucleic acid and liposomes. Poly(L-lysine) (PLL) was an early polymer used in the complexation of DNA, with its ability to complex DNA known since the 1960s.[27] Many other cationic polymers with varying structures have been evaluated since, with branched poly(ethylenimine) (bPEI) being the "gold standard" due to a high transfection efficiency and high commercial availability.[28, 29] One advantage of polymer-based transfection vectors is the high level of control and variability over the polymer composition and topology. Furthermore, modification of the polymer to include targeting ligands or biodegradable segments is straightforward. Cationic polymers are known to be toxic due to their ability to disrupt cellular membranes, bind non-specifically with serum proteins, and interfere with cellular processes.[30] Modifications to the polymer can be made to alleviate these issues, such as the attachment of biocompatible polymers, however this is usually accompanied by a decrease in transfection efficiency.

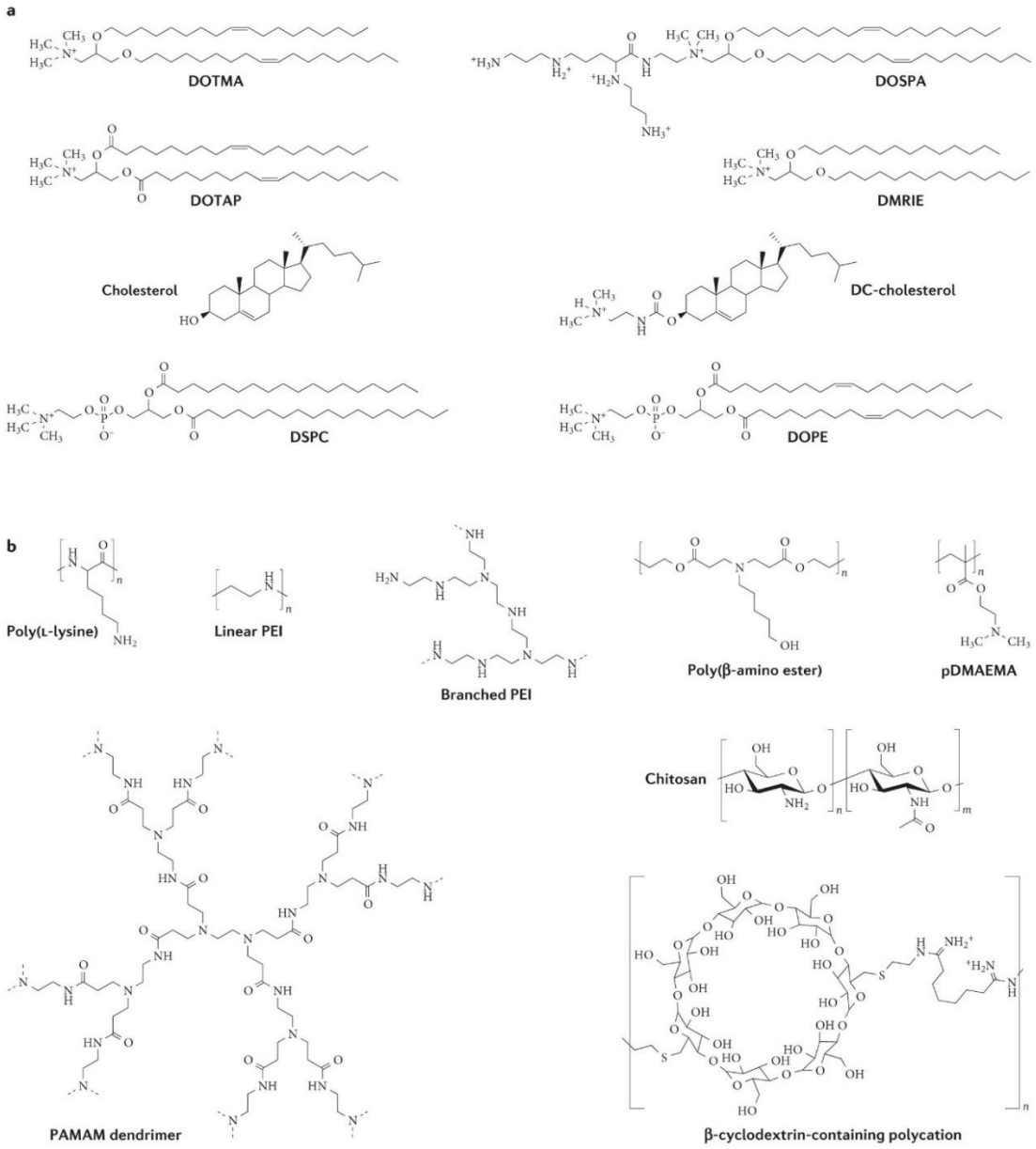

Figure 1.2 Overview of the lipids (a) and polymers (b) used to form non-viral vectors for gene transfection. Image adapted from reference 17.

1.1.2 Barriers to Gene Delivery

As mentioned previously, there are several barriers to be overcome for successful gene transfection, both within the body and in the design of successful transfection vectors. For vector design, the major obstacle is the design of a system with high transfection efficiency and low cytotoxicity, as one tends to go hand in hand with the other, for example bPEI.[31]

Once injected into the body the complexes face several challenges before complete transfection.[32] Nucleases in physiological fluids will rapidly degrade any foreign nucleic

acids, with the half-life of plasmid DNA (pDNA) determined to be 10 minutes in mice.[33] Complexation with a polymer or within a liposome will help to prevent degradation and improve the circulation time. Additionally, cationic macromolecules can non-specifically bind with serum proteins, hindering cellular uptake and causing rapid clearance from the body.[34] This is even seen *in vitro* where serum-free media is commonly used in transfection experiments. There is also the issue of crossing the cell membrane and nuclear envelope. Nucleic acids are negatively charged and crossing the negatively charged, hydrophobic barriers surrounding the cell and nucleus is challenging. This is highlighted in the poor transfection of non-proliferating cell lines.[35] Again, complexation with cationic polymers or lipids can aid in overcoming these barriers due to enhanced interaction with the cellular membrane due to the cationic surface charge of the vector, causing increased internalisation through processes such as endocytosis.

A major challenge faced by polyplexes during transfection is escaping from the endo-lysosomal compartments during cellular uptake. Only a small minority of polyplexes will escape from the endo-lysosome (1-2 %) with the majority being ejected or destroyed, by exocytosis or enzymatic degradation, respectively. The mechanism of escape is highly contested within the literature where three hypotheses are proposed.[36] The "proton sponge" effect is often used to describe the behaviour of polyplex escape, where protonation of the polymer leads to osmotic swelling of the lysosome, followed by rupture of the vesicle.[37] The other two mechanisms are based on the formation of pores in the membrane of the lysosome by interaction with either the polyplex or free polymer with the membrane lipids.[38, 39] No consensus on the mechanism of escape has been reached, with further experiments required to fully understand the process.

It is intuitive that dissociation of the polyplex must occur before the nucleic acid can undergo transcription.[40] The dissociation of the polymer and nucleic acid is seen as a rate limiting step in transfection, however, the mechanism by which this occurs is largely unknown.[41] Several mechanisms have been proposed such as competitive dissociation with anionic macromolecules in the cytoplasm or a spontaneous thermodynamic release, but there is no consensus, and the mechanism may vary for different vectors. For common transfection agents such as PEI there is no obvious degradation pathway for the polymer to undergo, however studies have shown that dissociation can take place in the nucleus, possibly arising from competing interactions with chromosomal DNA. Introduction of degradable units into the polymeric structure is thought to aid in the eventual polyplex dissociation, such as redox- or pH-responsive linkers.[42] Charge-shifting monomers may

also help in this process as their cationic residues can transform into anionic ones under stimuli.[43-45]

1.2 Complex Polymer Architectures in Gene Delivery

Advances in controlled polymerisation techniques such as controlled radical polymerisation, ionic polymerisation, or ring-opening polymerisation have enabled access to fine control over a polymer's composition and topology. Composition meaning the distribution of monomers within a polymeric chain, i.e., random, gradient, block, and topology describing the polymer's shape.[46, 47]

Both parameters can have significant influence over the properties and performance of the polymer for its intended application.[46] Whilst significant research has been undertaken into the effect of monomer composition within linear polymers, this section will focus on polymer topology instead. When discussing polymer topology, it is generally divided into five subsections; linear, graft, star, branched, and self-assembled. The former four topologies all arise from covalent linkages within polymeric chains, whereas self-assembled systems result from the assembly of multiple polymer chains into higher order structures.

After linear polymers, branched systems have received significant attention in nucleic acid delivery.[48] As previously discussed, branched polymers such as bPEI and PAMAM dendrimers have been thoroughly investigated, with bPEI being labelled the "gold standard" polymer-based transfection agent.[28] When considering branched polymers, bPEI and PAMAM represent the opposing sides on the spectrum of control. bPEI is a branched polymer with a broad molecular weight distribution, synthesised in an uncontrolled manner. On the other hand, PAMAM are dendritic materials possessing a monodisperse molecular weight distribution, the synthesis of which is much more controlled, but laborious.[49] Advances in controlled radical chemistry has allowed for the synthesis of branched polymers by copolymerisation of functional monomers with multifunctional crosslinkers.[48] This drastically increases the functionality of these systems due to a wider toolbox of comonomers to choose from, allowing for the incorporation of charge-shifting monomers or different cationic residues to name a few.[44, 50] Branched polymers have been seen as increasingly attractive non-viral vectors due to their three-dimensional morphology and high degree of structural variability.[51] They have been shown to possess enhanced transfection efficiency compared with linear polymers and can increase cellular uptake alongside protection from degradative enzymes.

Graft copolymers are similar in structure to branched polymers; however, the branches all emanate from a single polymer backbone. They can be synthesised in a controlled way

through grafting-through, grafting-from, or grafting-to chemistries, with each approach having their individual advantages and disadvantages.[52] It is possible to introduce a high level of topological variations with graft copolymers with parameters such as graft-length, grafting-density, and backbone length all having a major influence over the resulting structure of the polymer.[53] When applied to gene delivery, the drive to use graft copolymers is to mimic the properties of branched polymers but with lower molecular weight segments. The cationic residues can be places either on the backbone of the graft copolymer, or on the grafts themselves, with the location heavily influencing the toxicity and complexation properties of the polymer.[54, 55] Further structural variation is available with graft copolymers, such as the attachment of grafts through biodegradable linkers or use of a degradable backbone.[56, 57] Such degradation would allow for favourable decomplexation of the polyplex within a degradative environment and reduce the cytotoxicity of the polymer.

Star polymers possess a structure of linear arms radiating from a central core.[58] They can be synthesised in a convergent manner, where linear polymers are formed before attachment to a central core, either through efficient coupling chemistries or the crosslinking of the polymer chains with multi-reactive monomers. Alternatively, star polymers can be synthesised *via* a divergent process where polymer chains are grown from a multifunctional core. Star-shaped polymers show increased flexibility compared with branched or graft polymers, which has been exhibited to result in greater nucleic acid complexation.[59] This superior complexation has been shown to result in spherical polyplexes which, under certain conditions, can lead to greater internalisation within cells.[60, 61] Like graft copolymers, star polymers benefit from high structural variety, with parameters such as the number and length of arms, degradability, composition, and charge location all easily manipulated.

Moving away from linear polymers towards those with more complex architecture has been shown to be highly beneficial for the delivery of nucleic acids. Whether that be through the greater complexation ability of the nucleic acid or through the high degree of structural freedom, many studies have shown improved properties over linear polymers. The challenge will be in understanding of how these materials behave *in vivo*, as most work has focused on simple *in vitro* models, and whether these beneficial properties translate. Furthermore, consideration will need to be made on the complexity of polymer synthesis. This will no doubt add further hurdles to overcome as popular transfection agents such as bPEI are cheap and straightforward to synthesise.

1.3 Poly(2-oxazoline)s

Poly(2-oxazoline)s (POx) are a pseudo-peptide like polymer synthesised *via* the cationic ring-opening polymerisation (CROP) of 2-oxazolines, a 5-membered heterocycle containing a nitrogen and oxygen. POx is an extremely versatile polymer owing to the ease of introducing functionality, either through the choice of terminating agent, initiator, or monomer (**Figure 1.3**).[62] The synthesis of POx was first reported in 1966 by four independent studies and received intensive investigation after its initial report.[63-66]

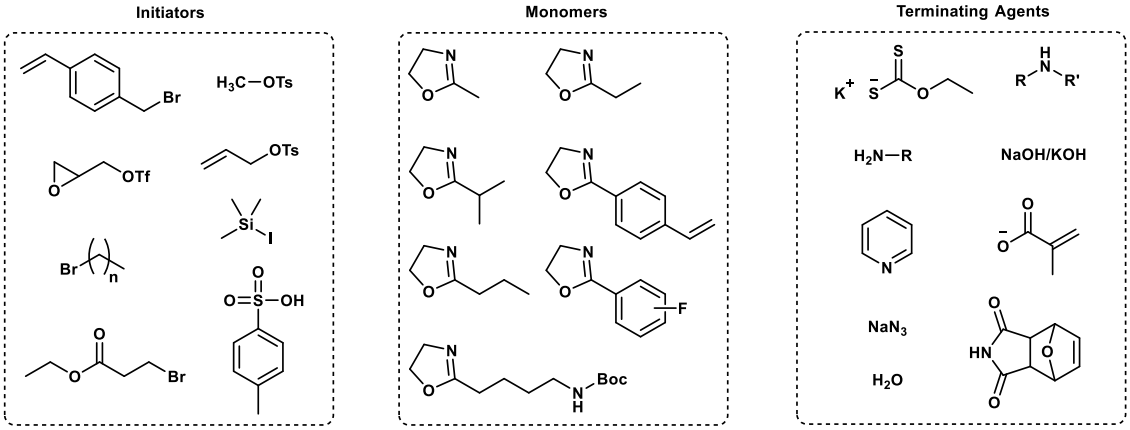

Figure 1.3 Overview of the functional initiators, monomers and terminating agents used in the preparation of poly(2-oxazoline)s.

1.3.1 Synthesis of 2-Oxazolines

2-Oxazolines can be synthesised *via* a variety of different pathways, with three synthetic routes commonly reported in the literature (**Figure 1.4**).[67]

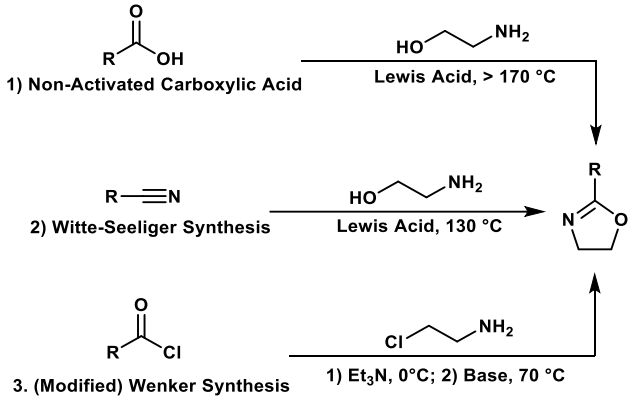

Figure 1.4 Overview of the synthetic approaches towards 2-oxazolines.

The first approach is the reaction of a non-activated carboxylic acids with ethanolamine, forming an amide bond at elevated temperatures (170 °C). This is followed by *in situ* cyclisation using a Lewis-acid catalyst such as $Ti(OBu)_4$ or $Zn(OAc)_2$. This method is preferred industrially but is less common on the laboratory scale due to the high pressure required for the use of low molecular weight, volatile carboxylic acids.[68]

In the laboratory, the most common method for the synthesis of 2-oxazolines is the Witte-Seeliger synthesis.[69] This involves the reaction of nitriles with ethanolamine, with the ring closure again catalysed by Lewis acids. Whilst this one-step synthesis is highly popular due to the ease of introducing a variety of functional groups at the 2-position, it is hindered by the release of ammonia as a side product. Ammonia acts as a chain-transfer agent in the polymerisation of 2-oxazolines and must be removed prior to polymerisation.[70] This is a challenging process as the ammonia bind strongly to the oxazoline, possibly through hydrogen bonding with the imine. In addition, the formed ammonia can be reactive towards certain functional groups, limiting the monomers that can be synthesised.

The third common method for the synthesis of 2-oxazolines is a modified Wenker synthesis, involving the reaction of an activated carboxylic acid with an acid chloride.[71] Ring-closure is achieved by addition of a base such as KOH or Na_2CO_3, under milder conditions compared to those required for the synthetic approaches above. The drawback of this approach is the required purification of the intermediate amide before the ring-closure can be attempted.

By using functional carboxylic acids or nitriles the 2-substituent on the synthesised oxazoline ring can be changed, allowing for a wide range of monomers available for subsequent polymerisation.[62, 69] In addition, functionalities can be added at the 3- and 4-position of the ring, however these monomers are more difficult to polymerise and there is limited literature on their use.[72, 73]

1.3.2 Mechanism of the CROP of 2-Oxazolines

The mechanism of polymerisation can be divided into four components, initiation, propagation, chain transfer, and termination (**Figure 1.5**).[74]

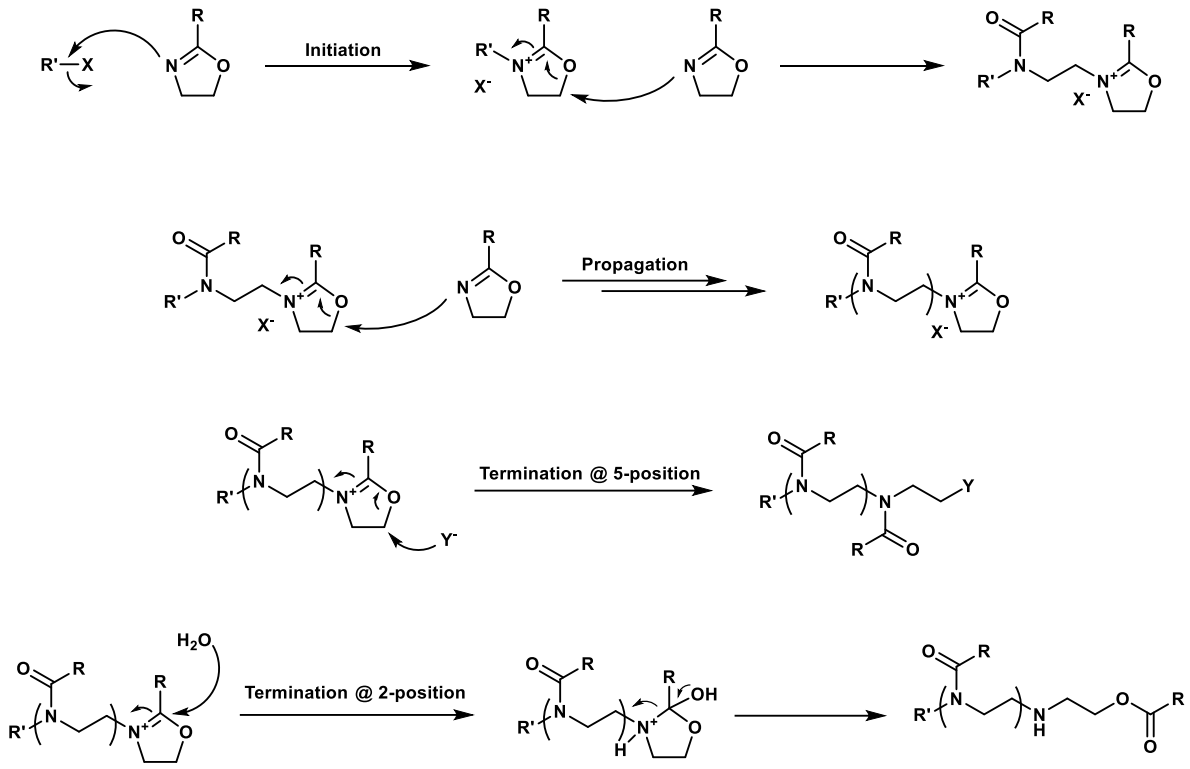

Figure 1.5 Mechanism for the polymerisation of 2-oxazolines, forming poly(2-oxazoline)s. X^- represents the counter ion, Y represents a terminating agent.

Initiation begins by a nucleophilic attack of the 2-oxazolines nitrogen lone pair onto an electrophilic initiator. This results in the formation of an oxazolinium cation and anionic counter ion. Common initiators include alkyl halides, alkyl tosylates, and alkyl triflates, with the leaving group influencing the rate of initiation (k_i) and propagation (k_p). Other initiators such as I_2,[75] Lewis acids,[76] and oxazolinium salts[77-79] have been reported, although their use is less common. To obtain good control over the resulting molar mass distributions k_i must be higher than k_p, with slow or incomplete initiation resulting in high dispersity polymers with broad molecular weight distributions. The counter ion can influence the equilibrium between the cationic and covalent propagating species (Table x), further exemplifying appropriate choice of initiator.

Providing the functionality does not interact with the CROP of 2-oxazolines functional initiators can be used to introduce functionalities at the α-end group. Protecting groups can be used to overcome incompatibility issues, although this adds an extra step in the deprotection of the functionality. Using functional initiators, a wide range of end-group functionalities have been reported such as unsaturated carbon-carbon bonds for post-polymerisation click reactions,[80-83] propagating species for further polymerisation[84] or initiators for controlled radical polymerisation.[85, 86] Multi-functional initiators have been utilised in the synthesis of star[87-91] or bottlebrush-shaped polymers.[79, 92, 93]

Propagation is a two-step mechanism, with the first step involving addition of monomer to the newly formed oxazolinium ion. This process is slow, making it the rate determining step of the polymerisation.[94] After addition of the first monomer the rate of propagation increases and the second stage of propagation commences with further addition of monomer to the oxazolinium species. This stage continues until all monomer has been consumed, leaving an active chain-end capable of further propagation, or the chain-end has undergone termination or chain-transfer.

During the propagation there is an equilibrium between a cationic and covalent propagating species (**Table 1.1**). This equilibrium depends on the counter ion present and the R-group of the 2-oxazoline monomer, in addition to the polarity of the solvent used in the polymerisation. In general, if the basicity of the counter ion is higher than the nucleophilicity of the monomer the covalent propagating species will be formed.[74] If however the nucleophilicity of the monomer is greater than the basicity of the counter ion then a cationic propagating species will be observed. Propagation predominantly proceeds via the cationic species, due to the increased electrophilicity compared to the covalent species and the apparent k_p scales linearly to the number of cationic species.[94, 95]

Table 1.1 Nature of the propagating groups for monomer and counter-ion pairs in the polymerisation of 2-oxazolines. R_f represents a perfluorated alkyl side chain. Table adapted from reference 74.

R-group	**Cl^-**	**Br^-**	**I^-**	**OTs^-**	**OTf^-**
Me	Covalent	Ionic	Ionic	Ionic	Ionic
Et	Covalent	Covalent/Ionic	Covalent/Ionic	Ionic	Ionic
H	Covalent	Covalent	Covalent/Ionic	Ionic	Ionic
Ph	-	Covalent	Covalent/Ionic	Ionic	Ionic
R_f	-	-	Covalent	Covalent	Ionic

The selection of monomer can also influence the k_p of the polymerisation. The reactivity of the monomer is determined by the substituent at the 2-position, as it influences the partial positive charge at the 5-position and the nucleophilicity of the imine.[96-98] 2-Oxazoline monomers with electron-donating substituents are the most prevalent in the literature, commonly bearing an alkyl functionality. The electron donating side chain makes the imine more reactive to nucleophilic attack of an oxazolinium propagating species, whilst reducing the partial positive charge at the 5-position, reduces the reactivity of the oxazolinium ion. This process is not fully understood and further parameters such

as steric bulk of the 2-substituent contributes to the k_p of the monomer. As the ability of the substituent to donate electron density increases the k_p of the monomer decreases, leading to the general trend of monomers with longer alkyl substituents polymerising slower than those with shorter alkyl chains. This effect is most pronounced in the difference in k_p for 2-methyl-2-oxazoline to 2-ethyl-2-oxazoline to 2-isopropyl-2-oxazoline. The use of fluorinated oxazoline monomers highlights the importance of the monomer substituents electron donating/withdrawing nature.[97, 99] A highly electron withdrawing trifluoromethyl substituent results in a monomer incapable of undergoing polymerisation. Increasing the alkyl spacer between the oxazoline ring and trifluoro moiety allows for the monomer to polymerise, with an increase in spacer length corresponding to an increase in k_p.

Whilst the polymerisation of 2-oxazolines is considered a living polymerisation, chain transfer reactions are known to occur.[100] The main chain transfer reaction observed is β-elimination leading to an imine-enamine rearrangement, caused by hydrogen abstraction from the propagating chain-end by a 2-oxazoline monomer.[101] The newly generated proton-initiated oxazolinium can undergo subsequent polymerisation resulting in a proton-initiated POx, generally observed with lower molecular weights to the main polymer distribution. In addition, the enamine formed during β-elimination can undergo chain coupling with another polymer chain through nucleophilic attack of the double bond to the oxazolinium propagating species.[102]

Termination of the CROP involves nucleophilic attack from a terminating agent at either the 2- or 5-position of the oxazolinium chain end. The position of attack is rationalised using the hard and soft acid and bases (HSAB) theory, whereby soft terminating agents tend to terminate at the 2-position and hard terminating agents on the 5-position. The position of attack leads to two different end-groups, with attack at the 2-position resulting in the formation of an ester containing end-group and attack at the 5-position ring-opening the oxazoline and installing the functionality at the chain end.[103]

The possibility of introducing functional end-groups can be achieved using a functional terminating agent. Commonly used terminating agents include potassium hydroxide, resulting in a hydroxyl ω-end group, or piperidine forming a tertiary amine end-group including the piperidine ring. Similar to the initiator-based functionality, a wide range of functional groups have been reported *via* the termination process.[104-108]

1.3.3 The Hydrolysis of Poly(2-Oxazoline)s

The hydrolysis of POx was first reported alongside the initial work describing their synthesis.[65] Cleavage of the pendent amide bond by acidic or basic hydrolysis generates a linear polycation, poly(ethylenimine) (PEI), containing secondary amines (**Figure 1.6**).[109] This polymer is analogous to poly(ethylene glycol) (PEG), possessing a nitrogen instead of an oxygen. In their initial report on the synthesis of POx, Tomalia and Sheetz presented the subsequent hydrolysis of the polymer under acidic and basic conditions.[65] In both cases partially hydrolysed poly[(2-oxazoline)-*co*-(ethylenimine)] (P(Ox-*co*-EI)) was observed and under basic hydrolysis precipitation of the polymer occurred.

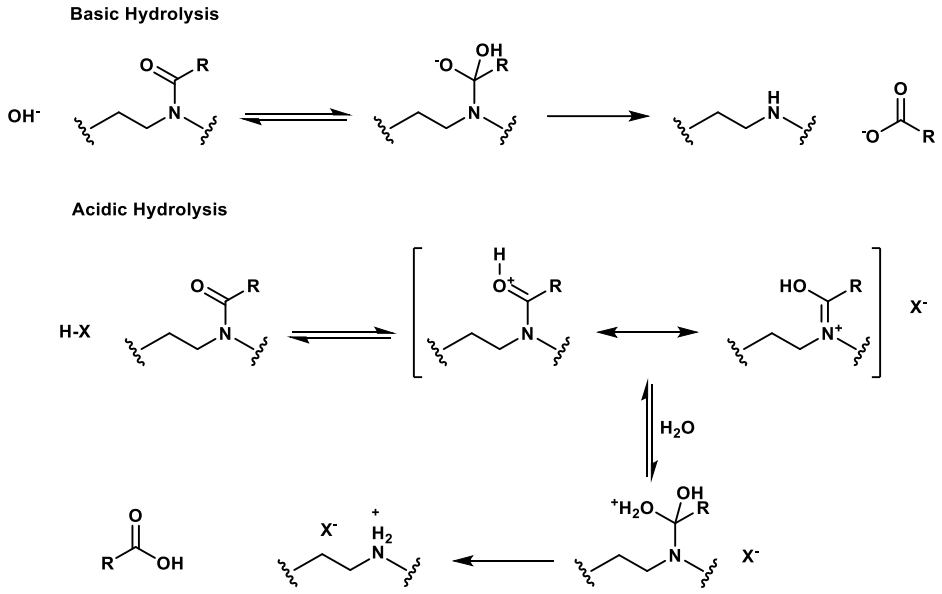

Figure 1.6 Mechanism for the basic or acidic hydrolysis of poly(2-oxazoline)s

Precipitation of the polymer is one drawback to the method of basic hydrolysis in the preparation of PEI. As the amide bonds are hydrolysed the secondary amines are deprotonated in solution, reducing the solubility of the polymer. Furthermore, basic hydrolysis has been shown to cause degradation of the polymer along the backbone, forming low molecular weight contaminants (Figure 1.7).[110]

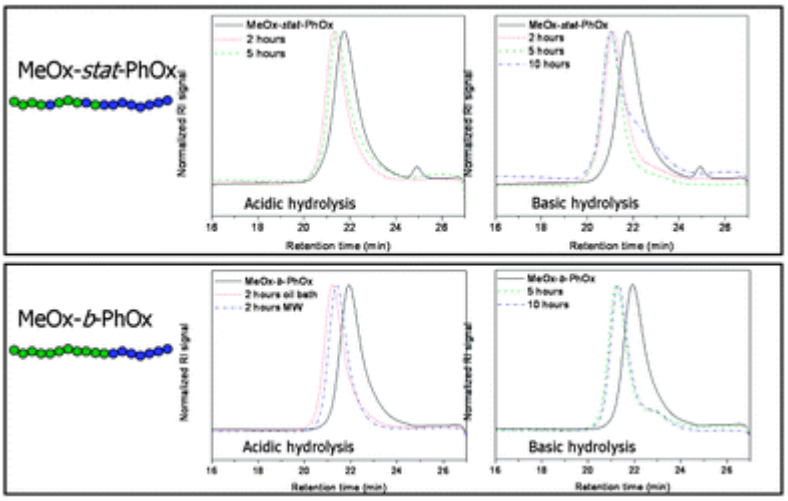

Figure 1.7 Hexafluoroisopropanol SEC of P(MeOx-*co*-PhOx) hydrolysed under acidic (left) and basic (right) conditions. Figure obtained from ref 110.

Acidic hydrolysis overcomes these limitations as the polymer remains soluble throughout the reaction and degradation is only observed when heating to high temperatures (180 °C) under pressure.[111]

Extensive studies have been carried out on the mechanism and kinetics of the acidic hydrolysis of POx.[112, 113] The amide is initially protonated, followed by nucleophilic attack of a water molecule forming a tetrahedral intermediate. Rearrangement of this species liberates a carboxylic acid leaving the secondary amine behind. The rate determining step of the hydrolysis is found to be the nucleophilic attack of water. It is postulated that the rate of hydrolysis is enhanced by interactions of the oxazoline unit with neighbouring PEIs. This forms a 7-membered ring like intermediate, activating the amide towards nucleophilic attack.

The distribution of hydrolysis events along the POx backbone was studied by tandem mass spectrometry (MS/MS).[114] A series of partially hydrolysed P(EtOx-*co*-EI)s were synthesised and their sequence analysed by electron capture dissociation fragmentation. This allowed for the exact position of a hydrolysis event along the backbone to be determined. It was postulated that if the 7-membered ring intermediate discussed above played a role in the hydrolysis of PEtOx that there would be an observed order to the hydrolysis locations, with groupings of EI units found. From the intensity of the fragments obtained by MS/MS the odds of finding a hydrolysed unit at each position along the backbone was determined and compared to that of a random distribution, generated by a modified Heap's algorithm. The results exhibited that the distribution of hydrolysis events along the backbone was random and uninfluenced by any neighbouring EI units.

In a study comparing the hydrolysis kinetics of MeOx and EtOx, MeOx was shown to be hydrolysed at a faster rate compared to EtOx, exhibiting linear hydrolysis kinetics up to 80 % hydrolysis.[112] The rate of hydrolysis was shown to also be independent of the molecular weight of the starting polymer as well as the concentration of monomer in solution, providing the concentration of acid was in excess.[113] The hydrolysis of EtOx was further studied in a subsequent publication, where the effect of reaction temperature and acid concentration were investigated.[111] Increasing the reaction temperature increased the rate of hydrolysis, with the maximum rate observed at 180 °C, as above this temperature the polymer was shown to degrade. In addition, acid-free hydrolysis under near-critical water conditions showed hydrolysis of the amide bond as well as decomposition into oligomers, rendering this approach unsuitable. Variation of the acid concentration showed a lower limit to the extent of hydrolysis. Sub-stoichiometric acid concentrations hydrolysed the polymer partially, but the extent was limited by the acid concentration. This is caused by the hydrolysed polymer scavenging hydronium ions, preventing further hydrolysis.

From the two studies described above it has been shown that by careful selection of the reaction time or acid concentration partially hydrolysed POx can be obtained in a reproducible way, allowing for the synthesis of random copolymers of POx and EI with targeted ratios between the two monomer units.

The secondary amine formed by the hydrolysis of POx is a useful handle for further post-polymerisation modification reactions, as it can undergo a wide range of reactions to introduce functionality into the polymer. Reactions such as Michael addition, epoxide ring-opening, carboxylic acid addition, and reductive amination have all been exploited to functionalise the secondary amine.[109, 115-117]

1.3.4 The Use of Poly(2-Oxazoline)s in Gene Therapy

Due to the biocompatibility of PEtOx and PMeOx and the ease of introducing charge through partial or complete hydrolysis POx has found use in a wide variety of gene transfection vectors. Hydrolysis of the amide bond to introduce a secondary amine is the most straightforward way to synthesise a transfection vector based on POx. Complete hydrolysis of linear POx is used to synthesise the commercially available transfection agent jetPEI®, a commonly used vector for transfection in the laboratory. Partially hydrolysing the POx is advantageous as it imparts a cationic component to the polymer

whilst retaining the biocompatibility properties of POx. The use of partially hydrolysed POx was first reported by Jeong *et al.* where a series of copolymers with different degrees of hydrolysis were evaluated for their ability to bind plasmid DNA (pDNA) and transfect NIH/3T3 cells, a fibroblast cell line from mouse embryo tissue.[118] It was found that the transfection efficiency was dependent on the charge density and molecular weight of the polymer, but independent of the total number of cationic residues. To match the transfection efficiency of branched PEI a degree of hydrolysis of 88 % was required. The cytotoxicity of the polymer was also dependent on molecular weight and charge density, with cell viability decreasing with increasing molecular weight and charge density. A similar study was conducted by Fernandes *et al.* who again studied the relationship between molecular weight and charge density on cytotoxicity and transfection efficiency.[119] This study expanded the degrees of hydrolysis investigated and found that below 70 % hydrolysis the polymers exhibit very low cytotoxicity towards HeLa cells. Above this percentage the polymers were highly cytotoxic, preventing their use as transfection agents. The ability to transfect siRNA was investigated and polymers with 30 % hydrolysis were shown to exhibit negligible transfection across a range of N/P ratios. Increasing the charge density resulted in greater transfection efficiency, with 96 % hydrolysis showing higher degrees of knockdown than 70 %, however the extent to which 70 % hydrolysed polymers knocked down the gene of interest was high enough to make it a viable transfection agent. This coupled with the negligible cytotoxicity of the polymer makes it an ideal candidate for a transfection vector.

Two detailed studies on the ability of partially hydrolysed POx were published independently, giving greater insight into the behaviour of these vectors.[120, 121] Bauer *et al.* compared partially hydrolysed POx with linear PEIs possessing the same number of amines, allowing insights into the effect of charge density. When comparing the transfection efficiency and toxicity of the library of polymers it was found that the reduction of charge density had a much greater effect on the transfection efficiency than it did on the cytotoxicity, causing a large payoff in transfection efficiency for a small reduction in cytotoxicity. Blakney *et al.* utilised a library of partially and fully hydrolysed PEtOx to determine the optimal polymer for complexing various sized polynucleotides using a design of experiment approach (DoE). From this study it was shown that there is not a single polymer that efficiently complex all forms of polynucleotide, but that careful consideration needs to be made to pair the combination. In most cases a fully hydrolysed PEtOx was the most efficient at complexing and transfecting the nucleic acids, with the

exception of messenger RNA (mRNA) which appeared to be more efficiently transfected by 80% hydrolysed PEtOx.

Partially hydrolysed poly(2-propyl-2-oxazoline)s with thermoresponsive behaviour were investigated for their ability to complex nucleic acids, although no studies were carried out on their transfection ability.[122, 123] For poly(2-isopropyl-2-oxazoline) (PiPrOx) the cloud point was unchanged for the partially hydrolysed copolymers, however, for poly(n-propyl-2-oxazoline) (PnPrOx) the cloud point was found to increase with increasing EI content. Both copolymers were heated above their cloud points and complexed with DNA. Upon complexation the polyplexes were cooled to room temperature and subsequently heated to 37 °C, upon which an increase in dimension was observed but the polyplexes remained intact.

In the reverse of partial hydrolysis, Blakney *et al.* partially reacetylated a linear PEI with adamantane to form a structure analogous to POx.[124] The adamantane moiety was used to bind to a mannosylated cyclodextrin *via* a host-guest interaction. Increasing the degree of mannosylation increased expression in epithelial cells when the polyplexes were used to transfect human skin explants. In a similar vein, Bus *et al*. reported the partial hydrolysis of EtOx, with alkene groups introduced through acetylation.[125] The alkene groups were subsequently modified with primary amines to form a copolymer containing secondary and primary amines which were used to complex and transfect siRNA. The transfection efficiency was slightly higher for polymers with greater secondary amine content, although the results were not significantly different.

Partially hydrolysed PEtOx has also been assembled into a hyperbranched structure and used to transfect HEK293T cells with a GFP expressing pDNA.[126] A telechelic PEtOx was synthesised with an alkyne and thiol which can undergo a radical promoted thiol-yne polymerisation to form hyperbranched polymers. Hydrolysis of the polymer formed a material analogous to PEI, containing only secondary amines. The partially hydrolysed polymers were found to match the transfection efficiency of bPEI at high degrees of hydrolysis and outperformed a linear analogue, indicating a positive influence of polymeric architecture.

As discussed above, the biocompatibility of certain oxazolines is a major drive for their use in biomedical applications such as gene transfection.[127] PEtOx and PMeOx have found use in a variety of systems to impart a reduction in cytotoxicity of the cationic residues. The first example of POx being used to shield polycation toxicity was reported

by Hsiue *et al*. in 2006, where a PEtOx-*b*-EI block copolymer was synthesised with a redox responsive disulphide linker between the EtOx and EI blocks.[128] The transfection efficiency of the diblock copolymers was similar to that of bPEI in HeLa cells, however, whilst the polymers had a reduced cytotoxicity compared to bPEI, they appeared to be relatively cytotoxic. Furthermore, the addition of the redox responsive linker was not studied in detail and appeared to not contribute anything to the results.

POx has been further incorporated into block copolymer structures for use in gene delivery. Cationic peptide residues are promising candidates for gene delivery due to their biodegradability. Block copolymers of POx and cationic peptides have been reported in the literature, with their synthesis approached *via* post-polymerisation chain coupling or using POx as a macroinitiator for the polymerisation of *N*-carboxyanhydrides.[129, 130] Witzigmann *et al.* transfected HeLa and HEK293 cells with a block copolymer of PEtOx and poly(aspartic acid) modified with diethylenetriamine. Transfection efficiency of the diblock was comparable to bPEI in both cell lines with a significant reduction in cytotoxicity.

As previously discussed, one advantage of POx is the ease of introducing functionality through the monomer. This has been exploited to introduce primary and tertiary amines by post-polymerisation modification.[131] Two alkene-functional oxazoline monomers with different spacer lengths between the backbone and alkene were copolymerised with MeOx. These were modified with primary or tertiary amines *via* a thiol-ene reaction. Primary amines exhibited greater transfection efficiencies than tertiary amines for the short linker length, with little difference observed between the two when a longer linker was used. However, the transfection efficiency was much lower for the polymers with the longer linker and they exhibited much greater cytotoxicity towards L929 cells.

Amine-containing oxazoline monomers have also been reported in the literature. Due to the nature of CROP, these monomers must be protected during polymerisation and deprotected after to activate the amine. He *et al*. synthesised a secondary amine containing oxazoline monomer and copolymerised it with MeOx to form block copolymers.[132] The transfection efficiency and cytotoxicity were compared with a PEG-PLL block copolymer, with the oxazoline block copolymer found to give higher cell viability. Whilst the oxazoline block copolymer could effectively complex pDNA, it was unable to transfect efficiently, unless in the presence of Pluronic P85, a gene transfection adjuvant. It should be noted that transfection was carried out on RAW264.7 and B16 cell lines, which are particularly challenging to transfect.

A different amine-containing oxazoline monomer was reported by Hertz *et al.*[133] containing a longer alkyl spacer than the one reported by He. Interestingly, the difference in polymerisation constants between the amine oxazoline and MeOx or EtOx resulted in different monomer distributions. Copolymerisation with MeOx resulted in a random monomer distribution, whereas EtOx gave a gradient distribution. Neither polymer composition had a significant influence on the resulting properties and, like with the system above, very little transfection occurred.

As discussed in **Section 1.2**, polymeric architectures can be exploited to impart beneficial properties to gene transfection vectors. Subsequently, POx chains have been grafted onto cationic backbones or copolymerised with cationic monomers to shield the charge in the backbone. von Erlach *et al*. carried out an extensive study on PMeOx-grafted poly(lysine) (PLL), studying the effect of graft length and grafting density on toxicity and transfection.[134] Furthermore, these polymers were compared with PEG-grafted PLL. Shorter graft lengths resulted in greater transfection efficiencies in COS-7 cells, presumably due to lower shielding of the backbone charge. A lower grafting density also resulted in increased transfection, although the number of charged units was not kept consistent. The toxicity towards COS-7 cells appeared unaffected by changes to the polymer structure, however it was the toxicity of the polyplex that was investigated, potentially obscuring any toxic effects of the free polymer. Overall, the toxicity was comparable to that of a PEG-grafted PLL.

A similar study was carried out using PEI as the cationic backbone by Haladjova *et al.*[135] Toxicity of the polymers and polyplexes was carried out on a suite of cell lines, with limited cytotoxicity observed for all samples. However, the transfection efficiency of the polyplexes was significantly lower than bPEI. The graft length was much longer than the POx-grafted PLL, which could be a significant contribution to the reduced transfection.

The copolymerisation of a PEtOx macromonomer with a secondary or primary amine containing monomer was presented by Trützschler *et al.*[136] Variation of the grafting density, graft length and amine nature allowed for a series of structure-property relationships to be established. There was no significant effect on polymer cytotoxicity, except for the graft copolymer containing the shortest graft length and primary amine cationic residues, which exhibited a lower cell viability. For transfection efficiency, the two copolymers with the shortest graft length and highest charge density were the only two polymers to show any significant transfection, with primary amine containing polymers outperforming those containing secondary amines.

A further example of polymeric architectures used in gene delivery are those based on self-assembling polymers. Amphiphilic polymers containing regions of hydrophobicity and hydrophilicity will self-assemble in aqueous systems to form micellar structures. These have been used in the delivery of nucleic acids by complexation with cationic residues in the micelle's corona. POx has found a use in these systems either in the complexation of nucleic acid, providing a biocompatible corona, or as the hydrophobic block used for assembly.[137-139]

POx has shown itself to be a versatile material in the generation of gene transfection vectors. Whether through imparting biocompatibility and shielding charge, or providing the cationic residues, many efficient and non-toxic vectors have been reported. Most studies have focused on using POx to reduce the cytotoxicity of cationic polymers, in a fashion similar to PEGylation. In all cases the addition of POx had a positive effect on the cytotoxicity of the system, however, it generally caused a decrease in the transfection efficiency. This is a common issue with modifications to cationic polymers and not just limited to POx. Furthermore, through amine-containing oxazoline monomers or the partial hydrolysis of 2-alkyl-2-oxazolines, oxazolines have been used to introduce charge to a polymeric system, often being copolymerised with biocompatible oxazoline monomers. The use of POx as a platform for the generation of gene delivery materials has shown great promise, especially with the facile introduction of cationic moieties through backbone hydrolysis or the large amount of structural variety achievable. POx provides an excellent option for the next generation of functional materials.

1.4 Aims and Objectives

The aim of this thesis is to study the impact of complex polymeric architectures on the ability of a polymer to complex and transfect plasmid DNA. The materials synthesised are based on a poly(2-ethyl-2-oxazoline) macromonomer, highlighting the versatility of the polymer to form a wide variety of materials.

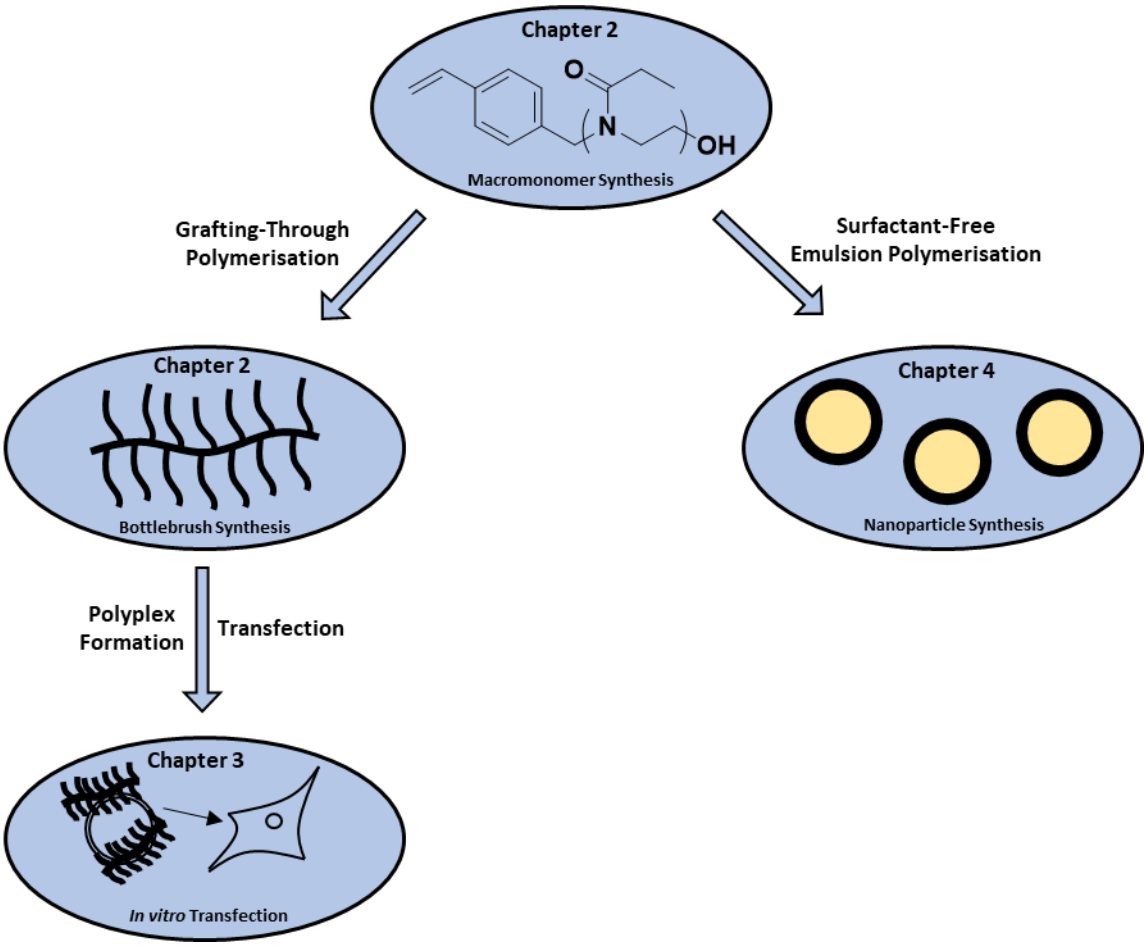

Scheme 1.1 Overview and aims of thesis chapters.

The first chapter focuses on the optimisation of the macromonomer synthesis, followed by its polymerisation to form bottlebrush polymer. Detailed understanding of the bottlebrush polymer synthesis and structure are gained before the polymers are hydrolysed to introduce ethylenimine residues within the structure. Further characterisation are undertaken to determine the structural effects of this hydrolysis procedure.

The second chapter uses the cationic bottlebrush polymers synthesised in the first chapter and evaluates their ability to complex pDNA. Once an optimal ratio between polymer and pDNA has been established and their complexation understood, the polymers is used to transfect a GFP expressing pDNA in mammalian cells and compared against linear controls to ascertain the influence of architecture on the transfection ability.

In the final chapter the macromonomer is used to synthesise alternative nanostructures, nanoparticles, by surfactant-free emulsion polymerisation. Adjusting the ratio between macromonomer and core-forming, hydrophobic comonomer results in a system easily tuned for the preparation of nanoparticles. Extensive experiments on the effect of comonomer choice and macromonomer ratio is undertaken. The particles are then exposed to hydrolysis conditions, followed by evaluation on their ability to complex pDNA.

1.5 References

1. C. E. Dunbar, K. A. High, J. K. Joung, D. B. Kohn, K. Ozawa and M. Sadelain, *Science*, 2018, **359**, eaan4672.
2. X. M. Anguela and K. A. High, *Annual Review of Medicine*, 2019, **70**, 273-288.
3. T. Friedmann and R. Roblin, *Science*, 1972, **175**, 949.
4. S. Jenks, *JNCI: Journal of the National Cancer Institute*, 2000, **92**, 98-100.
5. https://www.fda.gov/news-events/press-announcements/fda-approves-novel-gene-therapy-treat-patients-rare-form-inherited-vision-loss, (accessed 07/05/2021, 2021).
6. H. Ameri, *Journal of Current Ophthalmology*, 2018, **30**, 1-2.
7. F. P. Polack, S. J. Thomas, N. Kitchin, J. Absalon, A. Gurtman, S. Lockhart, J. L. Perez, G. Pérez Marc, E. D. Moreira, C. Zerbini, R. Bailey, K. A. Swanson, S. Roychoudhury, K. Koury, P. Li, W. V. Kalina, D. Cooper, R. W. Frenck, L. L. Hammitt, Ö. Türeci, H. Nell, A. Schaefer, S. Ünal, D. B. Tresnan, S. Mather, P. R. Dormitzer, U. Şahin, K. U. Jansen and W. C. Gruber, *New England Journal of Medicine*, 2020, **383**, 2603-2615.
8. N. Pardi, M. J. Hogan, F. W. Porter and D. Weissman, *Nature Reviews Drug Discovery*, 2018, **17**, 261-279.
9. H. Herweijer and J. A. Wolff, *Gene Therapy*, 2003, **10**, 453-458.
10. Y. K. Sung and S. W. Kim, *Biomaterials Research*, 2019, **23**, 8.
11. J. T. Bulcha, Y. Wang, H. Ma, P. W. L. Tai and G. Gao, *Signal Transduction and Targeted Therapy*, 2021, **6**, 53.
12. M. A. Kotterman, T. W. Chalberg and D. V. Schaffer, *Annual Review of Biomedical Engineering*, 2015, **17**, 63-89.
13. S. L. Ginn, A. K. Amaya, I. E. Alexander, M. Edelstein and M. R. Abedi, *The Journal of Gene Medicine*, 2018, **20**, e3015.
14. N. Bessis, F. J. GarciaCozar and M. C. Boissier, *Gene Therapy*, 2004, **11**, S10-S17.
15. C. E. Thomas, A. Ehrhardt and M. A. Kay, *Nature Reviews Genetics*, 2003, **4**, 346-358.
16. O. W. Merten, C. Gény-Fiamma and A. M. Douar, *Gene Therapy*, 2005, **12**, S51-S61.
17. H. Yin, R. L. Kanasty, A. A. Eltoukhy, A. J. Vegas, J. R. Dorkin and D. G. Anderson, *Nature Reviews Genetics*, 2014, **15**, 541-555.

18. D. Putnam, *Nature Materials*, 2006, **5**, 439-451.
19. D. A. Balazs and W. T. Godbey, *Journal of Drug Delivery*, 2011, **2011**, 326497.
20. M. A. Mintzer and E. E. Simanek, *Chemical Reviews*, 2009, **109**, 259-302.
21. C. Zylberberg and S. Matosevic, *Drug Delivery*, 2016, **23**, 3319-3329.
22. R. Fraley, S. Subramani, P. Berg and D. Papahadjopoulos, *Journal of Biological Chemistry*, 1980, **255**, 10431-10435.
23. C. Lonez, M. Vandenbranden and J.-M. Ruysschaert, *Progress in Lipid Research*, 2008, **47**, 340-347.
24. K. A. Whitehead, R. Langer and D. G. Anderson, *Nature Reviews Drug Discovery*, 2009, **8**, 129-138.
25. D. W. Pack, A. S. Hoffman, S. Pun and P. S. Stayton, *Nature Reviews Drug Discovery*, 2005, **4**, 581-593.
26. M. Patrick, B. Gilles, G. Jean Pierre and P. Chantal, *Current Gene Therapy*, 2008, **8**, 335-352.
27. D. E. Olins, A. L. Olins and P. H. von Hippel, *Journal of Molecular Biology*, 1967, **24**, 157-176.
28. S. Taranejoo, J. Liu, P. Verma and K. Hourigan, *Journal of Applied Polymer Science*, 2015, **132**.
29. O. Boussif, Lezoualc, F. h, M. A. Zanta, M. D. Mergny, D. Scherman, B. Demeneix and J. P. Behr, *Proceedings of the National Academy of Sciences*, 1995, **92**, 7297.
30. H. Lv, S. Zhang, B. Wang, S. Cui and J. Yan, *Journal of Controlled Release*, 2006, **114**, 100-109.
31. S. M. Moghimi, P. Symonds, J. C. Murray, A. C. Hunter, G. Debska and A. Szewczyk, *Molecular Therapy*, 2005, **11**, 990-995.
32. C. M. Wiethoff and C. R. Middaugh, *Journal of Pharmaceutical Sciences*, 2003, **92**, 203-217.
33. K. Kawabata, Y. Takakura and M. Hashida, *Pharmaceutical Research*, 1995, **12**, 825-830.
34. M. Ogris, S. Brunner, S. Schüller, R. Kircheis and E. Wagner, *Gene Therapy*, 1999, **6**, 595-605.
35. M. Wilke, M. Fortunati E Fau - van den Broek, A. T. van den Broek M Fau - Hoogeveen, B. J. Hoogeveen At Fau - Scholte and B. J. Scholte.
36. T. Bus, A. Traeger and U. S. Schubert, *Journal of Materials Chemistry B*, 2018, **6**, 6904-6918.

37. J.-P. Behr, *CHIMIA International Journal for Chemistry*, 1997, **51**, 34-36.
38. Z. u. Rehman, D. Hoekstra and I. S. Zuhorn, *ACS Nano*, 2013, **7**, 3767-3777.
39. S. Vaidyanathan, B. G. Orr and M. M. Banaszak Holl, *Accounts of Chemical Research*, 2016, **49**, 1486-1493.
40. C. L. Grigsby and K. W. Leong, *Journal of The Royal Society Interface*, 2010, **7**, S67-S82.
41. D. V. Schaffer, N. A. Fidelman, N. Dan and D. A. Lauffenburger, *Biotechnology and Bioengineering*, 2000, **67**, 598-606.
42. Q. Peng, Z. Zhong and R. Zhuo, *Bioconjugate Chemistry*, 2008, **19**, 499-506.
43. H. T. Ho, S. Pascual, V. Montembault, N. Casse and L. Fontaine, *Polymer Chemistry*, 2014, **5**, 5542-5545.
44. A. B. Cook, R. Peltier, M. Hartlieb, R. Whitfield, G. Moriceau, J. A. Burns, D. M. Haddleton and S. Perrier, *Polymer Chemistry*, 2018, **9**, 4025-4035.
45. P. Gurnani, A. K. Blakney, R. Terracciano, J. E. Petch, A. J. Blok, C. R. Bouton, P. F. McKay, R. J. Shattock and C. Alexander, *Biomacromolecules*, 2020, **21**, 3242-3253.
46. A. C. Rinkenauer, S. Schubert, A. Traeger and U. S. Schubert, *Journal of Materials Chemistry B*, 2015, **3**, 7477-7493.
47. F. J. Xu and W. T. Yang, *Progress in Polymer Science*, 2011, **36**, 1099-1131.
48. A. B. Cook and S. Perrier, *Advanced Functional Materials*, 2020, **30**, 1901001.
49. E. Abbasi, S. F. Aval, A. Akbarzadeh, M. Milani, H. T. Nasrabadi, S. W. Joo, Y. Hanifehpour, K. Nejati-Koshki and R. Pashaei-Asl, *Nanoscale Research Letters*, 2014, **9**, 247.
50. A. B. Cook, R. Peltier, T. R. Barlow, J. Tanaka, J. A. Burns and S. Perrier, *Journal of Interdisciplinary Nanomedicine*, 2018, **3**, 164-174.
51. M. Jäger, S. Schubert, S. Ochrimenko, D. Fischer and U. S. Schubert, *Chemical Society Reviews*, 2012, **41**, 4755-4767.
52. S. S. Sheiko, B. S. Sumerlin and K. Matyjaszewski, *Progress in Polymer Science*, 2008, **33**, 759-785.
53. C. Feng, Y. Li, D. Yang, J. Hu, X. Zhang and X. Huang, *Chemical Society Reviews*, 2011, **40**, 1282-1295.
54. J. M. Benns, J.-S. Choi, R. I. Mahato, J.-S. Park and S. W. Kim, *Bioconjugate Chemistry*, 2000, **11**, 637-645.
55. X. Jiang, M. C. Lok and W. E. Hennink, *Bioconjugate Chemistry*, 2007, **18**, 2077-2084.

56. J. Liu, Y. Xu, Q. Yang, C. Li, W. E. Hennink, R. Zhuo and X. Jiang, *Acta Biomaterialia*, 2013, **9**, 7758-7766.
57. X. C. Yang, M. Y. Chai, Y. Zhu, W. T. Yang and F. J. Xu, *Bioconjugate Chemistry*, 2012, **23**, 618-626.
58. J. M. Ren, T. G. McKenzie, Q. Fu, E. H. H. Wong, J. Xu, Z. An, S. Shanmugam, T. P. Davis, C. Boyer and G. G. Qiao, *Chemical Reviews*, 2016, **116**, 6743-6836.
59. R. Whitfield, A. Anastasaki, N. P. Truong, A. B. Cook, M. Omedes-Pujol, V. Loczenski Rose, T. A. H. Nguyen, J. A. Burns, S. Perrier, T. P. Davis and D. M. Haddleton, *ACS Macro Letters*, 2018, **7**, 909-915.
60. T. K. Georgiou, *Polymer International*, 2014, **63**, 1130-1133.
61. M. Byrne, D. Victory, A. Hibbitts, M. Lanigan, A. Heise and S.-A. Cryan, *Biomaterials Science*, 2013, **1**, 1223-1234.
62. B. Guillerm, S. Monge, V. Lapinte and J.-J. Robin, *Macromolecular Rapid Communications*, 2012, **33**, 1600-1612.
63. T. Kagiya, S. Narisawa, T. Maeda and K. Fukui, *Journal of Polymer Science Part B: Polymer Letters*, 1966, **4**, 441-445.
64. W. Seeliger, E. Aufderhaar, W. Diepers, R. Feinauer, R. Nehring, W. Thier and H. Hellmann, *Angewandte Chemie International Edition in English*, 1966, **5**, 875-888.
65. D. A. Tomalia and D. P. Sheetz, *Journal of Polymer Science Part A-1: Polymer Chemistry*, 1966, **4**, 2253-2265.
66. T. G. Bassiri, A. Levy and M. Litt, *Journal of Polymer Science Part B: Polymer Letters*, 1967, **5**, 871-879.
67. J. A. Frump, *Chemical Reviews*, 1971, **71**, 483-505.
68. M. Beck, P. Birnbrich, U. Eicken, H. Fischer, W. E. Fristad, B. Hase and H. J. Krause, *Die Angewandte Makromolekulare Chemie*, 1994, **223**, 217-233.
69. K. Kempe, M. Lobert, R. Hoogenboom and U. S. Schubert, *Journal of Combinatorial Chemistry*, 2009, **11**, 274-280.
70. B. D. Monnery, S. Shaunak, M. Thanou and J. H. G. Steinke, *Macromolecules*, 2015, **48**, 3197-3206.
71. H. Wenker, *Journal of the American Chemical Society*, 1935, **57**, 1079-1080.
72. M. M. Bloksma, U. S. Schubert and R. Hoogenboom, *Macromolecular Rapid Communications*, 2011, **32**, 1419-1441.
73. R. Luxenhofer, S. Huber, J. Hytry, J. Tong, A. V. Kabanov and R. Jordan, *Journal of Polymer Science Part A: Polymer Chemistry*, 2013, **51**, 732-738.

74. B. Verbraeken, B. D. Monnery, K. Lava and R. Hoogenboom, *European Polymer Journal*, 2017, **88**, 451-469.
75. B. Guillerm, S. Monge, V. Lapinte and J.-J. Robin, *Macromolecules*, 2010, **43**, 5964-5970.
76. T. Saegusa, H. Ikeda and H. Fujii, *Polymer Journal*, 1972, **3**, 176-180.
77. B. D. Monnery, V. V. Jerca, O. Sedlacek, B. Verbraeken, R. Cavill and R. Hoogenboom, *Angewandte Chemie International Edition*, 2018, **57**, 15400-15404.
78. S. Cesana, J. Auernheimer, R. Jordan, H. Kessler and O. Nuyken, *Macromolecular Chemistry and Physics*, 2006, **207**, 183-192.
79. N. Zhang, S. Huber, A. Schulz, R. Luxenhofer and R. Jordan, *Macromolecules*, 2009, **42**, 2215-2221.
80. B. Guillerm, V. Darcos, V. Lapinte, S. Monge, J. Coudane and J.-J. Robin, *Chemical Communications*, 2012, **48**, 2879-2881.
81. S. Kobayashi, H. Uyama, T. Mori and Y. Narita, *Chemistry Letters*, 1991, **20**, 1771-1774.
82. Y. Chujo, E. Ihara, H. Ihara and T. Saegusa, *Macromolecules*, 1989, **22**, 2040-2043.
83. M. W. M. Fijten, C. Haensch, B. M. van Lankvelt, R. Hoogenboom and U. S. Schubert, *Macromolecular Chemistry and Physics*, 2008, **209**, 1887-1895.
84. D. Pizzi, J. Humphries, J. P. Morrow, N. L. Fletcher, C. A. Bell, K. J. Thurecht and K. Kempe, *European Polymer Journal*, 2019, **121**, 109258.
85. C. R. Becer, R. M. Paulus, S. Höppener, R. Hoogenboom, C.-A. Fustin, J.-F. Gohy and U. S. Schubert, *Macromolecules*, 2008, **41**, 5210-5215.
86. Y. C. Yu, H. S. Cho, W.-R. Yu and J. H. Youk, *Polymer*, 2014, **55**, 5986-5990.
87. R. Hoogenboom, M. W. M. Fijten, G. Kickelbick and U. S. Schubert, *Beilstein Journal of Organic Chemistry*, 2010, **6**, 773-783.
88. R. Luxenhofer, M. Bezen and R. Jordan, *Macromolecular Rapid Communications*, 2008, **29**, 1509-1513.
89. G. Pereira, C. Huin, S. Morariu, V. Bennevault-Celton and P. Guégan, *Australian Journal of Chemistry*, 2012, **65**, 1145-1155.
90. R. H. Jin, *Advanced Materials*, 2002, **14**, 889-892.
91. R. Weberskirch, R. Hettich, O. Nuyken, D. Schmaljohann and B. Voit, *Macromolecular Chemistry and Physics*, 1999, **200**, 863-873.

92. N. Zhang, R. Luxenhofer and R. Jordan, *Macromolecular Chemistry and Physics*, 2012, **213**, 1963-1969.
93. P. D. Trivedi and D. N. Schulz, *Polymer Bulletin*, 1980, **3**, 37-44.
94. T. Saegusa and H. Ikeda, *Macromolecules*, 1973, **6**, 808-811.
95. A. Dworak, *Macromolecular Chemistry and Physics*, 1998, **199**, 1843-1849.
96. R. Hoogenboom, M. W. M. Fijten, H. M. L. Thijs, B. M. van Lankvelt and U. S. Schubert, *Designed Monomers and Polymers*, 2005, **8**, 659-671.
97. L. I. Kaberov, B. Verbraeken, A. Riabtseva, J. Brus, Y. Talmon, P. Stepanek, R. Hoogenboom and S. K. Filippov, *ACS Macro Letters*, 2018, **7**, 7-10.
98. H. Goossens, S. Catak, M. Glassner, V. R. de la Rosa, B. D. Monnery, F. De Proft, V. Van Speybroeck and R. Hoogenboom, *ACS Macro Letters*, 2013, **2**, 651-654.
99. R. Ivanova, T. Komenda, T. B. Bonné, K. Lüdtke, K. Mortensen, P. K. Pranzas, R. Jordan and C. M. Papadakis, *Macromolecular Chemistry and Physics*, 2008, **209**, 2248-2258.
100. M. Litt, A. Levy and J. Herz, *Journal of Macromolecular Science: Part A - Chemistry*, 1975, **9**, 703-727.
101. J. M. Warakomski and B. P. Thill, *Journal of Polymer Science Part A: Polymer Chemistry*, 1990, **28**, 3551-3563.
102. F. J. Arraez, X. Xu, P. H. M. Van Steenberge, V.-V. Jerca, R. Hoogenboom and D. R. D'hooge, *Macromolecules*, 2019, **52**, 4067-4078.
103. O. Nuyken, G. Maier, A. Groß and H. Fischer, *Macromolecular Chemistry and Physics*, 1996, **197**, 83-95.
104. M. Hartlieb, T. Floyd, A. B. Cook, C. Sanchez-Cano, S. Catrouillet, J. A. Burns and S. Perrier, *Polymer Chemistry*, 2017, **8**, 2041-2054.
105. A. Krieg, C. Weber, R. Hoogenboom, C. R. Becer and U. S. Schubert, *ACS Macro Letters*, 2012, **1**, 776-779.
106. C. Weber, C. Remzi Becer, W. Guenther, R. Hoogenboom and U. S. Schubert, *Macromolecules*, 2010, **43**, 160-167.
107. C. J. Waschinski and J. C. Tiller, *Biomacromolecules*, 2005, **6**, 235-243.
108. G. Volet, T.-X. Lav, J. Babinot and C. Amiel, *Macromolecular Chemistry and Physics*, 2011, **212**, 118-124.
109. M. A. Mees and R. Hoogenboom, *Polymer Chemistry*, 2018, **9**, 4968-4978.
110. H. M. L. Lambermont-Thijs, J. P. A. Heuts, S. Hoeppener, R. Hoogenboom and U. S. Schubert, *Polymer Chemistry*, 2011, **2**, 313-322.

111. V. R. de la Rosa, E. Bauwens, B. D. Monnery, B. G. De Geest and R. Hoogenboom, *Polymer Chemistry*, 2014, **5**, 4957-4964.
112. K. M. Kem, *Journal of Polymer Science: Polymer Chemistry Edition*, 1979, **17**, 1977-1990.
113. H. P. C. Van Kuringen, J. Lenoir, E. Adriaens, J. Bender, B. G. De Geest and R. Hoogenboom, *Macromolecular Bioscience*, 2012, **12**, 1114-1123.
114. T. Morgan, PhD Thesis, University of Warwick, 2020
115. C. Englert, M. Fevre, R. J. Wojtecki, W. Cheng, Q. Xu, C. Yang, X. Ke, M. Hartlieb, K. Kempe, J. M. García, R. J. Ono, U. S. Schubert, Y. Y. Yang and J. L. Hedrick, *Polymer Chemistry*, 2016, **7**, 5862-5872.
116. C. Englert, M. Hartlieb, P. Bellstedt, K. Kempe, C. Yang, S. K. Chu, X. Ke, J. M. García, R. J. Ono, M. Fevre, R. J. Wojtecki, U. S. Schubert, Y. Y. Yang and J. L. Hedrick, *Macromolecules*, 2015, **48**, 7420-7427.
117. O. Sedlacek, O. Janouskova, B. Verbraeken and R. Hoogenboom, *Biomacromolecules*, 2019, **20**, 222-230.
118. J. H. Jeong, S. H. Song, D. W. Lim, H. Lee and T. G. Park, *Journal of Controlled Release*, 2001, **73**, 391-399.
119. Q. X. Fernandes JC, Winnik FM, Benderdour M, Zhang X, Dai K, Shi Q, *International Journal of Nanomedicine*, **1**, 4091-4102.
120. M. Bauer, L. Tauhardt, H. M. L. Lambermont-Thijs, K. Kempe, R. Hoogenboom, U. S. Schubert and D. Fischer, *European Journal of Pharmaceutics and Biopharmaceutics*, 2018, **133**, 112-121.
121. A. K. Blakney, G. Yilmaz, P. F. McKay, C. R. Becer and R. J. Shattock, *Biomacromolecules*, 2018, **19**, 2870-2879.
122. M. Mees, E. Haladjova, D. Momekova, G. Momekov, P. S. Shestakova, C. B. Tsvetanov, R. Hoogenboom and S. Rangelov, *Biomacromolecules*, 2016, **17**, 3580-3590.
123. N. Toncheva-Moncheva, E. Veleva-Kostadinova, C. Tsvetanov, D. Momekova and S. Rangelov, *Polymer*, 2017, **111**, 156-167.
124. A. K. Blakney, Y. Abdouni, G. Yilmaz, R. Liu, P. F. McKay, C. R. Bouton, R. J. Shattock and C. R. Becer, *Biomacromolecules*, 2020, **21**, 2482-2492.
125. T. Bus, C. Englert, M. Reifarth, P. Borchers, M. Hartlieb, A. Vollrath, S. Hoeppener, A. Traeger and U. S. Schubert, *Journal of Materials Chemistry B*, 2017, **5**, 1258-1274.

126. A. B. Cook, R. Peltier, J. Zhang, P. Gurnani, J. Tanaka, J. A. Burns, R. Dallmann, M. Hartlieb and S. Perrier, *Polymer Chemistry*, 2019, **10**, 1202-1212.
127. T. Lorson, M. M. Lübtow, E. Wegener, M. S. Haider, S. Borova, D. Nahm, R. Jordan, M. Sokolski-Papkov, A. V. Kabanov and R. Luxenhofer, *Biomaterials*, 2018, **178**, 204-280.
128. G.-H. Hsiue, H.-Z. Chiang, C.-H. Wang and T.-M. Juang, *Bioconjugate Chemistry*, 2006, **17**, 781-786.
129. D. Witzigmann, D. Wu, S. H. Schenk, V. Balasubramanian, W. Meier and J. Huwyler, *ACS Applied Materials & Interfaces*, 2015, **7**, 10446-10456.
130. B. S. Kim, S. Osawa, J. Yum, M. Naito and K. Miyata, *Bioconjugate Chemistry*, 2020, **31**, 1320-1326.
131. A. C. Rinkenauer, L. Tauhardt, F. Wendler, K. Kempe, M. Gottschaldt, A. Traeger and U. S. Schubert, *Macromolecular Bioscience*, 2015, **15**, 414-425.
132. Z. He, L. Miao, R. Jordan, D. S-Manickam, R. Luxenhofer and A. V. Kabanov, *Macromolecular Bioscience*, 2015, **15**, 1004-1020.
133. D. Hertz, M. N. Leiske, T. Wloka, A. Traeger, M. Hartlieb, M. M. Kessels, S. Schubert, B. Qualmann and U. S. Schubert, *Journal of Polymer Science Part A: Polymer Chemistry*, 2018, **56**, 1210-1224.
134. T. von Erlach, S. Zwicker, B. Pidhatika, R. Konradi, M. Textor, H. Hall and T. Lühmann, *Biomaterials*, 2011, **32**, 5291-5303.
135. E. Haladjova, S. Halacheva, D. Momekova, V. Moskova-Doumanova, T. Topouzova-Hristova, K. Mladenova, J. Doumanov, M. Petrova and S. Rangelov, *Macromolecular Bioscience*, 2018, **18**, 1700349.
136. A.-K. Trützschler, T. Bus, M. Sahn, A. Traeger, C. Weber and U. S. Schubert, *Biomacromolecules*, 2018, **19**, 2759-2771.
137. M. N. Leiske, F. H. Sobotta, F. Richter, S. Hoeppener, J. C. Brendel, A. Traeger and U. S. Schubert, *Biomacromolecules*, 2018, **19**, 748-760.
138. A. Kara, N. Ozturk, G. Esendagli, U. U. Ozkose, S. Gulyuz, O. Yilmaz, D. Telci, A. Bozkir and I. Vural, *Artificial Cells, Nanomedicine, and Biotechnology*, 2018, **46**, S264-S273.
139. S. Osawa, K. Osada, S. Hiki, A. Dirisala, T. Ishii and K. Kataoka, *Biomacromolecules*, 2016, **17**, 354-361.

2 The Synthesis of Cationic Poly[(2-oxazoline)-*co*-(ethylenimine)] Bottlebrush Copolymers for the Delivery of Genetic Material

2.1 Introduction

Bottlebrush copolymers, or molecular brushes, are a subsection of graft copolymers. Each repeating unit along the linear backbone of a bottlebrush copolymers carries a polymeric side chain, resulting in a densely grafted copolymer.[1-3] Due to their highly grafted structure, bottlebrush copolymers exhibit unique properties such as stretched polymeric backbone, high persistence lengths, decreased chain entanglement, and anisotropic conformations.[1] These properties make bottlebrush copolymers interesting for a number of applications, including lubricants,[4] drug delivery vehicles,[5, 6] surface coatings,[7] and responsive materials.[6]

The development of controlled polymerisation techniques such as reversible-deactivation radical polymerisation (RDRP) and ring-opening polymerisation have enabled straightforward access to these polymeric architectures,[8] and their synthesis can be achieved *via* three different processes: grafting-from, grafting-to, and grafting-through.[9] Each process has its own advantages and disadvantages, requiring selection of the appropriate route for the desired material properties.

Grafting-from polymerisation involves the polymerisation of a monomer from a macro-initiator, which forms the backbone of the bottlebrush. This method affords excellent control over the backbone of the bottlebrush, and copolymerisation with non-initiating comonomers can reduce the density of the grafts. However, side reactions such as brush-brush coupling can cause deviations from the bottlebrush structure and the dispersity of the grafted chains can be higher than those found in other techniques.[10]

Grafting-to bottlebrush formation is achieved by attaching polymer chains to an activated backbone *via* a coupling reaction. This technique enables excellent control over the size and dispersity of both the bottlebrush backbone and grafted sidechains. In addition, the introduction of functionalities incompatible with the chosen polymerisation technique can be achieved. The efficiency of the coupling step to form the bottlebrush polymers is the main limitation with this method. Each additional side chain increases the steric demand of the polymer, making subsequent graft additions challenging. This is especially prevalent for the attachment of long grafts, limiting the size of the polymer chains that can be efficiently attached.

The grafting-through approach is based on the polymerisation of a macromonomer. Conceptually, this is the most straightforward route to the synthesis of bottlebrush polymers resulting in a graft at every position along the backbone, however in practice it

is more challenging. The lack of commercially available macromonomers requires the synthesis of macromonomers if certain properties are required. Furthermore, the concentration of the polymerisable end-group is effectively diluted by attachment to a large polymer chain, with high monomer concentrations resulting in highly viscous reaction mixtures. This approach is therefore suited to the synthesis of bottlebrush polymers with low molecular weight grafts.

Poly(2-oxazoline) (POx) bottlebrush polymers have been synthesised by all of the approaches mentioned above, present as the polymeric backbone, grafts, or both. Due to the facile introduction of functionalities to either the α- or ω-end group of the polymer,[11] POx provides an excellent platform for the synthesis of bottlebrush polymers. In addition, the choice of monomer can provide a functional handle for attaching grafts or imparting properties such as biocompatibility[12] or thermoresponsiveness.[13] A plethora of end-groups capable of undergoing further polymerisation have been incorporated into POxs,[14] with (meth)acrylate,[15-21] styryl,[15, 22-24] diene, cyclic alkenes such as norbornene,[25] and pyrrole[26] macromonomers reported. Functional groups for click reactions such as alkynes, azides and thiols are also readily accessible, allowing for grafting-to reactions to be undertaken. Macro-initiators and their subsequent use to synthesise bottlebrush polymers have also been reported such as poly(2-isopropenyl-2-oxazoline),[27] which contains pendent 2-oxazoline rings, or 2-oxazoline monomers containing SET-LRP initiators.[28, 29]

In this chapter, a series of styryl-containing poly(2-ethyl-2-oxazoline)s (PEtOx) are synthesised and their subsequent RAFT-mediated polymerisation to form bottlebrush polymers investigated. The bottlebrush polymers are further hydrolysed to form poly[(2-ethyl-2-oxazoline)-*co*-(ethylenimine)] [P(Ox-*co*-EI)] copolymers, and their structure analysed by a suite of techniques to determine the structure after hydrolysis.

2.2 Results and Discussion

Poly(2-oxazoline)s can undergo hydrolysis of the pendent amide bond to form poly(ethylenimine), a secondary amine containing linear polymer.[30, 31] In order to hydrolyse the amide bond, harsh acidic or basic reaction conditions are required, involving high concentrations of the acid/base and high reaction temperatures (> 100 °C). Therefore, if one wishes to synthesise homo- or copolymers of poly(ethylenimine) with a more complex architecture than a linear polymer, the scaffold of the architecture must be able to withstand these reaction conditions.

For bottlebrush polymers, these restrictions limit the choice of the macromonomers propagating group, effectively ruling out (meth)acrylates and (meth)acrylamides for post-polymerisation hydrolysis. Styryl macromonomers provide an effective route towards non-degradable architectures. In addition, there have been several reports on their synthesis and subsequent polymerisation,[15, 22, 23] with Störkle *et al.* reporting their hydrolysis to form bottlebrush poly(ethylenimine).[24] Previous reports on the preparation of styryl poly(2-oxazoline) macromonomers describe two synthetic routes to introduce a styrene end-group, one using a functional initiator and the other using a functional terminating agent.

2.2.1 4-Vinylbenzyl Iodide as an Initiator for the Polymerisation of 2-Ethyl-2-Oxazoline

As mentioned previously, styrene functionalised POxs can be synthesised *via* use of a functional initiator or terminating agent. 4-vinylbenzyl chloride (4-VBC) was chosen to initiate the polymerisaton and install the styryl-functionality. Due to their electrophilic carbon-halide bond, alkyl halides can be used as initiators for the polymerisation of EtOx. Furthermore, 4-VBC is commercially available, alleviating the need for synthesising initiators or terminating agents.

Alkyl chlorides, are however, poor initiators due to their slow rate of initiation and propagation.[32] This is due to the chloride ion being a poor leaving group and its ability to ring-open the oxazolinium chain-end. This process is reversible and exists in equilibrium with formation of the covalent species favoured (**Scheme 2.1**).

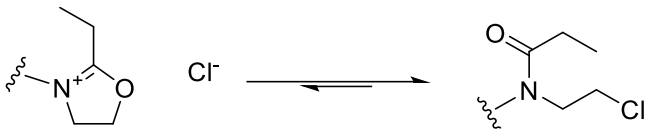

Scheme 2.1 Schematic representation of the equilibrium between ionic and covalent propagating species with a chloride counter ion.

To overcome the slow propagation rate of alkyl chlorides addition of sodium iodide (NaI) to the polymerisation mixture generates 4-vinylbenzyl iodide (4-VBI) *in situ* which has a much higher rate of initiation and propagation. The halogen exchange is driven by the Finkelstein reaction, where NaI reacts with an alkyl chloride to produce the corresponding alkyl iodide and NaCl.[33] Due to the insolubility of NaCl in acetonitrile it precipitates and the equilibrium is driven towards the formation of the alkyl iodide. Generation of 4-VBI *in situ* is advantageous due to the difficulties with storage and synthesis of alkyl iodides compared to alkyl chlorides or bromides.[34]

Initial studies revealed the importance of purifying NaI before addition to the reaction mixture. NaI is hygroscopic and can also oxidise to form iodine (I_2) in the presence of oxygen. Both impurities can have detrimental effects on the polymerisation as I_2 can initiate the polymerisation[35] and water can terminate and initiate it. Due to these impurities, initial experiments resulted in low yields and polymers with a mixture of end-groups. NaI can be purified by recrystallisation from a water:ethanol mixture, followed by drying overnight in a vacuum oven at 40 °C.

MALDI-TOF measurements of poly(2-methyl-2-oxazoline) (MeOx) initiated by purified and crude NaI revealed the detrimental effect of impure NaI on the end-groups of the polymer, with the main population possessing an α-hydrogen end-group, as opposed to the targeted α-styrene for the use of the crude salt (**Figure A2.1**). The low yield (10 %) of the polymerisation was attributed to the insolubility of H-initiated PMeOx in dichloromethane (DCM), which is used in the purification of the polymer.

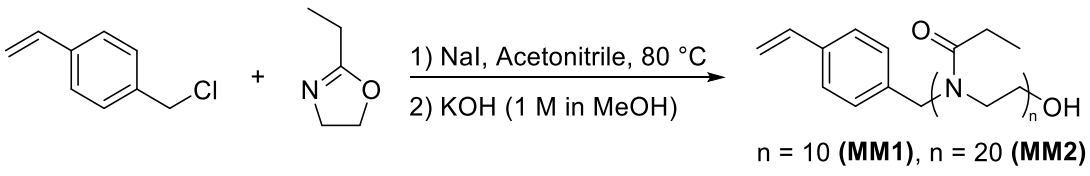

Scheme 2.2 Schematic representation of the synthesis of **MM1** and **MM2**.

Using purified NaI two PEtOx macromonomers were synthesised, targeting DP 10 and 20 (**MM1** and **MM2** respectively, **Scheme 2.2**). The targeted DP was calculated from the molar ratio of monomer to initiator. For the polymerisation, NaI (1.5 eq to 4-VBC) was added to a dry Schlenk flask under a flow of N_2 followed by addition of 4-VBC (1 eq) and acetonitrile. The flask was sealed and placed into an 80 °C oil bath for 1 hour to ensure full conversion of 4-VBC to 4-VBI, resulting in the precipitation of NaCl. Once the halide exchange had gone to completion, the Schlenk flask was reopened and EtOx was added under a flow of N_2. The sealed flask was transferred back into the oil bath and heated at 80 °C for 1 hour. Upon completion of the polymerisation, a methanolic solution of potassium hydroxide (KOH) was added to terminate the polymerisation and introduce a hydroxyl group at the ω-terminus (**Scheme 2.2**).

The polymer was first purified by centrifugation to remove the NaCl precipitate from the solution before removal of acetonitrile under reduced pressure. The product was dissolved in DCM and centrifuged once more to remove any insoluble salts. Subsequent washing of the organic layer with saturated Na_2CO_3 and brine was used to remove residual NaI and KOH from solution before precipitation in cold diethyl ether to yield the final macromonomers (**Table 2.1**).

Table 2.1 Characterisation data for macromonomers, **MM1** and **MM2**

			SEC[b]		**MALDI[c]**	
Polymer	**DP_{theo}**	**Conv. (%)[a]**	**M_n (g mol^{-1})**	**$Đ$**	**M_n (g mol^{-1})**	**$Đ$**
MM1	10	≥ 99	1,100	1.18	1,100	1.05
MM2	20	≥ 99	3,400	1.10	2,000	1.02

[a] Monomer conversion determined by ^{1}H-NMR. [b] M_n and $Đ$ calculated from SEC with DMF as the eluent and a PMMA calibration. [c] Matrix – DCTB, Salt – NaI, calibrant – PEG methyl ether methacrylate (M_n = 420 g mol^{-1}) or PEG methyl ether (M_n = 2000 g mol^{-1})

Characterisation of the macromonomers by nuclear magnetic resonance (NMR), size-exclusion chromatography (SEC) and Matrix-Assisted Laser Desorption/Ionisation Time of Flight Mass Spectrometry (MALDI-TOF MS) provided insight into the resulting structure of the macromonomers.

NMR was used to confirm the presence of the styryl α-end group after purification of the macromonomers. **Figure 2.1** shows the NMR spectrum of **MM1**. Peaks corresponding to

the vinyl group (δ = 6.76 (a), 5.82 (c), and 5.23 ppm (b)) were present indicating incorporation of the 4-vinylbenzyl moiety and their integrals match the theoretical ratios when compared to the benzyl protons (7.20-7.52 ppm) of 4:1:1:1, implying no consumption of the vinyl group during the polymerisation. In addition, the ratio of integrals between the vinyl protons and those corresponding to the PEtOx backbone indicate a DP of 13.

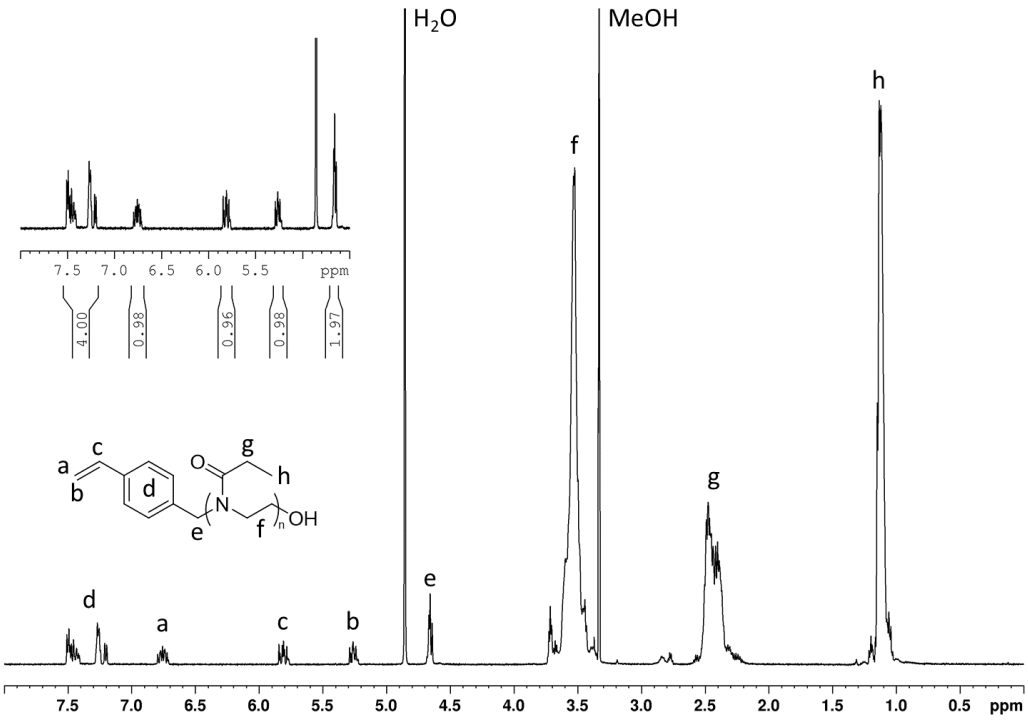

Figure 2.1 ^{1}H NMR (400 MHz) spectrum of **MM1** in MeOD. Insert shows the vinyl and aromatic protons of the α-styryl end-group.

SEC measurements of **MM1** (**Figure 2.2**) and **MM2** (**Figure A2.3**) revealed mono-modal molecular weight distributions with low polydispersity (*Đ*), with the molecular weights obtained closely matching those of MALDI and NMR.

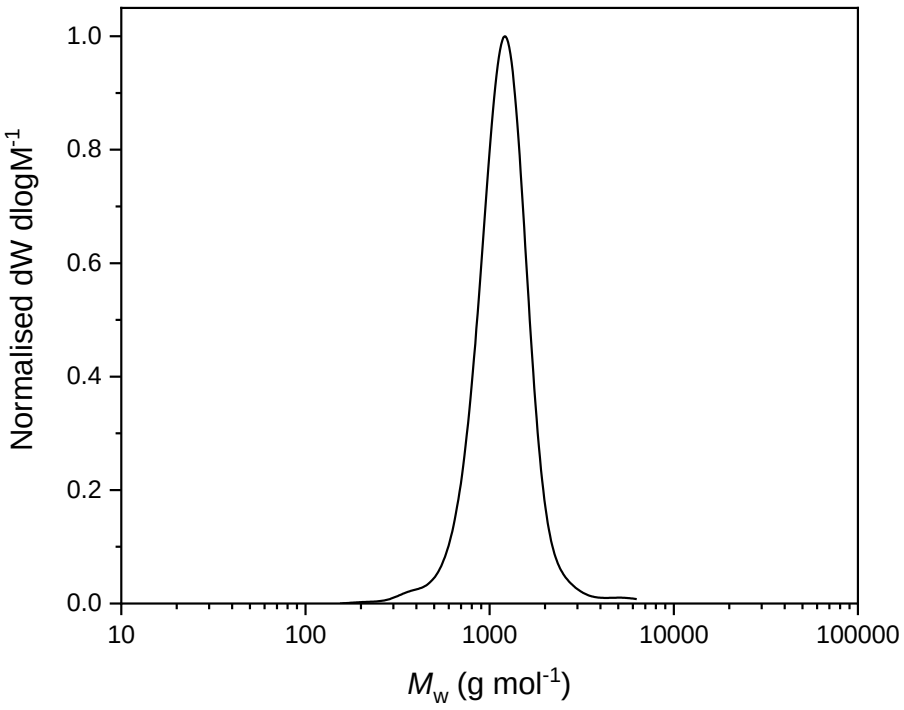

Figure 2.2 SEC graph of **MM1** using THF as an eluent (PMMA calibration).

MALDI-TOF MS is a powerful technique for the characterisation of low molecular weight polymers, allowing for the determination of end-groups, monomer distributions, and molecular weight distributions.[36] **MM1** and **MM2** were subsequently analysed by MALDI-TOF to determine their end-groups and molecular weights. **Figure 2.3** shows the MALDI-TOF spectra of **MM1** revealing two main polymer distributions. The difference in m/z between each peak is 99.068, representing the EtOx repeating unit.

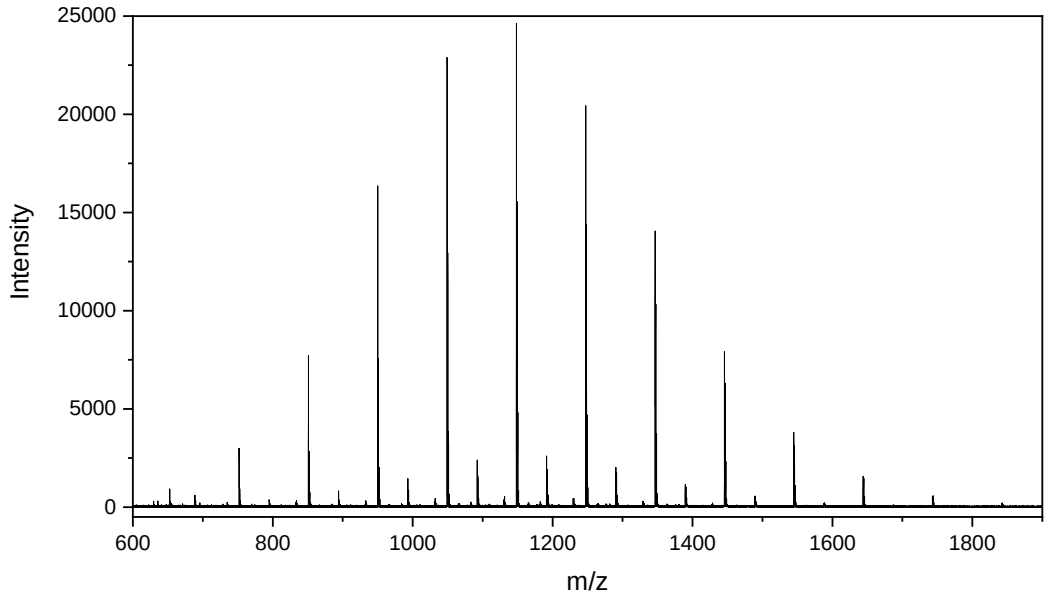

Figure 2.3 MALDI-TOF spectrum of **MM1**. MALDI collected using DCTB as a matrix and NaI as a salt. PEG methyl ether acrylate (M_n = 420 g mol^{-1}) was used to calibrate the instrument.

Using the software Isotope Pattern (Bruker) the end-groups were determined and assigned to the spectra shown in **Figure 2.4**. The main polymer distribution contains the desired α-styrene and ω-hydroxyl end groups. A secondary distribution is present owing to the presence of a ω-ethanolamine end-group. This is a common end-group arising from the nucleophilic attack of water at the 2-position of the oxazolinium propagating chain end, instead of attack at the 5-position which results in the presence of the hydroxyl functionality. A third distribution with very low intensity was observed in the spectrum where an α-hydrogen and ω-hydroxyl end groups can be assigned. H-initiated chains tend to arise from β-abstraction of a hydrogen on an oxazolinium chain end by an oxazoline monomer. This results in a monomer activated towards subsequent monomer addition and an ω-enamine end-group on the polymer where abstraction has taken place.[37]

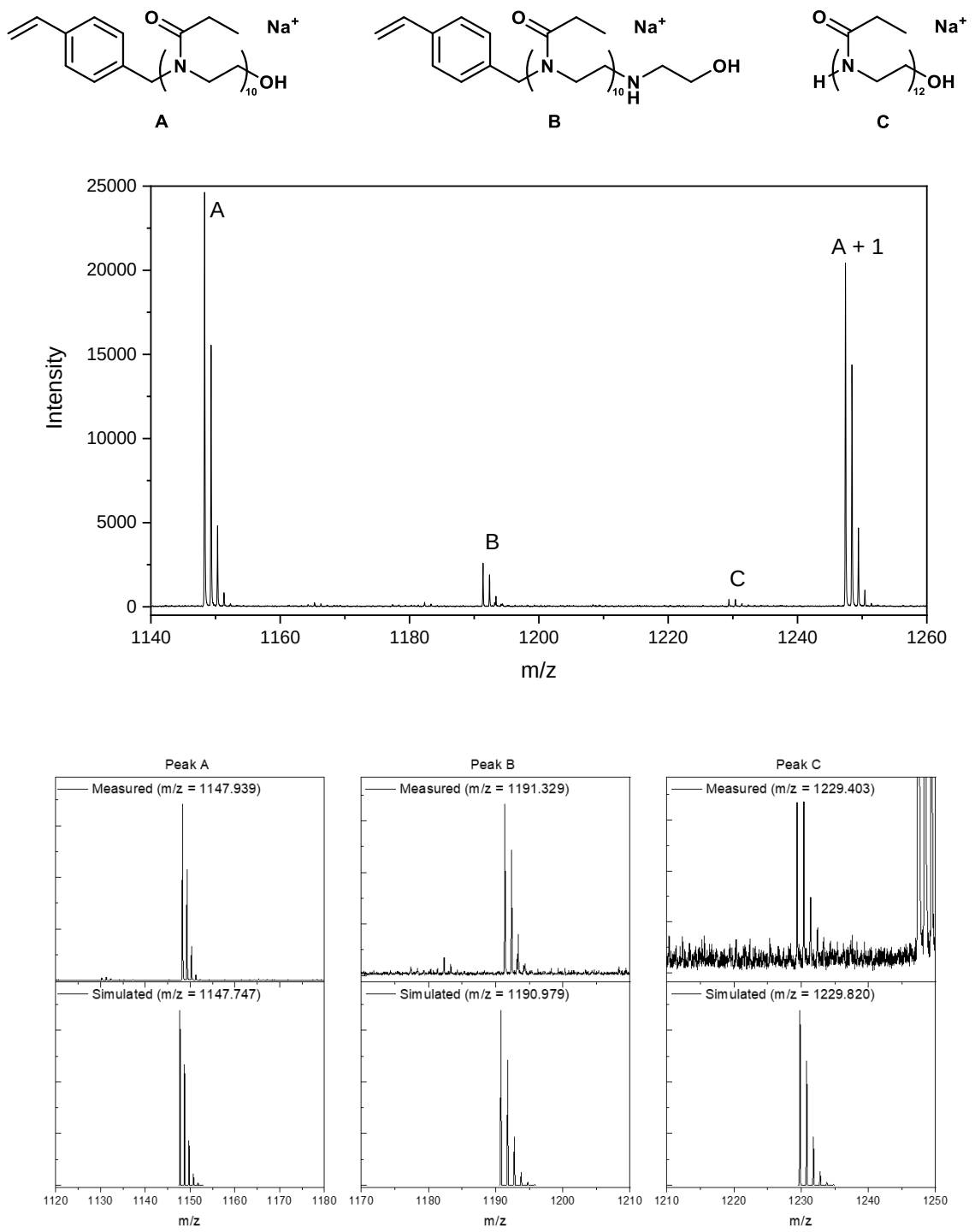

Figure 2.4 Magnified and assigned MALDI-TOF spectrum of **MM1**. Bottom figure exhibits simulated isotopic distributions and corresponding peak from measured spectra.

As mentioned previously, MALDI-TOF can also be used to determine the molecular weight distribution of the polymer using **Equation 2.1** and **Equation 2.2**, with the dispersity determined by **Equation 2.3**. The peak intensity is related to the number of moles of each polymer species and the m/z representing the polymer mass. The m/z determined by MALDI-TOF includes the mass of the counter ion, in this instance Na^+,

which needs to be subtracted from the m/z before calculation of the molecular weight distributions. Furthermore, an assumption is made that all polymers are proportionally represented in the MALDI-TOF distribution. At high molecular weights, the polymer species can become underrepresented as they are harder to desorb and detect. As the polymers analysed are of low molecular weights these effects are assumed to be negligible. The M_n and $Đ$ of **MM1** and **MM2** determined by MALDI-TOF are shown in **Table 2.1**, and closely match the targeted DP.

$$M_n = \frac{\sum(m/z - Na^+) \times intensity}{\sum intensity} \quad \textbf{2.1}$$

$$M_w = \frac{\sum(m/z - Na^+)^2 \times intensity}{\sum(m/z - Na^+) \times intensity} \quad \textbf{2.2}$$

$$Đ = \frac{M_w}{M_n} \quad \textbf{2.3}$$

2.2.2 RAFT-mediated Polymerisation of PEtOx Macromonomer

Bottlebrush synthesis was achieved *via* the grafting-through method using RAFT polymerisation to exert control over the molecular weight of the resulting copolymers. Using **MM1** and **MM2**, kinetic investigations followed by a series of polymerisations targeting varying molecular weights was undertaken to probe the limits of macromonomer polymerisation. Li *et al.* reported that under aqueous RAFT conditions, the polymerisation of amphiphilic macromonomers proceeded at an enhanced rate compared to polymerisation in organic solvents.[38] The polymerisations of **MM1** and **MM2** were therefore carried out in aqueous solution using the RAFT agent 3-((((1-carboxyethyl)thio)carbonothioyl)thio)propanoic acid (PAPATC) to control the polymerisation (**Scheme 2.3**).

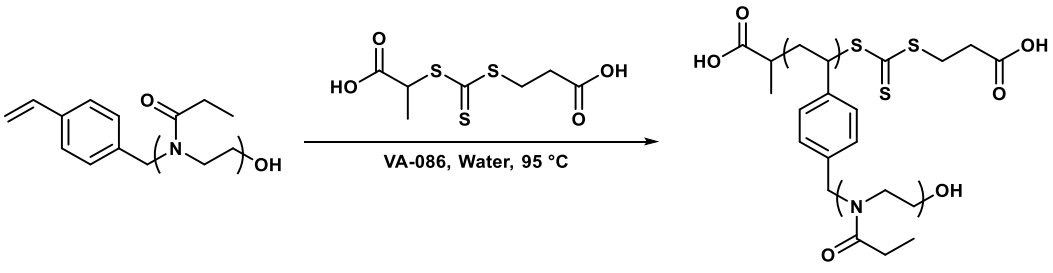

Scheme 2.3 Schematic representation of the synthesis of bottlebrush polymers from a PEtOx macromonomer.

2.2.2.1 Kinetics of Macromonomer Polymerisation

A kinetic study was undertaken to understand the evolution of molecular weight over the course of the polymerisation and to determine the time required to reach full conversion of the macromonomer **MM1** (**Figure 2.5**). A bottlebrush copolymer of DP 60 was targeted and samples for NMR and SEC were taken at various time points. The polymerisation was performed under aqueous conditions with an initial monomer concentration of 0.1 M and the water-soluble initiator VA-086 was used to initiate the polymerisation.

An induction period with no monomer conversion is observed at the beginning of the reaction. Conversion of the macromonomer was determined by comparing the PEtOx backbone to the vinyl protons corresponding to the styryl end-group. From the plot of conversion against time it appears that no conversion occurs during the first 20 minutes of the polymerisation. It is unknown if this phenomenon occurs in the polymerisation reported by Li *et al.* as their kinetic experiments did not sample at this early stage of the polymerisation.[38]

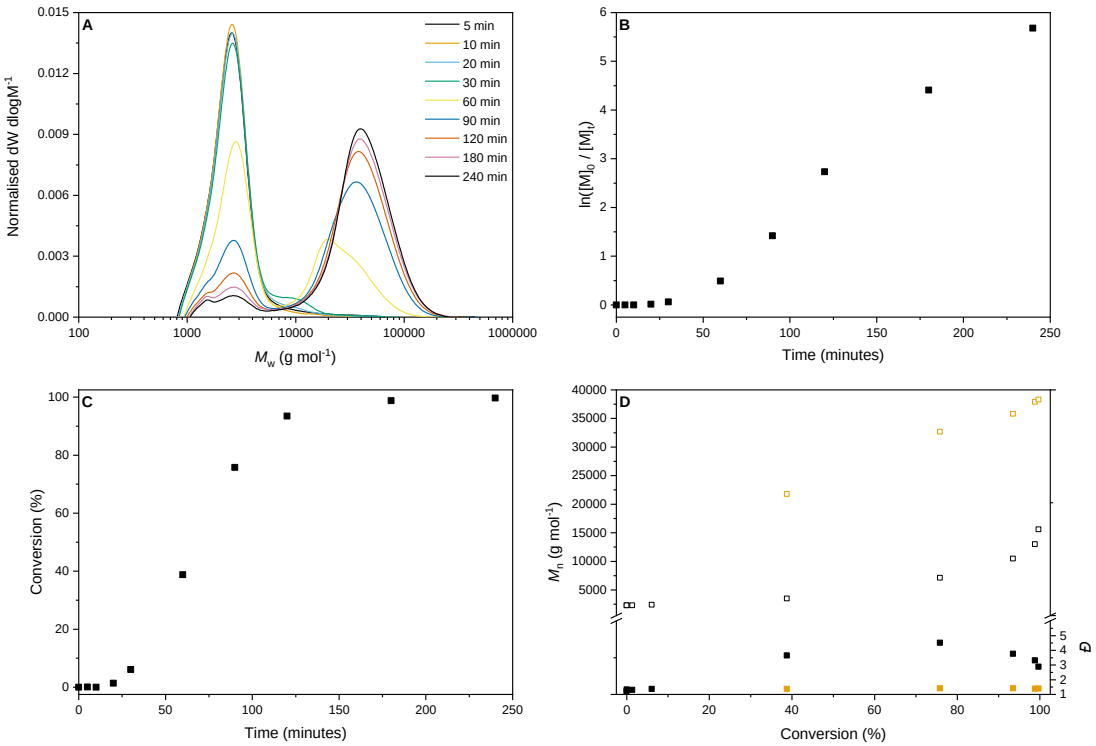

Figure 2.5 Kinetics for the polymerisation of **MM1** ([**MM1**] = 0.1 M, Target DP = 60) at 95 °C. A – Evolution of molecular weight over time. B – First-order kinetic plot. C – Conversion of MM1 over time. D – Evolution of molecular weight (hollow square) and dispersity (full square)

with increasing monomer conversion. Black trace represents the integration of the full SEC trace, Orange represents the integration of the peak associated with the bottlebrush polymer.

It was observed when carrying out the polymerisation kinetics that the reaction solution became turbid at the beginning of the polymerisation, before returning to a transparent yellow solution. This change correlates to the induction period observed in the polymerisation kinetics. A cloud point (Cp) measurement of **MM1** was undertaken to determine if the macromonomer possesses and thermal response. By measuring absorbance as a function of temperature using a UV-Vis spectrophotometer, a sharp increase in absorbance upon heating is observed. **Figure 2.20** shows that **MM1** possesses a Cp at 90 °C, indicating that the turbid nature of the polymerisation mixture could be caused by the thermal response of the macromonomer. PEtOx is known to possess a molecular weight dependent lower critical solution temperature (LCST) between 94 °C and 66 °C for polymers above DP 100 (M_w = 10,000 g mol^{-1}), however **MM1** has a much lower molecular weight, indicating a negative effect of the styryl end-group on the water solubility of the polymer.[39, 40] Despite the Cp, the polymerisation was carried out at 95 °C due to the favourable kinetics and no apparent negative effect of the Cp on the outcome of polymerisation

After the initial induction period the polymerisation of **MM1** proceeds under first-order kinetics indicated by a linear dependence of $\ln([M]_0/[M]_t)$ against time (**Figure 2.5**), with the monomer conversion reaching 99% within 4 hours.

2.2.2.2 Macromonomer Polymerisation

Using the information provided by the kinetic study, the polymerisation of **MM1** in aqueous conditions mediated with PAPATC at 95 °C using VA-086 as initiator and an initial [**MM1**] = 0.1 was investigated (**Table 2.3**). Initial polymerisation of **MM1** resulted in polymers with high dispersity and molecular weights (**B10-25A, Figure 2.6**). The pH of the polymerisation mixture was measured and found to be highly alkaline (pH > 10). This was rationalised to be caused by the presence of residual terminating agent, unremoved from the synthesis of the macromonomer, or due to the ethanolamine ω-end-group present as minor end group functionality of the macromonomer. Addition of 1 M HCl to reduce the pH to 7 resulted in RAFT polymerization producing a low dispersity polymer (**B10-25, Figure 2.6**). Further investigations are required to determine the cause

of this pH dependency; however, it is known that deprotonation of the carboxylic acid functionality on the R-group of similar RAFT agents reduces the control over the polymerisation. In addition, RAFT agents are susceptible to aminolysis by primary and secondary amines, converting the trithiocarbonate end-group into a free thiol.[41] The presence of the ω-ethanolamine terminated macromonomer may cause the aminolysis of the RAFT agent, with protonation of the secondary amine hindering this process.

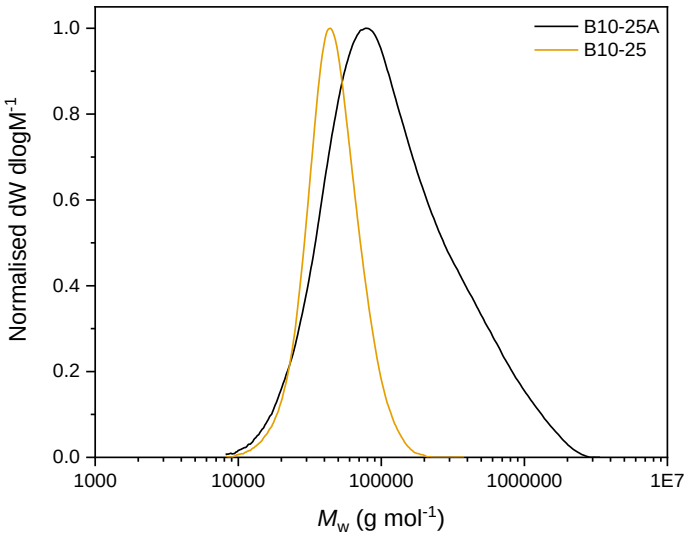

Figure 2.6 SEC chromatogram of **B10-25A** (black) and **B10-25** (orange) using DMF as an eluent (PMMA calibration).

By increasing the ratio of [M]/[CTA] various degrees of polymerisation were targeted, ranging from 10 – 100 (**Table 2.2**). The monomer and initiator concentration remained constant, with the RAFT agent concentration decreased to achieve the targeted ratio. The polymerisation of **MM1** proceeded with excellent control up to a targeted DP of 50, with $Đ \leq 1.3$ (RI detector). However, high dispersity polymers were obtained when targeting a DP of 100. At high molecular weight, the concentration of RAFT agent relative to the macromonomer is greater, causing side reactions such as aminolysis to be exacerbated leading to poorer control over the polymerisation.

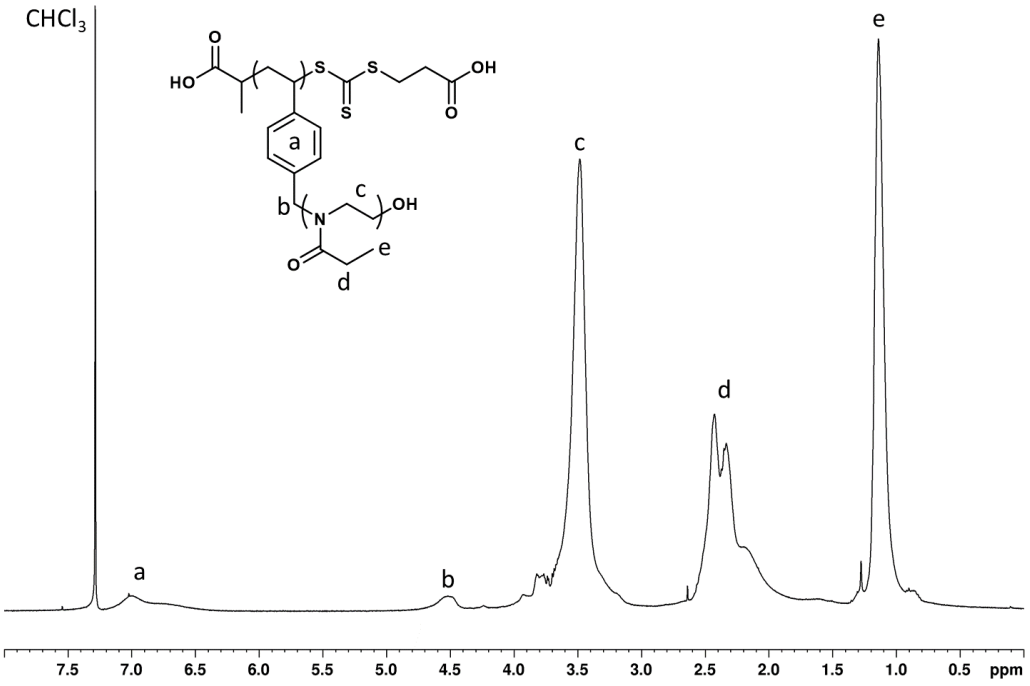

Figure 2.7 Assigned ^{1}H NMR spectrum of **B10-10** in $CDCl_3$.

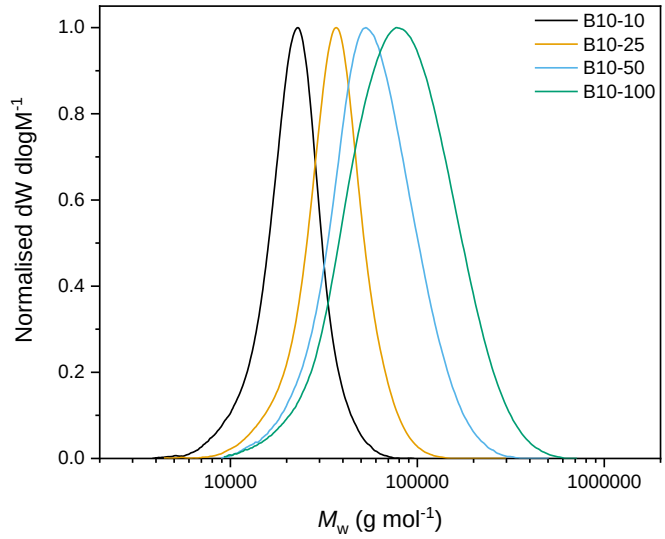

Figure 2.8 SEC chromatogram of **B10-10** (black), **B10-25** (orange), **B10-50** (blue), and **B10-100** (green) using DMF as an eluent (PMMA calibration).

The bottlebrush copolymers were analysed using universal calibration size exclusion chromatography (SEC) to obtain accurate molecular weight values (**Figure 2.8**). When analysing complex architectures by conventional SEC using a concentration detector,

such as RI, the molecular weight can often be underestimated as it is calculated based on the hydrodynamic volume of the polymer in solution. For certain polymeric architectures, the hydrodynamic volume is reduced compared to a linear analogue of the same molecular weight.

The results obtained by universal calibration SEC exhibited a large increase in M_n and $Đ$ compared to use of an RI detector. Interestingly, the M_n obtained with an RI detector closely matched the theoretical molecular weight.

Table 2.2 Characterisation data for bottlebrush polymers synthesised from **MM1**.

				RI[b]		VS[c]	
Polymer	**[M]/[CTA]**	**[CTA]/[I]**	**Conv.** [a] **(%)**	M_n **(g mol^{-1})**	$Đ$	M_n **(g mol^{-1})**	$Đ$
B10-25A	25	5	≥ 99	76,400	2.70	-	-
B10-10	10	10	≥ 99	20,000	1.15	33,900	1.34
B10-25	25	5	≥ 99	32,600	1.17	63,700	1.52
B10-50	50	2	≥ 99	49,800	1.32	117,000	1.84
B10-100	100	1	≥ 99	65,800	1.49	-	-

[a] Monomer conversion determined by ^{1}H-NMR. M_n and $Đ$ calculated from SEC with DMF as the eluent and a PMMA calibration (b) and universal calibration (c).

In an attempt to produce polymers with a DP of 100 and low dispersity an additional series of experiments were undertaken, varying the monomer and initiator concentrations (**Table 2.3**). For **B10-100A-C** the initial monomer concentration was changed. Decreasing [M] to 0.01 (**B10-100A**) resulted in incomplete conversion of **MM1**. When [M] = 0.05 (**B10-100B**) there was full conversion of the macromonomer, however the $Đ$ remained high. Increasing [M] to 0.2 (**B10-100C**) also resulted in complete conversion of the macromonomer, with a further increase in $Đ$ (**Figure A2.9**).

Because the initiator concentration was fixed during the initial experiments, the [CTA]/[I] ratio was low for **B10-100** compared with lower molecular weight bottlebrush copolymers. The ratio between [CTA] and [I] determines the "livingness" of the polymerisation, with a lower [CTA]/[I] causing a greater degree of irreversible termination during polymerisation.[42] This would lead to detrimental effects on the $Đ$ of

the resulting polymer. By decreasing the concentration of initiator relative to the CTA concentration, higher [CTA]/[I] ratios were investigated. In **B10-100D** and **B10-100E** the macromonomer went to full conversion, however the *Đ* remained high (**Figure A2.10**). These results exhibit a limitation of this system, but one that is not unique to these macromonomers. A PEG methacrylate macromonomer, with similar M_n, exhibits high *Đ* when targeting high DPs.[43]

Table 2.3 Characterisation data for bottlebrush copolymers synthesised from **MM1**, with a targeted DP of 100 of the polymer backbone.

Polymer	[M]	[CTA]/[I]	Conv. (%)[a]	M_n (g mol^{-1})[b]	*Đ*[b]
B10-100A	0.01	1	61	6,400	6.16
B10-100B	0.05	1	≥ 99	72,300	1.51
B10-100C	0.20	1	≥ 99	76,900	1.67
B10-100D	0.10	5	≥ 99	69,900	1.59
B10-100E	0.10	10	≥ 99	62,400	1.50

[a] Monomer conversion determined by ^{1}H-NMR. [b] M_n and *Đ* calculated from SEC with DMF as the eluent and a PMMA calibration.

Lastly, a series of polymerisations using **MM2** were carried out, allowing for bottlebrush copolymers with higher graft-lengths to be synthesised (**Table 2.4**). The polymerisation of **MM2** exhibited the same trend as **MM1** with good control over the polymerisation achieved for a targeted DP 10 (**B20-10**) and 50 (**B20-50**) and poor control when targeting DP 100 (**B20-100**) (**Figure 2.9**).

Table 2.4 Characterisation data for bottlebrush polymers synthesised from **MM2**.

Polymer	[M]/[CTA]	Conv. (%)[a]	M_n (g mol^{-1})[b]	*Đ*[b]
B20-10	10	≥ 99	21,900	1.19
B20-50	50	≥ 99	49,400	1.32
B20-100	100	≥ 99	91,900	1.87

[a] Monomer conversion determined by ^{1}H-NMR. [b] M_n and *Đ* calculated from SEC with DMF as the eluent and a PMMA calibration.

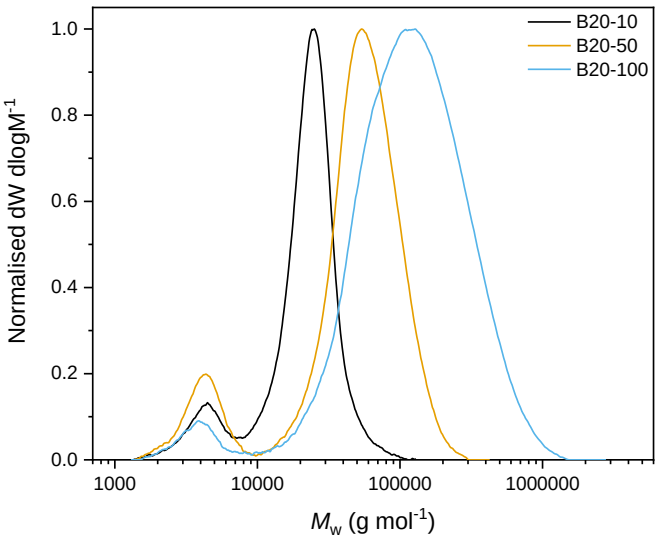

Figure 2.9 SEC chromatogram of **B20-10** (black), **B20-50** (orange), and **B20-100** (blue) using DMF as an eluent (PMMA calibration).

2.2.3 Hydrolysis Studies on the Bottlebrush Polymers

Under acidic or basic conditions, the pendent amide bond of poly(2-oxazoline)s can be hydrolysed forming a secondary amine containing polymer. Acidic hydrolysis is preferred, as basic hydrolysis has been observed to cause the degradation of the polymer backbone and deprotonates the polymer, rendering it insoluble in aqueous solvents above a certain ethyleneimine content.[30]

Conversion of poly(2-oxazoline) to poly(ethylenimine) is traditionally achieved by refluxing the polymer in a high concentration of acid to ensure full conversion of the oxazoline. Control over the hydrolysis to target partially hydrolysed poly[(2-oxazoline)-*co*-(ethylenimine)] with specific ratios between the two units can be achieved by reducing the concentration of acid and heating above the boiling point of water for a specific time. The acidic hydrolysis of poly(2-oxazoline)s has been shown to follow pseudo-first order reaction kinetics, as there is a high concentration of hydronium ions relative to the polymer throughout the process.[44]

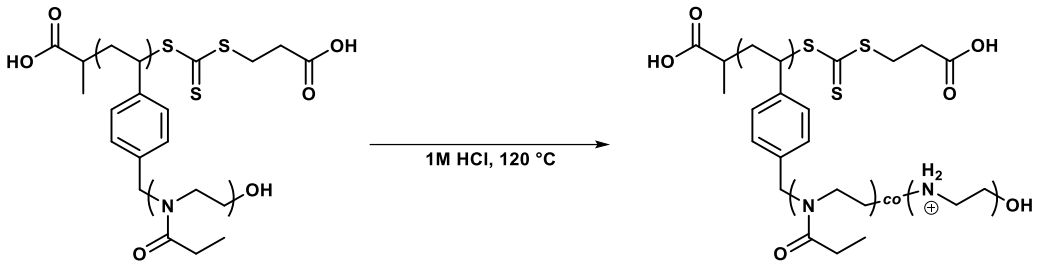

Scheme 2.4 Schematic representation of the hydrolysis of bottlebrush copolymers.

As the aim was to synthesise partially hydrolysed POx in a reproducible way, a low concentration of acid was used. In a typical reaction the polymer was dissolved in water followed by addition of 37% HCl ([HCl] = 1 M). The reaction mixture was sealed inside a microwave reaction vial and heated to 120 °C using a microwave reactor. After a predetermined time, 4 M aqueous NaOH was added to render the solution basic. The polymer was then dialysed against a 3 kDa MWCO dialysis membrane to remove the propanoic acid generated during the hydrolysis. The pure polymer was isolated by lyophilisation (**Scheme 2.4**).

2.2.3.1 Kinetics of Hydrolysis

A kinetic experiment on the hydrolysis of the bottlebrush polymers synthesised above was carried out to enable targeting of specific EtOx to EI ratios. The rate of hydrolysis for the bottlebrush polymer was compared with that of a linear PEtOx (**Chapter 3.2.1.1**) to determine if there was any difference on the rate caused by the difference in polymer architecture.

The polymers were heated for various times and the conversion was determined by comparing the NMR integrals for the oxazoline and ethylenimine backbones using **Equation 2.4**.

$$\%EI = \frac{I(PEI\ Backbone)}{I(PEI\ Backbone) + I(POx\ Backbone)} \qquad \textbf{2.4}$$

Initially there was little difference between the rate of hydrolysis of the bottlebrush and linear polymers. However, above 50 % hydrolysis the rate of hydrolysis deviated from one another, with the linear polymer reaching higher levels of EI content compared to the bottlebrush (**Figure 2.10**).

Previous studies on the effect of architecture on the rate of hydrolysis showed little difference between the two polymers.[45] One difference between the hyperbranched polymer used in the previous study and the bottlebrush polymers is the presence of a hydrophobic backbone on the bottlebrush, in addition the bottlebrush is much more sterically crowded. This could cause difficulty in hydrolysing the oxazoline units due to electrostatic repulsion.

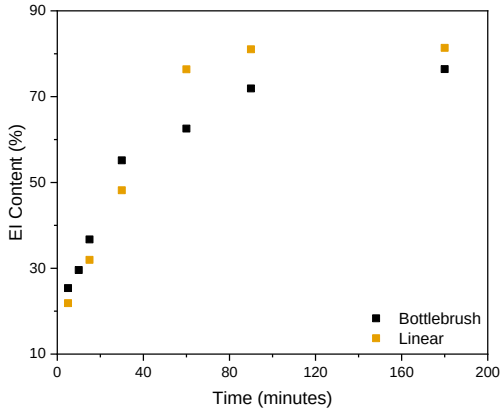

Figure 2.10 Kinetics of hydrolysis, showing conversion of EtOx to EI versus time. Bottlebrush (black) and linear (orange) polymers are compared.

2.2.3.2 Hydrolysis of Bottlebrush Polymers

Using the kinetic studies on the bottlebrush hydrolysis, a series of partially hydrolysed bottlebrush polymers were synthesised with varying degrees of hydrolysis (**Table 2.5**). The targeted degree of hydrolysis was chosen based on previous studies into P(Ox-*co*-EI) transfection agents which showed that EI content > 70% was required for efficient transfection.[45] Lower degrees of hydrolysis were synthesised to investigate whether the bottlebrush architecture allows for efficient transfection at lower EI content. Biological investigations of these polymers are carried out in **Chapter 3**.

Table 2.5 Characterisation data for hydrolysed bottlebrush polymers.

Polymer	Precursor	Time (min)	Hydrolysis (%)[a]
B10-10(32%)	B10-10	30	32
B10-10(45%)		40	45
B10-10(69%)		120	69
B10-10(78%)		180	78
B10-25(31%)	B10-25	40	31
B10-25(67%)		120	67
B10-50(37%)	B10-50	40	37
B10-50(67%)		120	67
B20-100(82%)	B20-100	120	82

[a] Conversion determined by ^{1}H-NMR.

The bottlebrush polymers were analysed by ^{1}H-NMR to determine the degree of hydrolysis using **Equation 2.4**, and further analysed below to investigate if any degradation of the architecture occurred during the hydrolysis.

2.2.3.3 Characterisation of Hydrolysed Polymers

Characterisation of the bottlebrush polymers in their pre- and post-hydrolysis state was carried out using a suite of techniques to gain greater understanding of their structure. Aqueous SEC was initially used to analyse the partially hydrolysed bottle brush copolymers using an acidic eluent (3% TFA in 0.1 mol L^{-1} NaCl) to ensure that cationic polymers are charged during the measurements and would not interact directly with the column materials. The SEC traces and light scattering data can be found in the supporting information (**Figure A2.23-A2.31**). Conventional calibration was performed using a poly(vinyl pyridine) (PVP) standard and the results can be found in **Table 6**. The obtained values for M_n are significantly lower that the molar mass of the polymer precursor or the theoretical values. This is expected as the nature of the sample and the calibration are different in chemical structure. Also, the bottle brush architecture likely leads to an underestimation of the molar mass when using a linear calibration standard.

It is interesting to note that the observed molar mass increases with increasing degree of hydrolysis. This seems counter intuitive as the ethylene imine repeating units have a lower mass than EtOx but can be explained well by an increase in hydrodynamic volume due

to charge repulsion within the polymer. The higher the charge density, the larger the polymer appears because chains are increasingly stretched out. The obtained curves appear mono modal and have narrow dispersity values except for **B20-100(82%)** which possess a high molar mass shoulder and a high dispersity, comparable to the values determined for the precursor, **B20-100**. The measurements show that hydrolysis of the EtOx units does not seem to lead to degradation or chain coupling between brushes.

Table 2.6 Characterisation data for hydrolysed bottlebrush polymers.

		SEC[a]		SEC (LS)[b]
Polymer	**Precursor**	M_n (g mol^{-1})	$Đ$	M_w (g mol^{-1})
B10-10(32%)	B10-10	7,300	1.24	4,800
B10-10(46%)		7,400	1.17	5,400
B10-10(67%)		9,700	1.19	3,100
B10-10(78%)		10,000	1.13	3,900
B10-25(31%)	B10-25	12,500	1.20	11,000
B10-25(67%)		15,900	1.16	34,700
B10-50(37%)	B10-50	19,900	1.26	75,000
B10-50(67%)		25,100	1.32	214,600
B20-100(82%)	B20-100	45,400	1.71	722,400

[a] Determined by SEC (Eluent: Water with 3% TFA and 0.1 mol L^{-1} NaCl, Calibration: Poly(vinylpyridine)), [b] Obtained by light scattering detector.

The samples were further investigated using a multi angle laser light scattering (MALLS) detector coupled to the same SEC setup. For smaller samples based on **B10-10**, the measured M_w was lower than the respective measurement with PVP calibration. This is not surprising as the scatting signal of these samples was weak, and the true mass is likely under-represented. For samples synthesized from larger precursors the molecular weight determined by light scattering is higher than the values from standard calibration giving a clear indication of a dense bottle brush architecture of the polymers. Interestingly, a trend for increasing molar masses with increasing degrees of hydrolysis can be observed. A potential reason for this could be that M_w is not a mean value over the whole sample, but rather derived from the size distribution of a SEC curve calibrated by the light

scattering detector. Thus, different elution behaviour based on hydrodynamic properties could also influence data from light scattering.

Small-angle neutron scattering (SANS) was used to determine the bottlebrush copolymers size and morphology in solution and to ascertain if the addition of cationic residues through hydrolysis caused any alteration. First, non-hydrolysed samples **B10-10**, **B10-25**, and **B10-50** were analysed in D_2O, a good solvent for the bottlebrush side chains, but a poor solvent for the poly(styrene) backbone (**Figure 2.11**). Whilst this is not completely representative of the structure of the bottlebrush polymers *in vitro*, it should give a good estimate for their conformation in solution and during complexation with nucleic acids.

The scattering intensity was fitted to a core-shell elliptical form factor for all samples, with a Hayter-Penfold rescaled mean spherical approximation structure factor to account for the structure factors observed at low-*q*. Fitting of the scattering intensity was attempted by fixing the scattering length density (SLD), which is a measure of the scattering power of a material, of the poly(styrene) core and solvent (D_2O) fixed at 1.2 x 10^{-6} Å^{-2} and 6.36 x 10^{-6} Å^{-2}, respectively. The model was then used to fit the SLD of the bottlebrush shell, along with the equatorial core radius, core-axial ratio, and shell thickness. The results of the fitting are presented in full in **Table A2.1**, with the key parameters presented in **Table 2.6**.

Table 2.7 Calculated parameters of bottlebrush polymers determined by small-angle neutron scattering.

	Length (nm)	**Diameter (nm)**	**SLD_{shell} / x 10^{-6} (Å^{-2})**
BB10-$_{10}$	10.5 ± 0.22	4.86 ± 0.27	5.81 ± 0.04
BB-10$_{25}$B	10.9 ± 0.18	6.56 ± 0.16	5.67 ± 0.04
BB-10$_{50}$	16.6 ± 0.10	7.28 ± 0.10	5.65 ± 0.03
HB0.67-10$_{50}$	14.2 ± 0.42	7.58 ± 0.42	5.91 ± 0.09

Scattering in the mid-*q* range (q = 0.02 – 0.1 Å^{-1}) is indicative of the size and shape of the bottlebrush polymers, with the region between 0.09 and 0.2 Å^{-1} corresponding to their equatorial cross-sectional diameter (**Equation 2.5**).[46] **B10-25** and **B10-50** overlap in this region, indicating similar equatorial cross-sectional diameter, with **B10-10** exhibiting a

smaller equatorial cross-sectional diameter in comparison. The cross-sectional diameter is dependent on the DP of the macromonomer.

Deviation in the scattering in the region between 0.02 and 0.09 $Å^{-1}$ is caused by the elongation of the backbone and resultant change in polymer morphology. The gradient of the slope provides information on the conformation of the polymer, with a plateau, as seen in **B10-10**, indicating more spherical objects, and an increasing gradient resulting from more elongated morphologies. This can be attributed to the increase in backbone length, causing an elongation of the bottlebrush polymer, which is more prominent at higher backbone lengths (**B10-50**). The polar radius of the core, or backbone length, was determined by multiplying the equatorial core radius by the core-axial ratio. The length of the bottlebrush in solution was determined by **Equation 2.6**, with **B10-50** exhibiting the longest backbone (16.6 ± 1.0 nm). **B10-10** and **B10-25** have similar lengths in solution of 10.5 ± 2.2 nm and 10.9 ± 1.8 nm, respectively. The maximum dimension of a bottlebrush polymer has been shown to be independent of backbone length below a certain DP, with this limit depending on the grafting density, graft length, and flexibility.[46] This could explain the similarity in length between **B10-10** and **B10-25**, with the length depending instead on side chain stretching, however further experiments with longer bottlebrush polymers would need to be undertaken to determine the DP limit.

$$Cross\ Sectional\ Diameter = (d_{shell} \times 2) + (R_{core,equatorial} \times 2) \qquad \textbf{2.5}$$

$$Length = (d_{shell} \times 2) + (R_{core,polar} \times 2) \qquad \textbf{2.6}$$

In all three bottlebrush polymers a structure factor at low-q (q = 0.004 – 0.03 $Å^{-1}$) was observed, which indicates repulsion between the individual bottlebrush polymers. This is generally observed for charged polymers which tend to repel each other in solution. The repulsive interactions between the bottlebrush polymers are attributed to the presence of the ω-ethanolamine end-group present as a minor functionality in the macromonomer. These end-groups would be deuterated in solution and can be modelled by fitting to a Hayter-Penfold rescaled mean spherical approximation structure factor.

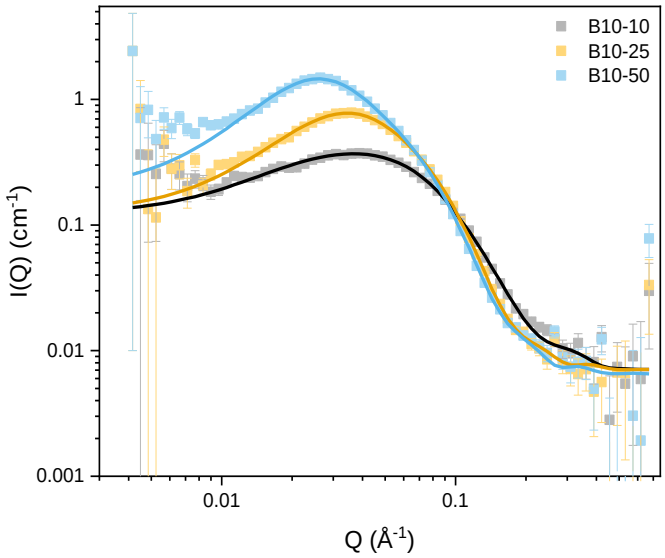

Figure 2.11 Small-angle neutron scattering of bottlebrush polymers at 10 mg mL^{-1}, fitted to a core-shell elliptical form factor (grey line). Black - **B10-10**, orange – **B10-25**, and blue - **B10-50**.

The structure factor was fitted by assuming that no salt ions are present and allowing for the fitting of the volume fraction and number of charged species. From the structure factor fitting, the number of charge units present on the bottlebrush polymer is found to increase with backbone DP. **B10-50** has 10 charged units on the polymer, indicating that 20 % of the macromonomers contain ω-ethanolamine end-groups.

A hydrolysed bottlebrush polymer, **B10-50(67%)**, was measured by SANS (**Figure 2.12**). Comparison with the parent polymer, **B10-50**, allows for the structural effects of hydrolysis to be investigated. The overlap observed at mid-*q* (q = 0.09 – 0.2 $Å^{-1}$) again indicates similar equatorial cross-sectional areas, showing that hydrolysis does not significantly alter this parameter. The scattering intensity deviates towards low-*q* and interestingly **B10-50(67%)** does not show a characteristic structure factor indicative of charged polymer species. It was rationalised that this was due to charge screening by residual propanoate ions which had not been fully removed by dialysis. Evidence for the presence of propanoate ions is found in the NMR spectra of the polymer (**Figure A2.22**), with the quartet of the -CH_2 adjacent to the carbonyl visible (δ = 2.18 ppm). **B10-50(67%)** was fitted with a core-shell elliptical form factor with a Hayter-Penfold rescaled mean spherical approximation structure factor. The total number of charged units was estimated to be 350 and this was held constant during the fitting, allowing for a monovalent salt concentration of 103 mM to be calculated. The length of **B10-50(67%)** was calculated using **Equation 2.6** and found to be 14.2 nm, slightly shorter than the **B10-50** (16.6 nm).

The SLD of the shell also increases, indicating a greater degree of solvation for **B10-50(67%)**, this could result in the contraction of the backbone due to the unfavourable interactions between styrene and D_2O.

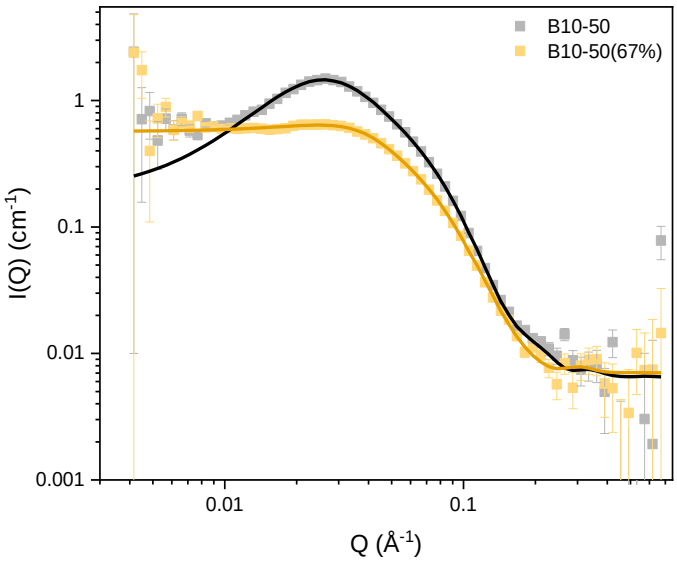

Figure 2.12 Small-angle neutron scattering of bottlebrush polymers at 10 mg mL^{-1}, fitted to a core-shell elliptical form factor (grey line). black – **B10-50**, and orange – **B10-50(67%)**.

Atomic force microscopy (AFM) was used to validate the SANS data and determine the size and shape of the bottlebrush polymers when absorbed onto a mica surface. Bottlebrush polymers of two different backbone and graft lengths were imaged in their pre- and post-hydrolysed state to elucidate any structural changes to the polymers after hydrolysis.

B10-50 (**Figure 2.13A**) and its hydrolysed analogue **B10-50(67%)** (**Figure 2.13B**) were chosen to confirm the elliptical shape of the bottlebrush polymer. The short backbone (DP 50) and graft length (DP 10) made these polymers difficult to analyse by AFM, but both **B10-50** and **B10-50(67%)** possess both elliptical and spherical morphologies, with average backbone lengths of 12.5 nm and 11.9 nm, respectively. The backbone lengths were determined by analysing the images in Fiji[47] with a minimum of 100 bottlebrush polymer backbones measured. A representative image of the analysis is presented in **Figure A2.33**. The inherent dispersity in the synthesis of **B10-50** leads to the different morphologies being observed, with shorter DP bottlebrushes showing little elongation.

Both **B10-50** and **B10-50(67%)** appear to behave as rigid rods when deposited on the mica surface, indicating that the backbone length is less than the persistence length.

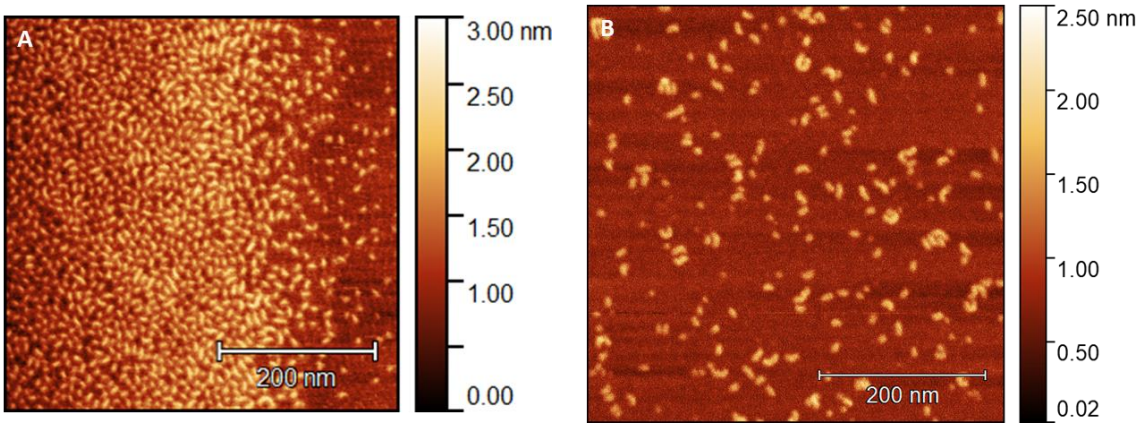

Figure 2.13 AFM micrographs of **B10-50** (A) and **B10-50(67%)** (B)

Bottlebrush polymers with longer backbone and graft lengths were synthesised to further investigate their structure. **B20-100** was synthesised with a targeted DP of 100. Due to the lack of control above a target DP of 50, the resulting polymer has a high *Đ*. This is observed by AFM, with a disperse series of bottlebrush polymers observed deposited on the mica surface. The bottlebrush polymers with longer backbones are no longer rigid, instead adopting a flexible morphology. **B20-100(82%)** (**Figure 2.14B**) possesses the same morphology as **B20-100** (**Figure 2.14A**), with a mixture of long flexible and shorter rigid rods. The measured average backbone length for **B20-100** appears to be significantly shorter than **B20-100(82%)**, this could be caused by a higher proportion of shorter bottlebrush polymers being visible in the obtained images of **B20-100**. The difference in measured backbone length could be caused by an elongation of the backbone in **B20-100(82%)** due to ionic repulsion between the grafts, however this seems unlikely given the observed flexible nature of the bottlebrush polymers.

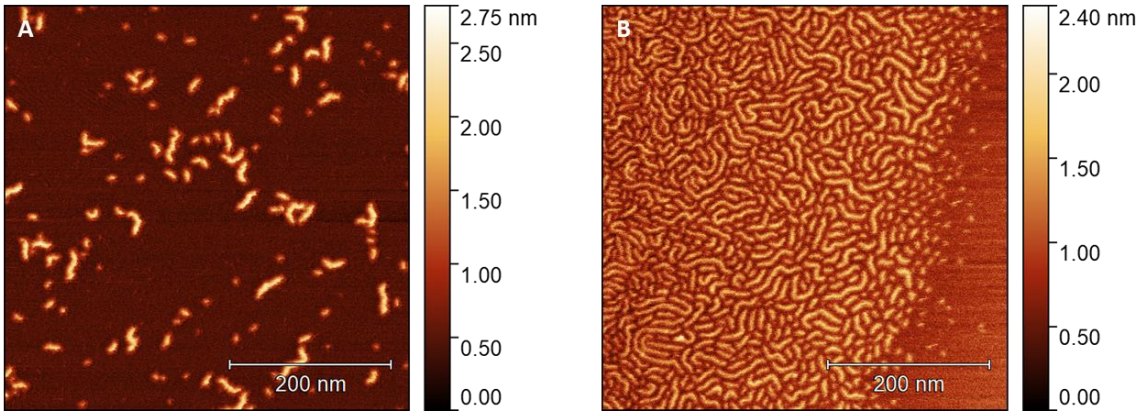

Figure 2.14 AFM micrographs of **B20-100** (A) and **B20-100(82%)** (B).

Table 2.8 Calculated backbone length of bottlebrush polymers determined by AFM.

Polymer	**Length (nm)**	**σ (nm)**
B10-50	12.5	2.7
B10-50(67%)	11.9	3.1
B20-100	17.3	11.3
B20-100(82%)	28.6	19.4

2.3 Conclusion

In this chapter a series of poly(2-oxazoline) macromonomers were synthesised and fully characterised to determine their end-group incorporation. The macromonomer was polymerised with RAFT-mediated polymerisation to impart control on the resulting bottlebrush copolymer molecular weight and molecular weight distribution. It was shown that the polymerisation of the macromonomer was well controlled up to a targeted DP of 50. Above this target it proved difficult to control the dispersity, with broad molecular weight distributions observed. These materials are of particular interest in biomedical applications, such as gene delivery, where architecture has been shown to play an important role.

Once a procedure for the synthesis of bottlebrush polymers was established the pendant amide groups of the poly(2-oxazoline) grafts were hydrolysed under acidic conditions. This introduced ethylenimine groups into the grafts, with the extent of hydrolysis controlled by varying the reaction time.

These cationic bottlebrush polymers were then analysed by SANS and AFM, where little structural changes were observed after hydrolysis and greater insights into their structure in solution were made. The bottlebrush polymers possessed rigid rod-like morphologies in solution up to DP 50, with flexible structures observed at higher DPs.

These materials will be evaluated for the ability to form polymer-DNA complexes and transfect mammalian cells in **Chapter 3**.

2.4 Experimental

2.4.1 Materials

2-Ethyl-2-oxazoline (EtOx), 4-vinylbenzyl chloride (4-VBC), trans-2-[3-(4-tert-Butylphenyl)-2-methyl-2-propenylidene]malononitrile (DCTB), and sodium iodide (NaI) were purchased from Sigma-Aldrich. Methyl p-toluenesulfonate (MeTos) was purchased from VWR. 3-((((1-carboxyethyl)thio)carbonothioyl)thio)propanoic acid (PAPATC) was purchased from Boron Molecular (BM1429). VA-086 was purchased from Alpha Laboratories. Acetonitrile (99.9%, Extra Dry, AcroSeal™), 37% Hydrochloric Acid was purchased from Fisher Scientific. EtOx was distilled over barium oxide prior to use. 4-VBC and MeTos were distilled prior to use. Sodium iodide was re-crystallised from water/ethanol prior to use. All other chemicals were used as received.

2.4.2 Characterisation

2.4.2.1 Nuclear Magnetic Resonance Spectroscopy (NMR)

^{1}H-NMR spectra were recorded using a Bruker DPX-300 or DPX-400 NMR spectrometer which operated at 300.13 and 400.05 MHz, respectively. The residual solvent peaks were used as internal references. Deuterated chloroform ($CDCl_3$) (δ_H = 7.26 ppm) and deuterated methanol (MeOD) (δ_H = 3.31 ppm) were used as the solvents for all measurements.

2.4.2.2 Size-Exclusion Chromatography (SEC)

An Agilent Infinity II MDS instrument equipped with differential refractive index (DRI), viscometry (VS), dual angle light scatter (LS) and multiple wavelength UV detectors was used for SEC analysis. The system was fitted with 2 x PLgel Mixed D columns (300 x 7.5 mm) and a PLgel 5 µm guard column. The eluent used was DMF with 5 mmol NH_4BH_4 additive. Samples were run at 1 mL min^{-1} at 50 °C. Poly(methyl methacrylate) standards (Agilent EasyVials) were used for calibration between 955,500 – 550 g mol^{-1}. Analyte samples were filtered membrane with 0.22 µm pore size before injection. Respectively, experimental molar mass ($M_{n,SEC}$) and dispersity ($Đ$) values of synthesized polymers were determined by conventional calibration using Agilent GPC/SEC software.

2.4.2.3 Matrix-Assisted Laser Desorption/Ionisation Time of Flight Mass Spectrometry (MALDI-TOF MS)

MALDI-TOF was performed on a Bruker Daltonics Autoflex Speed, equipped with a 337 nm nitrogen laser and operating in reflectron positive mode. Trans-2-[3-(4-tert-Butylphenyl)-2-methyl-2-propenylidene]malononitrile (DCTB), was used as a matrix (20

mg mL^{-1} in acetonitrile) without further purification. NaI salt was used as an ionization agent (10 mg mL^{-1} in Acetonitrile). Matrix, salts and polymer solution (10 mg mL^{-1} in Acetonitrile) were mixed in a 5 : 2 : 5 ratio, followed by deposition of 0.5 μL of the mixture onto the MALDI target before insertion into the ion source chamber. The instrument was calibrated prior to measurement using 1 KDa poly(ethylene glycol) as an external standard.

2.4.2.4 Atomic Force Microscopy (AFM)

Samples were prepared by drop-casting a 0.05 mg mL^{-1} polymer solution in $CHCl_3$ onto freshly cleaved mica and drying under a gentle N_2 flow for 5 seconds. Images were collected directly after sample preparation using a Bruker Dimension Icon instrument with ScanAsyst in Air and PeakForce tapping. Images were processed with Gwyddion software.

2.4.2.5 Cloud Point Measurements

Cloud point measurements were obtained using a Cary 60 UV-vis spectrophotometer. An aqueous solution of **MM1** (10 mg mL^{-1}) was heated from 5 °C to 95 °C at a rate of 1 °C $minute^{-1}$ and cooled at the same rate. This procedure was repeated twice.

2.4.2.6 Small-Angle Neutron Scattering (SANS) Acquisition

All samples were prepared to a concentration of 10 mg mL^{-1} in D_2O and loaded into rectangular 2 mm path length quartz cuvettes. SANS data were collected using the LARMOR instrument at the ISIS Neutron and Muon Source (Rutherford Appleton Laboratory, UK). SANS measures the scattered neutron intensity as a function of momentum transfer, $Q = 4\pi \sin\theta / \lambda$, where 2θ is the scattering angle and λ is the neutron wavelength. Spectra were collected using time-of-flight employing a neutron wavelength range of 0.9 – 13.3 Å. 2-Dimensional scattering patterns were collected using a ^{3}He-tube array area detector (660×664 mm, 512×80 pixels) 4.1 m from the sample position. Samples were illuminated using a rectangular beam (6×8 mm) centred on the detector. This covers an effective Q-range of 0.004 – 0.67 $Å^{-1}$. These data were reduced using Mantid Workbench software.[48] All samples produced isotropic scattering, allowing radial averaging of the detector intensities after correcting for the detector pixel efficiencies. Data were normalised to the incident flux and the spectrum of the direct beam, prior to subtraction of SANS data collected for D_2O under identical conditions. These data were placed on an absolute intensity scale using the scattering from a standard sample (a solid blend of hydrogenous and deuterated polystyrene) in accordance with established procedures.[49]

2.4.2.7 Small-Angle Neutron Scattering (SANS) Fitting

SANS data were analysed using SasView 5.0.3 using an included model describing a core-shell elliptical form factor,[50, 51] with a Hayter-Penfold Rescaled Mean Spherical Approximation structure factor for charged spherical particles.[52] Due to the elliptical structure of samples investigated here, the β-correction was applied,[50] where the effective radius used for structure factor calculation was calculated based on the average outer curvature of the elliptical particles. In all cases, the scattering length density (SLD) of the polystyrene core and D_2O solvent were calculated and fixed at 1.2×10-6 $Å^{-2}$ and 6.36×10-6 $Å^{-2}$, respectively, and the incoherent background fixed independently for each sample. The SLD of the pEtOX or pEtOx-co-pEI shell was fitted, taking into account solvent penetration into the hydrophilic shell. The equatorial core radius and core axial ratio were fitted, along with the shell thickness (no ellipticity was applied for the shell). In the structure factor calculation, slightly different approaches were taken for non-hydrolysed and hydrolysed samples. In all cases, the temperature was fixed at 298 K, the dielectric constant of the solvent fixed at 78, and the volume fraction was fitted. For the non-hydrolysed samples, no salt ions are expected to be present, so the monovalent salt concentration was fixed to 0 M and the charge on the bottlebrushes fitted, accounting for amine groups present at the termini of each graft. For the hydrolysed samples, the number averaged quantity of charged pEI monomers was estimated from ^{1}H-NMR and held constant throughout fitting. However, during hydrolysis propionate ions are generated which are not entirely removed by dialysis, as evidenced by 1H-NMR spectra. Therefore, the monovalent salt concentration was fit, to take into account residual propionate ions remaining in solution. It is worth noting that due to the strong positive correlation between charge and salt concentration, simultaneously fitting both parameters was not deemed to provide statistically reliable results.

2.4.3 Synthetic Procedures

2.4.3.1 Synthesis of α-Styrene-ω-Hydroxyl Poly(2-Ethyl-2-Oxazoline)

Sodium iodide (NaI) was added to a Schlenk flask and heated at 70 °C under vacuum for 2 hours. Acetonitrile (ACN) and 4-vinylbenzyl chloride (4-VBC) was added and the flask sealed. After 1 hour heating at 80 °C, 2-ethyl-2-oxazoline (EtOx) was transferred to the flask and heated for 1 hour. To terminate the polymerisation, potassium hydroxide dissolved in methanol was added to the flask and left to react overnight at room temperature. The precipitate was filtered, and the volatiles removed by rotary evaporation. The polymer was dissolved in dichloromethane and washed with saturated Na_2CO_3 (x 3) and brine (x 3) before precipitation into ice-cold diethyl ether (x 3). Lyophilisation yielded a white crystalline solid. ^{1}H-NMR (400 MHz, MeOD) 7.52-7.18 (m, 4H, ArH), 6.76 (m, 1H, vinyl proton), 5.81 (m, 1H, vinyl proton), 5.26 (m, 1H, vinyl proton), 4.66 (m, 2H, Ar-**CH_2**-N), 3.66-3.36 (m, 54H, **N(C(O))**-CH_2-CH_2-), 2.57-2.32 (m, 27H, C(O)-**CH_2**-CH_3), 1.21-1.00 (m, 40H, C(O)-CH_2-**CH_3**)

Table 2.9 Summary of polymerisation conditions for the synthesis of macromonomers, **MM1** and **MM2**.

	NaI		**4-VBC**		**EtOx**		**ACN**
	Mass (g)	**Mol.**	**Vol. (mL)**	**Mol.**	**Vol. (mL)**	**Mol.**	**Vol. (mL)**
MM1	4.80	0.032	2.25	0.016	16.15	0.16	21.60
MM2	4.80	0.032	2.25	0.016	32.30	0.32	45.44

2.4.3.2 Kinetics of Macromonomer Polymerisation

The polymerisation kinetics of **MM1** was determined from a polymerisation targeting DP 60, following the same procedure below (**2.4.3.3**). The polymerisation was sampled at pre-determined time points and measured using ^{1}H NMR and SEC. The polymer conversion was determined by ^{1}H NMR, comparing the integrals of the PEtOx backbone to the styryl end-group.

Table 2.10 Summary of kinetic time points for the polymerisation of **MM1**.

Time (minutes)	Conversion (%)[a]	M_n (g mol^{-1})[b]	$Đ$[b]	M_n (g mol^{-1})[c]	$Đ$[c]
5	0.0	2,300	1.33	-	-
10	0.0	2,300	1.22	-	-
20	1.4	2,300	1.31	-	-
30	6.1	2,400	1.38	-	-
60	38.8	3,500	3.65	21,800	1.37
90	75.8	7,100	4.51	32,700	1.42
120	93.5	10,500	3.76	35,800	1.41
180	98.8	13,000	3.31	37,900	1.39
240	99.7	15,600	2.89	38,300	1.40

[a] Conversion determined by ^{1}H-NMR. [b] M_n and $Đ$ determined by integrating the entire molecular weight trace. [c] M_n and $Đ$ determined by integrating the bottlebrush polymer distribution.

2.4.3.3 Macromonomer Polymerisation

Macromonomer was dissolved in water and added to a 7 mL scintillation vial along with a magnetic stirring bar, followed by addition of 1 M aqueous HCl. Stock solutions of PAPATC (10 mg mL^{-1}) and VA-086 (15 mg mL^{-1}) were prepared in water and an appropriate amount added to the vial. The vial was fitted with a rubber septum and bubbled with N_2 for 15 minutes before placing into an oil bath at 95 °C overnight. After opening the vial to quench the reaction, the solution was diluted with water and dialysed using an Amicon Ultra-15 centrifugal filter unit with 3 kDa MWCO. The solution was lyophilised to yield a pale yellow solid. ^{1}H-NMR (400 MHz, MeOD) 7.16-6.16 (m, 4H, ArH), 4.71-4.43 (m, 2H, Ar-**CH$_2$**-N), 3.88-3.36 (m, 54H, N(C(O))-**CH$_2$**-**CH$_2$**-), 2.57-2.18 (m, 27H, C(O)-**CH$_2$**-CH$_3$), 1.21-1.00 (m, 40H, C(O)-CH$_2$-**CH$_3$**)

Table 2.11 Summary of polymerisation conditions for the synthesis of bottlebrush polymers.

	Macromonomer			PAPATC		VA-086		HCl	Water
	MM	**Mass (mg)**	**Mol. (mmol)**	**Mass (mg)**	**Mol. (μmol)**	**Mass (mg)**	**Mol. (μmol)**	**Vol. (μL)**	**Vol. (mL)**
B10-25A	MM1	130	0.12	1.0	3.9	0.15	0.5	0	1.0
B10-10	MM1	520	0.47	10.2	40.0	0.58	2.0	200	3.8
B10-25	MM1	520	0.47	4.1	16.0	0.58	2.0	200	3.8
B10-50	MM1	520	0.47	2.0	8.0	0.58	2.0	200	3.8
B10-100	MM1	50	0.045	0.1	0.4	0.11	0.4	19	0.365
B10-100A	MM1	140	0.13	0.28	1.1	0.16	0.56	50	10.8
B10-100B	MM1	130	0.12	0.26	1.1	0.15	0.52	50	2.0
B10-100C	MM1	260	0.24	0.5	2.0	0.29	1.01	100	0.9
B10-100D	MM1	50	0.045	0.1	0.4	0.02	0.08	19	0.365
B10-100E	MM1	50	0.045	0.1	0.4	0.01	0.04	19	0.365
B20-10	MM2	50	0.025	0.63	2.5	0.057	0.20	12.5	0.24
B20-50	MM2	50	0.025	0.13	0.5	0.057	0.20	12.5	0.24
B20-100	MM2	50	0.025	0.06	0.24	0.057	0.20	12.5	0.24

2.4.3.4 Kinetics of Poly(2-Ethyl-2-Oxazoline) Hydrolysis

Polymer was dissolved in water and hydrolysed according to **2.4.3.5**. A series of reactions were carried out for varying times, followed by analysis with ^{1}H NMR to determine the extent of hydrolysis.

Table 2.12 Summary of kinetic results for the hydrolysis of bottlebrush and linear PEtOx.

	Bottlebrush	Linear
Time (minutes)	**Hydrolysis (%)**	**Hydrolysis (%)**
5	25.4	21.9
10	29.6	-
15	36.7	32.0
30	55.2	48.2
60	62.5	76.4
90	71.9	81.0
180	76.4	81.4

2.4.3.5 Bottlebrush Polymer Hydrolysis

PEtOx containing polymer was dissolved in 1 M HCl (concentration of amide = 0.48 M) and added to a microwave reaction vial with a magnetic stirrer and sealed. The vial was placed in a Biotage Initiator+ Eight microwave reactor at 120 °C for a predetermined amount of time. After the reaction, the solution was made basic by addition of 4 M NaOH, before dialysis using an Amicon Ultra-15 centrifugal filter unit (MWCO = 3 kDa) to remove any salt formed. The solution was lyophilised to yield the product. ^{1}H-NMR (400 MHz, MeOD) 7.26-6.20 (m, 4H, ArH), 4.71-4.43 (m, 2H, Ar-**CH_2**-N), 4.07-3.36 (m, 22H, N(C(O))-**CH_2-CH_2**-), 2.97-2.62 (m, 33H, NH-**CH_2-CH_2**-), 2.57-2.22 (m, 8H, C(O)-**CH_2**-CH_3), 1.34-0.93 (m, 14H, C(O)-CH_2-**CH_3**)

2.5 References

1. G. Xie, M. R. Martinez, M. Olszewski, S. S. Sheiko and K. Matyjaszewski, *Biomacromolecules*, 2019, **20**, 27-54.
2. J. C. Foster, S. Varlas, B. Couturaud, Z. Coe and R. K. O'Reilly, *Journal of the American Chemical Society*, 2019, **141**, 2742-2753.
3. R. Verduzco, X. Li, S. L. Pesek and G. E. Stein, *Chemical Society Reviews*, 2015, **44**, 2405-2420.
4. X. Banquy, J. Burdyńska, D. W. Lee, K. Matyjaszewski and J. Israelachvili, *Journal of the American Chemical Society*, 2014, **136**, 6199-6202.
5. J. A. Johnson, Y. Y. Lu, A. O. Burts, Y. Xia, A. C. Durrell, D. A. Tirrell and R. H. Grubbs, *Macromolecules*, 2010, **43**, 10326-10335.
6. J. Zou, G. Jafr, E. Themistou, Y. Yap, Z. A. P. Wintrob, P. Alexandridis, A. C. Ceacareanu and C. Cheng, *Chemical Communications*, 2011, **47**, 4493-4495.
7. X. Li, S. L. Prukop, S. L. Biswal and R. Verduzco, *Macromolecules*, 2012, **45**, 7118-7127.
8. C. Feng, Y. Li, D. Yang, J. Hu, X. Zhang and X. Huang, *Chemical Society Reviews*, 2011, **40**, 1282-1295.
9. S. S. Sheiko, B. S. Sumerlin and K. Matyjaszewski, *Progress in Polymer Science*, 2008, **33**, 759-785.
10. A. Kerr, M. Hartlieb, J. Sanchis, T. Smith and S. Perrier, *Chemical Communications*, 2017, **53**, 11901-11904.
11. B. Guillerm, S. Monge, V. Lapinte and J.-J. Robin, *Macromolecular Rapid Communications*, 2012, **33**, 1600-1612.
12. T. Lorson, M. M. Lübtow, E. Wegener, M. S. Haider, S. Borova, D. Nahm, R. Jordan, M. Sokolski-Papkov, A. V. Kabanov and R. Luxenhofer, *Biomaterials*, 2018, **178**, 204-280.
13. R. Hoogenboom and H. Schlaad, *Polymer Chemistry*, 2017, **8**, 24-40.
14. D. Pizzi, J. Humphries, J. P. Morrow, N. L. Fletcher, C. A. Bell, K. J. Thurecht and K. Kempe, *European Polymer Journal*, 2019, **121**, 109258.
15. Y. Shimano, K. Sato and S. Kobayashi, *Polymer Journal*, 1999, **31**, 219-225.
16. C. Weber, K. Babiuch, S. Rogers, I. Y. Perevyazko, R. Hoogenboom and U. S. Schubert, *Polymer Chemistry*, 2012, **3**, 2976-2985.
17. D. Christova, R. Velichkova and E. J. Goethals, *Macromolecular Rapid Communications*, 1997, **18**, 1067-1073.

18. C. Weber, R. C. Becer, A. Baumgaertel, R. Hoogenboom and U. S. Schubert, *Designed Monomers and Polymers*, 2009, **12**, 149-165.
19. H. Zhu, F. Mumtaz, C. Zhang, L. Tan, S. Liu, Y. Zhang, C. Pan and Y. Wang, *Applied Surface Science*, 2017, **426**, 817-826.
20. A.-K. Trützschler, T. Bus, M. Sahn, A. Traeger, C. Weber and U. S. Schubert, *Biomacromolecules*, 2018, **19**, 2759-2771.
21. C. Weber, S. Rogers, A. Vollrath, S. Hoeppener, T. Rudolph, N. Fritz, R. Hoogenboom and U. S. Schubert, *Journal of Polymer Science Part A: Polymer Chemistry*, 2013, **51**, 139-148.
22. J. C. Rueda, H. Komber, J. C. Cedrón, B. Voit and G. Shevtsova, *Macromolecular Chemistry and Physics*, 2003, **204**, 947-953.
23. S. Kobayashi, M. Kaku, S. Sawada and T. Saegusa, *Polymer Bulletin*, 1985, **13**, 447-451.
24. D. Störkle, S. Duschner, N. Heimann, M. Maskos and M. Schmidt, *Macromolecules*, 2007, **40**, 7998-8006.
25. G. G. Alvaradejo, H. V. T. Nguyen, P. Harvey, N. M. Gallagher, D. Le, M. F. Ottaviani, A. Jasanoff, G. Delaittre and J. A. Johnson, *ACS Macro Letters*, 2019, **8**, 473-478.
26. A. Cirpan, S. Alkan, L. Toppare, G. David and Y. Yagci, *European Polymer Journal*, 2001, **37**, 2225-2229.
27. N. Zhang, S. Huber, A. Schulz, R. Luxenhofer and R. Jordan, *Macromolecules*, 2009, **42**, 2215-2221.
28. J. Kim, C. Waldron, B. Cattoz and C. R. Becer, *Polymer Chemistry*, 2020, **11**, 6847-6852.
29. V. P. Beyer, B. Cattoz, A. Strong, A. Schwarz and C. R. Becer, *Macromolecules*, 2020, **53**, 2950-2958.
30. M. A. Mees and R. Hoogenboom, *Polymer Chemistry*, 2018, **9**, 4968-4978.
31. H. P. C. Van Kuringen, J. Lenoir, E. Adriaens, J. Bender, B. G. De Geest and R. Hoogenboom, *Macromolecular Bioscience*, 2012, **12**, 1114-1123.
32. M. W. M. Fijten, R. Hoogenboom and U. S. Schubert, *Journal of Polymer Science Part A: Polymer Chemistry*, 2008, **46**, 4804-4816.
33. H. Finkelstein, *Berichte der deutschen chemischen Gesellschaft*, 1910, **43**, 1528-1532.
34. L. Xiao, K. Sakakibara, Y. Tsujii and A. Goto, *Macromolecules*, 2017, **50**, 1882-1891.

35. B. Guillerm, S. Monge, V. Lapinte and J.-J. Robin, *Macromolecules*, 2010, **43**, 5964-5970.
36. M. Dey, J. A. Castoro and C. L. Wilkins, *Analytical Chemistry*, 1995, **67**, 1575-1579.
37. J. M. Warakomski and B. P. Thill, *Journal of Polymer Science Part A: Polymer Chemistry*, 1990, **28**, 3551-3563.
38. N. Li, W. Liu, L. Xu, J. Xu and J. Du, *Macromolecular Chemistry and Physics*, 2015, **216**, 172-181.
39. R. Hoogenboom, H. M. L. Thijs, M. J. H. C. Jochems, B. M. van Lankvelt, M. W. M. Fijten and U. S. Schubert, *Chemical Communications*, 2008, DOI: 10.1039/B813140F, 5758-5760.
40. S. Furyk, Y. Zhang, D. Ortiz-Acosta, P. S. Cremer and D. E. Bergbreiter, *Journal of Polymer Science Part A: Polymer Chemistry*, 2006, **44**, 1492-1501.
41. H. Willcock and R. K. O'Reilly, *Polymer Chemistry*, 2010, **1**, 149-157.
42. G. Gody, R. Barbey, M. Danial and S. Perrier, *Polymer Chemistry*, 2015, **6**, 1502-1511.
43. D. Neugebauer, Y. Zhang, T. Pakula, S. S. Sheiko and K. Matyjaszewski, *Macromolecules*, 2003, **36**, 6746-6755.
44. V. R. de la Rosa, E. Bauwens, B. D. Monnery, B. G. De Geest and R. Hoogenboom, *Polymer Chemistry*, 2014, **5**, 4957-4964.
45. A. B. Cook, R. Peltier, J. Zhang, P. Gurnani, J. Tanaka, J. A. Burns, R. Dallmann, M. Hartlieb and S. Perrier, *Polymer Chemistry*, 2019, **10**, 1202-1212.
46. S. L. Pesek, X. Li, B. Hammouda, K. Hong and R. Verduzco, *Macromolecules*, 2013, **46**, 6998-7005.
47. J. Schindelin, I. Arganda-Carreras, E. Frise, V. Kaynig, M. Longair, T. Pietzsch, S. Preibisch, C. Rueden, S. Saalfeld, B. Schmid, J.-Y. Tinevez, D. J. White, V. Hartenstein, K. Eliceiri, P. Tomancak and A. Cardona, *Nature Methods*, 2012, **9**, 676-682.
48. O. Arnold, J. C. Bilheux, J. M. Borreguero, A. Buts, S. I. Campbell, L. Chapon, M. Doucet, N. Draper, R. Ferraz Leal, M. A. Gigg, V. E. Lynch, A. Markvardsen, D. J. Mikkelson, R. L. Mikkelson, R. Miller, K. Palmen, P. Parker, G. Passos, T. G. Perring, P. F. Peterson, S. Ren, M. A. Reuter, A. T. Savici, J. W. Taylor, R. J. Taylor, R. Tolchenov, W. Zhou and J. Zikovsky, *Nuclear Instruments and Methods in Physics Research Section A: Accelerators, Spectrometers, Detectors and Associated Equipment*, 2014, **764**, 156-166.

49. G. D. Wignall and F. S. Bates, *Journal of Applied Crystallography*, 1987, **20**, 28-40.
50. M. Kotlarchyk and S. H. Chen, *The Journal of Chemical Physics*, 1983, **79**, 2461-2469.
51. S. S. Berr, *The Journal of Physical Chemistry*, 1987, **91**, 4760-4765.
52. J. B. Hayter and J. Penfold, *Molecular Physics*, 1981, **42**, 109-118.

2.6 **Appendix**

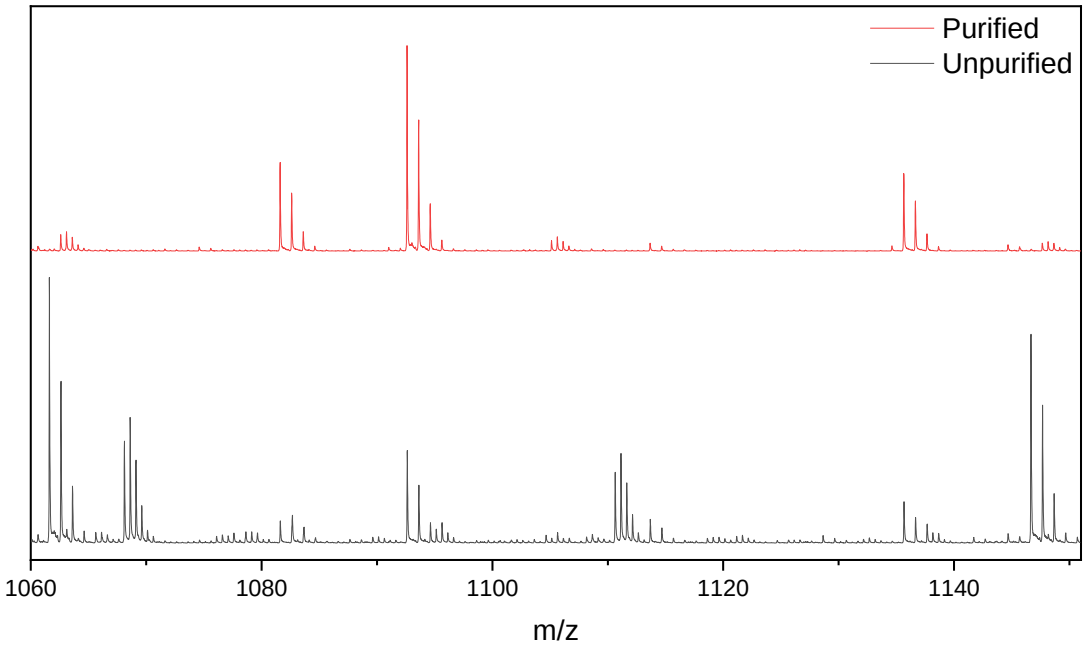

Figure A2.1 MALDI-TOF Spectrum of PMeOx macromonomers prepared using impure (black) and pure (red) NaI.

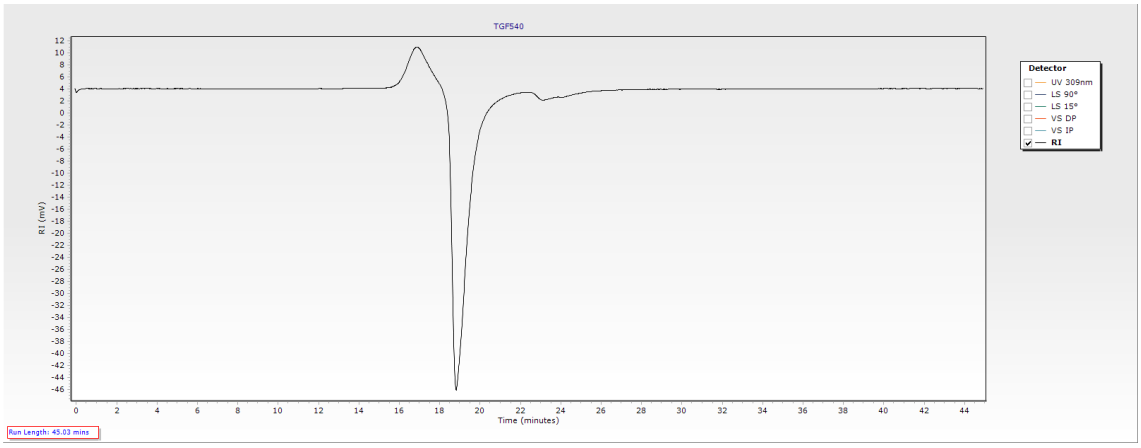

Figure A2.2 Complete SEC chromatogram for **MM1** using DMF as an eluent.

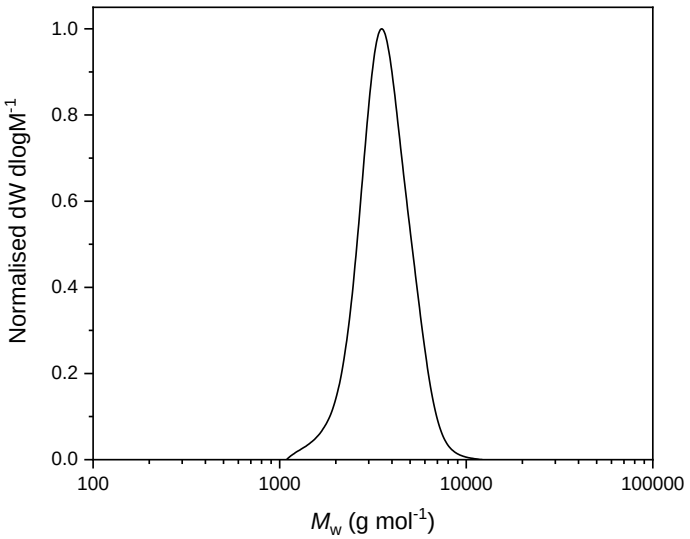

Figure A2.3 SEC chromatogram of **MM2** using DMF as an eluent (PMMA calibration)

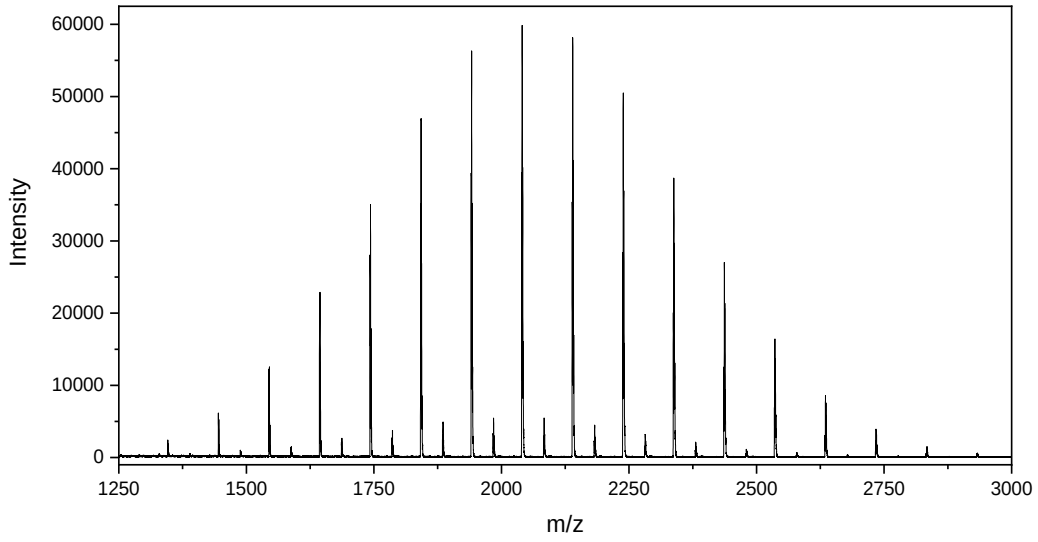

Figure A2.4 MALDI-TOF spectrum of **MM2**.

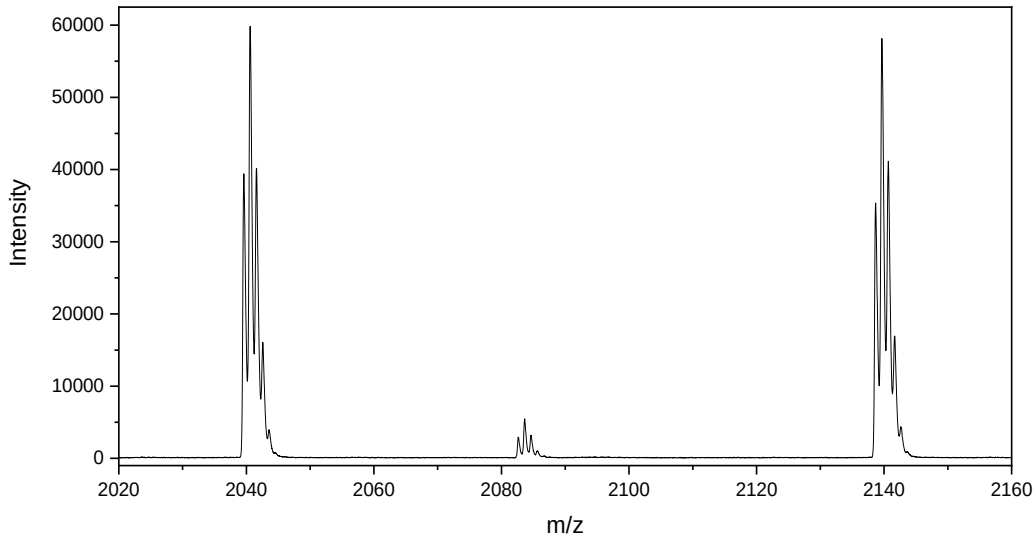

Figure A2.5 Magnified MALDI-TOF spectrum of **MM2**.

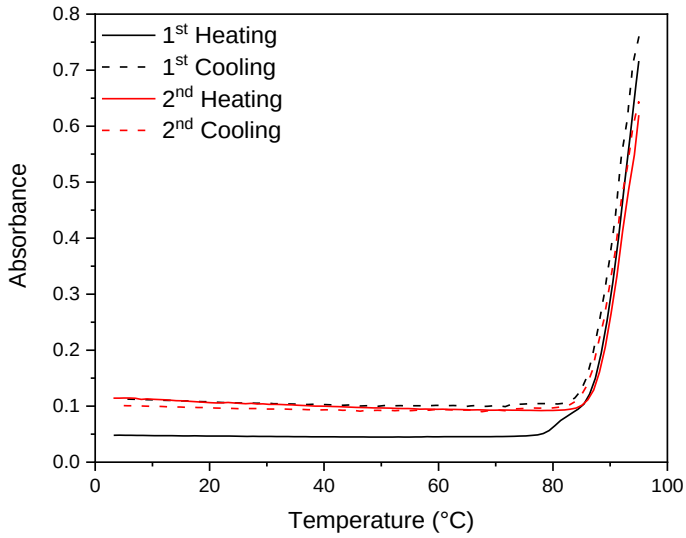

Figure A2.6 Cloud point measurement of **MM1** in water (10 mg mL^{-1}, 0.009 M). Solid line represents heating and dashed line cooling. Black - measurement 1, red - measurement 2.

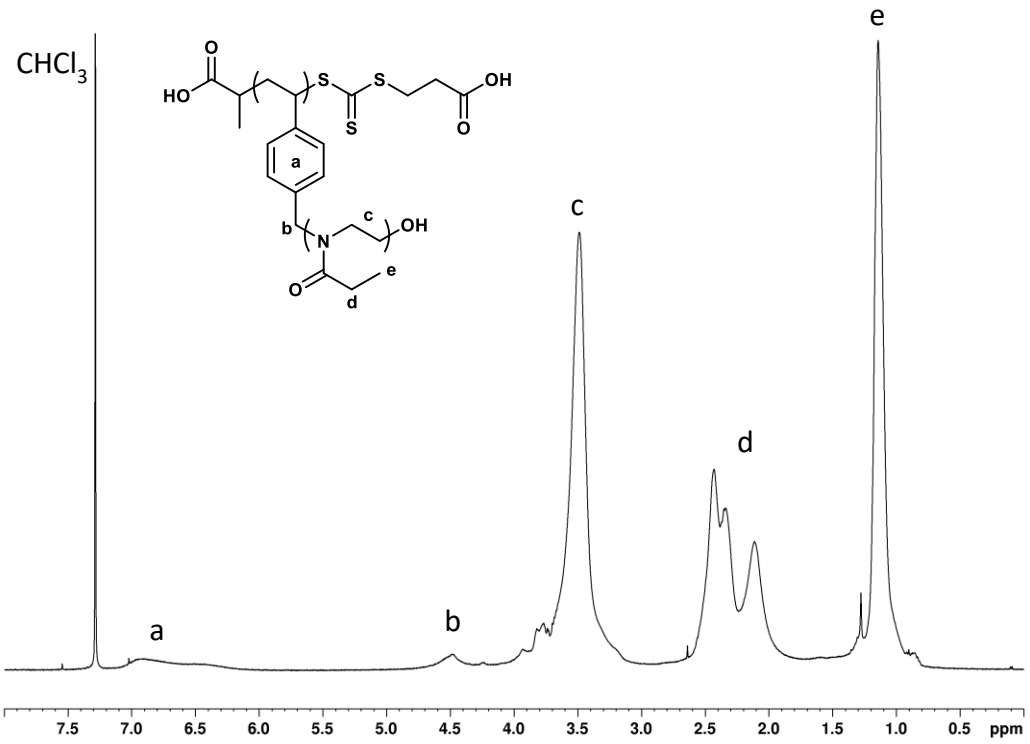

Figure A2.7 ^{1}H NMR spectrum of **B10-25** in $CDCl_3$.

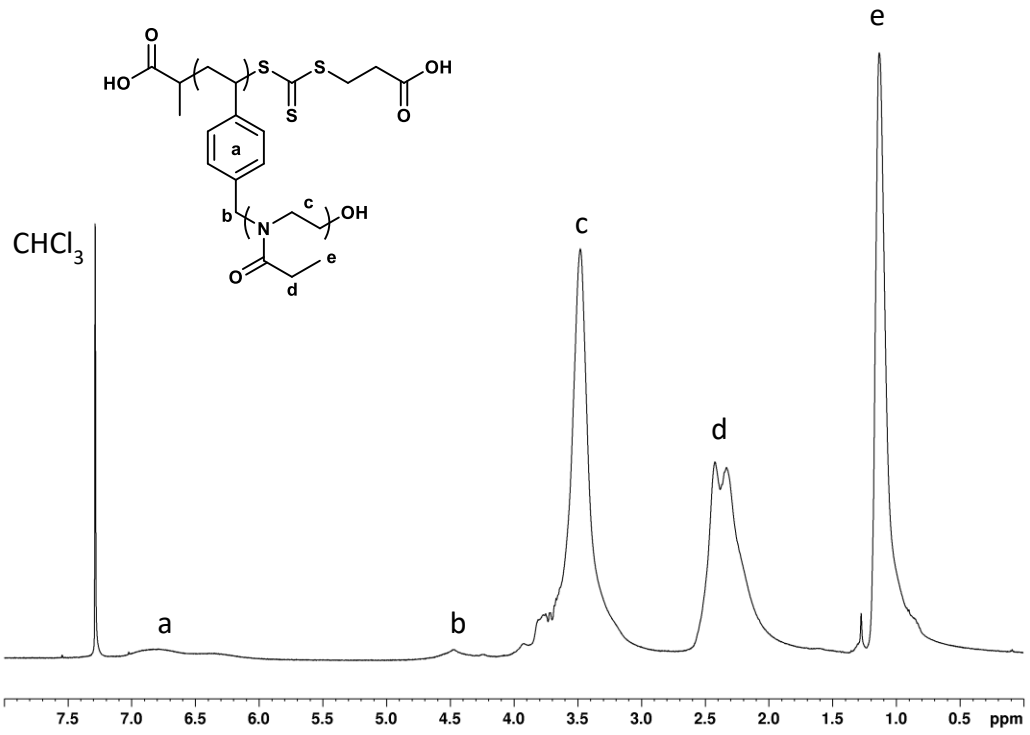

Figure A2.8 ^{1}H NMR spectrum of **B10-50** in $CDCl_3$.

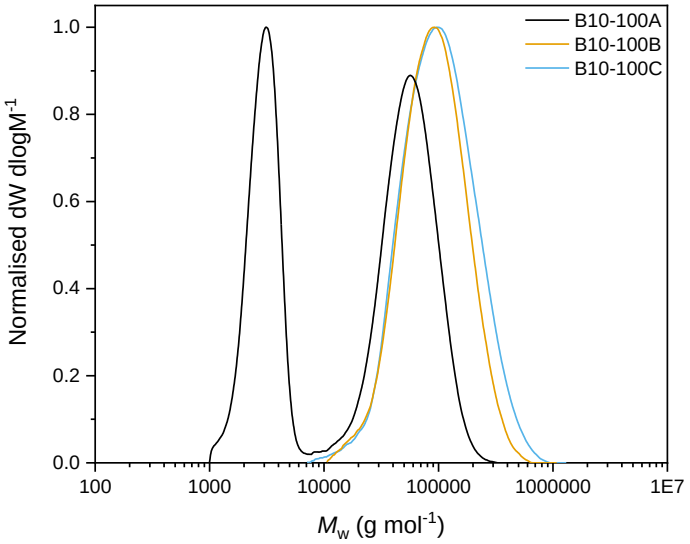

Figure A2.9 SEC chromatograms of **B10-100A**, **B10-100B**, and **B10-100C**.

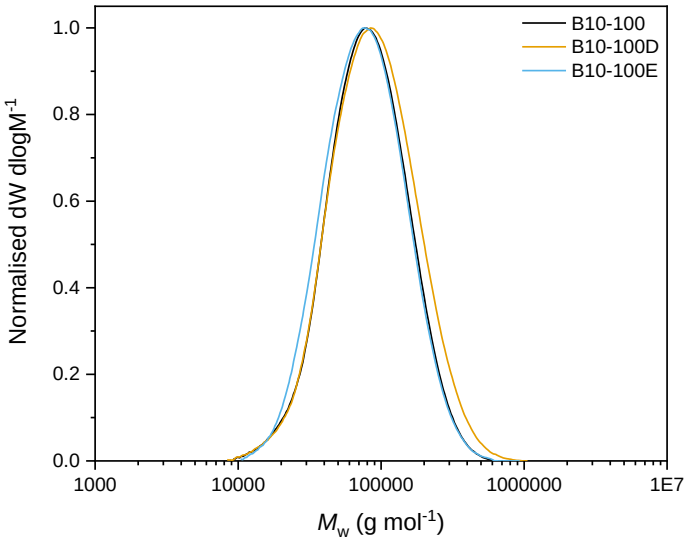

Figure A2.10 SEC chromatogram of **B10-100**, **B10-100D**, and **B10-100E**.

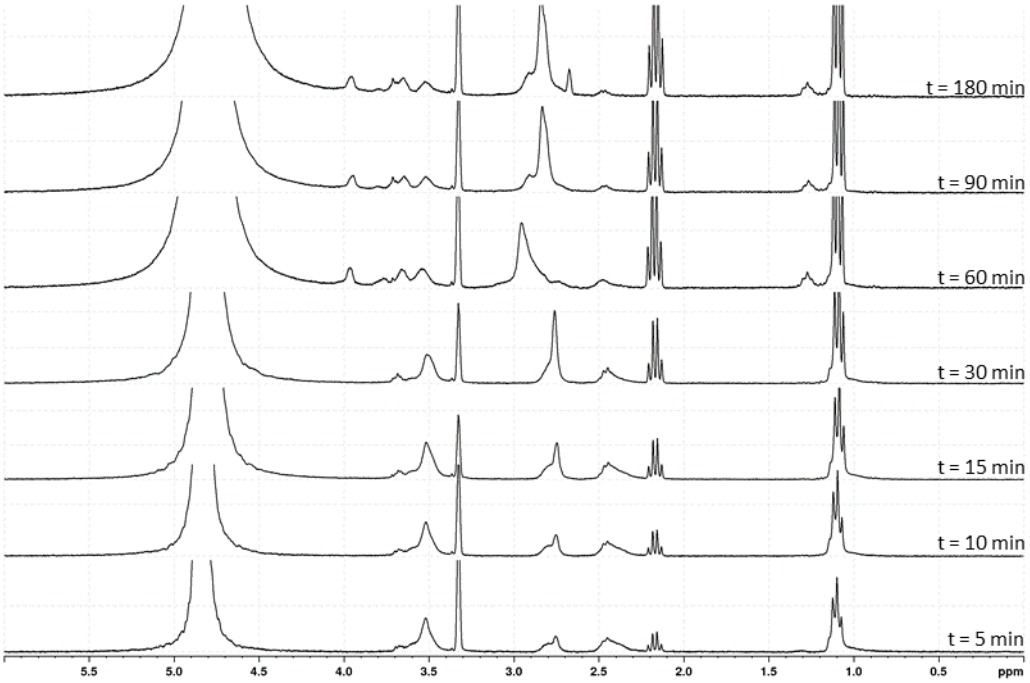

Figure A2.11 ^{1}H-NMR kinetics for the hydrolysis of bottlebrush PEtOx.

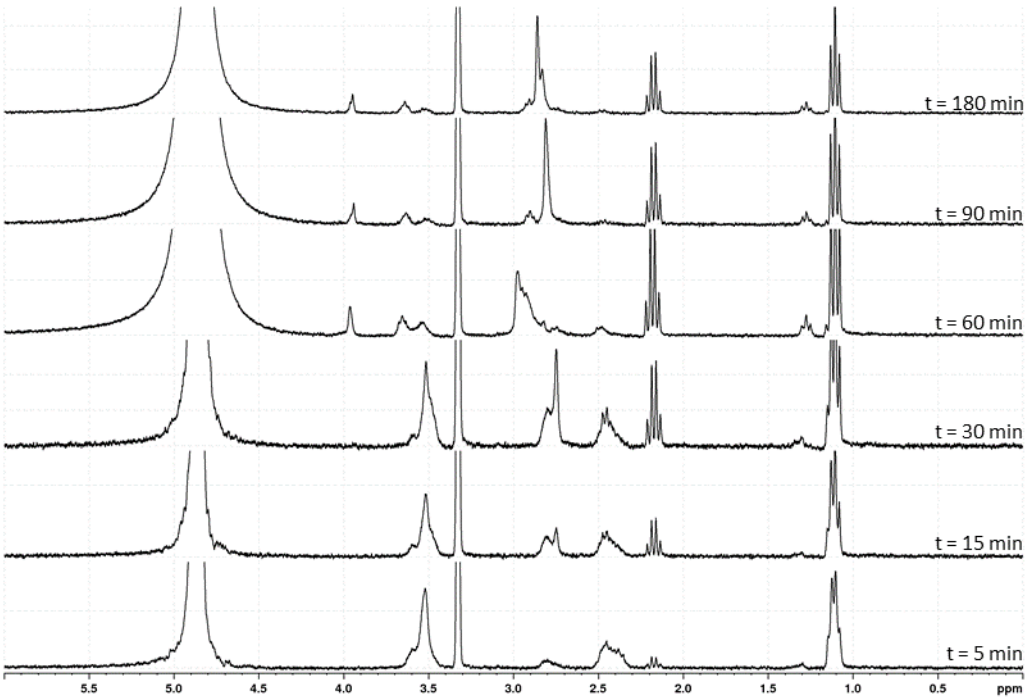

Figure A2.12 ^{1}H-NMR kinetics for the hydrolysis of linear PEtOx.

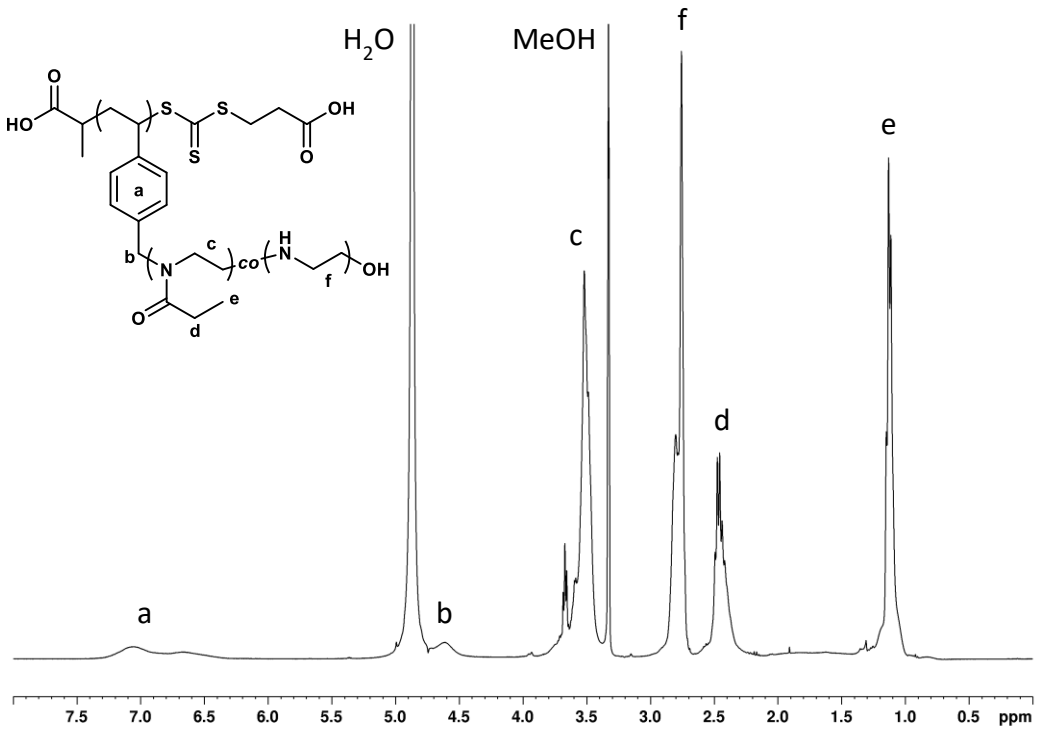

Figure A2.13 [1]H-NMR spectrum of **B10-10(32%)** in MeOD.

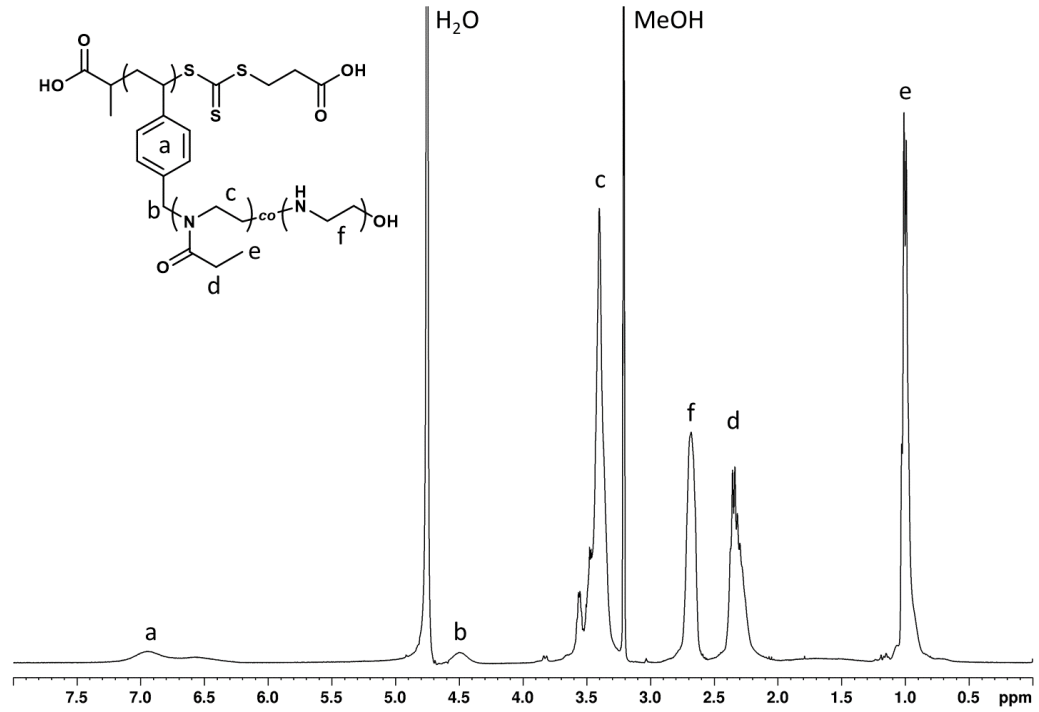

Figure A2.14 Assigned [1]H-NMR spectrum of **B10-10(45%)** in MeOD.

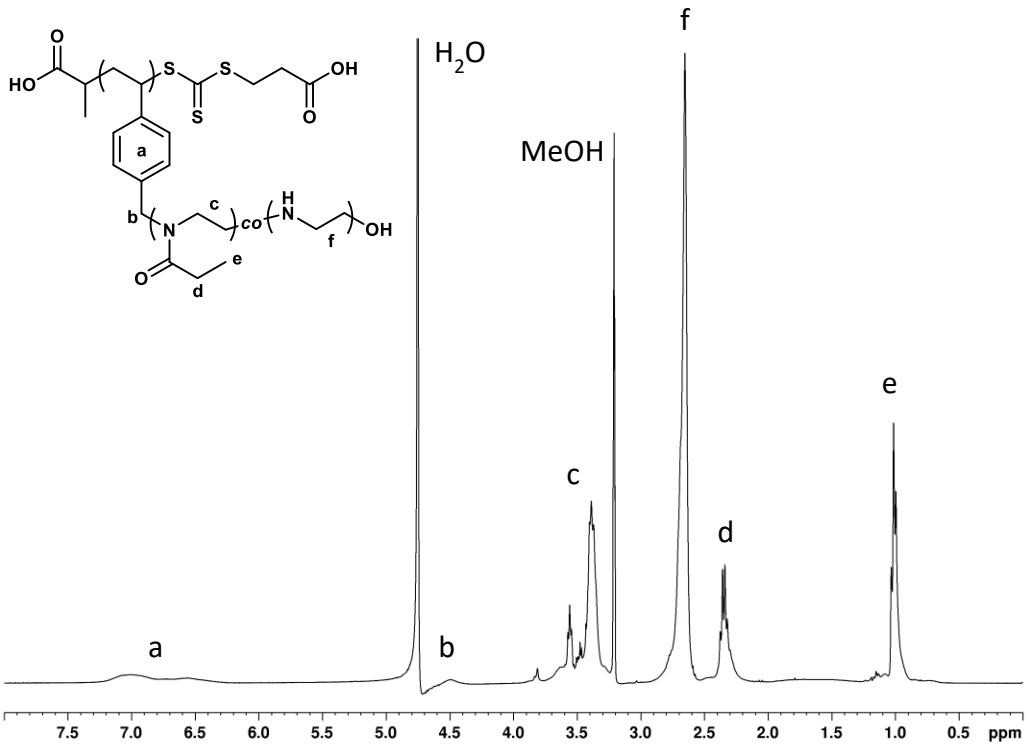

Figure A2.15 [1]H-NMR spectrum of **B10-10(69%)** in MeOD.

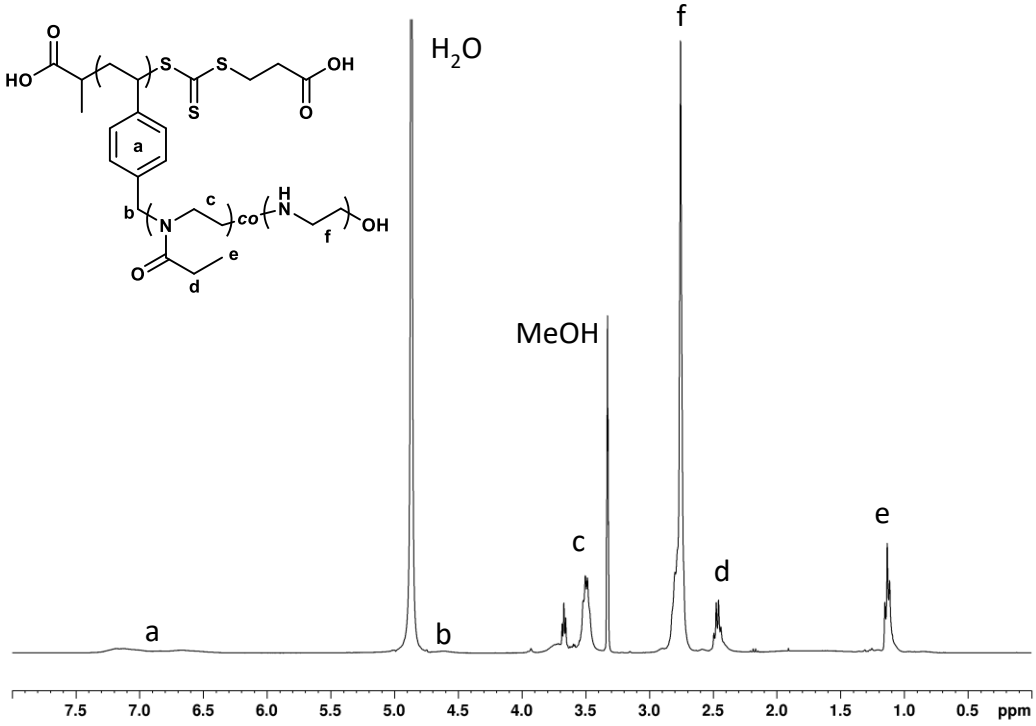

Figure A2.16 [1]H-NMR spectrum of **B10-10(78%)** in MeOD.

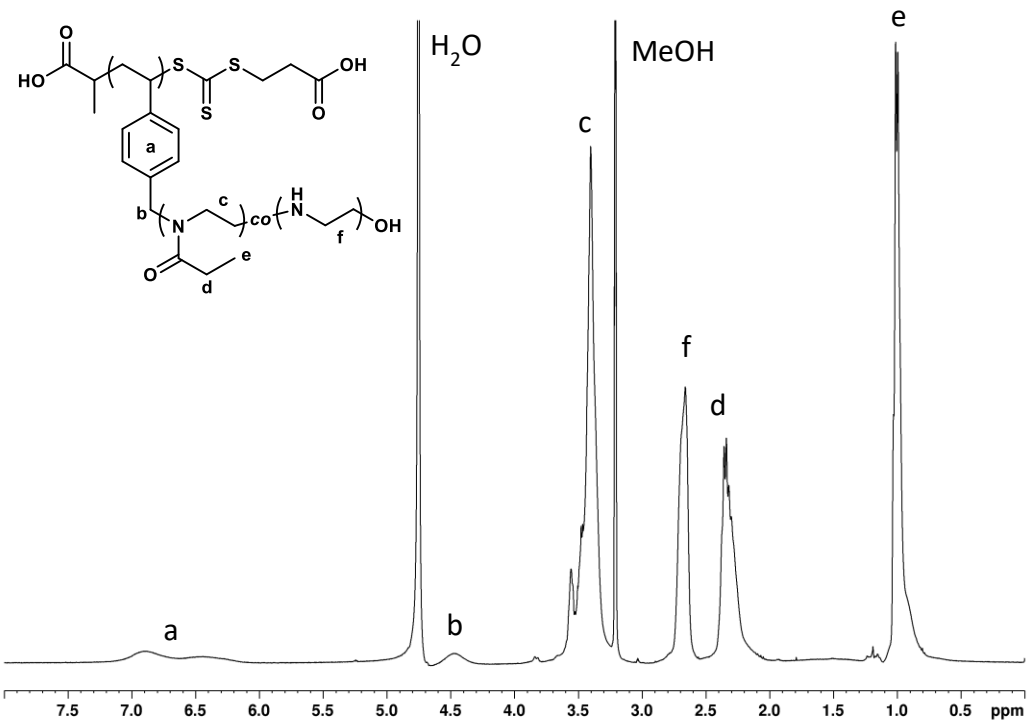

Figure A2.17 ^{1}H-NMR spectrum of **B10-25(31%)** in MeOD.

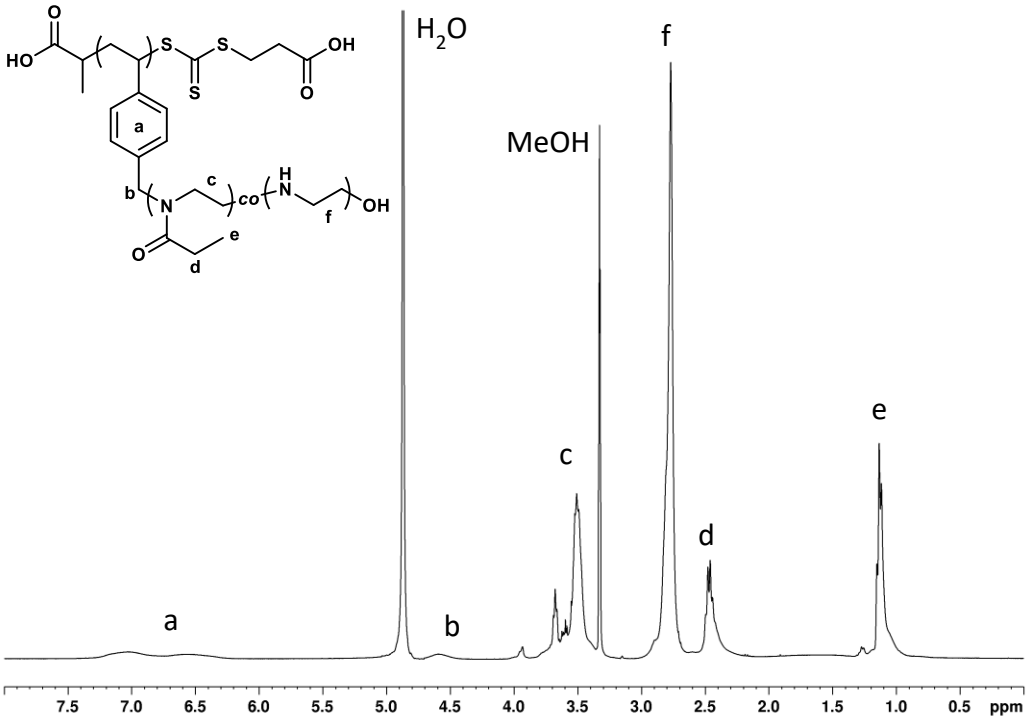

Figure A2.18 ^{1}H-NMR spectrum of **B10-25(67%)** in MeOD.

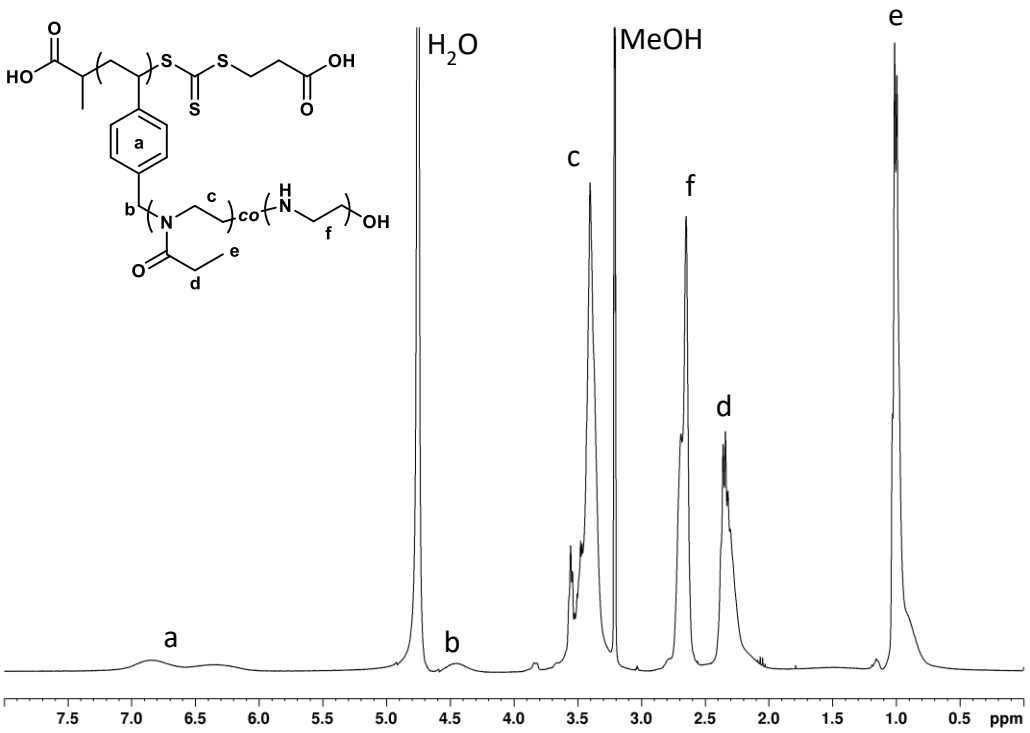

Figure A2.19 [1]H-NMR spectrum of **B10-50(37%)** in MeOD.

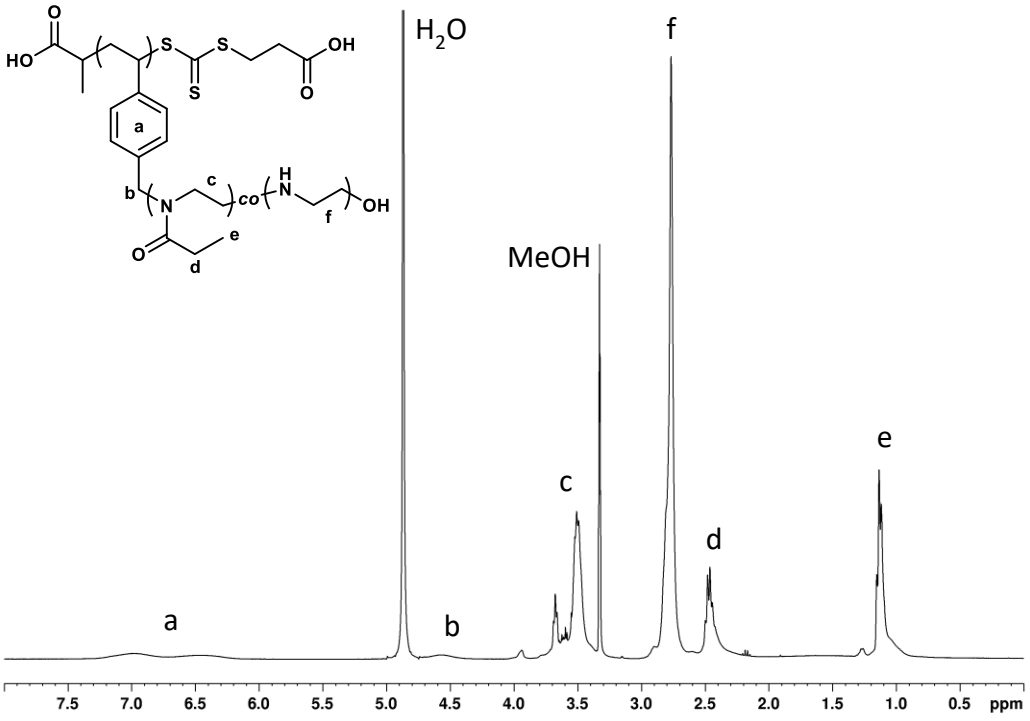

Figure A2.20 [1]H-NMR spectrum of **B10-50(67%)** in MeOD.

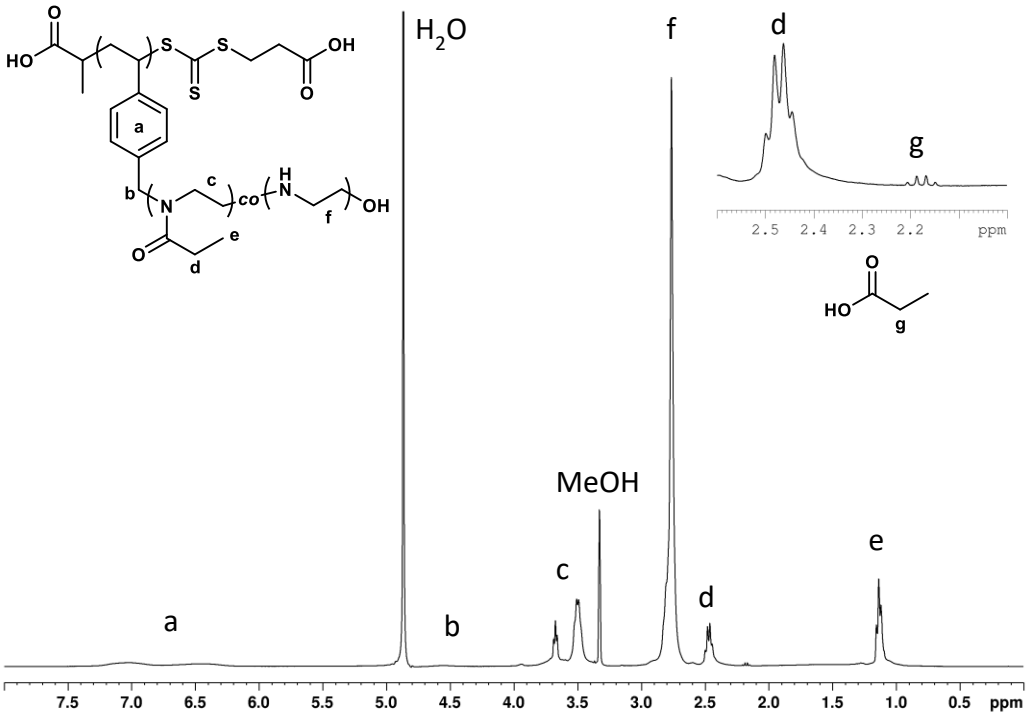

Figure A2.21 ^{1}H-NMR spectrum of **B10-50(67%)** in MeOD. Insert shows the presence of propanoic acid quartet at δ = 2.18 ppm.

Table A2.1 Concentration and determined dn/dc values of hydrolysed SEC samples.

Sample	**dn/dc***	**Concentration (mg ml^{-1})**
B10-10(32%)	0.208	10
B10-10(46%)	0.218	3
B10-10(67%)	0.259	10
B10-10(78%)	0.229	2
B10-25(31%)	0.220	5
B10-25(67%)	0.268	5
B10-50(37%)	0.203	3
B10-50(67%)	0.273	3
B20-100(82%)	0.127	3.8

*obtained via concentration dependent RI measurements.

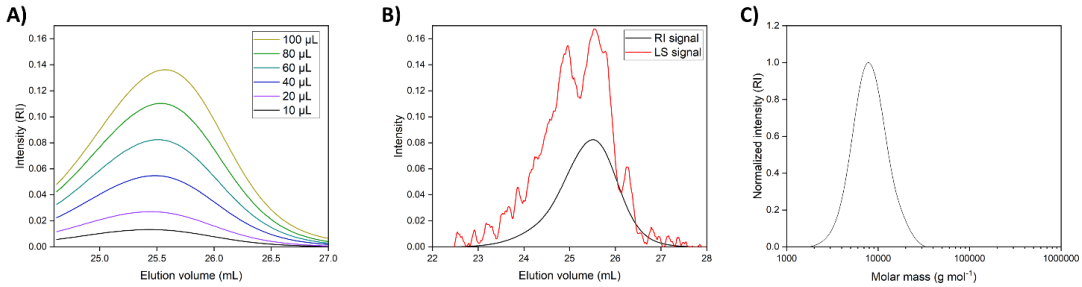

Figure A2.22 Aqueous SEC measurements of polymer **B10-10(32%)**

Aqueous SEC measurements (Eluent: Water with 3% TFA and 0.1 mol L^{-1} NaCl) of polymer **B10-10(32%)**, at a concentration of 10 mg ml^{-1}; A) Determination of dn/dc using various injection volumes, integrals under the curves are correlated with injected polymer mass to determine dn/dc as the slope of the linear regression; B) Elugram of polymer with RI and LS detection; C) molecular weight distribution using PVP-calibration.

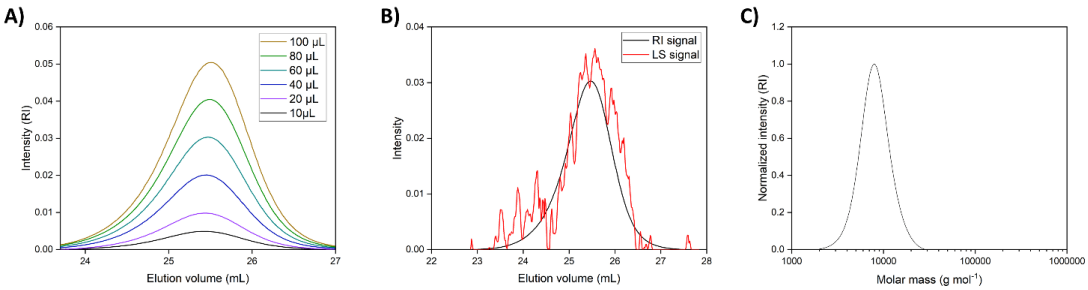

Figure A2.23 Aqueous SEC measurements of polymer **B10-10(46%)**

Aqueous SEC measurements (Eluent: Water with 3% TFA and 0.1 mol L^{-1} NaCl) of polymer **B10-10(46%)**, at a concentration of 3 mg ml^{-1}; A) Determination of dn/dc using various injection volumes, integrals under the curves are correlated with injected polymer mass to determine dn/dc as the slope of the linear regression; B) Elugram of polymer with RI and LS detection; C) molecular weight distribution using PVP-calibration.

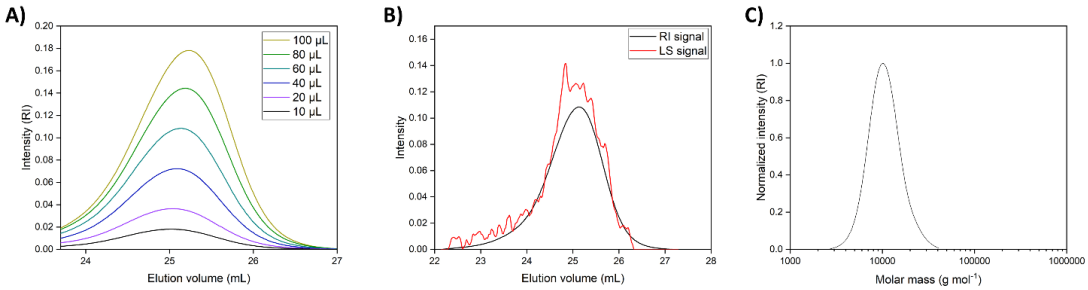

Figure A2.24 Aqueous SEC measurements of polymer **B10-10(67%)**

Aqueous SEC measurements (Eluent: Water with 3% TFA and 0.1 mol L^{-1} NaCl) of polymer **B10-10(67%)**, at a concentration of 10 mg ml^{-1}; A) Determination of dn/dc using various injection volumes, integrals under the curves are correlated with injected polymer mass to determine dn/dc as the slope of the linear regression; B) Elugram of polymer with RI and LS detection; C) molecular weight distribution using PVP-calibration.

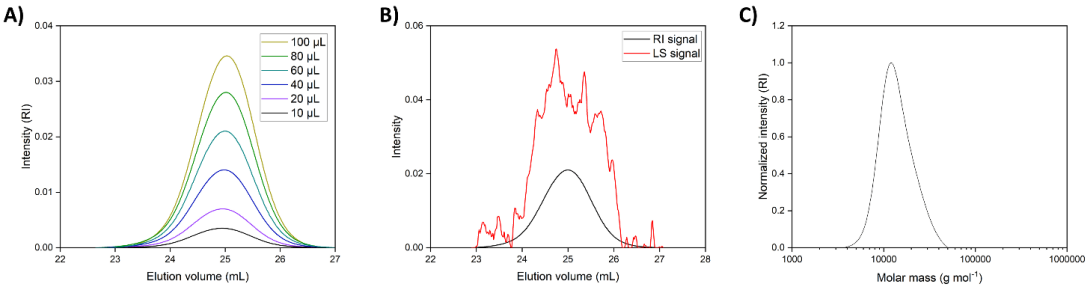

Figure A2.25 Aqueous SEC measurements of polymer **B10-10(78%)**

Aqueous SEC measurements (Eluent: Water with 3% TFA and 0.1 mol L^{-1} NaCl) of polymer **B10-10(78%)**, at a concentration of 2 mg ml^{-1}; A) Determination of dn/dc using various injection volumes, integrals under the curves are correlated with injected polymer mass to determine dn/dc as the slope of the linear regression; B) Elugram of polymer with RI and LS detection; C) molecular weight distribution using PVP-calibration.

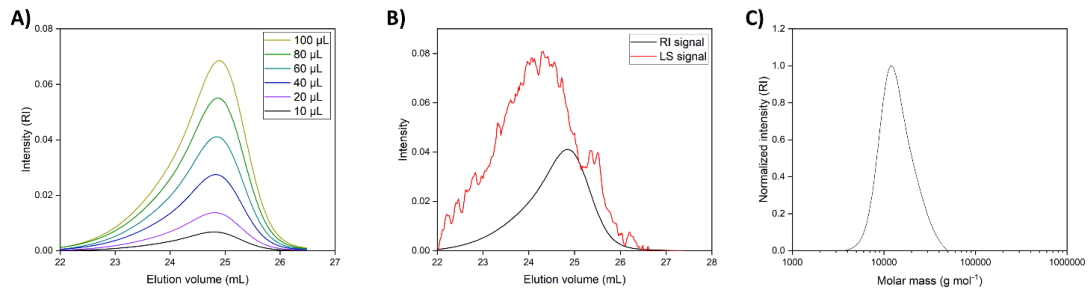

Figure A2.26 Aqueous SEC measurements of polymer **B10-25(31%)**

Aqueous SEC measurements (Eluent: Water with 3% TFA and 0.1 mol L^{-1} NaCl) of polymer **B10-25(31%)**, at a concentration of 5 mg ml^{-1}; A) Determination of dn/dc using various injection volumes, integrals under the curves are correlated with injected polymer mass to determine dn/dc as the slope of the linear regression; B) Elugram of polymer with RI and LS detection; C) molecular weight distribution using PVP-calibration.

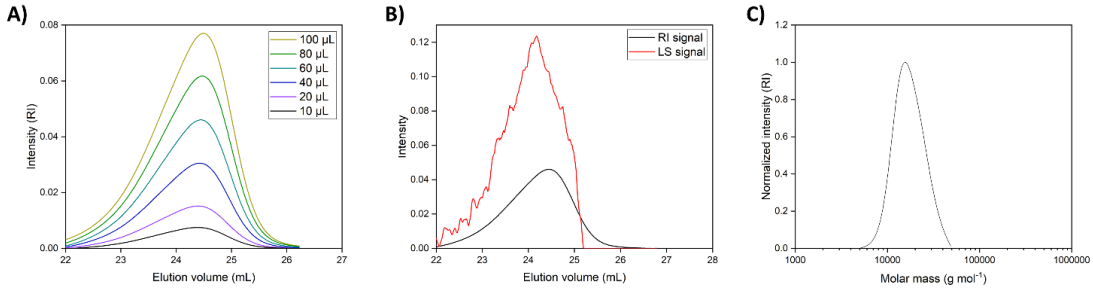

Figure A2.27 Aqueous SEC measurements of polymer **B10-25(67%)**

Aqueous SEC measurements (Eluent: Water with 3% TFA and 0.1 mol L^{-1} NaCl) of polymer **B10-25(67%)**, at a concentration of 5 mg ml^{-1}; A) Determination of dn/dc using various injection volumes, integrals under the curves are correlated with injected polymer mass to determine dn/dc as the slope of the linear regression; B) Elugram of polymer with RI and LS detection; C) molecular weight distribution using PVP-calibration.

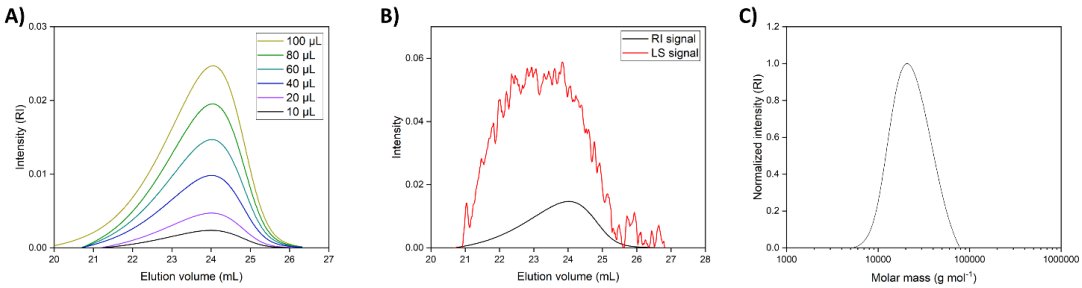

Figure A2.28 Aqueous SEC measurements of polymer **B10-50(37%)**

Aqueous SEC measurements (Eluent: Water with 3% TFA and 0.1 mol L^{-1} NaCl) of polymer **B10-50(37%)**, at a concentration of 3 mg ml^{-1}; A) Determination of dn/dc using various injection volumes, integrals under the curves are correlated with injected polymer mass to determine dn/dc as the slope of the linear regression; B) Elugram of polymer with RI and LS detection; C) molecular weight distribution using PVP-calibration.

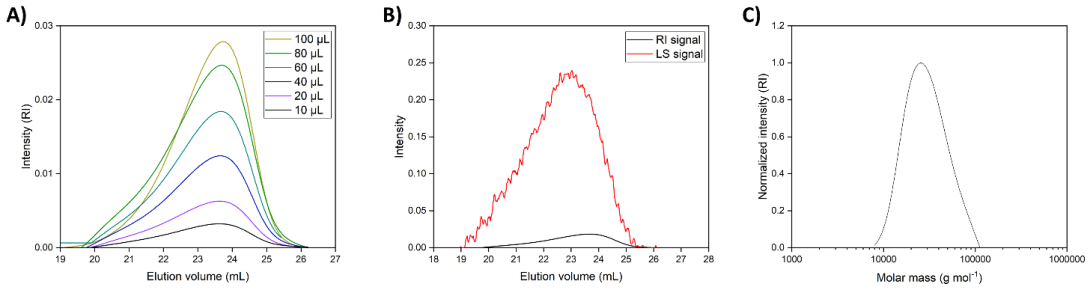

Figure A2.29 Aqueous SEC measurements of polymer **B10-50(67%)**

Aqueous SEC measurements (Eluent: Water with 3% TFA and 0.1 mol L^{-1} NaCl) of polymer **B10-50(67%)**, at a concentration of 3 mg ml^{-1}; A) Determination of dn/dc using various injection volumes, integrals under the curves are correlated with injected polymer mass to determine dn/dc as the slope of the linear regression; B) Elugram of polymer with RI and LS detection; C) molecular weight distribution using PVP-calibration.

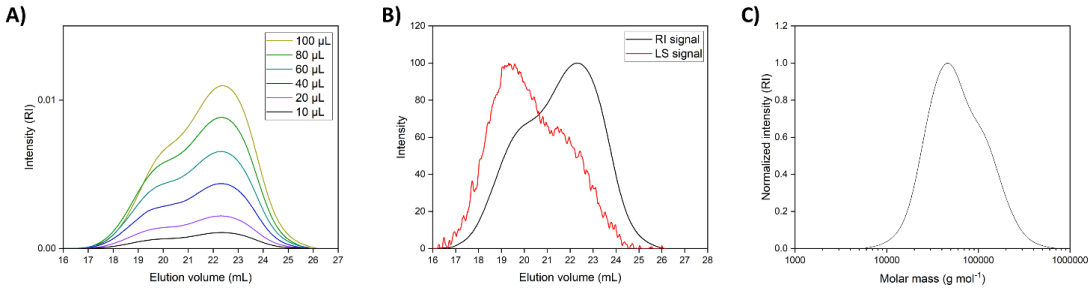

Figure A2.30 Aqueous SEC measurements of polymer **B20-100(82%)**

Aqueous SEC measurements (Eluent: Water with 3% TFA and 0.1 mol L^{-1} NaCl) of polymer **B20-100(82%)**, at a concentration of 3,8 mg ml^{-1}; A) Determination of dn/dc using various injection volumes, integrals under the curves are correlated with injected polymer mass to determine dn/dc as the slope of the linear regression; B) Elugram of polymer with RI and LS detection; C) molecular weight distribution using PVP-calibration.

Table A2.2 Parameters obtained through fitting SANS data of bottlebrush copolymers before and after hydrolysis to a model comprised of a core-shell elliptical form factor with a Hayter-Penfold Rescaled Mean Spherical Approximation structure factor for charged spherical particles.

	Parameter	B10-10	B10-25	B10-50	B10-50(67%)
P(Q)	Background / cm^{-1}	0.007*	0.007*	0.0065*	0.007*
	$R_{core,\ equatorial}$ / Å	8.6 ± 0.8	13.7 ± 0.4	15.0 ± 0.3	17.5 ± 0.8
	$R_{core,\ polar}$ / Å	37 ± 1.1	35.3 ± 0.5	61.8 ± 0.3	50.8 ± 0.8
	d_{shell} / Å	15.7 ± 0.3	19.1 ± 0.4	21.4 ± 0.2	20.4 ± 1.3
	ρ_{core} / $\times 10^{-6}$ Å $^{-2}$	1.2*	1.2*	1.2*	1.2*
	ρ_{shell} / $\times 10^{-6}$ Å $^{-2}$	5.81 ± 0.04	5.67 ± 0.04	5.65 ± 0.03	5.91 ± 0.09
	$\rho_{solvent}$ / $\times 10^{-6}$ Å $^{-2}$	6.36*	6.36*	6.36*	6.36*
S(Q)	Volume Fraction	0.048 ± 0.006	0.030 ± 0.001	0.027 ± 0.001	0.014 ± 0.001
	Charge	3.6 ± 0.1	7.9 ± 0.1	10.4 ± 0.1	350*
	Monovalent Salt Conc. / mM	0*	0*	0*	103 ± 8

Parameters marked * were held constant throughout the fitting procedure.

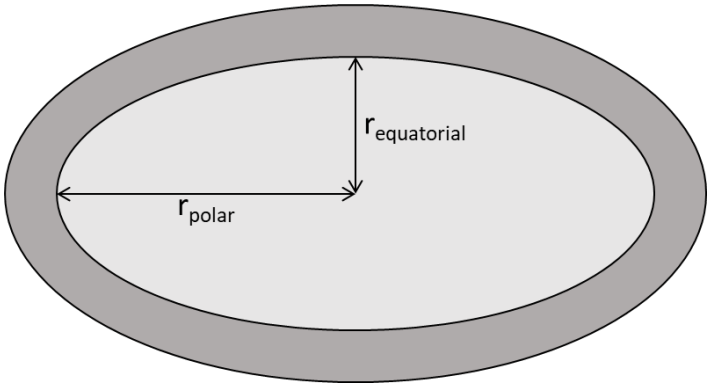

Figure A2.31 Representation of core-shell elliptical form factor used to fit bottlebrush polymers in small-angle neutron scattering. Dimensions labelled.

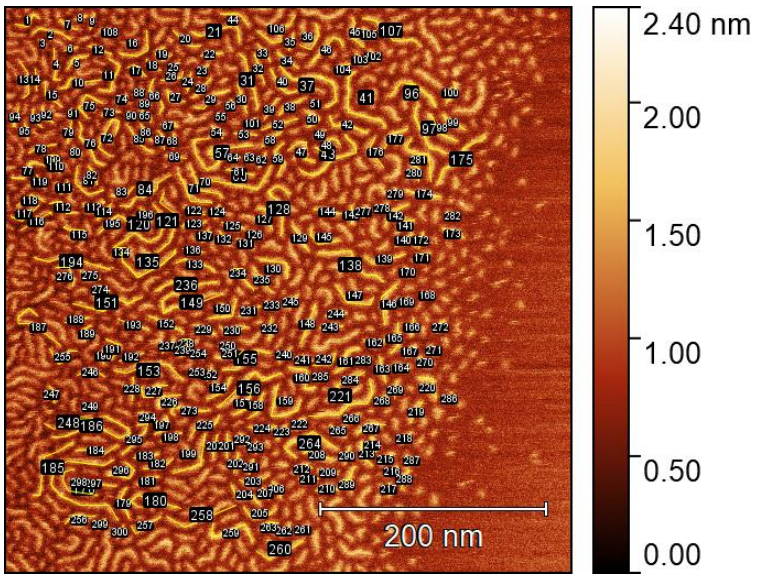

Figure A2.32 AFM image of **B20-100(82%)**, overlaid with the selections used for size measurements.

3 Evaluation of Cationic Bottlebrush Polymers for *in vitro* Gene Transfection

3.1 Introduction

The design of polymeric vectors with low toxicity and high transfection efficiency has long been a goal in gene delivery.[1, 2] With increasing control over polymer synthesis, complex architectures such as star, graft, or hyperbranched polymers are more accessible for application to drug and gene delivery.[3] By introducing a complex architecture, polymers will behave differently to their linear counterparts, often with favourable properties such as reduced toxicity.[4, 5]

Many polymers commonly employed in gene delivery possess a complex architecture, such as branched PEI (bPEI)[6, 7] or poly(amidoamine) (PAMAM) dendrimers.[8, 9] These two polymers contain opposing degrees of control, with PAMAM dendrimers having a monodisperse molecular weight distribution and bPEI being highly disperse with little control over the final polymer structure. Their prevalence in gene transfection indicates an advantage over other (linear) polymers, for instance associated to the ease of synthesis for bPEI or reproducible synthesis and degradability of PAMAM dendrimers, alongside their high charge densities.

Other branched systems have been evaluated for use in gene delivery,[3] such as polymers synthesised through the copolymerisation of a cationic and di-functional monomer,[10] or *via* AB_n or $A_2 + B_m$ step growth polymerisations.[11] These polymerisation methods lead to the formation of highly branched polymers with high structural variation, including degradable or responsive bonds,[12, 13] degree of branching, cationic nature,[14] or biocompatible motifs.[5] In most cases higher transfection and lower toxicity was reported compared to linear analogues.

Bottlebrush polymers can imitate some of the beneficial properties of branched polymers and can be synthesised in a highly controlled manner with a high degree of structural variation.[15, 16] In terms of the bottlebrush polymer structure, variations in the graft density, graft length, or backbone length can all effect the resulting properties. The placement of the charged units can also play a role, with placement on the backbone or grafts effecting the complexation of polynucleotides and polyplex structure. Furthermore, neutral bottlebrush polymers can be used as a prodrug for the delivery of covalently bound nucleotides.[17, 18]

An early example in the use of bottlebrush polymers was reported by Jiang *et. al.* who grafted poly((dimethylamino)ethyl methacrylate) (DMAEMA) to a poly(hydroxyethyl methacrylate) (HEMA) backbone with degradable linkages between the backbone and

graft.[19] These polymers exhibited significant transfection of plasmid DNA (pDNA) in fibroblast cells (COS-7) and showed a reduced toxicity compared to a linear DMAEMA of similar molecular weight.

POx has been employed in the synthesis of bottlebrush polymers for gene delivery in several studies. In all cases, POx was used for its biocompatible properties to reduce toxicity and shield the cationic moieties, rather than to introduce charge into the polymer. The first example was reported by von Erlach *et. al.* where an ester-functionalised PMeOx (DP 50 or DP 100) was grafted onto a DP 20 poly(L-lysine) (PLL) at various densities and compared to a DP 100 PEG grafted PLL.[20] As the grafting density increased the transfection efficiency decreased, likely due to an inability to complex DNA. In addition, the transfection efficiency for DP 100 grafted PMeOx was reduced in comparison to DP 50 PMeOx at similar grafting densities. The resulting toxicity of the polyplexes decreased with increasing grafting densities. No comparison was made between PEG and PMeOx grafted polymers for transfection, however, the cell viability was similar between the two.

In a similar study, Haladjova *et. al.* grafted PEtOx to a lPEI by termination of a growing PEtOx chain with the secondary amines of the lPEI.[21] The transfection efficiency of these polymers was much lower than bPEI, which was used as a positive control, however they exhibited very little toxicity across a wide range of cell lines.

In a different approach Trützschler *et. al.* employed a methacrylate terminated PEtOx in the copolymerisation of a primary or secondary amine containing methacrylate monomer.[22] Grafting densities of 10 or 30 % were used with either a DP 5 or DP 20 PEtOx macromonomer. All graft polymers exhibited lower cytotoxicity and an increased hemocompatibility compared to linear homopolymers of the two amine monomers. The transfection efficiency was greatest for bottlebrush polymers with the shortest macromonomer and lowest grafting density. This was the case for both primary and secondary amine containing copolymers. The transfection efficiency was comparable to the linear homopolymers but less than that of lPEI.

The application of P(Ox-*co*-EI) copolymers has not been studied with bottlebrush polymers, however, previous work in our group investigated the use of hyperbranched P(Ox-*co*-EI) copolymers in the transfection of pDNA.[5] It was found that the hyperbranched polymers preformed comparably with bPEI and a linear analogue in terms of transfection and offered a reduced toxicity. Furthermore, a dependency on the degree

of cationic charge in the copolymer was observed, with transfection efficiency increasing with increasing charge density.

The aim of this chapter is to investigate the ability of bottlebrush polymers to act as gene transfection agents. The bottlebrush polymers synthesised in **Chapter 2** will be applied to the delivery of genetic material. Their ability to condense pDNA into polyplexes and then transfect mammalian cells *in vitro* is extensively studied, with the aim of drawing conclusions on the effect of introducing a bottlebrush architecture.

3.2 Results and Discussion

A library of partially hydrolysed PEtOx-based bottlebrush copolymers with varying degrees of hydrolysis and molecular weights were evaluated for their ability to complex and transfect pDNA. To discern any positive or negative effects of using the bottlebrush architecture a linear copolymer was synthesised, analogous in molecular weight and hydrolysis percentage to one of the bottlebrush polymers. Extensive studies have previously been undertaken on the ability of these linear copolymers to transfect DNA,[23, 24] so this study will primarily focus on the effect of architecture. In addition to the linear copolymer, a linear PEI (lPEI, 25 kDa) was also used to compare the bottlebrush polymers to a commercially relevant transfection agent.

3.2.1 Polymer Synthesis

Table 3.1 Library of polymers used in this study; bottlebrush polymers synthesised in **Chapter 2**.

Polymer	n	m	M_n (g mol^{-1})[a]	$Đ$[a]	Hydrolysis (%)[b]
B10-10(32%)	10	10	7,300	1.24	32
B10-10(46%)	10	10	7,400	1.17	46
B10-10(69%)	10	10	9,700	1.19	69
B10-10(78%)	10	10	10,000	1.13	78
B10-25(31%)	10	25	12,500	1.20	31
B10-25(67%)	10	25	34,700	1.16	67
B10-50(37%)	10	50	19,900	1.26	37
B10-50(67%)	10	50	25,100	1.32	67
L-242(81%)	-	-	-	-	81
lPEI	-	-	-	-	-

Key: **Bn-m(x%)** – x = degree of hydrolysis, n = macromonomer DP, m = bottlebrush copolymer backbone DP. [a] Determined by SEC (Eluent: Water with 3% TFA and 0.1 mol L^{-1} NaCl, Calibration: Poly(vinylpyridine)), [b] Hydrolysis percentage determined from ^{1}H-NMR using **Equation 2.4.**

To assess the effect of architecture, a linear P(Ox-*co*-EI) copolymer was synthesised, with a targeted molecular weight corresponding to **B10-25** (32,600 g mol^{-1}, DP ~250). Initially a linear PEtOx was synthesised by polymerising EtOx using methyl tosylate as an initiator (MeTos). Under dry conditions EtOx, MeTos ([EtOx]/[MeTos] = 290) and acetonitrile were added to a microwave reaction vial and sealed. The polymerisation was carried out

using a microwave reactor at a temperature of 140 °C until the desired conversion had been achieved.

Table 3.2 Characterisation data for **L-242**.

	$[M]_0/[I]_0$[a]	Conv. (%)[a]	DP[b]	M_n (g mol^{-1})[c]	$Đ$[c]
L-242	299	81	242	21,000	1.49

[a] Determined by ^{1}H-NMR. [b] Calculated by multiplying $[M]_0/[I]_0$ by conversion. [c] Calculated from SEC with DMF as the eluent and a PMMA calibration.

The synthesised polymer exhibited a high dispersity, caused by low molecular weight tailing (**Figure 3.1**). This issue is known for the synthesis of high molecular weight PEtOx and can be overcome by laborious purification of the starting materials.[25] However, in the current case a narrow molecular weight distribution is not necessary as the dispersity of the linear PEtOx is in the same range as produced bottle brushes. In addition, as the polymers were to be dialysed after hydrolysis, the tailing should be reduced in the purified polymer. Hydrolysis was carried out as described in **Chapter 2.2.3** using the kinetic graph (**Figure 2.10**) to target specific degrees of hydrolysis.

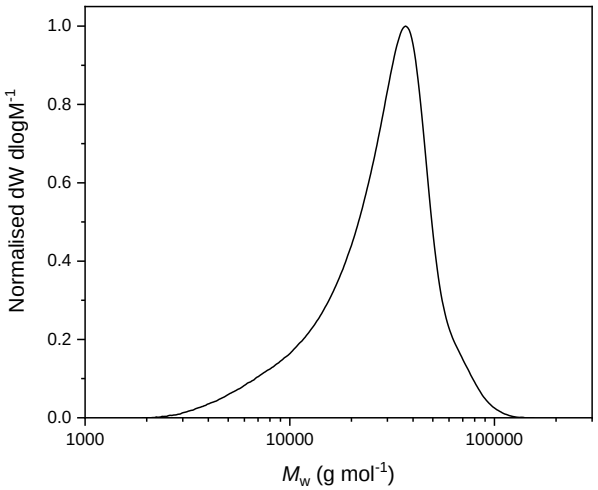

Figure 3.1 SEC curve for **L-242**, measured in DMF with a PMMA calibration.

The hydrolysed polymers (**Table 3.3**) were analysed by ^{1}H-NMR (**Figure A3.3**) to determine the degree of hydrolysis before dialysis and lyophilisation to yield the purified polymers with a degree of hydrolysis equalling 81 %.

Table 3.3 Characterisation data for **L-242(81%)**.

Polymer	Precursor	Time (min)	Hydrolysis (%)[a]
L-242(81%)	L-242	120	81

[a] Conversion determined by ^{1}H-NMR using **Equation 2.4.**

3.2.2 Polyplex Formation

The ability of bottlebrush copolymers to bind and complex pDNA was investigated using a variety of established assays. These parameters greatly determine how well a polymer will transfect DNA and should allow for tuning of the polymer library before *in vitro* experiments. All studies on polyplex formation were carried out using a pHR' CMV GFP plasmid, a 10.8 kbp plasmid encoding for the enhanced green fluorescent protein (EGFP).[26] This enables quantification of *in vitro* transfection by measuring the expression of the fluorescent protein. The vector is derived from the human immunodeficiency virus (HIV) and contains the cytomegalovirus (CMV) promoter, required for efficient transcription in mammalian cells.[27]

3.2.2.1 Determination of pDNA Binding by Agarose Gel Electrophoresis

Agarose gel electrophoresis was initially used to quantify the required N/P ratio for complete complexation of pDNA by the library of polymers described above. The N/P ratio is the molar ratio of cationic residues on the polymer (N) to anionic residues on the pDNA (P). By measuring the polyplexes formed at different N/P ratios, a crude determination of the ability of the polymer to bind pDNA can be made. Polyplexes are loaded into the wells and an application of a voltage across the gel causes any unbound pDNA to migrate towards the anode, allowing separation between bound and unbound pDNA. The complexation with polymers reduces the ability of the complex to migrate through the gel due to the increased size of the complex and the reuction in negative surface charge, causing no migration and retention in the well.

B10-10(32%), a DP10 bottlebrush polymer with 32 % cationic units exhbited very little pDNA binding across a range of N/P ratios (**Figure 3.2A**). Free pDNA was observed in all wells of the gel indicating the inability of **B10-10(32%)** to fully complex pDNA. By increasing the charge density to 46 %, **B10-10(46%)**, full complexation of the pDNA is achieved at an N/P ratio of 5 (**Figure 3.2B**), and N/P 2 for a bottlebrush polymer with 69 % charge density (**B10-10(69%)**, **Figure 3.2C**).

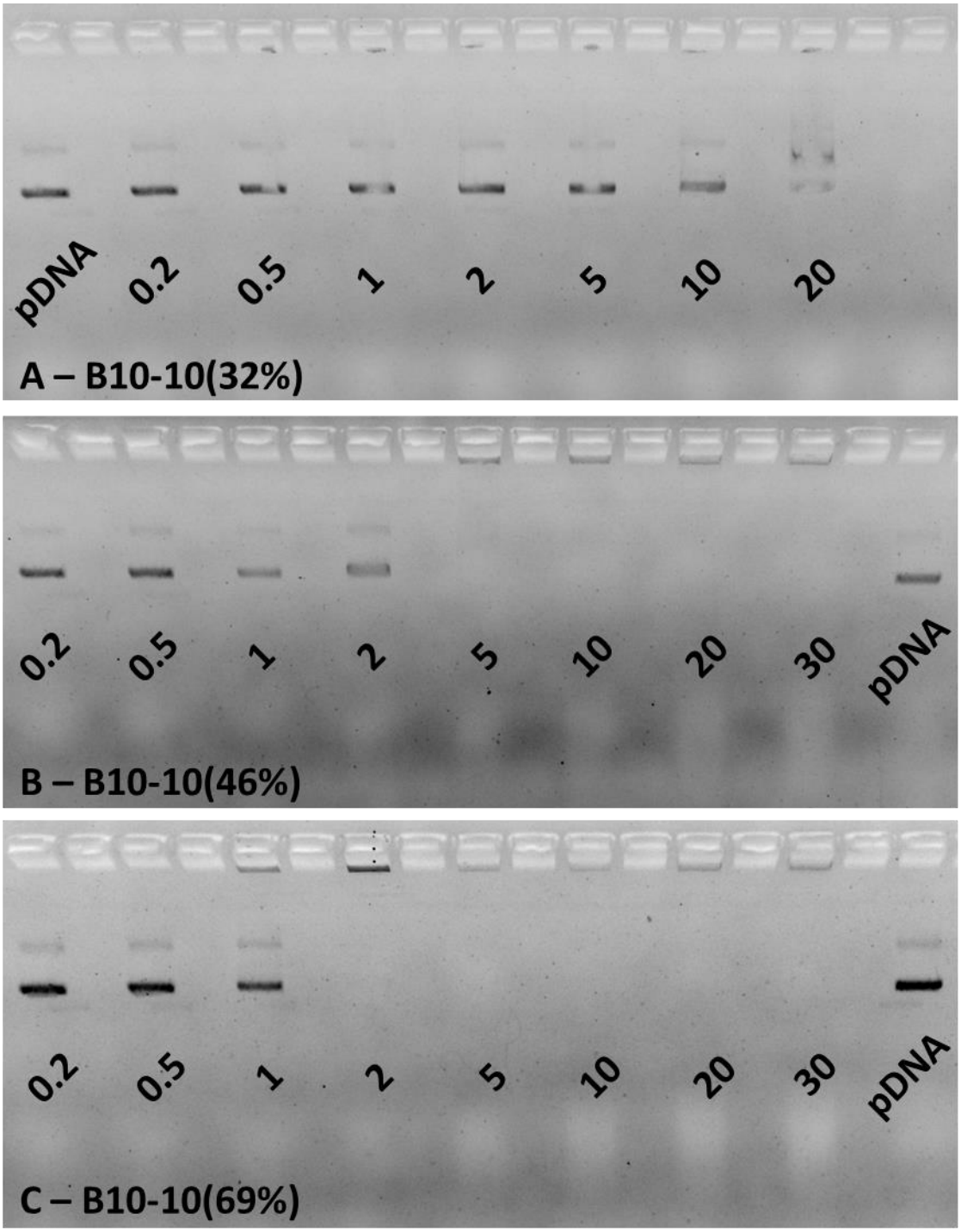

Figure 3.2 Polyplex formation determined by agarose gel electrophoresis. 0.8% agarose gels were run at 100 V for 30 minutes using 1 X TAE running buffer. **A – B10-10(32%)**, **B – B10-10(46%)**, **C – B10-10(69%)**.

All polymers were analysed by this method and the same trend was observed regardless of molecular weight (**Figure A3.4-A3.6**). The complexation of pDNA by bottlebrush polymers appears to be dependent only on the cationic density, with complexation at lower molar ratios observed for polymers with higher charge density.

lPEI (**Figure A3.8**) and **L-242(81%)** (**Figure A3.7**) were also analysed and exhibited similar binding efficiencies to the bottlebrush polymers with similar charge densities. Therefore the architecture of the polymer does not appear to play a significant role in its ability to complex pDNA.

3.2.2.2 Ethidium Bromide Displacement Assay

Polyplex formation can also be studied by looking at the displacement of intercalating agents, such as ethidium bromide (EthBr), from between the base pairs of double-stranded DNA.[28] When EthBr is placed in the hydrophobic region between the base pairs it exhibits a strong fluorescence, however, when it is displaced this fluorescence is quenched by water leading to a decrease in fluorescence intensity. This change can be used to monitor the binding of polymers to DNA, as the binding of the polymer causes EthBr to be displaced, leading to a decrease in fluorescence.

EthBr and pDNA were mixed and allowed to form a fluorescent complex. Polymer was then added in increasing N/P ratios and incubated with the pDNA/EthBr complex for 15 minutes. After this time, the fluorescence of the solution was measured and compared to a control where no polymer was added to determine the percentage of EthBr displaced from within the pDNA. **Figure 3.3A** shows the level of EthBr displacement for a series of bottlebrush polymers with the same molecular weight but increasing in charge density from 30 – 80 %. **B10-10(32%)** exhibits very little displacement of the EthBr, which correlates with the results from the agarose gel polyplex formation assay where no polyplex formation was observed. As the charge density increases greater amounts of EthBr are displaced from within the pDNA, with **B10-10(78%)** exhibiting the greatest degree of displacement of 55 % at N/P 20.

The effect of molecular weight is less pronounced than that of charge density. A series of bottlebrush polymers with the same charge density and different molecular weight were compared (**Figure 3.3B**). As the molecular weight increased there is a slight increase in the amount of EthBr displaced, with **B10-50(67%)** displacing 20 % more EthBr than **B10-10(69%)**. **L-242(81%)** displaces a similar amount of EthBr to the bottlebrush polymer with a corresponding molecular weight (**B10-25(67%)**), again indicating little influence of the architecture on pDNA binding. However, higher molecular weight brushes with lower charge density, **B10-50(67%)**, are found to displace more EthBr than **L-242(81%)** further exemplifying the molecular weight dependence of EthBr binding.

lPEI exhibits the greatest level of EthBr displacement of all polymers assessed, displacing a maximum of 60 % at N/P 20. This is comparable with **B10-10(78%)** which has a charge density of 78 %, compared to lPEI with 100 % charge density.

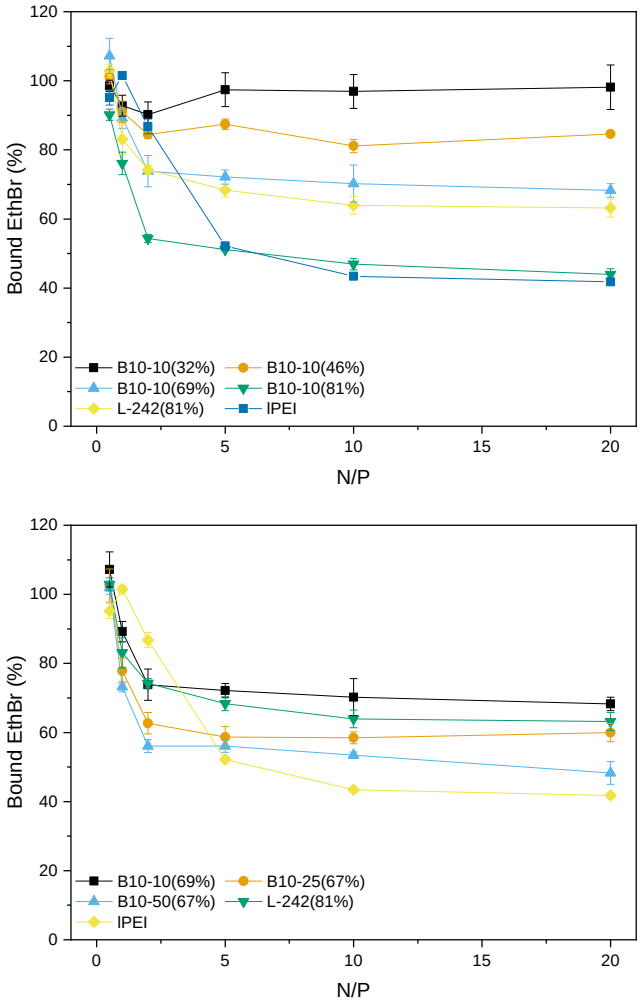

Figure 3.3 Ethidium bromide displacement assay. A - Comparison of effect of increasing charge density on displacement. B - Comparison on effect of molecular weight and architecture on displacement.

3.2.2.3 Size and Morphology of Polyplexes

Cellular uptake of nanoparticles is greatly influenced by their size and morphology. The optimal size for polyplex uptake is generally considered to be between 100 – 200 nm, with other factors such as surface charge also having an effect.[29] Therefore, in order to understand any differences observed in cellular uptake, the size of the polyplex must be determined.

Polyplexes were prepared at N/P 20 in HEPES buffer to mimic the media used in cell culture and their size measured using dynamic light scattering (DLS). The charge of the polyplex was determined using zeta-potential measurements, which gives an estimate of the particles surface charge. Polyplexes formed from bottlebrush and linear P(Ox-*co*-EI) all had a similar size, in the range of 90 – 120 nm. lPEI was observed to form the smallest polyplex with a diameter of 77 nm (**Figure 3.4A**). lPEI has the highest charge density and chain flexibility of the polymers tested which could explain the greater ability to condense pDNA. There was little difference in size between the linear and bottlebrush polymers, or any observable trend in size caused by differences in molecular weight and charge density. This is inconsistent with previous work by Cook *et. al.* on similar systems where a considerable size difference was observed between linear and hyperbranched polymer-containing polyplexes.[5] However, the molecular weight of the linear polymer used in this study was much greater than Cook *et. al.* The molecular weight of linear P(Ox-*co*-EI) was shown to influence the resulting size of the polyplex in a study by Bauer *et. al.* where high molecular weight polymers were able to form smaller polyplexes.[23]

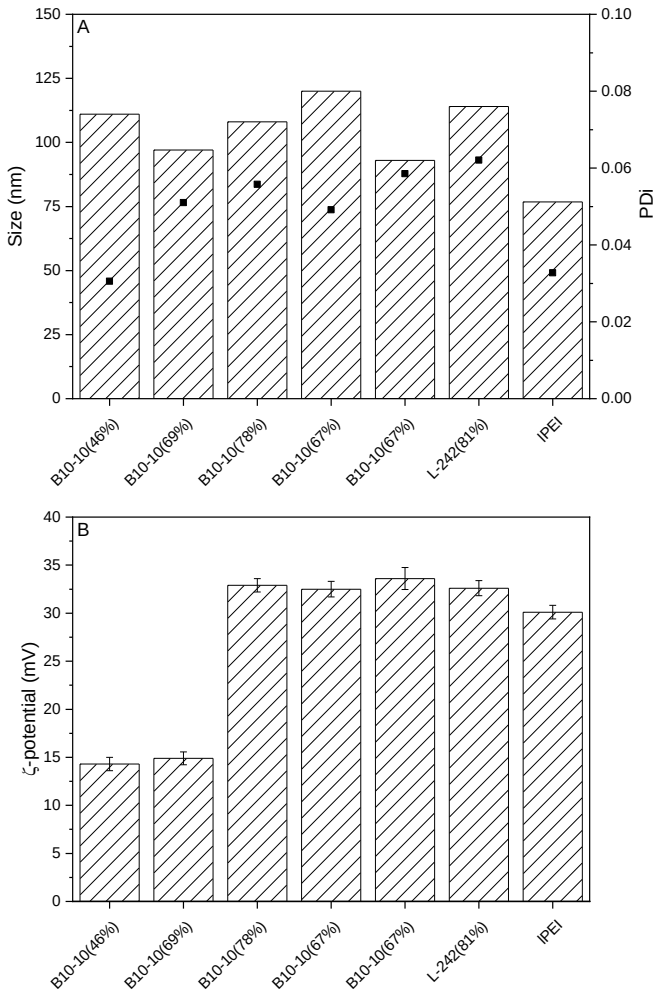

Figure 3.4 A - Size of nanoparticles determined by DLS. Polydispersity index (PDi) calculated using **Equation 3.2**. B - Zeta-potential measurements of polyplexes at N/P 20.

By measurement of zeta-potential, all polyplexes were observed to have a positive surface charge, between 15 and 35 mV (**Figure 3.4B**). The only difference was observed in the surface charge of polyplexes formed by **B10-10(46%)** and **B10-10(69%)**, which exhibited lower zeta-potentials than the other polyplexes. For **B10-10(46%)** this could be caused by the lower charge density of the polymer. It is unclear as to why **B10-10(69%)** possesses a lower zeta-potential than **B10-10(78%)**, given the similarity in charge density and molecular weight. This will need to be investigated further in order to clarify.

In addition to size, morphology also effects the uptake efficiency of nanoparticles.[30] DLS does not give any information on the morphology of the nanoparticles and is only accurate in measuring the size of spherical objects. To compliment the DLS measurements

transmission electron microscopy (TEM) was used to determine the morphology of the polyplexes. Polyplexes were prepared and deposited onto a formvar/carbon coated grid before staining with uranyl acetate.

The major and minor axis of each polyplex was measured for all samples and are plotted in **Figure 3.6A** and **Figure 3.6B**. In addition, the aspect ratio was determined which is the ratio between the major and minor axis. A value close to 1 indicates spherical objects, with an increase in aspect ratio indicating elongated structures. For all bottlebrush polymers, except for **B10-10(46%)**, an average aspect ratio > 1.5 was observed, indicating the formation of elongated structures. These elongated structures can be seen in the TEM images, which show a mixture of elongated and spherical structures. **lPEI**, **L-242(81%)**, and **B10-10(46%)** exhibit more spherical polyplexes, with an aspect ratio closer to 1.

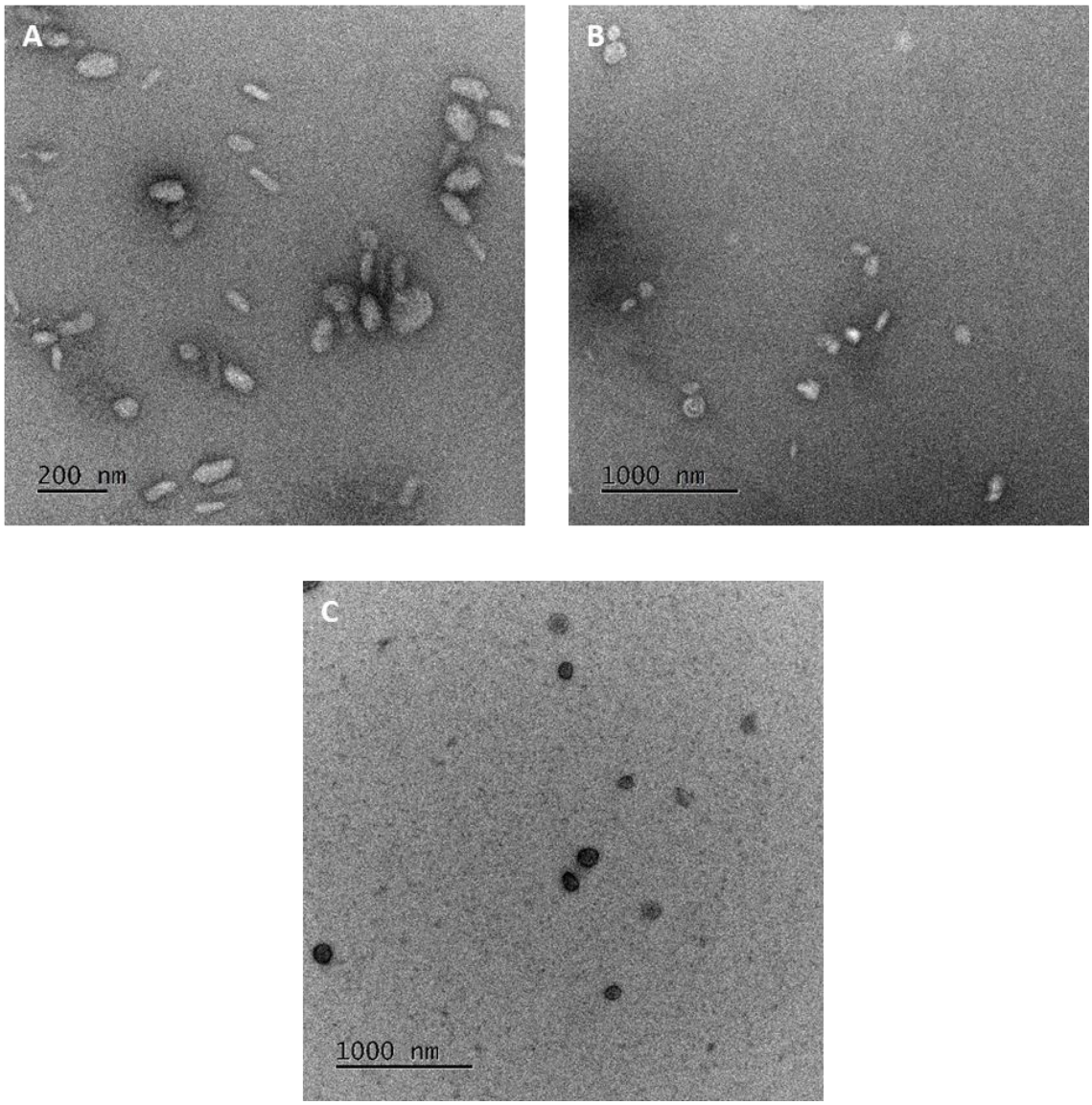

Figure 3.5 Transmission Electron Microscopy (TEM) images of polyplexes formed with **B10-10(69%)** (A), **L-242(81%)** (B), and **lPEI** (C). Polyplexes deposited on formvar/carbon grids and stained with uranyl acetate.

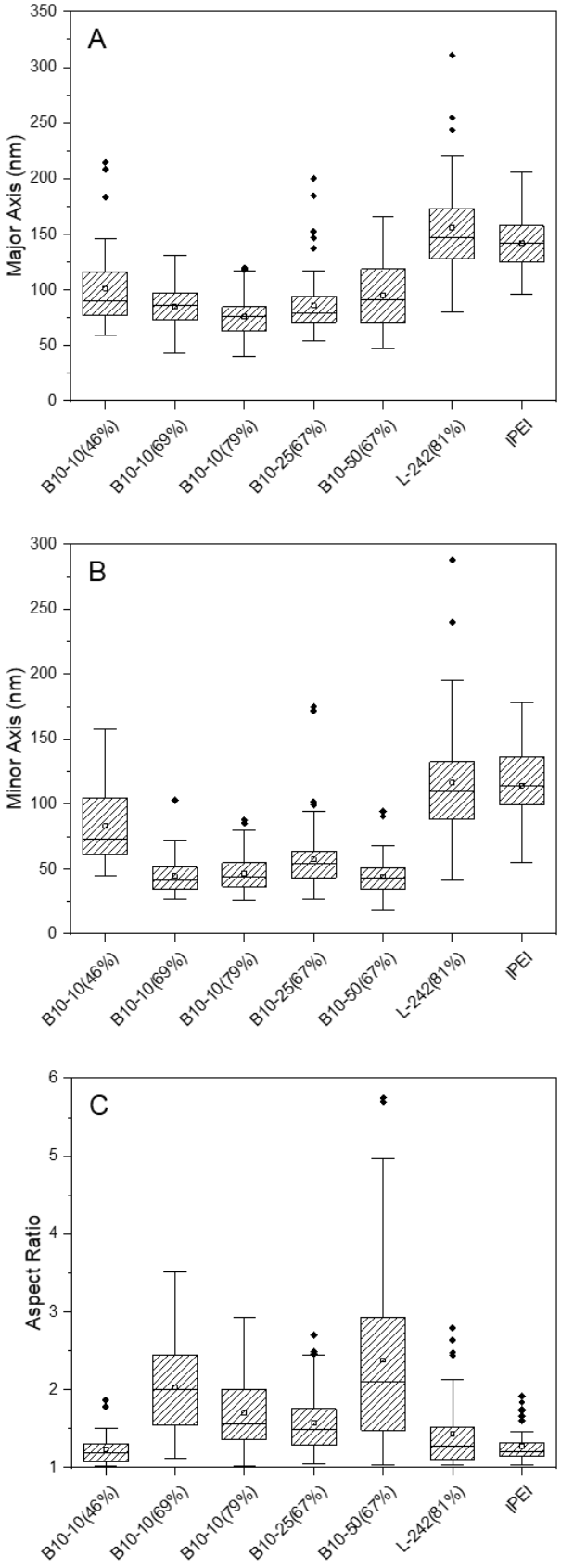

Figure 3.6 Major (A) and minor (B) axis lengths determined from TEM images. C - Aspect ratio of polyplexes. n = 42 for **B10-10(46%)**,n = 55 for **B10-10(69%)**, n = 79 for **B10-10(79%)**, n = 90 for **B10-25(67%)**, n = 80 for **B10-50(67%)**, n = 54 for **L-242(81%)**, n = 43 for **lPEI**. (□) = mean, (♦) = outliers.

For a subpopulation of some polyplexes it is possible to observe the pDNA partially complexed, rather than completely condensed. It is likely that this occurs for all samples and is not visible due to inefficient staining. The extent of partial complexation cannot be determined from the TEM and further studies would be required to understand why this occurs. This observation suggests a limitation in the application of agarose gel electrophoresis to study polyplex formation as these partially complexed species would be unable to migrate through the gel. It would therefore underestimate the amount of polymer required for full complexation.

3.2.2.4 Polyplex Stability towards Competing Anions

One barrier for the efficient delivery of pDNA is the competing interactions between the polyplexes and anionic macromolecules, such as glycosaminoglycans (GAGs). These polysaccharides are major components of the extracellular matrix of tissues and can also be found inside cells or on their surface. GAGs play a positive and negative role in internalisation of polyplexes.[31] They can facilitate cellular uptake, with membrane-associated GAGs acting as receptors for the binding of polyplexes to the cell membrane.[32] However, GAGs can destabilise polyplexes *via* competitive binding with nucleotides, causing their displacement.

To study the effects of competitive binding with polyanions, polyplexes in the presence of EthBr were incubated with increasing concentrations of heparin, a highly sulfonated GAG with the greatest negative charge density of all GAGs. After each addition of heparin, the fluorescence of the solution was measured and compared to the fluorescence of naked pDNA and EthBr. As heparin displaces pDNA from the complex EthBr can bind with the minor groove causing an increase in fluorescence. The polymers were compared by calculating the recovered fluorescence with increase of heparin concentration.

$$Fluorescence\ Recovered = \frac{fluorescence_{polyplex+heparin}}{fluorescence_{EtBr+pDNA}} \times 100 \qquad \textbf{3.1}$$

Figure 3.7A displays the change in fluorescence for polymers with increasing charge density. Before any addition of heparin **B10-10(45%)** shows a significant level of fluorescence. This corresponds to the results from the EthBr displacement assay (**Section 2.2.2.2**) where the polymer showed a lower level of EthBr displacement compared to polymers with greater charge density. A lower concentration of heparin is also required

to disrupt the polyplex as indicated by an increase in fluorescence at lower heparin concentrations. For **B10-10(6%)** and **B10-10(79%)** similar levels of pDNA displacement are observed at the same concentration of heparin, indicating similar stability towards competing anions.

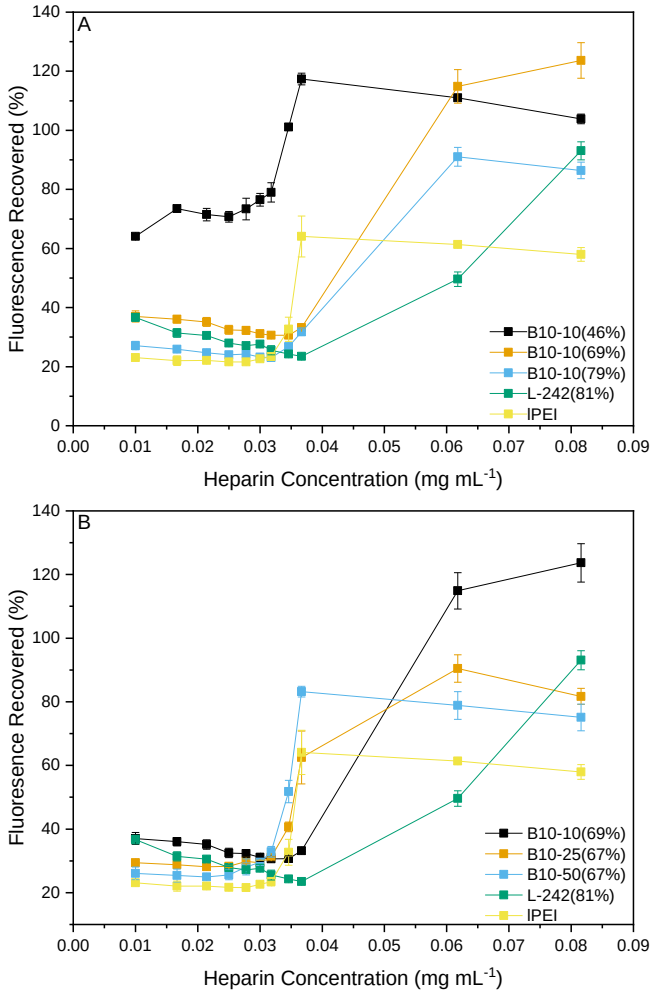

Figure 3.7 Determination of pDNA released from the polyplex upon incubation with heparin. A - Comparison of the effect of charge density on resistance to heparin induced displacement. B - Comparison of the effect of molecular weight and architecture on resistance to heparin induced displacement. Measurements obtained in triplicate.

Figure 3.7B shows the level of displacement for bottlebrush copolymers with increasing molecular weights and the linear copolymer and lPEI control. Displacement of pDNA appears to occur at similar heparin concentrations for the bottlebrush copolymers with higher levels of fluorescence observed for lower molecular weight copolymers. The linear copolymer appears to show a stronger affinity for pDNA than the bottlebrush copolymers,

with **L-242(81%)** requiring higher concentrations of heparin to reach the same level of fluorescence as the bottlebrush copolymers. lPEI appears to withstand displacement to a higher degree than all polymers with a lower level of recovered fluorescence observed at the maximum concentration of heparin administered.

3.2.3 *In Vitro* Experiments

3.2.3.1 Polymer Toxicity towards Human Embryonic Kidney (HEK293T) Cells

The toxicity of polymeric vectors is one of the biggest challenges to overcome when designing new systems for the delivery of pDNA. Cationic polymers can be highly toxic both *in vitro* and *in vivo* by disrupting the cell membrane, lysing red blood cells, causing red blood cells and negatively charged proteins to aggregate, and interfering with cellular processes once internalised within the cell. This has driven the development of cationic polymers that are still able to condense DNA but have a reduced cytotoxicity.

The toxicity of the polymers was determined by using a metabolic activity assay based on the reduction of tetrazolium dyes. If a cell is metabolically active, NAD(P)H-dependent cellular oxidoreductase enzymes can reduce the tetrazolium dye causing a change in colour. Under certain conditions this colour change is reflective of the number of viable cells and can be used to determine the toxicity of compounds.

2,3-bis-(2-methoxy-4-nitro-5-sulfophenyl)-2H-tetrazolium-5-carboxanilide (XTT) was used as the tetrazolium dye due to the solubility of the formazan product, avoiding the need for solubilisation of the dye. The assay was first optimised to determine the appropriate cell density and incubation time for human embryonic kidney 293 (HEK293T) cells (**Figure A3.13**). Cells were seeded at various densities and incubated with XTT. The absorbance was monitored over time and plotted as a function of cell density. A linear increase in absorbance with time is required for the assay to detect changes in cell viability. A cell density of 10,000 cells per well was chosen for the cell viability assays as it fit these criteria and provided a significant absorbance.

Polymers were incubated with HEK293T cells at varying concentrations (15.63 – 1000 μg mL^{-1}) for 24 hours, before their removal and addition of XTT. The cell viability was determined with three technical and three biological replicates and is presented in **Figure 3.8**. The toxicity of the bottlebrush polymers was compared to a linear polymer and lPEI to ascertain the influence of architecture on toxicity and compare to a relevant standard. **Figure 3.8B** presents the toxicity of a DP10 bottlebrush polymer with differing

degrees of charge density. All polymers exhibit neglectable toxicity towards HEK293T cells at typical therapeutic concentrations, even at high degrees of hydrolysis.

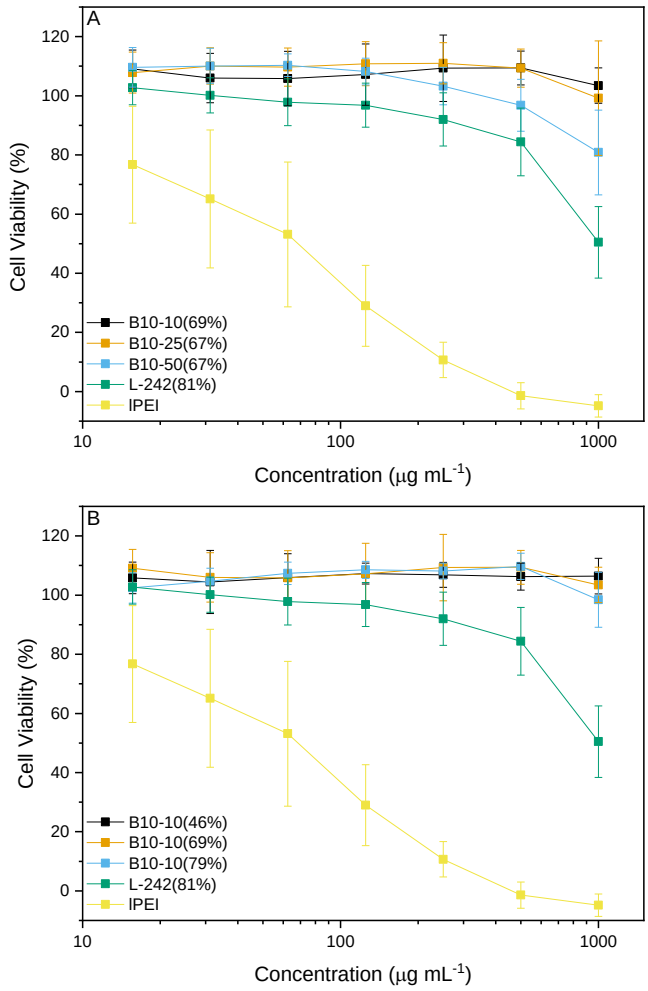

Figure 3.8 Cell viability, as determined by the XTT assay, on HEK293T cells. Polymers were incubated with cells for 24 hours. A – Effect of molecular weight and architecture on cell viability. B – Effect of charge density on cell viability.

Bottlebrush polymers with the same charge density but different molecular weights were compared (**Figure 3.8A**). At higher concentrations, polymers with higher molecular weights exhibit greater toxicity towards HEK293T cells. However, the cell viability is still greater than 80 %, which is considered below the threshold for toxic polymers. Comparison of a linear and bottlebrush polymer with similar molecular weights reveals that linear polymers have an increased toxicity compared to their bottlebrush counterparts. This trend has been observed before in several studies. lPEI exhibited high

toxicity across a range of concentrations, with cell viability below 80 % for all concentrations.

The toxicity of the bottlebrush polymers appears to be dependent on molecular weight to a greater extent than charge density. Studies have shown that there is a molecular weight-dependent toxicity associated with cationic polymers, with higher molecular weight polymers exhibiting greater lactate dehydrogenase release and lower mitochondrial activity.[33] Furthermore, the toxicity was measured for pure polymers rather than the polyplex, often the toxicity of polyplexes is reported which will have a reduced toxicity compared to the pure polymer, obscuring any high toxicity associated with the polymer. Interestingly, the polymers only exhibited significant toxicity at concentrations much higher than that of a relevant therapeutic concentration.

3.2.3.2 Transfection of HEK293T Cells by Bottlebrush Polymers

HEK293T cells were transfected with polyplexes formed using a plasmid encoding for EGFP, this enables quantification of transfection as the cells will fluoresce once the plasmid has been transcribed. The bottlebrush polymers were compared to lPEI (+ve control) and naked pDNA (-ve control) to determine their effectiveness in the transfection of pDNA. Naked pDNA should undergo very little transfection due to difficulties in cellular uptake and degradation by nucleases.

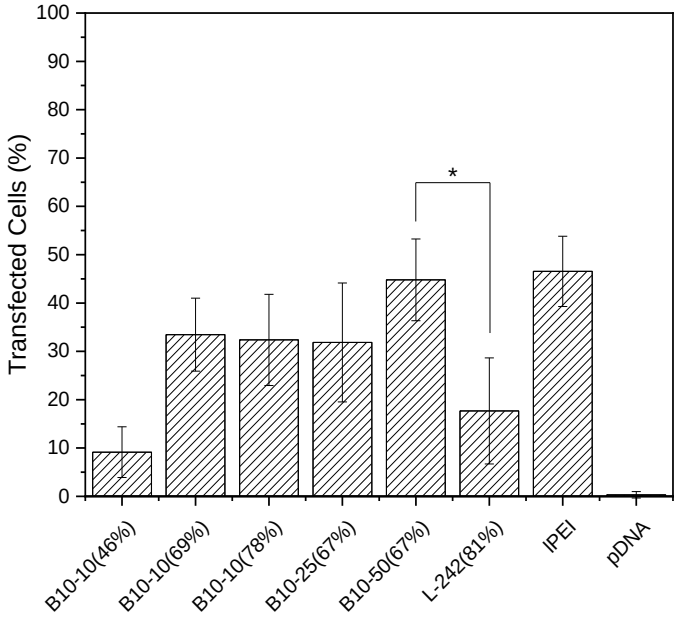

Figure 3.9 Transfection of HEK293T cells using polyplexes ([pDNA] = 10 μg mL^{-1}) comprised of polymers and a pDNA encoding for EGFP. Expression of EGFP was measured using flow cytometry. Values represent mean ± SD (n = 5). * significant difference ($p < 0.001$) by ANOVA analysis.

The results from transfection are presented in **Figure 3.9**. The percentage of cells transfected was determined by flow cytometry by comparing the number of cells exhibiting EGFP fluorescence compared to the total number of cells.

In terms of transfection some immediate trends are noticed. First, bottlebrush polymers with charge density < 67 % exhibited poor transfection compared to polymers with charge density ≥ 67 %. Comparison of **B10-10(46%)** and **B10-10(69%)** showed a 3.5 x increase in cells transfected by increasing the charge density from 46 % to 69 %. There was little difference in transfection efficiency between **B10-10(69%)** and **B10-10(78%)** suggesting a negligible effect in charge density above a certain threshold. With toxicity dependent on the charge density, this result indicates the ability to use lower toxicity polymers without sacrificing transfection efficiency, something rarely found in the literature.

Secondly, molecular weight appeared to also play a role in the transfection efficiency of the polyplexes with **B10-50(67%)** exhibiting the highest percentage of cells expressing EGFP for all bottlebrush polymers measured, with comparable levels of expression to lPEI. This result is particularly promising as the toxicity of **B10-50(67%)** is much lower than that of lPEI, making it a promising candidate for wider use in gene delivery.

Lastly, the influence of architecture is visible with **L-242(81%)** exhibiting lower levels of transfection than all bottlebrush polymers, except for the low charge density **B10-10(46%)**. Comparing **L-242(81%)** with **B10-25(67%)** allows for the determination of architecture effect as these polymers have similar molecular weights. It is evident that the use of a bottlebrush polymer has its advantages over linear polymers as the transfection efficiency is higher and the toxicity lower. Statistical analysis for the bottlebrush and linear copolymers revealed a significant difference between **L-242(81%)** and **B10-50(67%)** only.

To visualise the expression of EGFP, HEK293T cells were imaged post-transfection with **B10-10(69%)** using a Cytation3 cell imager. The nuclei of the cells were stained with DAPI to visualise individual cells. **Figure 3.10A** shows the cells imaged through the EGFP filter, so only cells expressing EGFP can be visualised. A second image was taken using the DAPI filter and the images overlayed (**Figure 3.10B**), to show the number of transfected cells in a population.

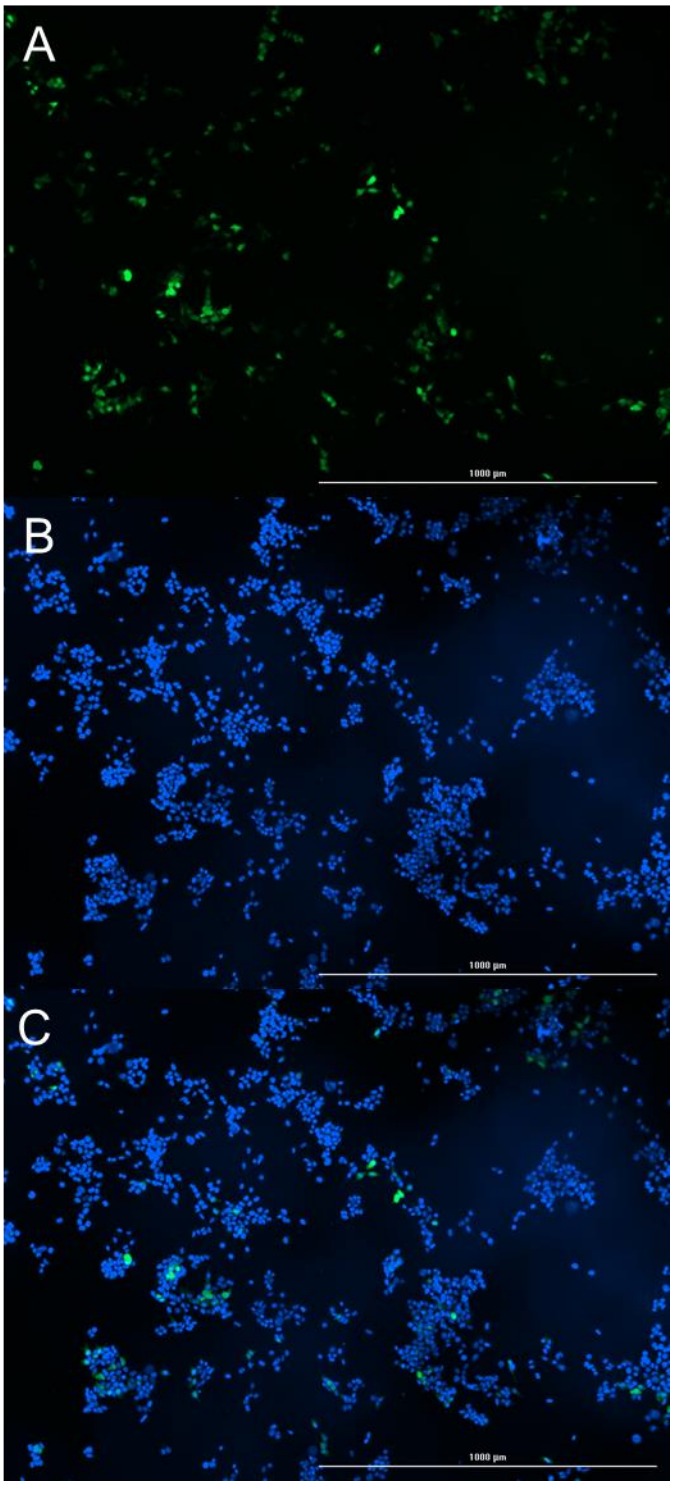

Figure 3.10 HEK293T transfected using **B10-10(69%)** expressing EGFP imaged using a Cytation3 cell imaging multi-mode reader. A - GFP channel, B – DAPI channel, C - Overlay of DAPI and EGFP channels.

3.2.3.3 Formation of Aggregates in the Presence of Serum Proteins

Polyplexes are known to aggregate under high salt concentrations or through non-specific interactions with negatively charged proteins or red blood cells.[34, 35] When carrying out

the transfection experiments, aggregates were observed in the wells when viewed under a microscope. These aggregates were observed in all wells containing polyplexes, but not in wells containing naked pDNA.

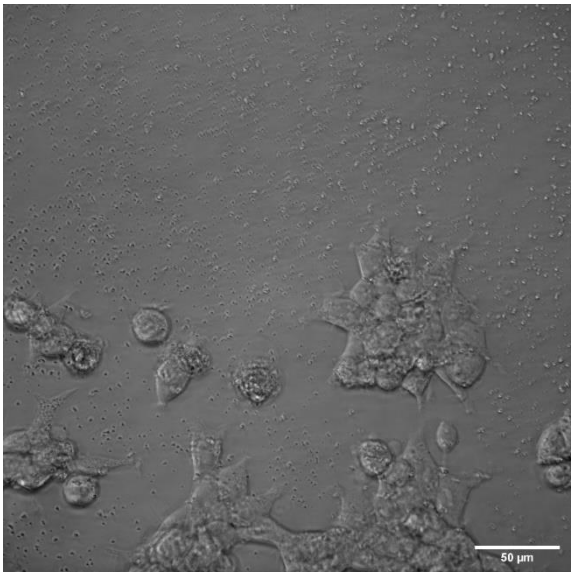

Figure 3.11 Formation of aggregates in the presence of **B10-10(69%)** polyplexes. Image obtained using Leica DMi8 microscope (100 x objective).

Figure 3.11 shows the presence of aggregates for polyplexes derived from **$HB_{0.69}$-10_{10}** when incubated with cells. To determine the cause of aggregation polyplexes were incubated with different media and visualised under a microscope to check for aggregates. Polyplexes were incubated with Opti-MEM, either fresh or taken from the supernatant of growing cells, and water, to see if the aggregation is inherent to the formation of polyplexes or only occurs when incubated in the presence of cellular proteins (**Figure 3.12**).

Aggregates are observed in fresh Opti-MEM and supernatant Opti-MEM, but not water, indicating that the composition of Opti-MEM is causing the aggregation of the polyplexes. Opti-MEM is often used in transfection as there are reduced levels of serum proteins which in turn increases the transfection efficiency of the polyplex, due to the aforementioned aggregation in the presence of proteins. It would appear that the reduced level of proteins in Opti-MEM is still able to cause the aggregation of polyplexes. From the transfection results, this aggregation does not appear to significantly hinder the ability of the polyplexes to transfect cells, however, this is an undesired process that could hinder the use of these materials in further study. However, if it is possible to overcome the aggregation greater transfection efficiencies may be possible. Further modifications to

the polyplex may be required to overcome this aggregation and should be the focus of future work.

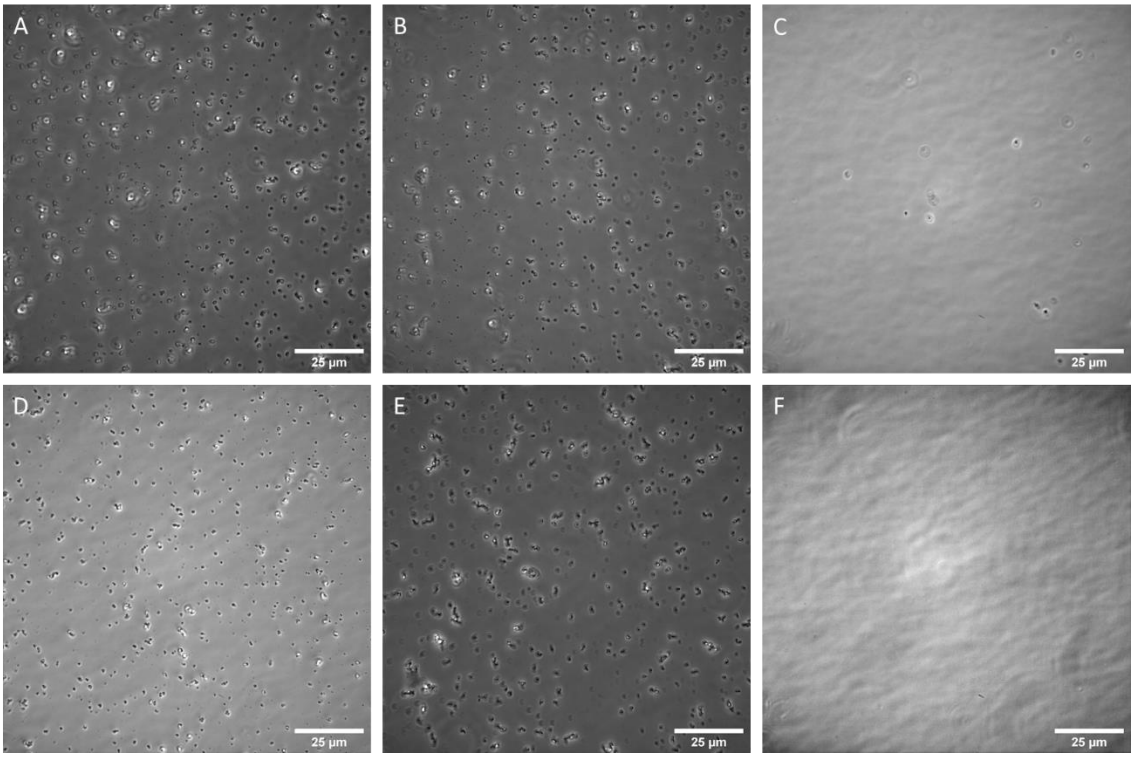

Figure 3.12 Incubation of **B10-10(69%)** (A-C) or lPEI (D-F) polyplexes incubated with fresh Opti-MEM (A, D), cell supernatant Opti-MEM (B, E), or water (C, F). Scale bar = 25 µm. Images obtained using a Leica DMi8 microscope (100 x objective).

3.3 Conclusions

In this study, bottlebrush polymers have been assessed for the delivery of genetic materials; their ability to condense pDNA and deliver it to mammalian cells were investigated. Structural parameters such as molecular weight, architecture, and charge density have been varied to understand the role that each play on the efficacy of the polymer. In the complexation of pDNA, the charge density of the polymer played an important role, with polymers with higher charge density able to condense pDNA at lower N/P ratios. Below a charge density of 45 % very little complexation was observed. The size and morphology were also studied, and bottlebrush polymers were found to form more elongated polyplexes compared to the spherical particles of their linear counterparts.

Promisingly, bottlebrush polymers with charge density > 65 % showed excellent transfection of HEK293T cells, with a significant increase in transfection observed compared to a linear analogue. The transfection rate was also comparable to lPEI, a commercially used reagent for transfection. Lower toxicity of the bottlebrush polymers compared to linear copolymers and lPEI also makes these materials highly promising as new transfection reagents.

3.4 Experimental

3.4.1 Materials

pHR' CMV GFP plasmid was provided by Dr John James (University of Wawick) and isolated using a Qiagen Maxi Prep kit, following the established protocol. Opti-MEM and Dulbecco's Modified Eagle Media (DMEM) were purchased from Thermo Fisher. Foetal bovine serum (FBS) was purchased from LabTech.com. Ethidium bromide (10 mg mL^{-1} solution), Heparin (sodium salt from porcine intestinal mucosa), and 2-Ethyl-2-Oxazoline were purchased from Sigma-Aldrich. Human embryonic kidney cells 293 (HEK293T, CRL-3216) were purchased from American type culture collection (ATCC). Methyl p-toluenesulfonate (MeTos) was purchased from VWR. Acetonitrile (99.9%, Extra Dry, AcroSeal™) was purchased from Fisher Scientific.

3.4.2 Characterisation

3.4.2.1 Proton Nuclear Magnetic Resonance (^{1}H-NMR)

^{1}H-NMR spectra were recorded using a Bruker DPX-300 or DPX-400 NMR spectrometer which operated at 300.13 and 400.05 MHz, respectively. The residual solvent peaks were used as internal references. Deuterated chloroform ($CDCl_3$) (δ_H = 7.26 ppm) and deuterated methanol (MeOD) (δ_H = 3.31 ppm) were used as the solvents for all measurements.

3.4.2.2 Size Exclusion Chromatography (SEC)

An Agilent Infinity II MDS instrument equipped with differential refractive index (DRI), viscometry (VS), dual angle light scatter (LS) and multiple wavelength UV detectors was used for SEC analysis. The system was fitted with 2 x PLgel Mixed D columns (300 x 7.5 mm) and a PLgel 5 µm guard column. The eluent used was DMF with 5 mmol NH_4BH_4 additive. Samples were run at 1 mL min^{-1} at 50 °C. Poly(methyl methacrylate) standards (Agilent EasyVials) were used for calibration between 955,500 – 550 g mol^{-1}. Analyte samples were filtered membrane with 0.22 µm pore size before injection. Respectively, experimental molar mass ($M_{n,SEC}$) and dispersity ($Đ$) values of synthesized polymers were determined by conventional calibration using Agilent GPC/SEC software.

3.4.2.3 Transmission Electron Microscopy

In all cases the Formvar/carbon coated copper grids were subjected to glow discharge to render their surface hydrophilic. Then, 5 µl of sample was added to the grid and incubated for 1 min. After addition of the sample, excess solution was removed by blotting with tissue. 2 % uranyl acetate was added for a total of 3 min incubation (3 drops of 1 minute

each). Again, excess liquid was removed by blotting and the grid was allowed to airdry. Imaging was done on a Jeol 2100Plus TEM fitted with a Gatan OneView IS camera and images analysed by Fiji (www.fiji.sc).

3.4.2.4 Dynamic Light Scattering/Zeta-Potential Measurements

Size and zeta-potential measurements were carried out using an Anton Paar Litesizer 500 at a polymer concentration of 0.1 mg mL^{-1} and a temperature of 25 °C. The instrument is equipped with a semiconductor laser diode (40 mW, 658 nm). Size measurements were obtained at a scattering angle of 173 ° (back scatter). PDi was calculated using **Equation 3.2**. Zeta-potential measurements were carried out using Anton Paar omega cuvettes and modelled using the Smoluchowski theory.

$$PDi = \frac{\sigma^2}{d^2} \qquad \textbf{3.2}$$

3.4.2.5 Statistical Analysis

To determine the statistical significance, analysis of variance (ANOVA) was performed using a Bonferroni test for means comparison. Statistically significant differences were indicated with * for $p < 0.001$. All statistical analyses were performed with data of $n = 5$ in OriginPro (Version 2019b).

3.4.3 Synthetic Procedures

3.4.3.1 Synthesis of Poly(2-Ethyl-2-Oxazoline)

To a dry microwave vial was added methyl tosylate (9 µL, 0.06 mmol), 2-ethyl-2-oxazoline (1.8 mL, 18 mmol) and acetonitrile (2.7 mL). The vial was sealed and placed into a microwave reactor before heating at 140 °C for 15 minutes. After polymerisation, the vial was opened to air and the solvent removed using rotary evaporation. The polymer was dissolved in dichloromethane and washed with 3 x Na_2CO_3 and 3 x brine. Precipitation in diethyl ether and filtration yielded the purified polymer.

3.4.3.2 Synthesis of Poly[(2-Ethyl-2-Oxazoline)-*co*-(Ethylenimine)]

PEtOx containing polymer was dissolved in 1 M HCl (concentration of amide = 0.48 M) and added to a microwave reaction vial with a magnetic stirrer and sealed. The vial was placed in a Biotage Initiator+ Eight microwave reactor at 120 °C for a predetermined amount of time. After the reaction, the solution was made basic by addition of 4 M NaOH, before dialysis using an Amicon Ultra-15 centrifugal filter unit (MWCO = 3 kDa) to remove any salt formed. The solution was lyophilised to yield the product.

3.4.4 Experimental Procedures

3.4.4.1 Cell Culture

Human embryonic kidney cells 293 (HEK293T) were grown in DMEM (Dulbecco's Modified Eagle Medium) supplemented with 10 % foetal bovine serum (FBS) and 1 % penicillin/streptomycin. Cells were grown as monolayers at 310 K under an atmosphere of 5 % CO_2, and passaged once they have reached 70-80 % confluency (once every three days).

3.4.4.2 Polyplex Formation

Polyplex formation was carried out as follows. To an Eppendorf tube was added water and polymer followed by thorough mixing. pDNA ($[pDNA]_{final}$ = 35 μg mL^{-1}) was added to the Eppendorf tube to make a total volume of 100 μL and vortexed for 30 seconds before a 30 minute incubation at room temperature. The concentration of pDNA was fixed in all samples and the concentration of polymer varied to the make the targeted N/P ratio.

Agarose gels (0.8 % w/v) were prepared by adding 1.6 g agarose powder to 200 mL 1 X TAE buffer and heating in a microwave to dissolve the agarose. The solution was cooled before addition of ethidium bromide (EthBr) (20 μL of 10 mg mL^{-1} EthBr stock). The gel was poured into a casting tray and combs inserted to form the wells. To visualise polyplex formation, 20 μL of the polyplex prepared above was added to 5 μL SDS-free loading buffer and added to the wells of the agarose gel. The gel was run in 1 X TAE buffer at 100 V for 30 minutes before imaging with an Azure 600 imaging system.

3.4.4.3 Ethidium Bromide Displacement

Ethidium bromide/pDNA complexes were first prepared by incubating EthBr (1 μg mL^{-1}) and pDNA (15 μg mL^{-1}) in H_2O for 30 minutes at room temperature. 50 μL of polymer was aliquoted into a black 96-well plate at appropriate concentrations for the targeted N/P ratio. 50 μL of pDNA/EthBr was added to the well and mixed before incubation for 30 minutes at 37 °C. The fluorescence of each well was measured using a Cytation3 plate reader ($\lambda_{excitation}$ = 525 nm, $\lambda_{emission}$ = 605 nm). pDNA/EthBr in the absence of polymer was used as the control.

3.4.4.4 Polyplex Stability towards Heparin

Polyplexes were prepared as described above (**Section 2.4.4.2**) and 20 μL added to a black 96-well plate along with 1 μL EthBr (2.5 μg mL^{-1} in H_2O). Heparin solution (0.05 or 0.25 mg mL^{-1}) was added in 5 or 10 μL increments. After each addition the solution was incubated for 10 minutes at 37 °C before reading the fluorescence of each well using

a Cytation3 plate reader ($\lambda_{excitation}$ = 525 nm, $\lambda_{emission}$ = 605 nm). A control of pDNA/EthBr complex was measured and diluted equally with H_2O throughout the experiment.

3.4.4.5 Polymer Toxicity Against HEK293T Cells

The cytotoxicity of the polymers was determined in HEK293T using the XTT assay. Cells were seeded in a 96-well plate at 10,000 cells/well and left to incubate at 37 °C for 24 hr in DMEM. Polymers were dissolved in serum free DMEM at 1.1 mg mL^{-1} and filtered through a 0.22 µm filter. Foetal bovine serum (FBS) was added, and the concentration adjusted to 1 mg mL^{-1}. The media was replaced with polymer containing media, using serial dilutions to incubate the cells with polymers at different concentrations (1 mg mL^{-1} to 0.0156 mg mL^{-1}) and incubated for 18 hr at 37 °C. After drug exposure, the XTT assay was used to determine cell viability. Cell viability was determined in triplicate in three independent sets of experiments and their standard deviation calculated.

3.4.4.6 Transfection of HEK293T Cells

HEK293T cells were seeded in a 24-well plate at a density of 100,000 cells/well and incubated for 18 hours. After incubation, the media was removed and replaced with 300 uL of Opti-MEM Reduced Serum Media. Polyplexes were prepared as described above and incubated for 30 minutes, before dilution with 350 µL of Opti-MEM. After 1 hour the media was removed from the wells and replaced with polyplex containing media ([pDNA] = 10 µg mL^{-1}) and incubated at 37 °C for 5 hours. After incubation, the media was removed and the cells washed once with warm DMEM. The media was replaced with fresh DMEM and incubated for 43 hours. The cells were then washed with 500 µL PBS and harvested with trypsin/EDTA (150 µL) before addition of 300 µL DMEM. The suspended cells were transferred to an Eppendorf tube and centrifuged at 1000 rpm for 5 minutes. The supernatant was removed, and the cells washed with 500 µL PBS then centrifuged at 1000 rpm for 5 minutes. The supernatant was removed, and the cells resuspended in 100 µL PBS before addition of 100 µL of 8 % formaldehyde and 15 minutes incubation at room temperature to fix the cells. Once fixed the cells were centrifuged at 1000 rpm for 5 minutes and the pellet washed with 200 µL of PBS followed by re-centrifugation and resuspension in 200 µL of fresh PBS. The suspension was transferred into FACS tubes for analysis by flow cytometry. Samples were analysed using a LSRII flow cytometer (488 nm laser with 530/30 filter and 561 nm laser with 585/15 filter).

3.5 References

1. D. W. Pack, A. S. Hoffman, S. Pun and P. S. Stayton, *Nature Reviews Drug Discovery*, 2005, **4**, 581-593.
2. H. Yin, R. L. Kanasty, A. A. Eltoukhy, A. J. Vegas, J. R. Dorkin and D. G. Anderson, *Nature Reviews Genetics*, 2014, **15**, 541-555.
3. A. B. Cook and S. Perrier, *Advanced Functional Materials*, 2020, **30**, 1901001.
4. A. C. Rinkenauer, S. Schubert, A. Traeger and U. S. Schubert, *Journal of Materials Chemistry B*, 2015, **3**, 7477-7493.
5. A. B. Cook, R. Peltier, J. Zhang, P. Gurnani, J. Tanaka, J. A. Burns, R. Dallmann, M. Hartlieb and S. Perrier, *Polymer Chemistry*, 2019, **10**, 1202-1212.
6. W. T. Godbey, M. A. Barry, P. Saggau, K. K. Wu and A. G. Mikos, *Journal of Biomedical Materials Research*, 2000, **51**, 321-328.
7. A. P. Pandey and K. K. Sawant, *Materials Science and Engineering: C*, 2016, **68**, 904-918.
8. F. Abedi-Gaballu, G. Dehghan, M. Ghaffari, R. Yekta, S. Abbaspour-Ravasjani, B. Baradaran, J. Ezzati Nazhad Dolatabadi and M. R. Hamblin, *Applied Materials Today*, 2018, **12**, 177-190.
9. J. D. Eichman, A. U. Bielinska, J. F. Kukowska-Latallo and J. R. Baker, *Pharmaceutical Science & Technology Today*, 2000, **3**, 232-245.
10. J. H. Tan, N. A. J. McMillan, E. Payne, C. Alexander, F. Heath, A. K. Whittaker and K. J. Thurecht, *Journal of Polymer Science Part A: Polymer Chemistry*, 2012, **50**, 2585-2595.
11. G. Chen, K. Wang, Q. Hu, L. Ding, F. Yu, Z. Zhou, Y. Zhou, J. Li, M. Sun and D. Oupický, *ACS Applied Materials & Interfaces*, 2017, **9**, 4457-4466.
12. L. Tao, W. C. Chou, B. H. Tan and T. P. Davis, *Macromolecular Bioscience*, 2010, **10**, 632-637.
13. A. B. Cook, R. Peltier, M. Hartlieb, R. Whitfield, G. Moriceau, J. A. Burns, D. M. Haddleton and S. Perrier, *Polymer Chemistry*, 2018, **9**, 4025-4035.
14. A. B. Cook, R. Peltier, T. R. Barlow, J. Tanaka, J. A. Burns and S. Perrier, *Journal of Interdisciplinary Nanomedicine*, 2018, **3**, 164-174.
15. C. Feng, Y. Li, D. Yang, J. Hu, X. Zhang and X. Huang, *Chemical Society Reviews*, 2011, **40**, 1282-1295.
16. R. Verduzco, X. Li, S. L. Pesek and G. E. Stein, *Chemical Society Reviews*, 2015, **44**, 2405-2420.

17. D. Wang, J. Lin, F. Jia, X. Tan, Y. Wang, X. Sun, X. Cao, F. Che, H. Lu, X. Gao, J. C. Shimkonis, Z. Nyoni, X. Lu and K. Zhang, *Science Advances*, 2019, **5**, eaav9322.
18. F. Jia, X. Lu, D. Wang, X. Cao, X. Tan, H. Lu and K. Zhang, *Journal of the American Chemical Society*, 2017, **139**, 10605-10608.
19. X. Jiang, M. C. Lok and W. E. Hennink, *Bioconjugate Chemistry*, 2007, **18**, 2077-2084.
20. T. von Erlach, S. Zwicker, B. Pidhatika, R. Konradi, M. Textor, H. Hall and T. Lühmann, *Biomaterials*, 2011, **32**, 5291-5303.
21. E. Haladjova, S. Halacheva, D. Momekova, V. Moskova-Doumanova, T. Topouzova-Hristova, K. Mladenova, J. Doumanov, M. Petrova and S. Rangelov, *Macromolecular Bioscience*, 2018, **18**, 1700349.
22. A.-K. Trützschler, T. Bus, M. Sahn, A. Traeger, C. Weber and U. S. Schubert, *Biomacromolecules*, 2018, **19**, 2759-2771.
23. M. Bauer, L. Tauhardt, H. M. L. Lambermont-Thijs, K. Kempe, R. Hoogenboom, U. S. Schubert and D. Fischer, *European Journal of Pharmaceutics and Biopharmaceutics*, 2018, **133**, 112-121.
24. A. K. Blakney, G. Yilmaz, P. F. McKay, C. R. Becer and R. J. Shattock, *Biomacromolecules*, 2018, **19**, 2870-2879.
25. B. D. Monnery, V. V. Jerca, O. Sedlacek, B. Verbraeken, R. Cavill and R. Hoogenboom, *Angewandte Chemie International Edition*, 2018, **57**, 15400-15404.
26. B. P. Cormack, R. H. Valdivia and S. Falkow, *Gene*, 1996, **173**, 33-38.
27. H. Miyoshi, M. Takahashi, F. H. Gage and I. M. Verma, *Proceedings of the National Academy of Sciences*, 1997, **94**, 10319.
28. W. C. Tse and D. L. Boger, *Current Protocols in Nucleic Acid Chemistry*, 2005, **20**, 8.5.1-8.5.11.
29. E. Fröhlich, *Int J Nanomedicine*, 2012, **7**, 5577-5591.
30. J. Shi, J. L. Choi, B. Chou, R. N. Johnson, J. G. Schellinger and S. H. Pun, *ACS Nano*, 2013, **7**, 10612-10620.
31. M. Ruponen, S. Rönkkö, P. Honkakoski, J. Pelkonen, M. Tammi and A. Urtti, *Journal of Biological Chemistry*, 2001, **276**, 33875-33880.
32. K. A. Mislick and J. D. Baldeschwieler, *Proceedings of the National Academy of Sciences*, 1996, **93**, 12349.

33. B. D. Monnery, M. Wright, R. Cavill, R. Hoogenboom, S. Shaunak, J. H. G. Steinke and M. Thanou, *International Journal of Pharmaceutics*, 2017, **521**, 249-258.
34. F. J. Verbaan, C. Oussoren, I. M. van Dam, Y. Takakura, M. Hashida, D. J. A. Crommelin, W. E. Hennink and G. Storm, *International Journal of Pharmaceutics*, 2001, **214**, 99-101.
35. Y. Liu and T. M. Reineke, *Bioconjugate Chemistry*, 2006, **17**, 101-108.

3.6 **Appendix**

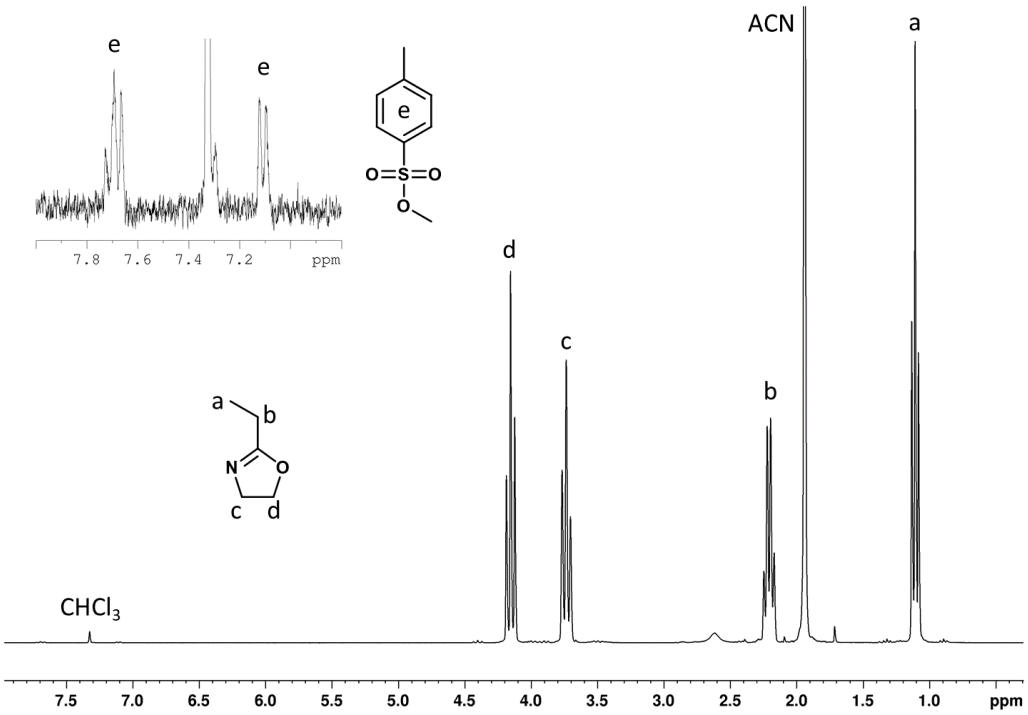

Figure A3.1 Assigned t = 0 ^{1}H NMR spectrum of **L-242** in $CDCl_3$.

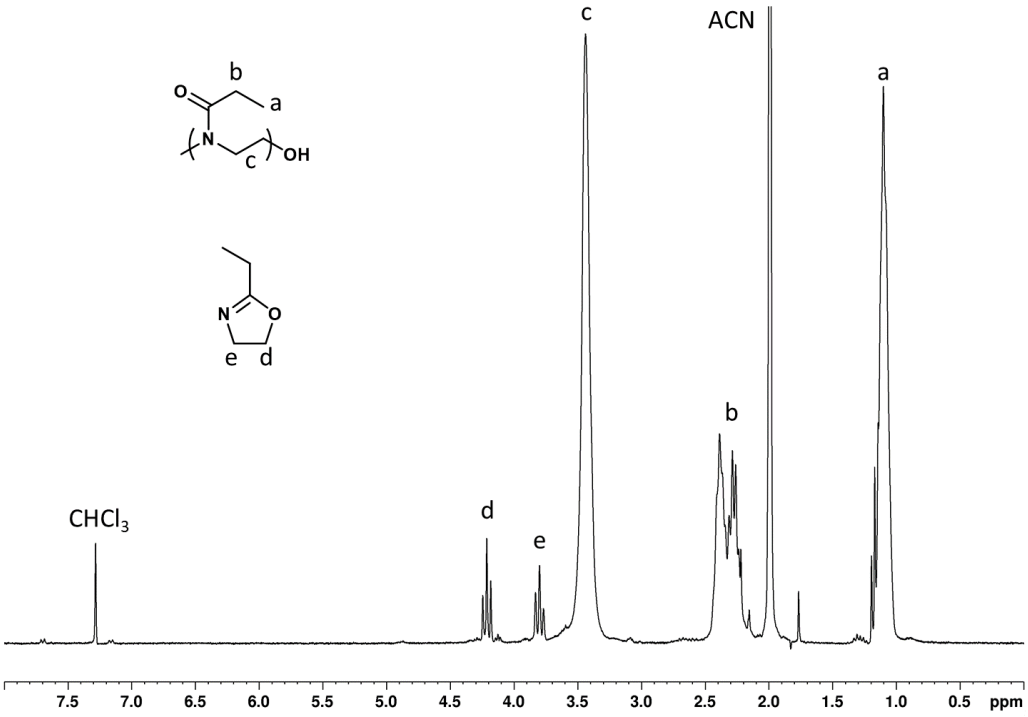

Figure A3.2 Assigned t = final ^{1}H NMR spectrum of **L-242** in $CDCl_3$.

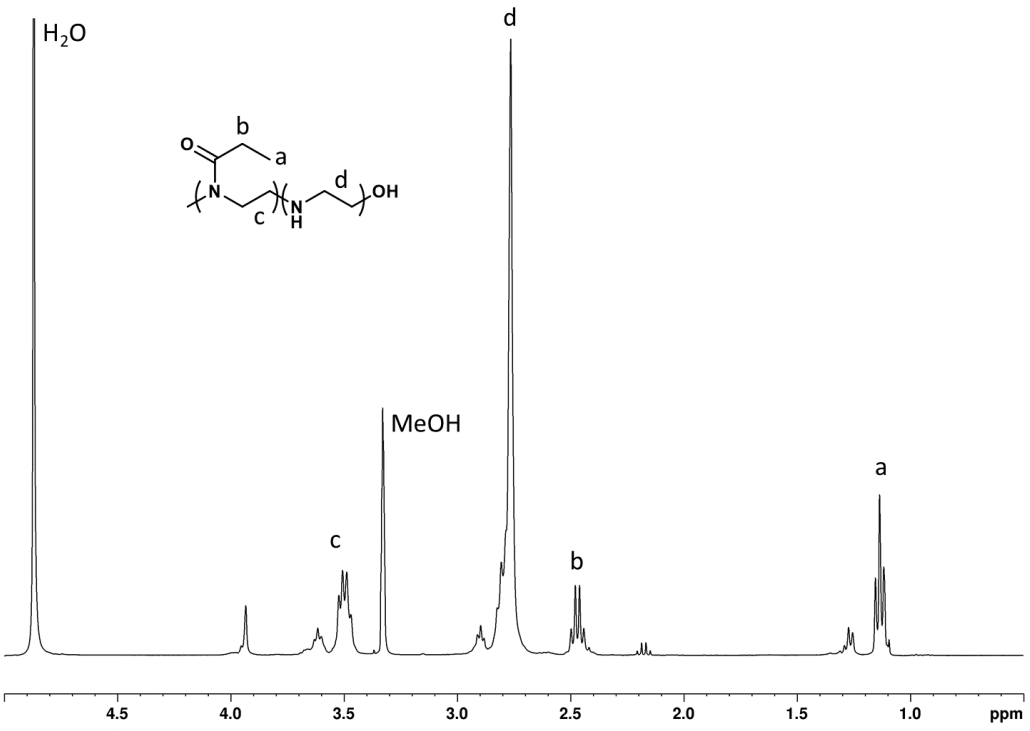

Figure A3.3 Assigned [1]H NMR spectrum of **$HL_{0.79}$-242** in MeOD.

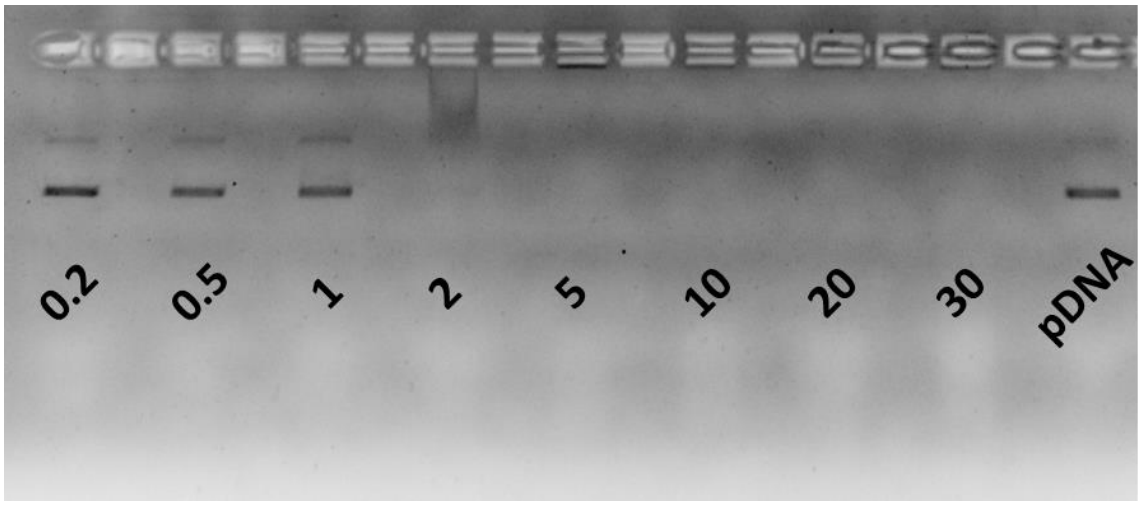

Figure A3.4 Polyplex formation of **B10-10(79%)** at different N/P ratios.

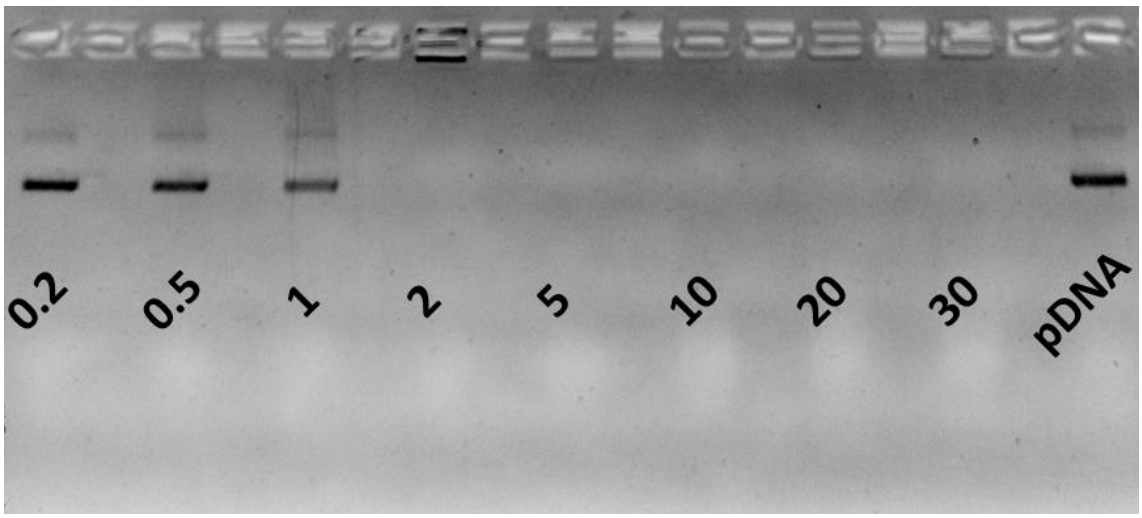

Figure A3.5 Polyplex formation of **B10-25(67%)** at different N/P ratios.

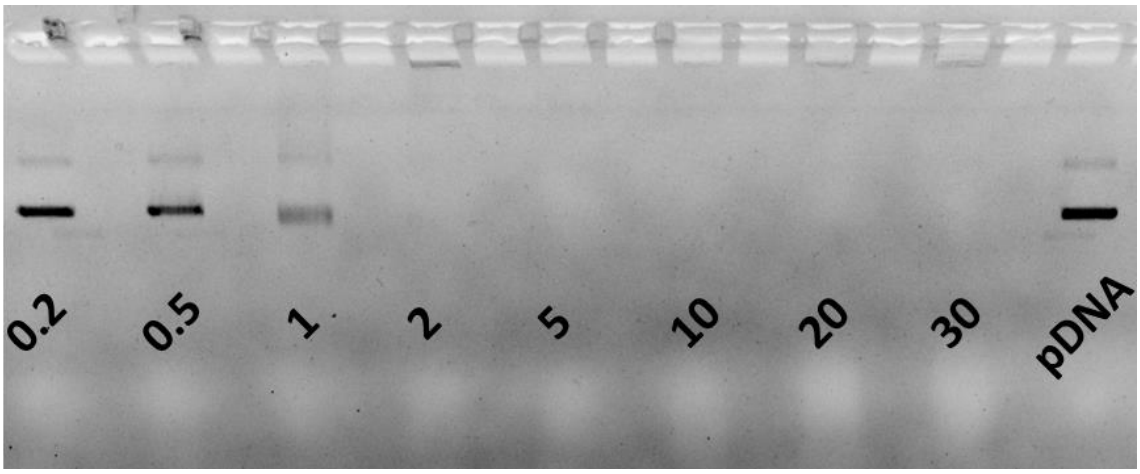

Figure A3.6 Polyplex formation of **B10-50(67%)** at different N/P ratios.

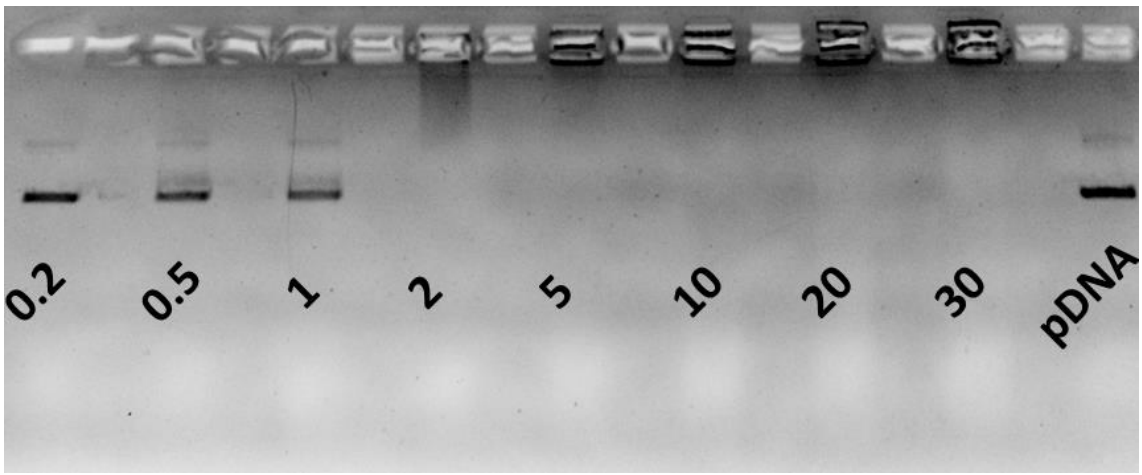

Figure A3.7 Polyplex formation of **L-242(81%)** at different N/P ratios.

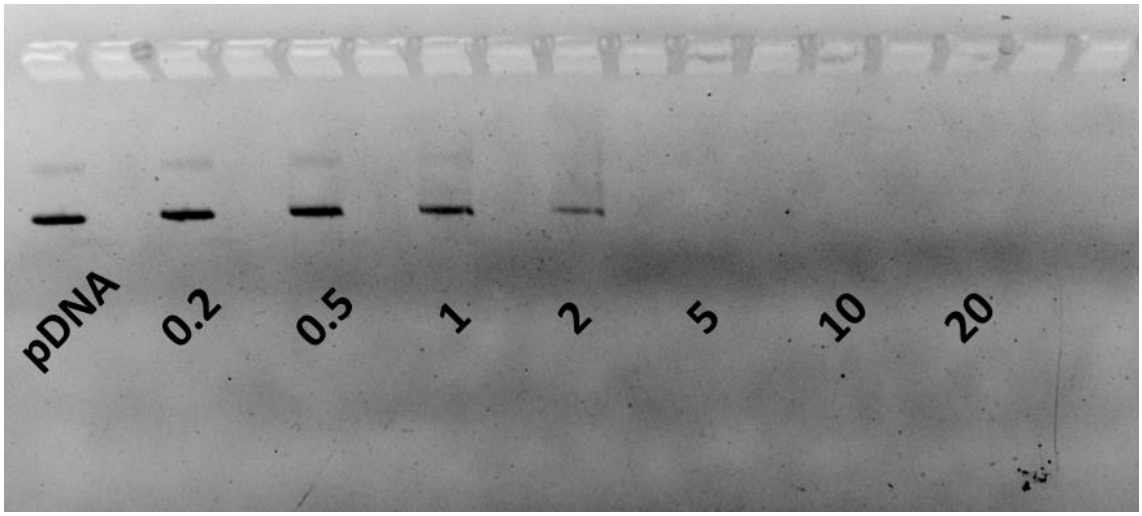

Figure A3.8 Polyplex formation of lPEI at different N/P ratios.

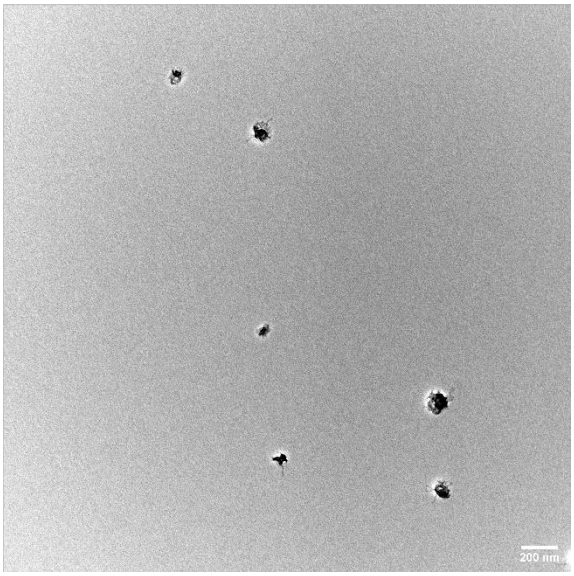

Figure A3.9 Transmission Electron Microscopy (TEM) images of polyplexes formed with **B10-10(45%).**

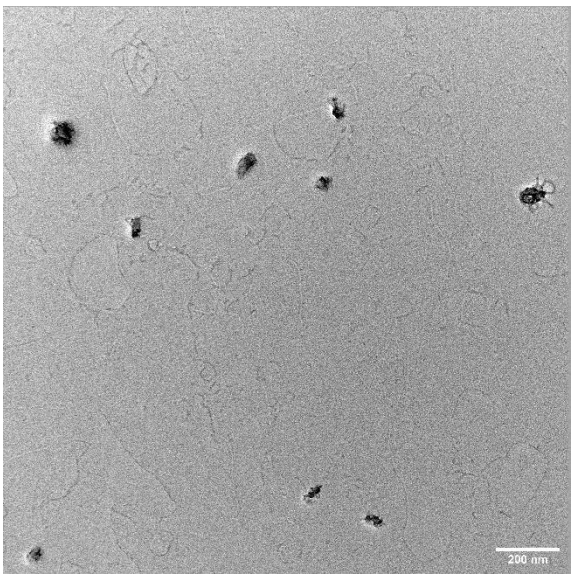

Figure A3.10 Transmission Electron Microscopy (TEM) images of polyplexes formed with **B10-10(79%)**

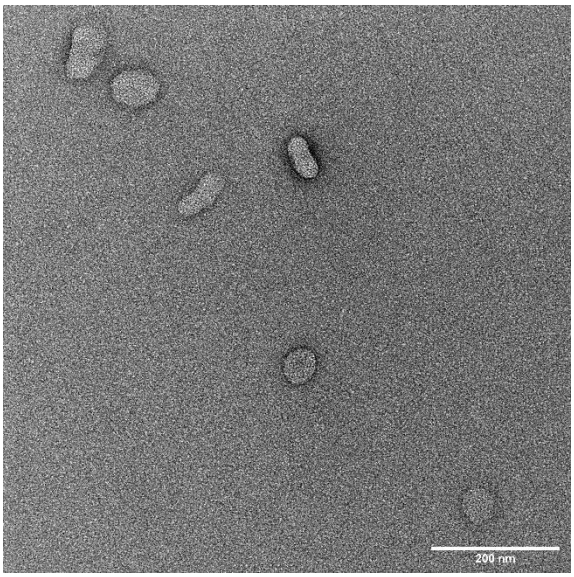

Figure A3.11 Transmission Electron Microscopy (TEM) images of polyplexes formed with **B10-25(67%)**

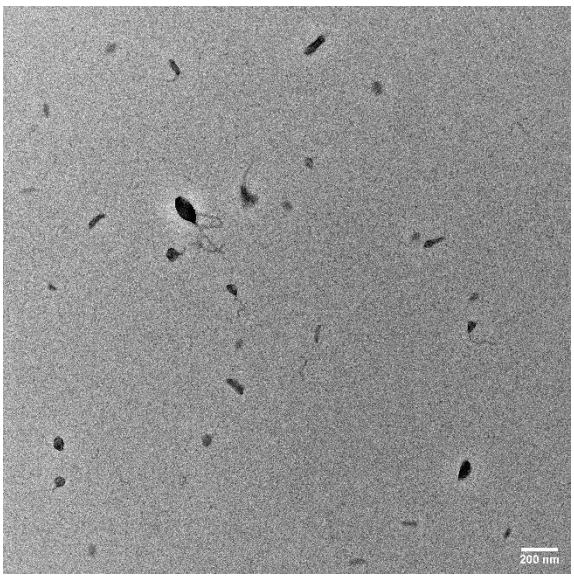

Figure A3.12 Transmission Electron Microscopy (TEM) images of polyplexes formed with **B10-50(67%)**

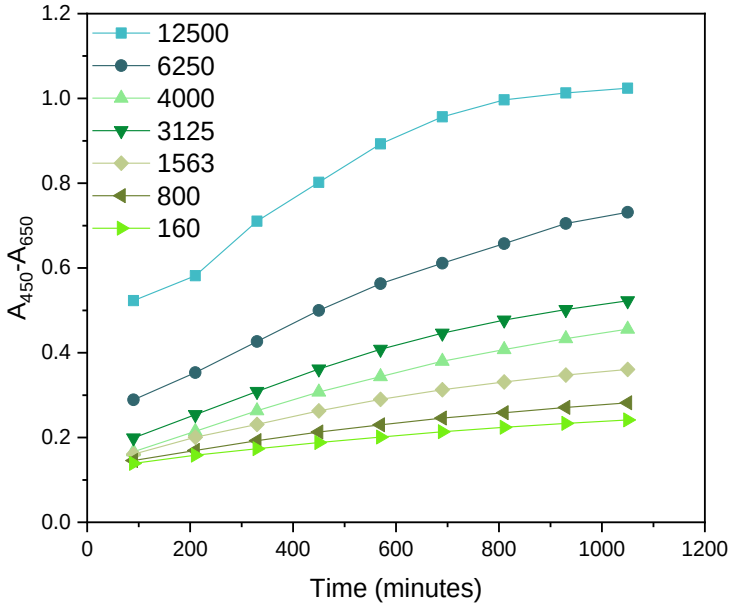

Figure A3.13 XTT optimisation assay, carried out according to established protocol.

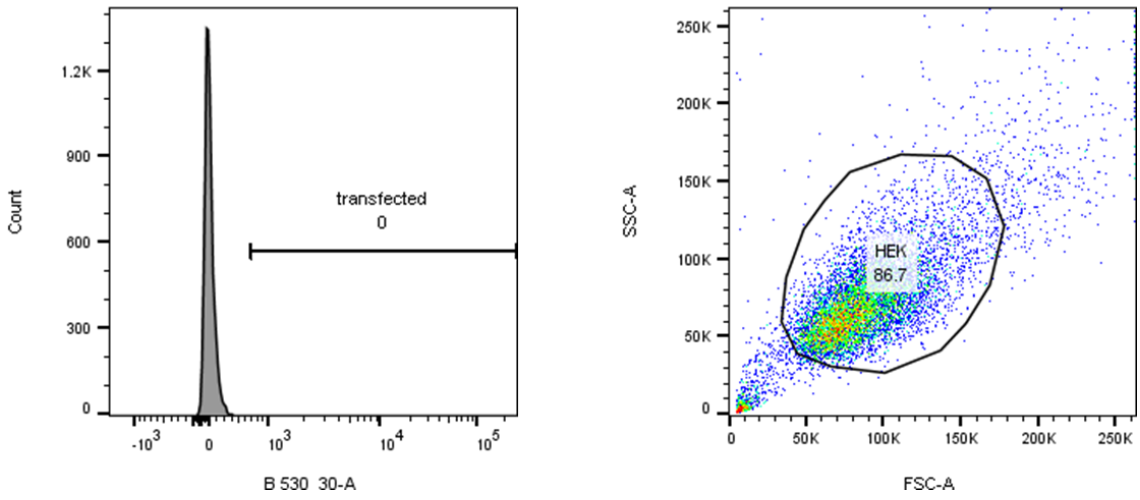

Figure A3.14 Flow cytometry results for transfection of HEK293T cells - blank (no transfection).

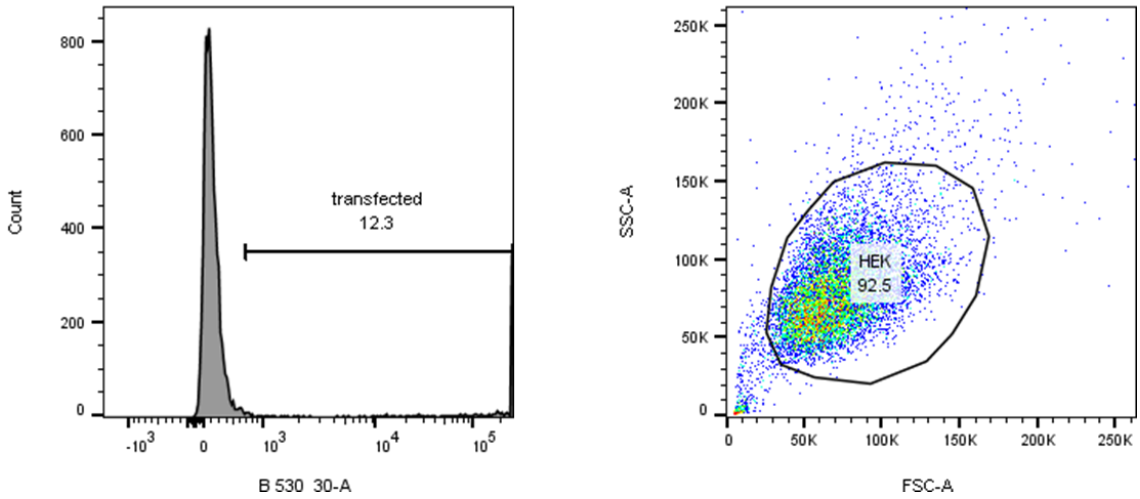

Figure A3.15 Flow cytometry results for transfection of HEK293T cells – **B10-10(45%)**.

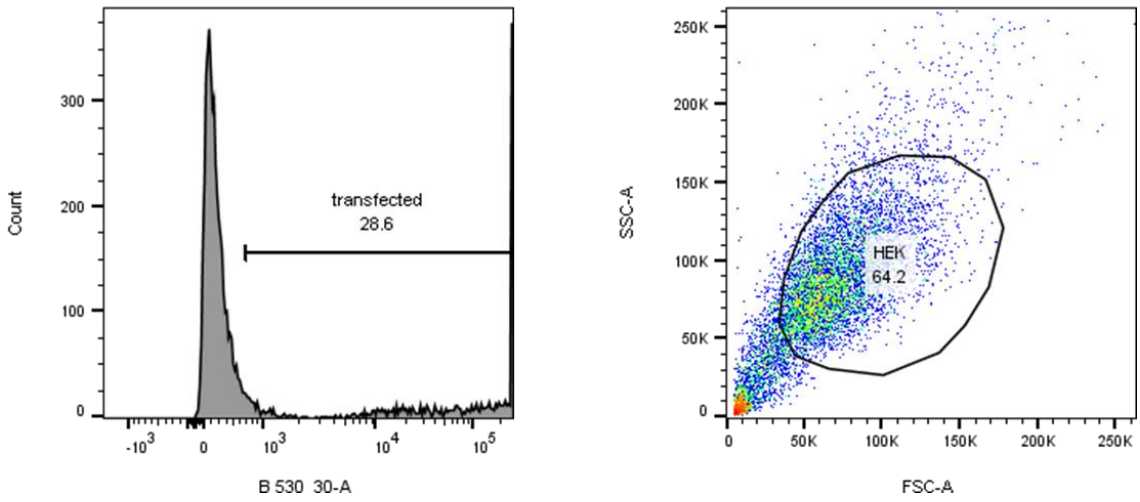

Figure A3.16 Flow cytometry results for transfection of HEK293T cells – **B10-10(69%)**.

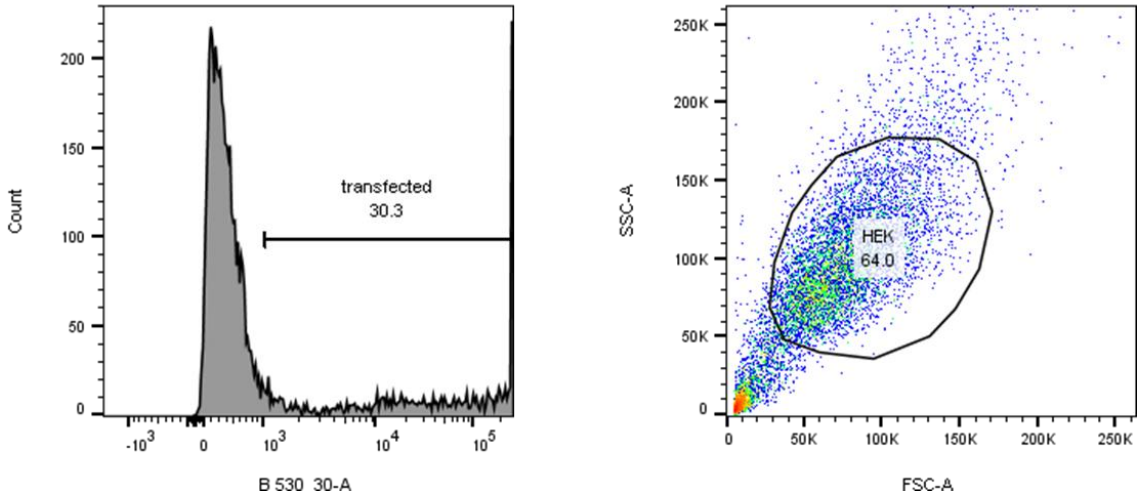

Figure A3.17 Flow cytometry results for transfection of HEK293T cells – **B10-10(79%)**.

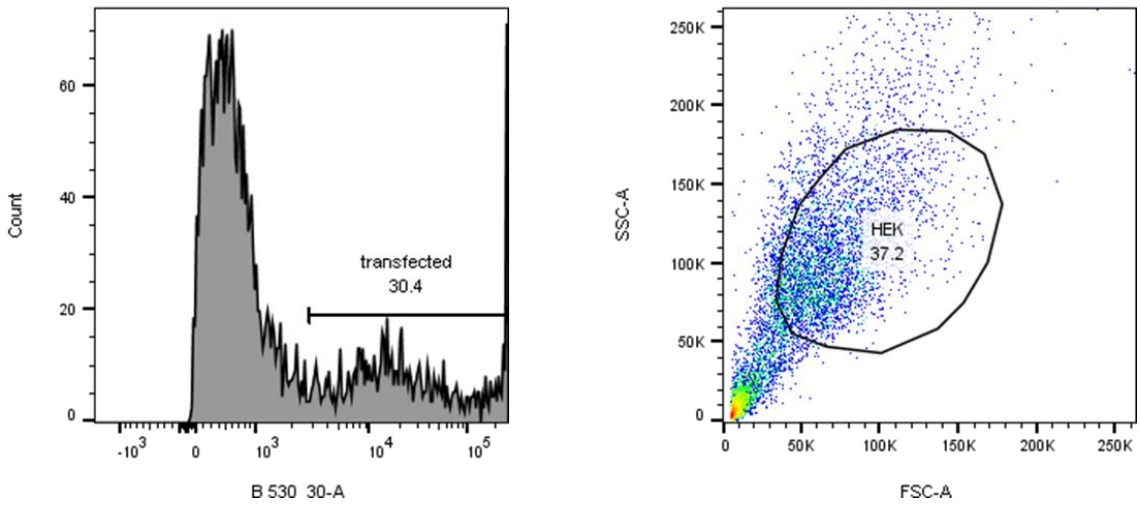

Figure A3.18 Flow cytometry results for transfection of HEK293T cells – **B10-25(67%)**.

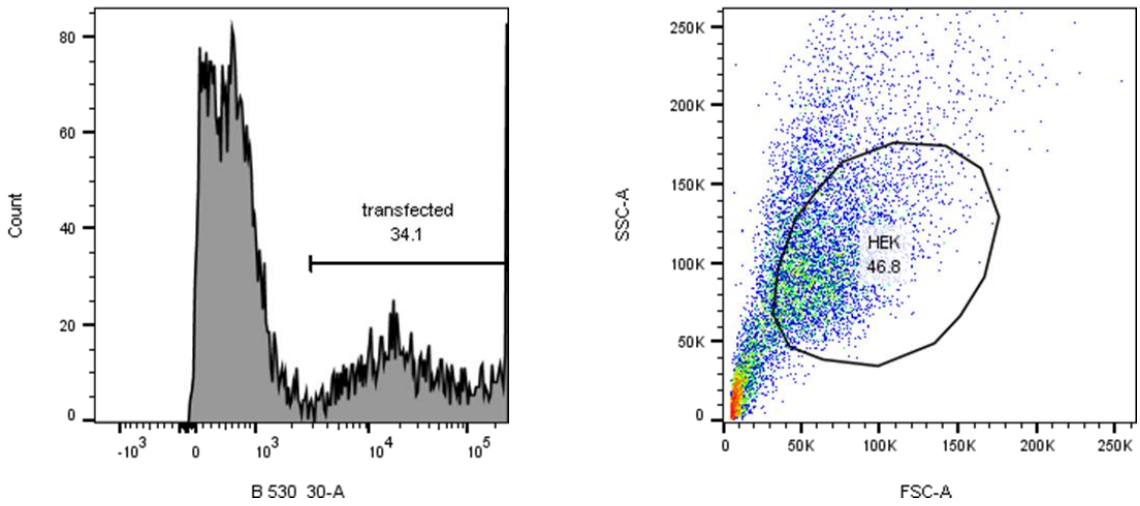

Figure A3.19 Flow cytometry results for transfection of HEK293T cells – **B10-50(67%)**.

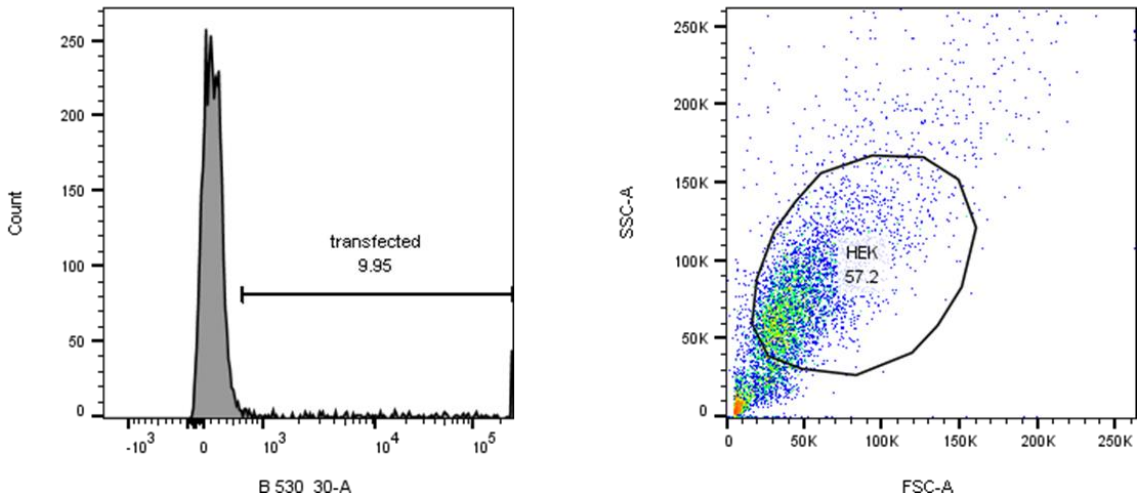

Figure A3.20 Flow cytometry results for transfection of HEK293T cells – **L-242(81%)**.

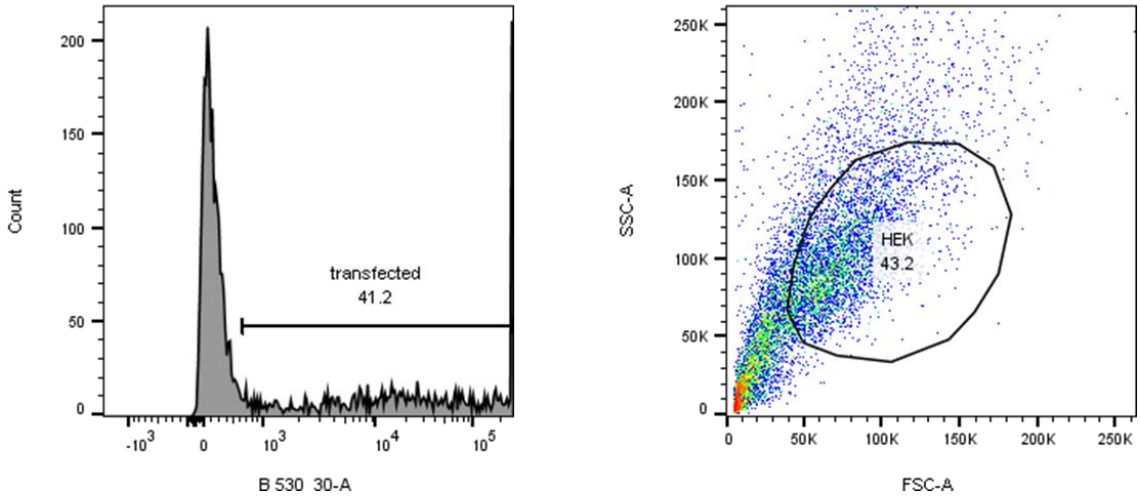

Figure A3.21 Flow cytometry results for transfection of HEK293T cells – **lPEI**.

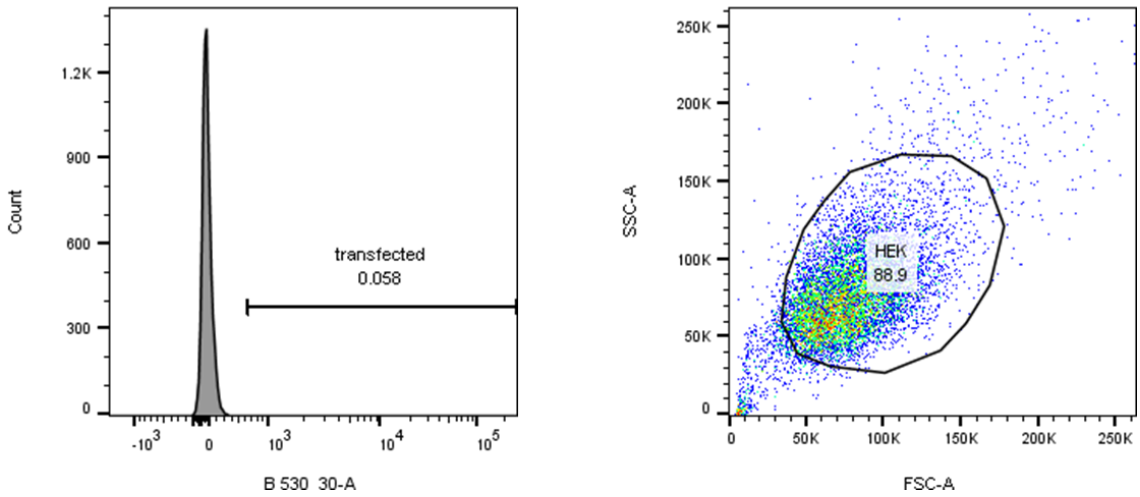

Figure A3.22 Flow cytometry results for transfection of HEK293T cells – **pDNA.**

4 Poly(2-Ethyl-2-Oxazoline) Macromonomers as Stabilisers for Surfactant-Free Emulsion Polymerisation

4.1 Introduction

Emulsion polymerisation is a heterogeneous polymerisation technique where a monomer is emulsified within an aqueous continuous phase.[1, 2] Due to the low viscosity, fast kinetics and high specific heat capacity of water, emulsion polymerisation is a useful industrial technique, providing a cheap and scalable process for the manufacturing of polymers. Traditionally emulsion polymerisation involves the use of a surfactant. Above their critical micelle concentrations, these surfactants form micelles which provide nucleation sites for growing polymer chains and become the locus of polymerisation within the system. The surfactant also provides stabilisation to the growing polymer particle, preventing aggregation and destabilisation. However, surfactants can be detrimental to certain applications, such as biomedical or in electronics, and must be removed before the material can be implemented.[2] This can be a laborious process involving extensive purification methods such as dialysis, increasing the final cost of the material.[3]

Several methods have been developed to alleviate the need for traditional surfactants in emulsion polymerisation. RAFT emulsion polymerisation using an amphiphilic diblock chain transfer agent can provide the stabilisation required. Particle growth occurs by chain extension of the macroCTA, forming particles with covalent tethers to the stabiliser.[4] This technique also allows for the facile introduction of surface functionality, such as sugar or PEG decorated nanoparticles, and can be achieved by introduction of a polymerisable group or by modifications to the macroCTA.[5-8] This process has been applied to similar polymerisation techniques such as nitroxide-mediated polymerisation and sulphur-free RAFT.[9-11]

Surfactants that contain a polymerisable group and can be incorporated onto the surface of a growing particle received extensive study in the past,[12, 13] but their popularity has since dwindled. These reactive surfactants are advantageous as they do not affect the rate of polymerisation or the molecular weight of the resulting polymer, unlike the methods described above.[14, 15]

The cost associated with all these methods limits their industrial applicability, especially when considering low-cost applications, such as paints. Removal of the surfactant entirely would be advantageous and can be achieved by use of an ionic initiator. Surfactant-free emulsion polymerisation generates a stabilising block *in situ* directly from the polymerisation of a hydrophobic monomer. A charged water-soluble initiator is used to

initiate the polymerisation of the small amount of hydrophobic monomer that exists in the aqueous phase. Due to the high water-solubility of the initiator, the polymer chains are initially soluble in water, however, once they reach a critical length, they will become insoluble and collapse to form nucleation sites for growing particles.[16, 17] Stabilisation of the particle is achieved solely through electrostatic interactions due to the charged initiator. This process can form well-defined nanoparticles with diameters ranging from hundreds of nanometres to micrometres. The majority of the studies have focused on the preparation of styrene nanoparticles, but it has also been applied to (meth)acrylates.[18-20]

Copolymerisation of hydrophilic monomers in a surfactant-free emulsion polymerisation generates nanoparticles with functional surfaces.[21, 22] It was found that by changing the ratio between hydrophilic and hydrophobic monomers the resulting size of the nanoparticle could be tuned. Furthermore, the hydrophilicity of the monomer appeared to regulate the nanoparticle size, with more hydrophilic monomers resulting in smaller particles. The mechanism for particle growth is postulated to proceed under similar conditions as classic surfactant-free emulsion polymerisation, however, during the initial stages of the polymerisation the hydrophilic monomer will polymerise due its presence in the aqueous phase. This will cause the formation of a gradient pseudo block copolymer which will go on to form the corona of the particle. The presence of hydrophilic monomer on the surface of the particle was confirmed by a lectin binding assay, where the presence of sugar moieties on the nanoparticle surface will cause the aggregation of Concanavalin A.

Prior to this work, Kobayashi *et al.* applied the copolymerisation of solvophilic and solvophobic monomers to dispersion polymerisation to generate poly(styrene) and poly(methyl methacrylate) particles with micron-scale dimensions.[23, 24] In an alcohol-water mixture, monomer along with a poly(2-alkyl-2-oxazoline) macromonomer are dispersed and polymerised. The macromonomer molecular weight and nature of the alkyl group all influence the dimensions of the resulting particle. Higher molecular weight macromonomers lead to the formation of smaller diameter nanoparticles, with the length of the oxazoline alkyl chain having very little influence. In the case of the styrene particles, the surface was analysed using electron spectroscopy for chemical analysis and the ratio of nitrogen to carbon measured. The resulting N/C ratio on the surface of the particle was greater than that in the reaction mixture indicating a gradient distribution of oxazoline macromonomer across the nanoparticle, with the majority existing at the surface.

Expanding on the work of Lunn and Perrier and Kobayashi *et al.*, the hydrophilic poly(2-oxazoline) macromonomers synthesised in **Chapter 2** were copolymerised with various hydrophobic monomers to establish a route to poly(2-oxazoline)-coated nanoparticles. These particles were subsequently exposed to the hydrolysis conditions required for partial hydrolysis to poly(ethylenimine) and the stability of the particles was investigated. Upon hydrolysis the particles were incubated with anionic biomacromolecules (pDNA) to assess their ability to form polyplexes.

4.2 Results and Discussion

4.2.1 Surfactant-free Emulsion Polymerisation of Styrene

4.2.1.1 Influence of Styrene Concentration

Initially variations in the concentration of hydrophobic monomer in the absence of a hydrophilic comonomer were undertaken using styrene and a cationic initiator, 2,2'-azobis[2-(2-imidazolin-2-yl)propane]dihydrochloride (VA-044). This resembles a classic surfactant-free emulsion polymerisation where the nanoparticles are stabilised exclusively through electrostatic interactions. Synthesis of styrene nanoparticles was carried out by first dissolving VA-044 in water (0.25 mM). This solution was fitted with a stirrer bar and rubber septum and purged with N_2 for 15 minutes. A vial of styrene was similarly purged before addition of styrene to the water mixture using a gas-tight syringe. The reaction vial was placed into an oil bath at 70 °C and stirred at 800 rpm for 3 hr.

Table 4.1 Characterisation data for styrene nanoparticles synthesised by surfactant free emulsion polymerisation at different wt% styrene.

			DLS		TEM	
Sample	**[Sty] (M)**	**ζ-Potential (mV)**	**Size (nm)[b]**	**PDi[c]**	**Size (nm)[d]**	**PDi[c]**
P(Sty)-01	0.2	43.4 ± 0.5	140.3	0.05	92.3	0.14
P(Sty)-02	0.4	32.9 ± 1.1	166.2	0.06	142.3	0.02
P(Sty)-03	0.6	30.7 ± 1.4	169.7	0.04	-	-

[a] Weight percentage of styrene in the reaction. [b] Particle diameter determined from DLS intensity distribution. [c] PDi calculated using **Equation 4.2**. [d] Diameter calculated by measuring the average diameter of particles on TEM micrographs (n = 227 for **P(Sty)-01**, n = 92 for **P(Sty)-02**)

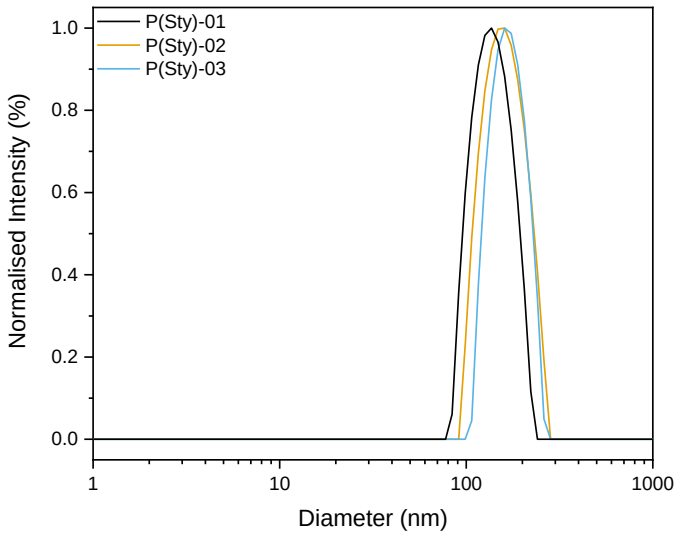

Figure 4.1 DLS traces of styrene nanoparticles synthesised at different styrene wt%.

By increasing the concentration of styrene and keeping the concentration of VA-044 constant an increase in particle size was observed. The nanoparticle diameter was determined by dynamic light scattering (DLS) and found to increase from 140.3 nm to 169.7 nm, with particles of narrow, monodisperse size distributions (PDi < 0.1) (**Figure 4.1**). Transmission electron microscopy was further used to characterise **P(Sty)-01** and resulted in a smaller average diameter of 92.3 nm (**Figure 4.2A**). The PDi was calculated using **Equation 4.2**, with the standard deviation and average diameter calculated from a sample of nanoparticles. TEM indicates a moderate polydisperse distribution of nanoparticles, with a PDi equalling 0.14.

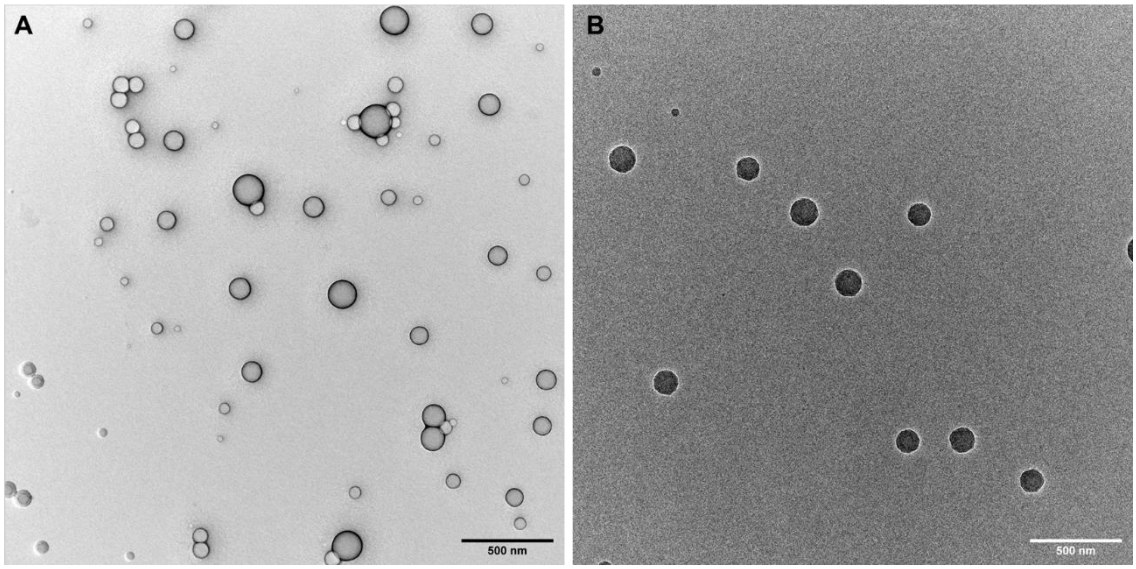

Figure 4.2 TEM micrograph for **P(Sty)-01** (A) and **P(Sty)-02** (B)

4.2.2 Surfactant-free Emulsion Copolymerisation of Poly(2-Ethyl-2-Oxazoline) Macromonomers and Styrene

4.2.2.1 Effect of Increasing the Styrene Concentration

Once the effect of hydrophobic monomer concentration on particle size was established addition of a hydrophilic macromonomer to the surfactant-free emulsion polymerisation of styrene was studied. A series of copolymerisations were carried out, increasing the molar ratio between **MM1** (synthesis described in **Chapter 2.2.2**) and styrene.

The concentration of **MM1** remained constant with the styrene concentration increased to target the desired molar ratio (**Table 4.2**). An initial comparison was made between the surfactant-free emulsion polymerisation of styrene in the presence and absence of **MM1**, at the same concentration of styrene in the reaction. **P(MM1-Sty)$_{20}$A** was prepared in an identical way to **P(Sty)$_{2.1}$**, with the addition of **MM1** to the aqueous initiator solution at a molar ratio of 1:20 (**MM1** : styrene). The resulting particles were analysed by DLS, zeta-potential measurements, and TEM to determine the effects of macromonomer copolymerisation on the particle morphology.

From the DLS measurements it is immediately obvious that the addition of **MM1** to the polymerisation effects the resulting nanoparticle morphology with a decrease in a diameter from 140.3 nm to 61.7 nm (**Figure 4.3**). Whilst nanoparticles formed by the homopolymerisation of styrene were solely stabilised by electrostatic interactions, addition of **MM1** introduces an additional stabilising effect through steric interactions.

The zeta-potential measurements of both nanoparticles reveal a positive surface potential, predominantly arising from the use of VA-044, a positively charged initiator.

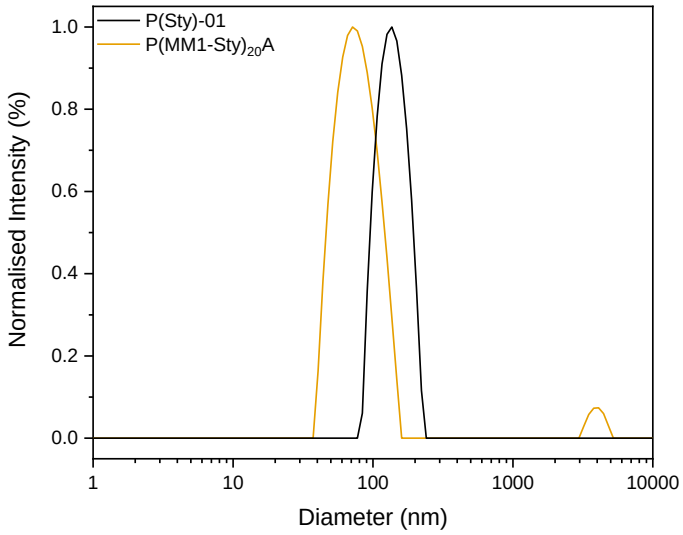

Figure 4.3 DLS intensity traces for **P(Sty)-01** (black) and **P(MM1-Sty)$_{20}$A** (orange).

Once the effect of macromonomer addition was established, a series of polymerisations with increasing molar ratios between **MM1** and styrene was undertaken. By increasing the amount of styrene relative to **MM1**, the size of the resulting nanoparticles increases, affording the ability to tune the nanoparticle size. By increasing the molar ratio from 1:20 to 1:100, nanoparticles with sizes ranging from 61.7 nm to 136.7 nm were synthesised (**Table 4.2**). The particle size was determined by DLS and all particles have a polydispersity index (PDi) of < 0.1, indicating a narrow, monodisperse distribution of particle sizes (**Figure 4.4**).

Table 4.2 Characterisation data for **P(MM1-Sty)$_x$**, where x represents the molar ratio between **MM1** and styrene. Concentration of styrene increased, **MM1** concentration kept constant (0.01 M).

Nanoparticle	[Sty] (M)	[Sty]/[MM]	ζ-Potential (mV)	Size (nm)[a]	PDi[b]
P(MM1-Sty)$_{20}$A	0.2	20	25.8 ± 0.5	61.7	0.05
P(MM1-Sty)$_{40}$A	0.4	40	28.2 ± 0.4	100.2	0.06
P(MM1-Sty)$_{60}$A	0.6	60	32.4 ± 0.7	127.8	0.07
P(MM1-Sty)$_{80}$A	0.8	80	31.5 ± 1.0	125.8	0.05
P(MM1-Sty)$_{100}$A	1.0	100	34.4 ± 1.0	136.7	0.05

[a] Particle diameter determined from DLS intensity distribution. [b] PDi calculated using **Equation 4.2**.

By plotting the resulting particle volume versus the molar ratio of styrene and **MM1** a linear relationship is observed (**Figure 4.4**). This allows for the synthesis of nanoparticles of pre-determined size by variation of the molar ratio of both monomers within the investigated range.

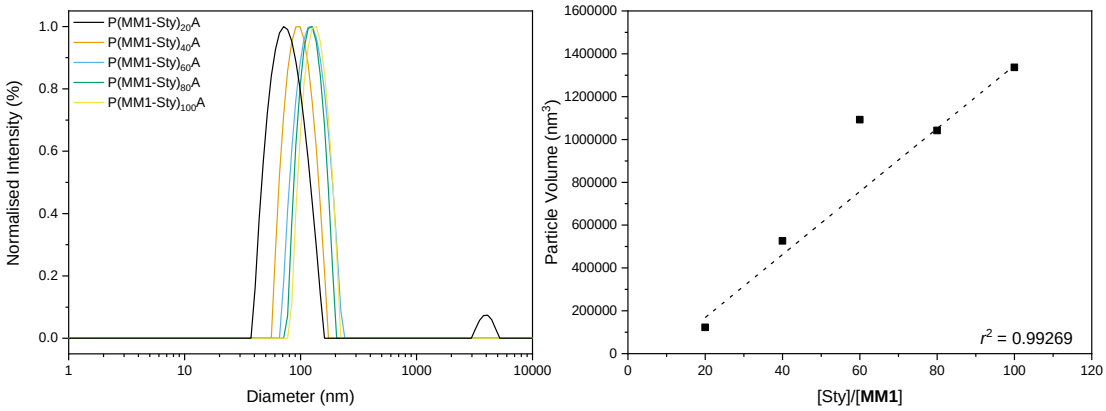

Figure 4.4 DLS intensity distribution traces of nanoparticles synthesised at different molar ratios of styrene and **MM1** and particle size calibration. Styrene concentration increased to target molar ratio.

TEM was used to analyse the size distribution and shape of the nanoparticles for styrene homopolymer nanoparticles and those synthesised *via* copolymerisation with **MM1** (**Figure 4.6**). Interestingly bimodal particle size distributions were observed for all particles synthesised with **MM1** (**Figure 4.5, A4.2, A4.4, A4.7**). Due to the sensitivity of DLS it would not be possible to detect this bimodal nature as the size difference in not large enough.

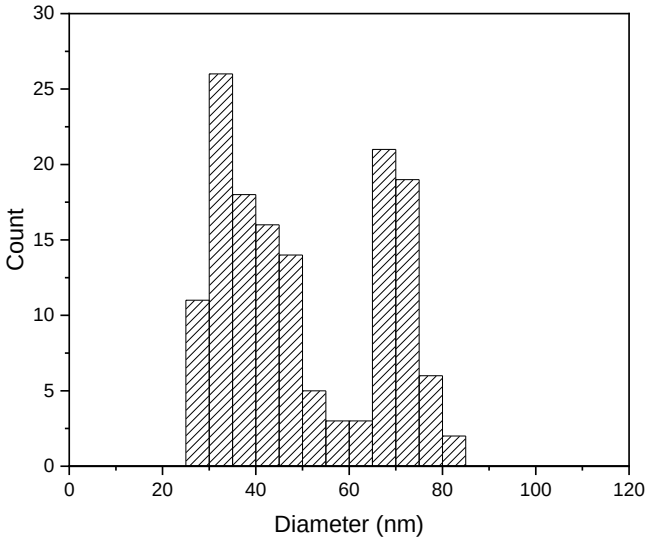

Figure 4.5 Nanoparticle size distribution determined from TEM micrographs (n = 144) of **P(MM1-Sty)$_{40}$A**.

It is postulated that one mechanism of particle growth in surfactant-free emulsion polymerisation is driven by the coagulation of smaller particles.[25] Small particles, around 5 nm in size, are observed in all micrographs except for those of styrene homopolymers which could form the basis of coagulation.

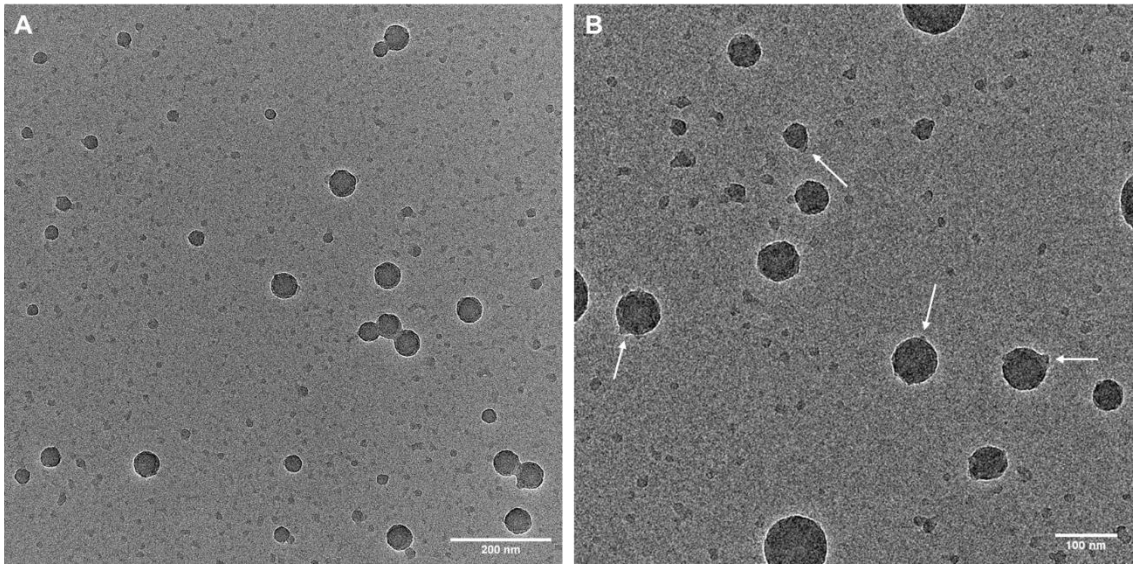

Figure 4.6 TEM micrographs for **P(MM1-Sty)$_{20}$A** (A) and **P(MM1-Sty)$_{60}$A** (B). Particle coagulation highlighted with white arrows.

Evidence of particle growth by coagulation is visible in the TEM micrograph of **P(MM1-Sty)$_{60}$A** where smaller particles appear to decorate the corona of larger particles, leading to a deviation from spherical particles (**Figure 4.6B**). These protrusions are highlighted with arrows to aid in visualisation.

4.2.2.2 Influence of Decreasing the Macromonomer Concentration

As shown previously, in the surfactant-free emulsion polymerisation of styrene the particle size can be altered by changing the concentration of styrene in the reaction. Therefore, it was imperative to determine if the size increase observed above was due to the presence of the macromonomer or the increasing concentration in styrene. To further prove the influence of the macromonomer on the synthesis of nanoparticles a series of experiments was carried out where the amount of styrene was fixed and the amount of macromonomer decreased to achieve the same molar ratios as above.

Surfactant-free emulsion polymerisations were carried out in the same manner described above and the results presented in **Table 4.3**. By decreasing the concentration of **MM1**, a similar trend is observed to the polymerisations above. An increase in the molar ratio gives an increase in particle diameter. This further illustrates the role of **MM1** copolymerisation in the resulting nanoparticle morphology.

Again, a linear relationship was observed between the molar ratio of MM1 and styrene and the particle volume (**Figure 4.7**). **P(MM1-Sty)$_{80}$B** appears to not follow this trend which may be caused by inaccuracies in measuring **MM1** as small quantities are required, especially at high molar ratios. Further repeats of these polymerisations would be needed to confirm this result.

Table 4.3 Characterisation data for **P(MM1-Sty)$_x$**, where x represents the molar ratio between **MM1** and styrene. Concentration of **MM1** decreased, styrene concentration kept constant (0.4 M).

Nanoparticle	[MM1] (M)	[Sty]/[MM]	ζ-Potential (mV)	Size (nm)[a]	PDi[b]
P(MM1-Sty)$_{20}$B	0.020	20	22.1 ± 0.7	74.3	0.06
P(MM1-Sty)$_{60}$B	0.007	60	30.7 ± 0.8	111.9	0.07
P(MM1-Sty)$_{80}$B	0.005	80	33.6 ± 0.8	126.5	0.05
P(MM1-Sty)$_{100}$B	0.004	100	31.6 ± 1.5	125.8	0.05
P(MM1-Sty)$_{120}$B	0.003	120	31.1 ± 1.5	132.2	0.05

[a] Particle diameter determined from DLS intensity distribution. [b] PDi calculated using **Equation 4.2**.

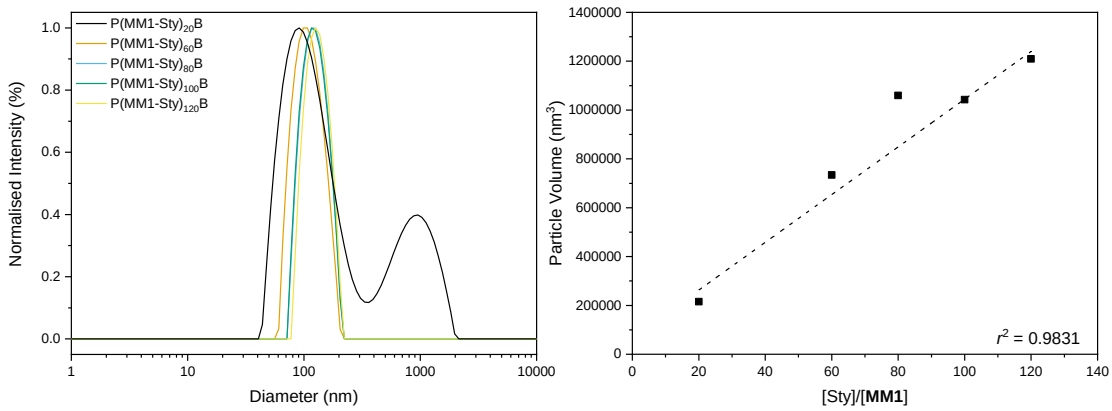

Figure 4.7 DLS intensity distribution traces of nanoparticles synthesised at different molar ratios of styrene and **MM1** and particle size calibration. **MM1** concentration decreased to target molar ratio.

4.2.2.3 Influence of Macromonomer Length

MM2 was employed as a comonomer in the synthesis of styrene nanoparticles to investigate the influence of macromonomer molecular weight on the particle size (**Table 4.4**, **Figure 4.8**). **MM2** is a DP 21 PEtOx, whereas **MM1** has a DP of 13. Comparison with particles synthesised using **MM1** shows that use of a higher molecular weight macromonomer results in smaller particle diameters (**Figure 4.9**). The same trend was observed by Kobayashi *et al.* in their study on the use of POx macromonomers for the synthesis of micron-sized styrene particles.

Table 4.4 Characterisation data for **P(MM2-Sty)$_x$**, where x represents the molar ratio between **MM2** and styrene. Concentration of styrene increased, **MM2** concentration kept constant (0.01 M).

Nanoparticle	[Sty] (M)	[Sty]/[MM]	ζ-Potential (mV)	Size (nm)[a]	PDi[b]
P(MM2-Sty)$_{20}$	0.2	20	20.1 ± 0.3	64.0	0.11
P(MM2-Sty)$_{40}$	0.4	40	21.6 ± 0.7	106.9	0.10
P(MM2-Sty)$_{60}$	0.6	60	29.1 ± 0.8	106.5	0.06
P(MM2-Sty)$_{80}$	0.8	80	30.0 ± 0.9	119.2	0.04
P(MM2-Sty)$_{100}$	1.0	100	31.7 ± 1.0	126.8	0.04

[a] Particle diameter determined from DLS intensity distribution. [b] PDi calculated using **Equation 4.2**.

The intensity trace for **P(MM2-Sty)$_{20}$** exhibits a bimodal size distribution, however above this molar ratio all intensity traces show monomodal distributions. As larger particles are known to scatter light at a greater intensity, the relative amount of this secondary distribution is low in comparison to the trace for the smaller particle.

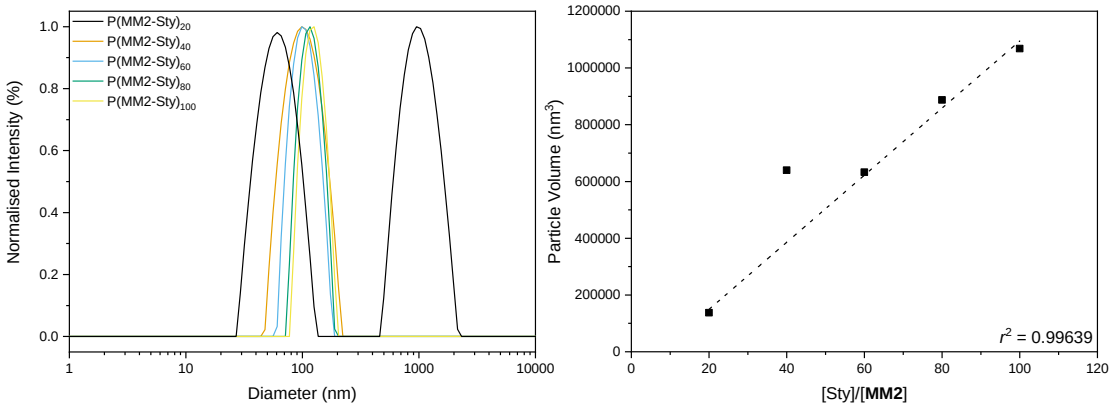

Figure 4.8 DLS intensity distribution traces of nanoparticles synthesised at different molar ratios of styrene and **MM2** and particle size calibration. Styrene concentration increased to target molar ratio.

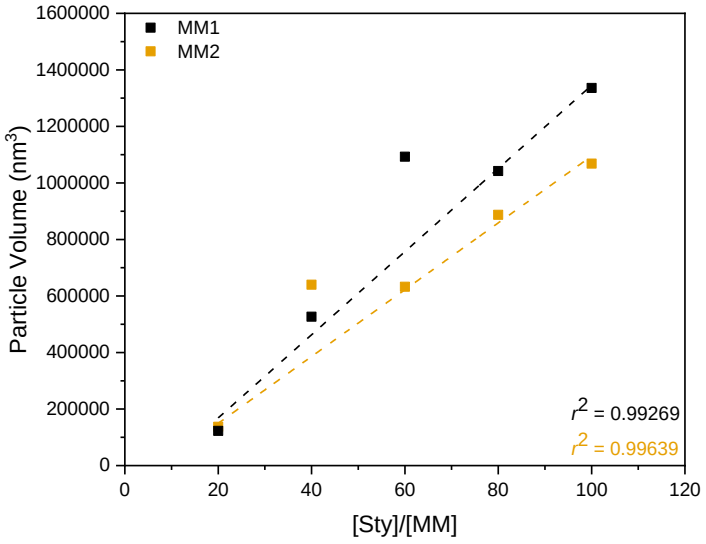

Figure 4.9 Comparison of particle volumes arising from copolymerisation of **MM1** (black) or **MM2** (orange) with styrene at various molar ratios.

One explanation for the smaller particle sizes observed using a higher molecular weight macromonomer could be due to greater stabilisation afforded to the growing nanoparticles. If the primary mechanism for particle growth is coagulation of smaller particles, then a higher molecular weight stabiliser should provide greater steric stabilisation than lower molecular weight stabilisers, preventing coagulation of particles.

The series of experiments above highlights the usefulness of PEtOx macromonomers in the surfactant-free emulsion polymerisation of styrene. Nanoparticles as small as 64.0 nm were synthesised *via* a straightforward copolymerisation. Furthermore, increasing the molar ratio of styrene to macromonomer enabled the synthesis of larger nanoparticles with a predictable trend in size increase. Adjusting the macromonomer molecular weight also allows for control over the particle size, with increasing molecular weights allowing the preparation of smaller nanoparticles.

4.2.2.4 Expanding Monomer Selection

The ability to form nanoparticles with a wide scope of monomer families would be advantageous in the addition of further functionality and control of nanoparticle properties. Methacrylates and acrylates were polymerised in a similar manner to styrene above, with **MM1** used as the stabilising monomer in all cases. Butyl acrylate (BA)

proved challenging to polymerise into stable monodisperse nanoparticles, with stable nanoparticles only being achieved at a monomer ratio of 1:20. Above this ratio aggregation followed by sedimentation was observed. In the absence of **MM1**, at a hydrophobic monomer loading equal to that of a 1:60 molar ratio, BA can form stable monodisperse nanoparticles without any observable sedimentation (**Figure A4.28**), suggesting a detrimental effect caused by addition of **MM1**. Lunn and Perrier reported the successful surfactant-free emulsion polymerisation of BA stabilised with a variety of hydrophilic monomers. The hydrophilic monomers employed in this work were acrylate or acrylamide based as opposed to styrene and possessed different structures. This indicated that finding a universal hydrophilic monomer maybe be challenging. From the studies on surface active monomers it was found that a balance of reactivity between the stabilising monomer and core-forming monomer was required.[15] If the difference in reactivity was too great then the surfmer could not be incorporated into the particle to provide stabilisation. This may be applicable to the systems reported in this chapter and further consideration should be made in the future regarding reactivity.

Butyl methacrylate formed stable nanoparticles with broad, disperse size distributions at low [Sty]/[**MM1**] ratios and narrow monodisperse size distributions above a molar ratio of 40 (**Table 4.5**, **Figure 4.10**). Increasing the monomer ratio from 1:20 to 1:100 changed the nanoparticle diameter from 109.6 nm to 245.7 nm. The butyl methacrylate particles are significantly larger than their styrene counterparts. A BMA homopolymerisation was carried out at similar hydrophobic monomer concentrations to **P(MM1-BMA)$_{60}$**, resulting in a particle diameter of 476.8 nm compared to a diameter of 177.8 nm when copolymerised with **MM1**, further indicating the influence of macromonomer on the resulting particles.

Benzyl methacrylate was employed to try and ascertain whether the difference in size results from the type of polymerisable group or the properties of the monomer. Like butyl methacrylate, polymerisation of benzyl methacrylate results in broad size distributions at low molar ratios and narrow, monodisperse particles above a molar ratio of 20 (**Table 4.5**, **Figure 4.11**). The particle diameters range between 218.5 nm and 263.9 nm.

Unlike copolymerisation with styrene, the particle volume did not increase linearly with increasing molar ratios for butyl and benzyl methacrylate. Calculating the volume from the intensity distribution resulted in a wide distribution of sizes with little correlation between them. However, if the volumes arising from the number distribution are plotted then a linear increase in particle volume is observed with increasing comonomer

concentration (**Figure 4.12**). Targeting of particle volume for methacrylate-based nanoparticles is not possible using the intensity-derived plot and number-derived volumes should be used. This discrepancy could arise due to the bimodal distributions observed in the intensity distribution and the overrepresentation of scattering intensity for larger particles.

The ability to copolymerise methacrylate monomers with **MM1** allows for the possibility of synthesising nanoparticles with functional cores, such as a stimuli response or conjugated drugs.

Table 4.5 Characterisation data for nanoparticles synthesised with acrylate and methacrylate monomers, **P(MM1-X)$_y$**, where x represents the hydrophobic monomer and y the molar ratio between **MM1** and monomer. Concentration of hydrophobic monomer increased, **MM1** concentration kept constant (0.01 M).

Nanoparticle	**M**	**[M] (M)**	**[M]/[MM]**	**ζ-Potential (mV)**	**Size (nm)[a]**	**PDi[b]**
P(MM1-BA)$_{20}$	BA	0.2	20	19.8 ± 1.0	144.9	0.09
P(MM1-BMA)$_{20}$		0.2	20	11.7 ± 0.4	109.6	0.17
P(MM1-BMA)$_{40}$		0.4	40	14.0 ± 0.5	199.6	0.17
P(MM1-BMA)$_{60}$	BMA	0.6	60	21.6 ± 0.9	177.8	0.05
P(MM1-BMA)$_{80}$		0.8	80	20.4 ± 0.5	245.7	0.08
P(MM1-BMA)$_{100}$		1.0	100	24.6 ± 0.5	226.6	0.04
P(MM1-BzMA)$_{20}$		0.2	20	11.0 ± 0.5	232.0	0.12
P(MM1-BzMA)$_{40}$		0.4	40	23.0 ± 0.6	227.9	0.08
P(MM1-BzMA)$_{60}$	BzMA	0.6	60	22.5 ± 0.9	218.5	0.04
P(MM1-BzMA)$_{80}$		0.8	80	20.6 ± 0.9	246.9	0.04
P(MM1-BzMA)$_{100}$		1.0	100	23.6 ± 0.9	263.9	0.05

[a] Particle diameter determined from DLS intensity distribution. [b] PDi calculated using **Equation 4.2**.

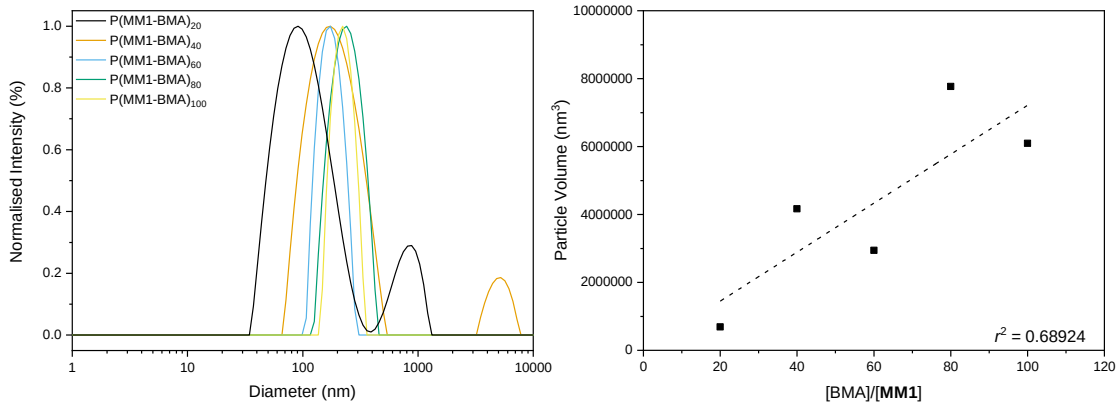

Figure 4.10 DLS intensity distribution traces of nanoparticles synthesised at different molar ratios of BMA and **MM1**. BMA concentration increased to target molar ratio. Particle size calibration with varying concentrations of BMA and **MM1**. BMA concentration increased to target molar ratio.

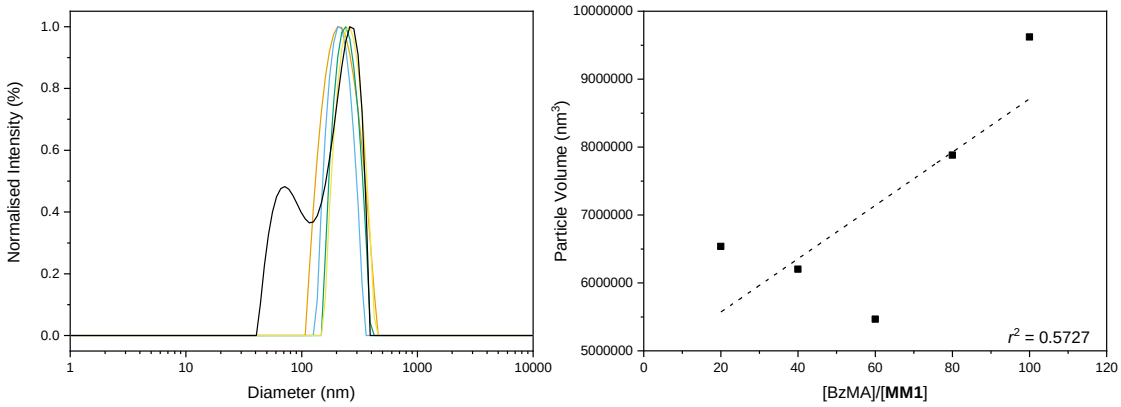

Figure 4.11 DLS intensity distribution traces of nanoparticles synthesised at different molar ratios of BzMA and **MM1**. BzMA concentration increased to target molar ratio. Particle size calibration with varying concentrations of BzMA and **MM1**. BMA concentration increased to target molar ratio.

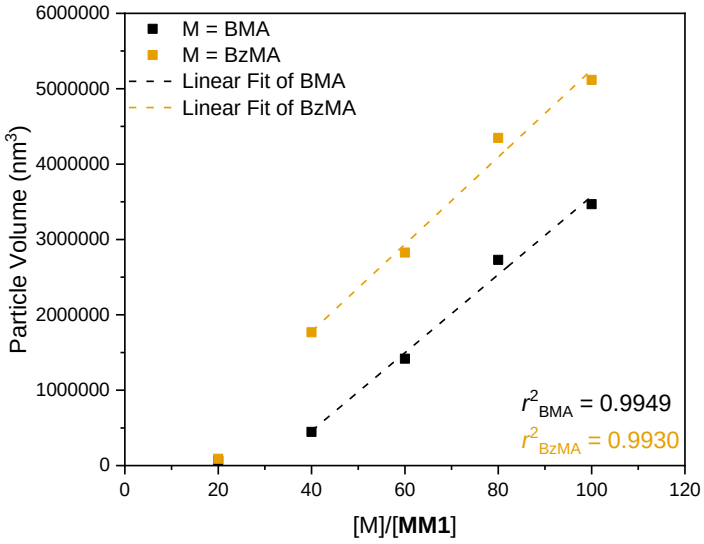

Figure 4.12 Comparison of particle volumes derived from DLS number distribution arising from copolymerisation of **MM1** with BMA (black) or BzMA (orange).

4.2.3 Hydrolysis of Poly(2-alkyl-2-oxazoline) Coronas

As described in previous chapters, PEtOx can undergo hydrolysis to form the secondary amine containing polymer, PEI. The nanoparticles were exposed to the hydrolysis conditions (1M HCl, 120 °C) for increasing amounts of time and their size distribution measured by DLS and conversion of EtOx to EI monitored by ^{1}H-NMR. Hydrolysis was achieved by addition of 37 % HCl to the crude **P(MM1-Sty)$_{20}$A** latex to a final acid concentration of 1 M. This solution was heated to 120 °C using a microwave reactor.

DLS indicates that in general the particles retain a similar size in solution after hydrolysis, however there is the presence of larger particles in the intensity trace for some samples (**Figure 4.13**). Comparison of the TEM micrographs also shows no significant changes to the nanoparticle morphology (**Figure 4.14**).

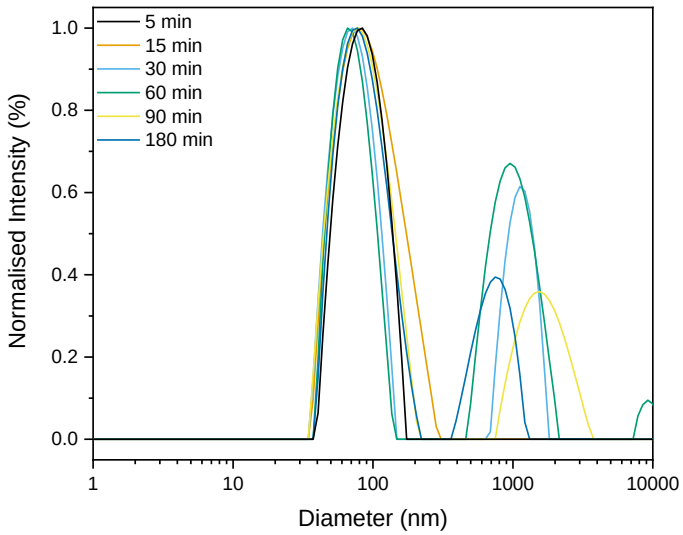

Figure 4.13 DLS intensity distribution traces of **P(MM1-Sty)$_{20}$A** that has been hydrolysed for various times.

This is further confirmed by TEM of the hydrolysed nanoparticles which exhibit spherical morphologies with no obvious structural perturbations (**Figure 4.14**).

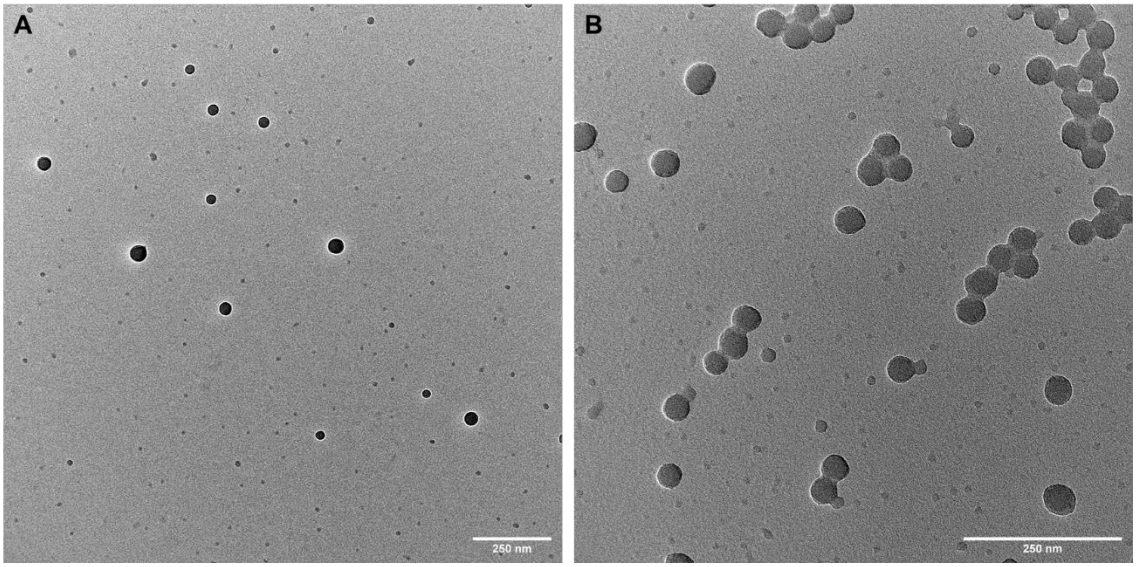

Figure 4.14 TEM micrograph of **P(MM1-Sty)$_{20}$A-55%** (A) and **P(MM1-Sty)$_{20}$A-82%** (B).

The conversion of EtOx to EI was determined by ^{1}H-NMR by comparing the backbone integrals of EtOx and EI (**Equation 2.4**). With increasing reaction time, the conversion of EtOx to EI increased, with similar progression to other reports on EtOx hydrolysis (**Table 4.6**, **Figure 4.15**). The kinetics of hydrolysis for the nanoparticle are similar to

those measured for a linear PEtOx (**Figure 2.9**), with both samples reaching 80% EI content after 90 minutes.

However, the extent of hydrolysis determined by ^{1}H-NMR may not reflect the true value as the polymers are surface bound and the section of corona closest to the core may not be properly solubilised.

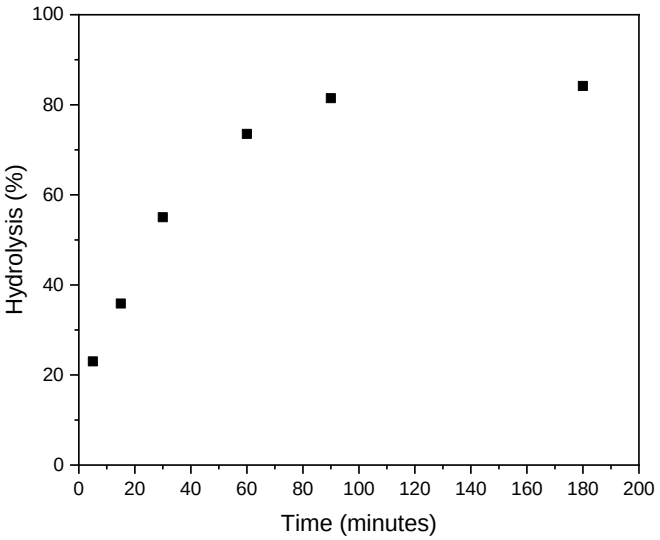

Figure 4.15 Kinetics of hydrolysis showing conversion of EtOx to EI over time.

As reported by Lunn and Perrier, during the surfactant-free emulsion copolymerisation there is a small amount of polymer not incorporated into the nanoparticle and found in solution.[21] It is unknown if this phenomenon exists with the copolymerisation of **MM1** and hydrophobic monomers. However, due to the prevalence of this free polymer across multiple systems reported by Lunn and Perrier, it is assumed that it takes place to some degree.

To remove any unincorporated polymer, purification by centrifugation was reported to be the preferred method, as dialysis has an upper limit to the molecular weight it can remove. However, all nanoparticles remained suspended in solution up to speeds of 20,000 rpm, preventing the separation of nanoparticles and any unincorporated polymer. Instead, the nanoparticles were concentrated using a 10 kDa centrifugal dialysis membrane to a volume of 0.1 mL. The particles were resuspended in H_2O and this process repeated a further two times. The concentrated particles were diluted with 0.4 mL d^{4}-MeOD, which should solubilise the PEtOx corona, and measured by ^{1}H-NMR to determine the degree of hydrolysis.

As this is a free radical polymerisation system it is assumed that some of the free polymer would be above 10 kDa in molecular weight, meaning it would not be removed by dialysis. Therefore, it is not possible to determine the true extent of hydrolysis on the corona as the sample could be contaminated with unincorporated polymer.

Table 4.6 Characterisation data for the hydrolysis of **P(MM1-Sty)$_{20}$A**

Nanoparticle	Time (min)	% Hydrolysis[a]	ζ-Potential (mV)	Size (nm)[b]	PDi[c]
P(MM1-Sty)$_{20}$A	5	23	22.3 ± 0.8	87.2	0.10
	15	36	25.3 ± 0.7	101.8	0.13
	30	55	23.6 ± 1.1	74.9	0.09
	60	74	20.0 ± 1.0	73.4	0.07
	90	82	21.6 ± 0.8	88.0	0.12
	180	84	17.4 ± 0.9	88.5	0.10

a Percentage hydrolysis calculated using **Equation 2.4** [b] Particle diameter determined from DLS intensity distribution. [c] PDi calculated using **Equation 4.2**.

4.2.4 SAXS Characterisation

Small-angle X-ray scattering (SAXS) was used to further characterise the nanoparticles in their pre- and post-hydrolysed states (**Figure 4.16**).

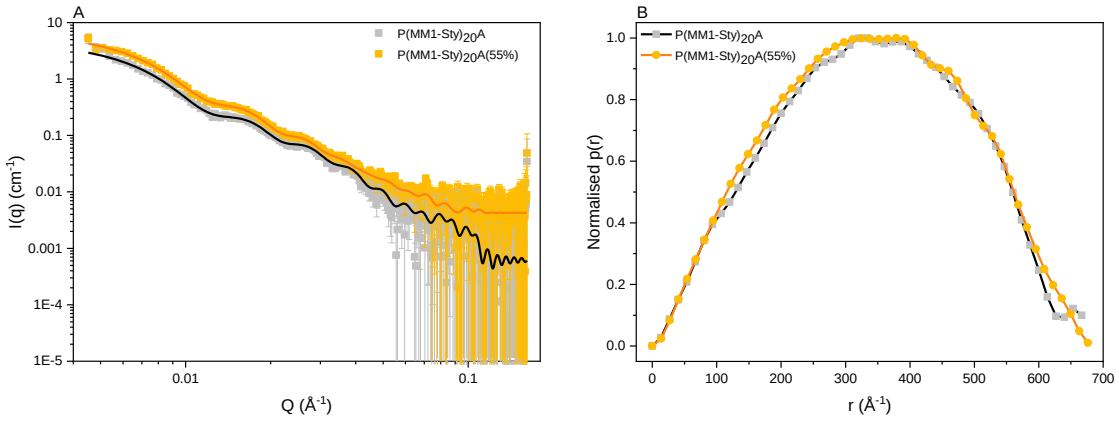

Figure 4.16 (A) Small-angle x-ray scattering of nanoparticles at 5 mg mL^{-1}, fitted with pair distance distribution. (B) Pair distance distribution plot for nanoparticles determined from small-angle x-ray scattering profile.

Fitting the SAXS data for the nanoparticles proved challenging and they could not be fit to a particular model. Therefore, the scattering data was analysed using a pair distance distribution, p(r), function. Pair distance distribution functions provide a contrast-weighted probability distribution of the distance between two scattering centres within a particle. This can be used to determine the size and morphology of the analysed particle, with spherical particles resulting in a gaussian-shaped pair distance distribution.

The obtained p(r) distribution was not gaussian, indicating that the particles are not truly spherical. This is confirmed by TEM micrographs which shows particles with rough surfaces. For **P(MM1-Sty)$_{20}$A**, a radius of 35 nm was obtained from the p(r) distribution, which results in a diameter slightly larger (70 nm) than those obtained by DLS (51.9 nm) and TEM (41.5 nm).

The scattering curve for the hydrolysed particle exhibited the same profile as the non-hydrolysed sample, again indicating no disruption to the particle morphology. The p(r) function of both samples was also identical.

4.2.5 Complexation of pDNA

Due to the presence of cationic residues on the corona of the nanoparticle their ability to complex anionically charged macromolecules was investigated. Hydrolysed nanoparticles were incubated with plasmid DNA (pDNA) (pHR' CMV, 10.8 kbp) at decreasing weight ratios of pDNA compared to the nanoparticle. Nanoparticles with two different levels of hydrolysis were employed, **P(MM1-Sty)$_{20}$A-55%** & **P(MM1-Sty)$_{20}$A-81%**, to study the effect of charge density on the nanoparticle surface on their ability to condense pDNA. Polyplex formation was studied by agarose gel electrophoresis and a select group of complexes analysed using DLS and TEM.

4.2.5.1 Agarose Gel Electrophoresis

Agarose gel electrophoresis allows for the point at which polyplexes form to be quantified. Application of a voltage across the gel will cause any unbound pDNA to migrate away from the wells towards the anode. Once bound within a polyplex the pDNA will be unable to migrate and will be retained within the well.

Polyplex formation was quantified at increasing weight ratios (**Equation 4.1**) between the hydrolysed nanoparticles and pDNA. For 55% hydrolysis, complexation of pDNA

was achieved at a weight ratio between 0.33 and 0.17. This was lower for 81% hydrolysed which appeared to complex pDNA between a weight ratio of 0.50 and 0.33 (**Figure 4.17**).

$$weight\ ratio\ (wt\%) = \frac{mass\ of\ pDNA}{mass\ of\ nanoparticle + mass\ of\ pDNA} \qquad \textbf{4.1}$$

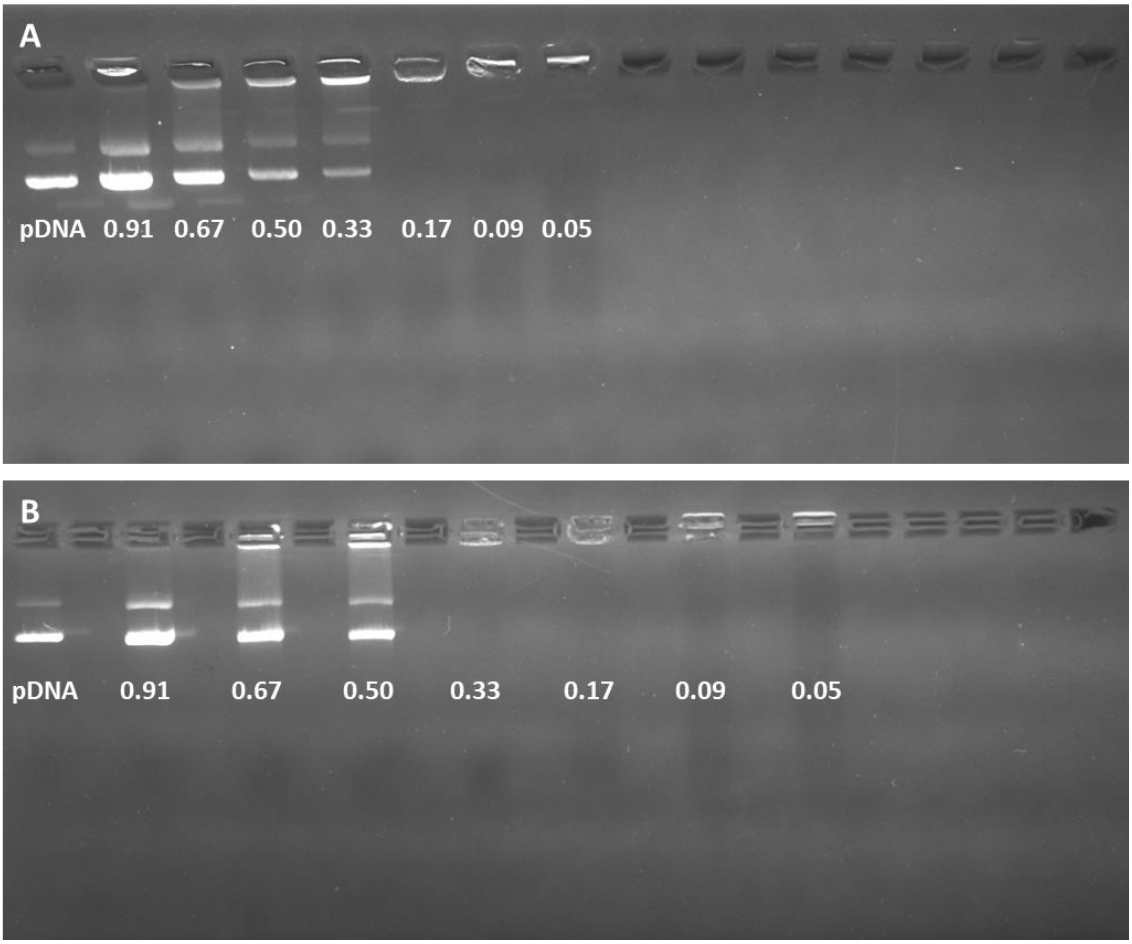

Figure 4.17 Agarose gel electrophoresis for **P(MM1-Sty)$_{20}$A-55%** (A) and P**(MM1-Sty)$_{20}$A-81%** (B).

The ability to complex pDNA highlights a potential application of these nanoparticles, either in the delivery of genetic material or in the complexation of anionic macromolecules. However, it is unknown to what extent the binding is caused by the nanoparticles or by free polymer that could not be removed from solution. Using DLS and TEM it should be possible to determine what causes the polyplex formation.

4.2.5.2 Polyplex Characterisation

Polyplexes were characterised using DLS and TEM to ascertain their structure. 80% hydrolysed nanoparticles were characterised by DLS at 0.17, 0.09, and 0.05 weight ratio, with all polyplexes exhibiting similar DLS traces to the nanoparticle before complexation. The size and PDi decrease with increasing nanoparticle concentration compared to pDNA (**Figure 4.18**). This could result from a greater contribution to the scattering profile from non-complexed nanoparticles. Furthermore, the ζ-potential increases with a greater concentration of nanoparticle due to the increase in ratio between cationic nanoparticles and anionic pDNA.

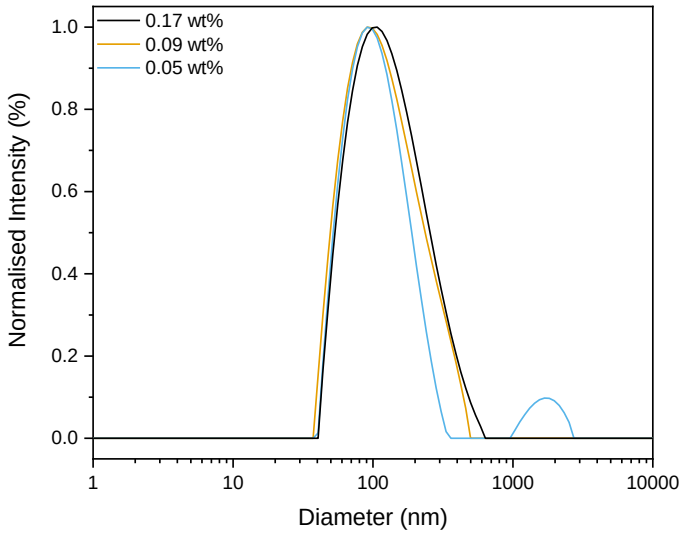

Figure 4.18 DLS intensity distribution traces for polyplexes prepared at various wt%.

Table 4.7 Characterisation data for polyplexes formed at different weight ratios of pDNA to **P(MM1-Sty)$_{20}$A**

pDNA wt %	Size (nm)[a]	PDi[b]	ζ-Potential (mV)
0.17	148.5	0.18	26.6 ± 4.6
0.09	136.5	0.15	24.2 ± 9.6
0.05	114.2	0.14	36.6 ± 1.1

[a] Particle diameter determined from DLS intensity distribution. [b] PDi calculated using **Equation 4.2**.

The intensity trace does show a large degree of broadening compared to the number trace, indicating the formation of larger aggregates. This is observed in TEM, where a 0.05 wt% polyplex was imaged. Large aggregates of pDNA and nanoparticles are found (**Figure 4.19**). It appears that a network of pDNA bound together by nanoparticles forms during polyplex formation. The nanoparticle shape remains relatively unperturbed with no observed changes caused by the binding of pDNA. The uncomplexed pDNA shown in the TEM micrograph could arise from poor access to the cationic groups on the surface of the nanoparticle. This could cause challenges in bundling pDNA into compact polyplexes as there are less cationic residues available to bind. Investigation into the complexation of lower molecular weight nucleotides, such as siRNA, would be advantageous to determine if the poor complexation results from the size of the pDNA in relation to the nanoparticle.

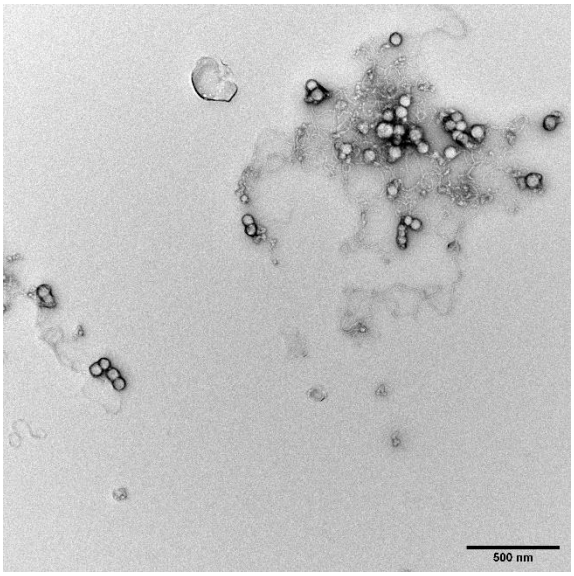

Figure 4.19 TEM micrograph for polyplexes formed at a weight ratio of 0.05 pDNA to **P(MM1-Sty)$_{20}$A**.

4.3 Conclusion

In this chapter poly(2-ethyl-2-oxazoline) macromonomers were used as comonomers in the surfactant-free emulsion polymerisation of various hydrophobic monomers. It was found that by increasing the molar ratio between the macromonomer and hydrophobic monomer that the resulting particle size could be accurately controlled. This was shown for both increasing the solution concentration of hydrophobic monomers and for decreasing the concentration of the macromonomer.

The macromonomer could successfully participate in the emulsion polymerisation of styrene, butyl methacrylate, and benzyl methacrylate, however copolymerisaiton with butyl acrylate resulted in particle aggregation and sedimentation while defined particles were formed in other cases. The molecular weight of the macromonomer was also found to play a role in the particle dimensions, with increased molecular weight macromonomers resulting in smaller diameters. This correlates with previously reported literature on similar systems.

Once the route to nanoparticle synthesis was established, the particles were subject to the hydrolysis conditions required to convert poly(2-ethyl-2-oxazoline) into poly(ethyleneimine). Any macromonomer on the corona of the particle should undergo hydrolysis to form highly cationic nanoparticles. DLS and TEM were used to confirm that no degradation occurred during the hydrolysis. These particles were then used to complex pDNA, and like previous work, a higher degree of hydrolysis was found to fully complex pDNA at lower ratios of pDNA to nanoparticle. Future work will examine the toxicity and transfection ability of these nanoparticles and improve the complexation of pDNA.

4.4 Experimental

4.4.1 Materials

Styrene, Butyl Methacrylate, Butyl Acrylate, and Benzyl Methacrylate were purchased from Sigma-Aldrich. 2,2'-Azobis[2-(2-imidazolin-2-yl)propane]dihydrochloride (VA-044) was purchased from FUJIFILM Wako Pure Chemical Corporation. 37% Hydrochloric Acid was purchased from Fisher Scientific. Styrene, Butyl Methacrylate, Butyl Acrylate, and Benzyl Methacrylate were passed through a basic aluminium oxide column prior to use to remove inhibitor.

4.4.2 Characterisation

4.4.2.1 Dynamic Light Scattering

Size and zeta-potential measurements were carried out using an Anton Paar Litesizer 500 at a polymer concentration of 0.1 mg mL^{-1} and a temperature of 25 °C. The instrument is equipped with a semiconductor laser diode (40 mW, 658 nm). Size measurements were obtained at a scattering angle of 173 ° (back scatter). PDi was calculated using **Equation 4.1**. Zeta-potential measurements were carried out using Anton Paar omega cuvettes and modelled using the Smoluchowski theory.

$$PDi = \frac{\sigma^2}{d^2} \qquad \textbf{4.2}$$

4.4.2.2 Transmission Electron Microscopy (TEM)

In all cases the Formvar/carbon coated copper grids were subjected to glow discharge to render their surface hydrophilic. Then, 5 µl of sample was added to the grid and incubated for 1 min. After addition of the sample, excess solution was removed by blotting with tissue and the grid allowed to airdry. Imaging was done using a Jeol 2100Plus TEM fitted with a Gatan OneView IS camera and images analysed by Fiji (www.fiji.sc).

4.4.2.3 Nuclear Magnetic Resonance Spectroscopy (NMR)

^{1}H-NMR spectra were recorded using a Bruker DPX-300 or DPX-400 NMR spectrometer which operated at 300.13 and 400.05 MHz, respectively. The residual solvent peaks were used as internal references. Deuterated methanol (MeOD) (δ_H = 3.31 ppm) was used as the solvent for all measurements.

4.4.3 Synthetic Procedures

4.4.3.1 General Procedure for Surfactant-Free Emulsion Polymerisation

Macromonomer and VA-044 (0.25 mM) were dissolved in water and added to a 7.5 mL vial fitted with a size 21 septum and 1 cm magnetic stirrer. The solution was purged with

N_2 to remove any oxygen. In a separate vial, the hydrophobic monomer was similarly purged with N_2. After 15 minutes purging the hydrophobic monomer was transferred to the initial vial using a Hamilton gas-tight syringe. The solution was placed into an oil bath with a temperature of 70 °C and stirring speed of 800 rpm. The vial was left in the oil bath for 3 hours before removal and exposure to oxygen.

4.4.3.2 Hydrolysis of Nanoparticle Corona

250 µL of latex solution was added to a microwave reaction vial along with 22.7 µL of 37 % HCl ($[H^+]$ = 1 M). The vial was fitted with a stirrer bar and sealed. The vial was placed in a Biotage Initiator+ Eight microwave reactor at 120 °C for a predetermined amount of time. After heating the solution was transferred to a Amicon Ultra centrifugal filter unit with a 10 kDa MWCO. The latex was spun down and fresh water added for a total of three washes. Following this the latex was diluted back to a total volume of 250 µL.

4.4.3.3 Plasmid Binding and Gel Electrophoresis

Polyplex formation was carried out as follows. To an Eppendorf tube was added water and nanoparticle followed by thorough mixing. pDNA ($[pDNA]_{final}$ = 35 µg mL^{-1}) was added to the Eppendorf tube to make a total volume of 100 µL and vortexed for 30 seconds before a 30 minute incubation at room temperature. The concentration of pDNA was fixed in all samples and the concentration of polymer varied to the make the targeted wt%.

Agarose gels (0.8 % w/v) were prepared by adding 1.6 g agarose powder to 200 mL 1 X TAE buffer and heating in a microwave to dissolve the agarose. The solution was cooled before addition of ethidium bromide (EthBr) (20 µL of 10 mg mL^{-1} EthBr stock). The gel was poured into a casting tray and combs inserted to form the wells. To visualise polyplex formation, 20 µL of the polyplex prepared above was added to 5 µL SDS-free loading buffer and added to the wells of the agarose gel. The gel was run in 1 X TAE buffer at 100 V for 30 minutes before imaging with an Azure 600 imaging system.

4.5 References

1. P. A. Lovell and F. J. Schork, *Biomacromolecules*, 2020, **21**, 4396-4441.
2. C. S. Chern, *Progress in Polymer Science*, 2006, **31**, 443-486.
3. A. Mahapatro and D. K. Singh, *Journal of Nanobiotechnology*, 2011, **9**, 55.
4. J. Zhou, H. Yao and J. Ma, *Polymer Chemistry*, 2018, **9**, 2532-2561.
5. P. Gurnani, C. P. Bray, R. A. E. Richardson, R. Peltier and S. Perrier, *Macromolecular Rapid Communications*, 2019, **40**, 1800314.
6. P. Gurnani, A. B. Cook, R. A. E. Richardson and S. Perrier, *Polymer Chemistry*, 2019, **10**, 1452-1459.
7. P. Gurnani, A. M. Lunn and S. Perrier, *Polymer*, 2016, **106**, 229-237.
8. P. Gurnani, C. Sanchez-Cano, K. Abraham, H. Xandri-Monje, A. B. Cook, M. Hartlieb, F. Lévi, R. Dallmann and S. Perrier, *Macromolecular Bioscience*, 2018, **18**, 1800213.
9. G. Nurumbetov, N. Engelis, J. Godfrey, R. Hand, A. Anastasaki, A. Simula, V. Nikolaou and D. M. Haddleton, *Polymer Chemistry*, 2017, **8**, 1084-1094.
10. G. Delaittre, J. Nicolas, C. Lefay, M. Save and B. Charleux, *Chemical Communications*, 2005, DOI: 10.1039/B415959D, 614-616.
11. C. Dire, S. Magnet, L. Couvreur and B. Charleux, *Macromolecules*, 2009, **42**, 95-103.
12. J. M. Asua, *Journal of Polymer Science Part A: Polymer Chemistry*, 2004, **42**, 1025-1041.
13. A. Guyot and K. Tauer, in *Polymer Synthesis*, Springer Berlin Heidelberg, Berlin, Heidelberg, 1994, DOI: 10.1007/BFb0024126, pp. 43-65.
14. A. Guyot, *Current Opinion in Colloid & Interface Science*, 1996, **1**, 580-586.
15. H. A. S. Schoonbrood and J. M. Asua, *Macromolecules*, 1997, **30**, 6034-6041.
16. J.-L. Ou, J.-K. Yang and H. Chen, *European Polymer Journal*, 2001, **37**, 789-799.
17. J. Zhang, Q. Zou, X. Li and S. Cheng, *Journal of Applied Polymer Science*, 2003, **89**, 2791-2797.
18. K. Tauer, R. Deckwer, I. Kühn and C. Schellenberg, *Colloid and Polymer Science*, 1999, **277**, 607-626.
19. Y. M. Wang and C. Y. Pan, *Colloid and Polymer Science*, 1999, **277**, 658-665.
20. M. Egen and R. Zentel, *Macromolecular Chemistry and Physics*, 2004, **205**, 1479-1488.

21. A. M. Lunn and S. Perrier, *Macromolecular Rapid Communications*, 2018, **39**, 1800122.
22. M. S.-D. Juang and I. M. Krieger, *Journal of Polymer Science: Polymer Chemistry Edition*, 1976, **14**, 2089-2107.
23. S. Kobayashi, H. Uyama, J. H. Choi and Y. Matsumoto, *Proceedings of the Japan Academy, Series B*, 1991, **67**, 140-143.
24. S. Kobayashi, H. Uyama, S. W. Lee and Y. Matsumoto, *Journal of Polymer Science Part A: Polymer Chemistry*, 1993, **31**, 3133-3139.
25. M. E. Dobrowolska, J. H. van Esch and G. J. M. Koper, *Langmuir*, 2013, **29**, 11724-11729.

4.6 **Appendix**

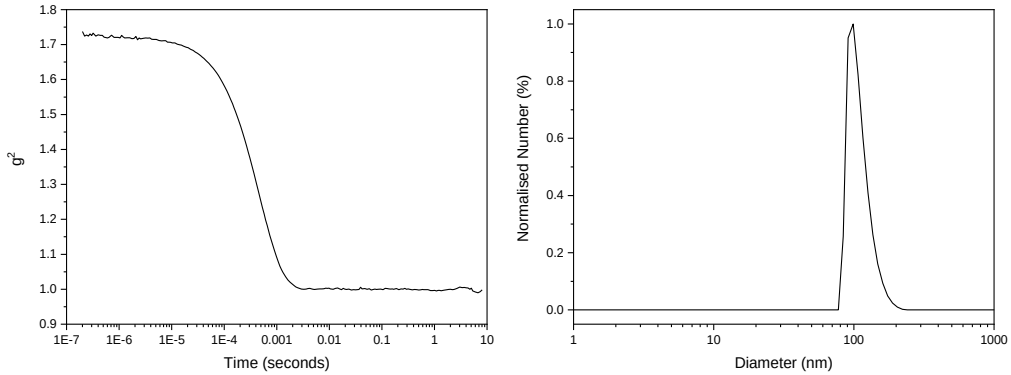

Figure A4.1 Normalised DLS number distribution and correlogram for **P(Sty)-01**

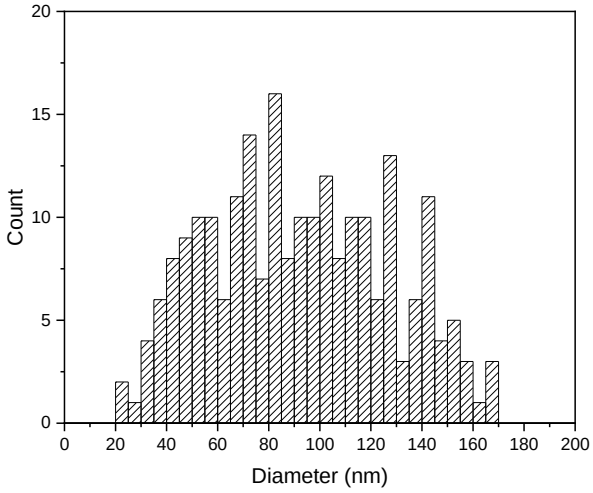

Figure A4.2 Nanoparticle size distribution determined from TEM micrographs (n = 227) of **P(Sty)-01**

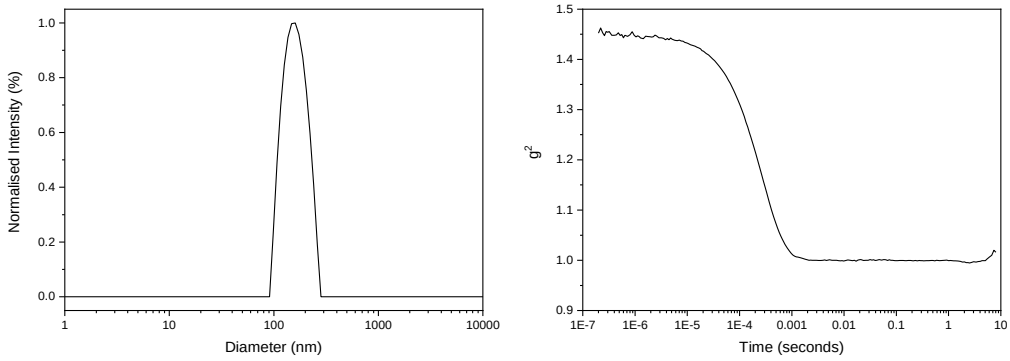

Figure A4.3 Normalised DLS intensity distribution and correlogram for **P(Sty)-02**

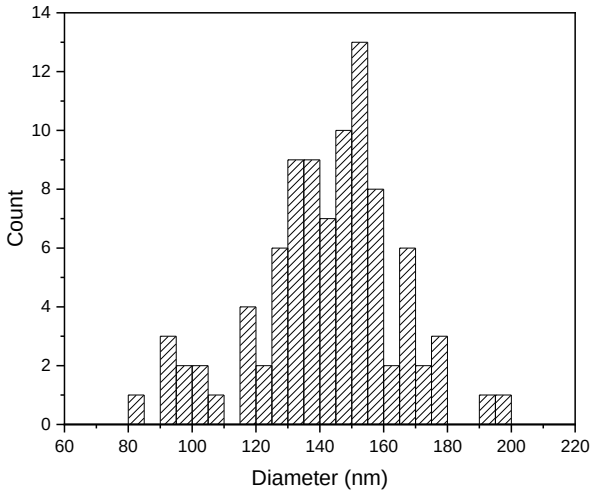

Figure A4.4 Nanoparticle size distribution determined from TEM micrographs (n = 92) of **P(Sty)-02**

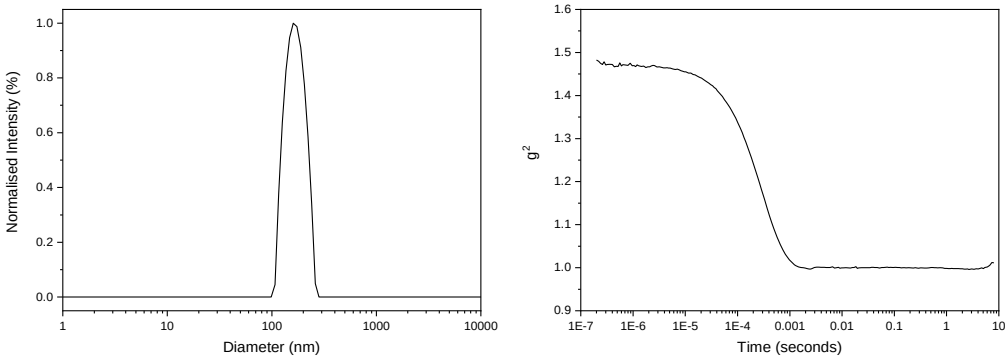

Figure A4.5 Normalised DLS intensity distribution and correlogram for **P(Sty)-03**

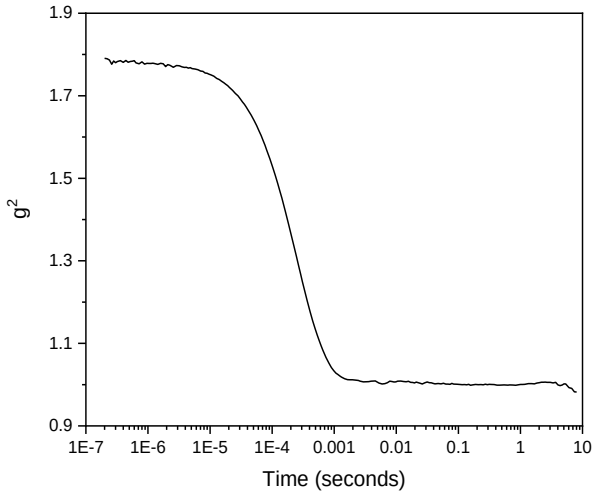

Figure A4.6 DLS correlogram for **P(MM1-Sty)$_{20}$A**

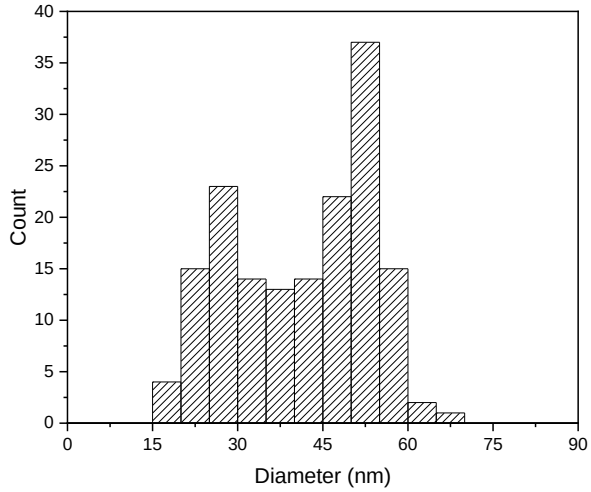

Figure A4.7 Nanoparticle size distribution determined from TEM micrographs (n = 160) of **P(MM1-Sty)$_{20}$A**.

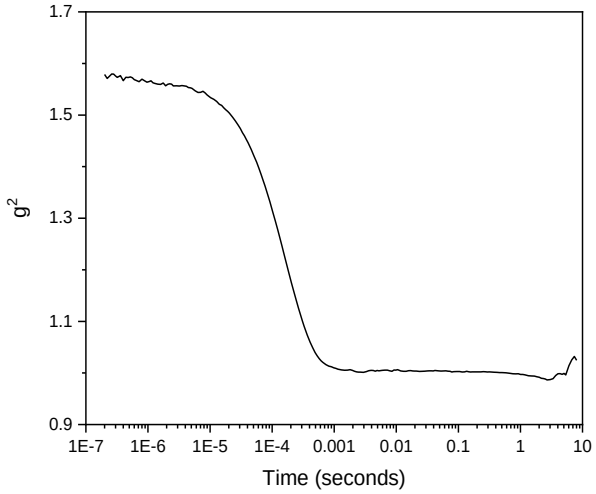

Figure A4.8 DLS correlogram for **P(MM1-Sty)$_{40}$A**

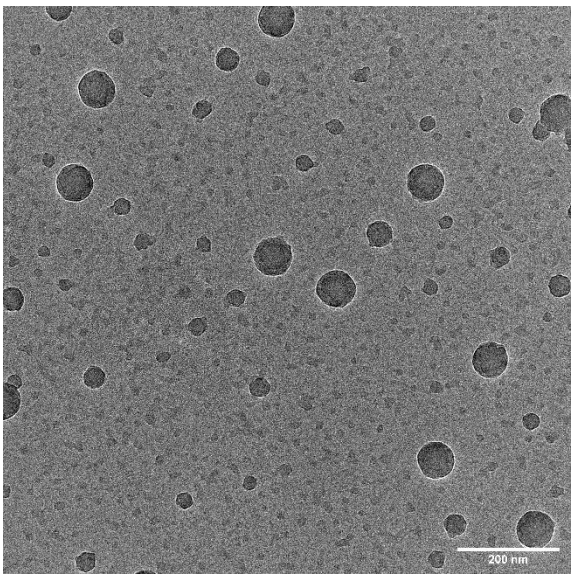

Figure A4.9 TEM micrograph for **P(MM1-Sty)$_{40}$A**.

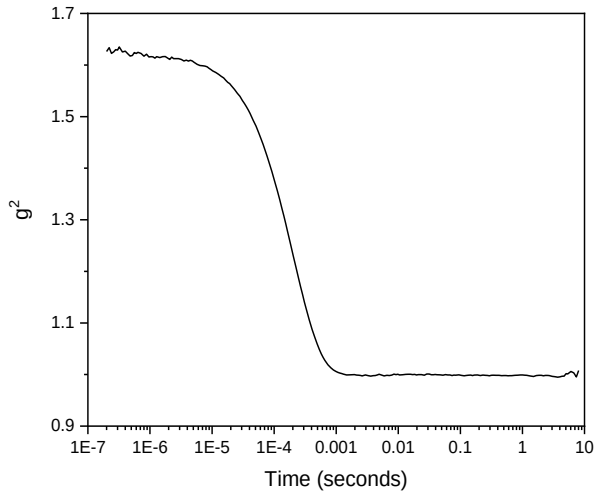

Figure A4.10 DLS correlogram for **P(MM1-Sty)$_{60}$A**

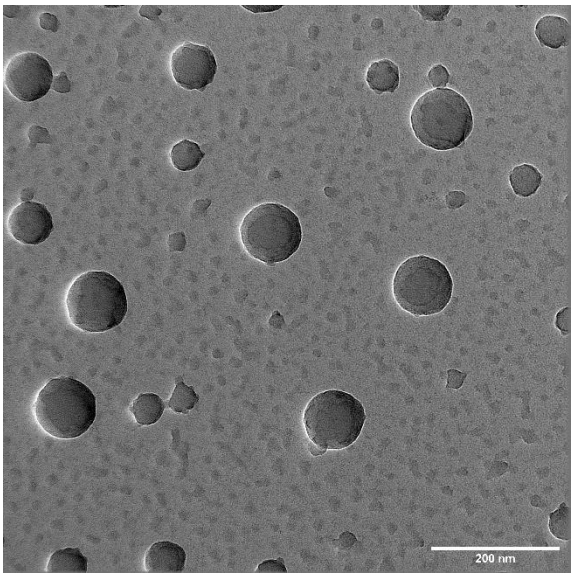

Figure A4.11 TEM micrograph for **P(MM1-Sty)$_{60}$A**.

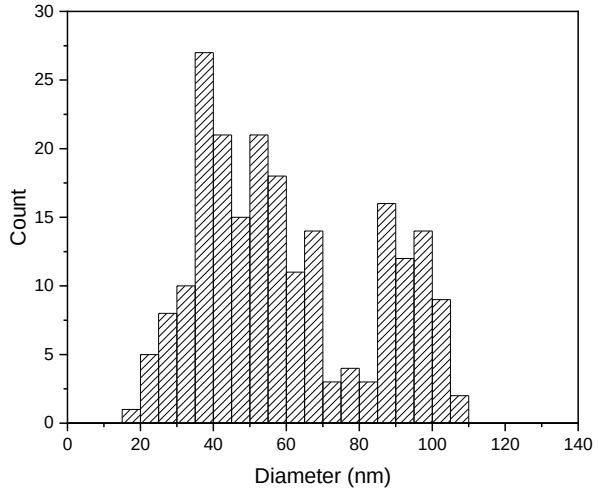

Figure A4.12 Nanoparticle size distribution determined from TEM micrographs (n = 214) of **P(MM1-Sty)$_{60}$A**.

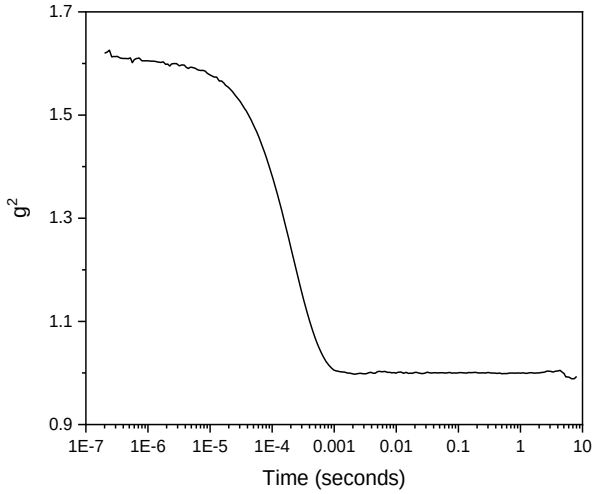

Figure A4.13 DLS correlogram for **P(MM1-Sty)$_{80}$A**

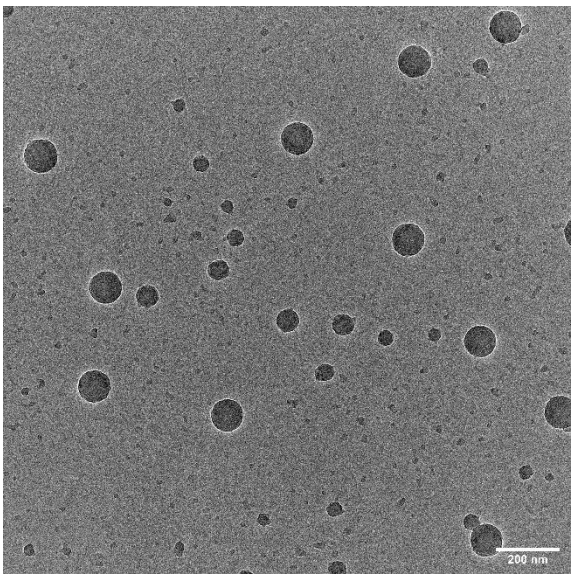

Figure A4.14 TEM micrograph for **P(MM1-Sty)$_{80}$A**.

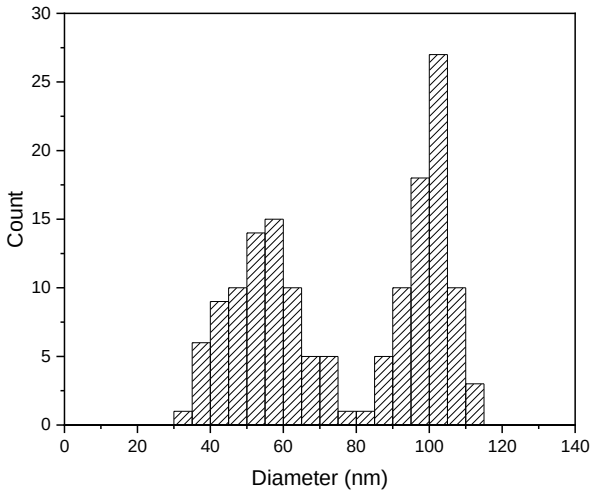

Figure A4.15 Nanoparticle size distribution determined from TEM micrographs (n = 150) of **P(MM1-Sty)$_{80}$A**.

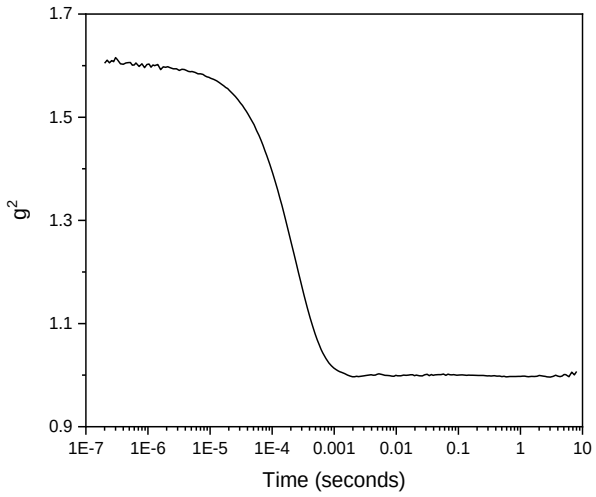

Figure A4.16 DLS correlogram for **P(MM1-Sty)$_{100}$A**

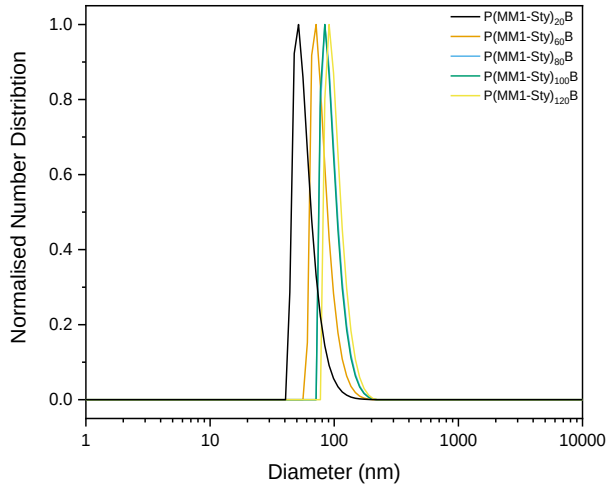

Figure A4.17 Overlay of DLS number traces for particles synthesised by the copolymerisation of **MM2** and styrene.

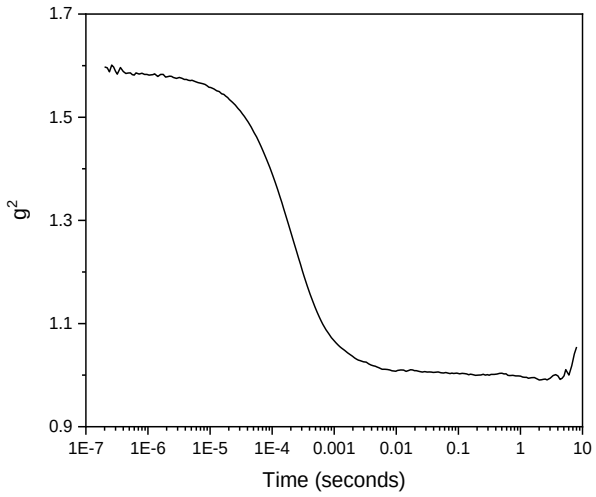

Figure A4.18 DLS correlogram for **P(MM1-Sty)$_{20}$B**

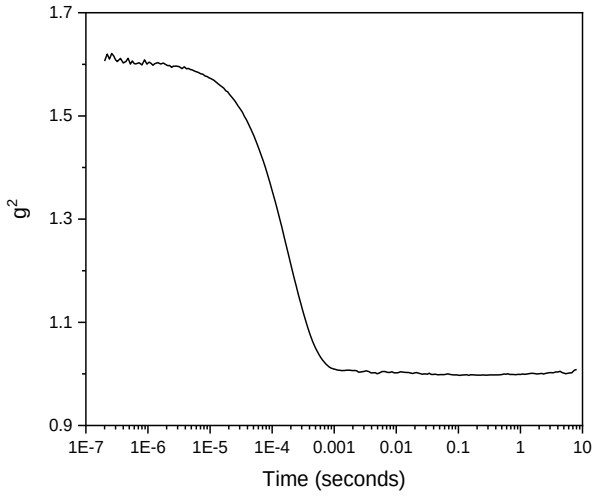

Figure A4.19 DLS correlogram for **P(MM1-Sty)$_{60}$B**

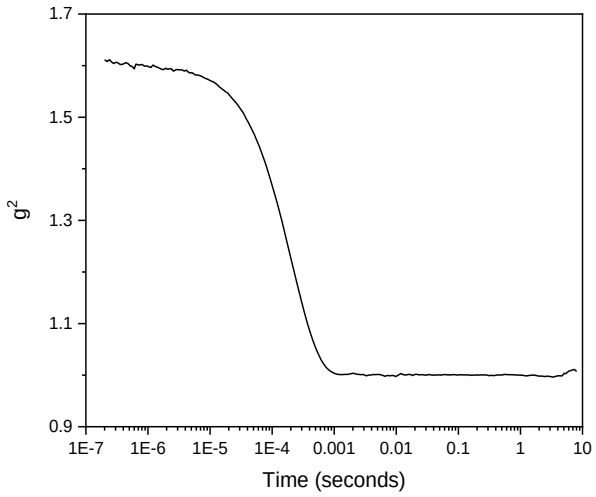

Figure A4.20 DLS correlogram for **P(MM1-Sty)$_{80}$B**

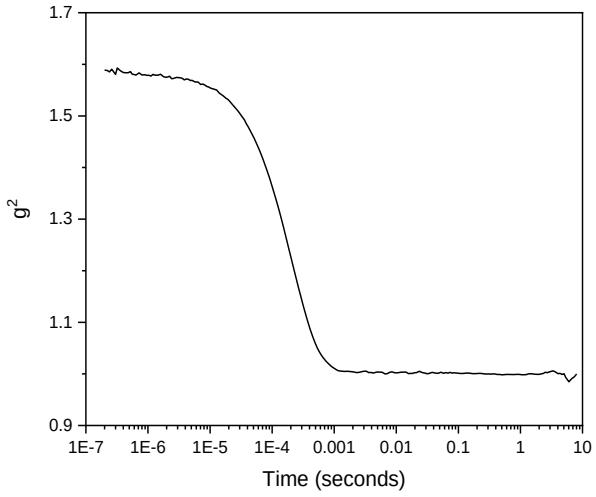

Figure A4.21 DLS correlogram for **P(MM1-Sty)$_{100}$B**

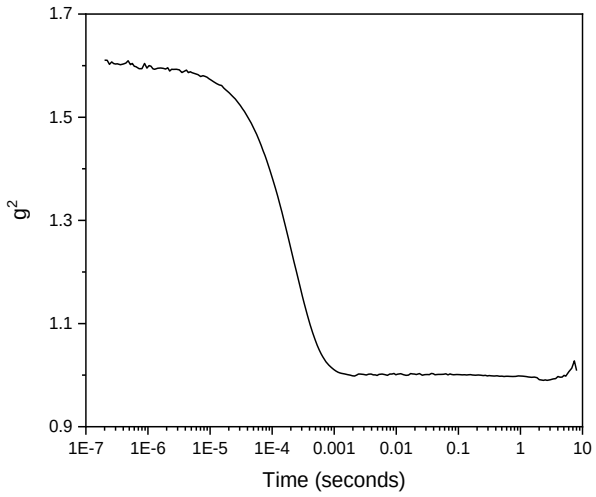

Figure A4.22 DLS correlogram for **P(MM1-Sty)$_{120}$B**

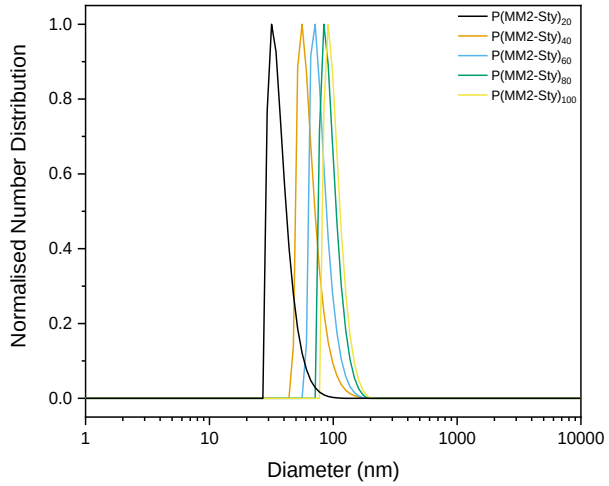

Figure 4.20 Overlay of DLS number traces for particles synthesised by the copolymerisation of **MM2** and styrene.

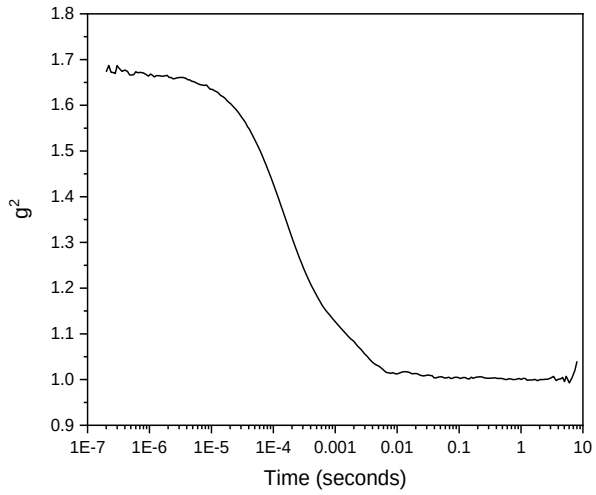

Figure A4.23 DLS correlogram for **P(MM2-Sty)$_{20}$**

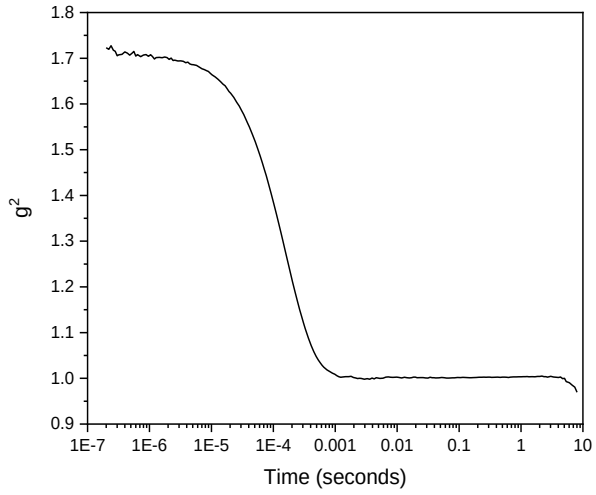

Figure A4.24 DLS correlogram for **P(MM2-Sty)$_{40}$**

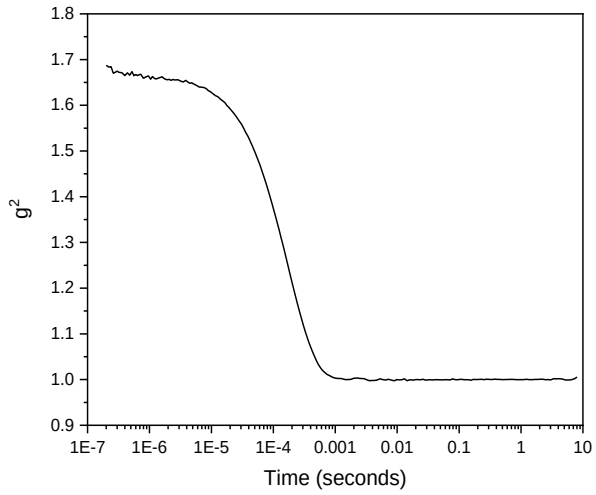

Figure A4.25 DLS correlogram for **P(MM2-Sty)$_{60}$**

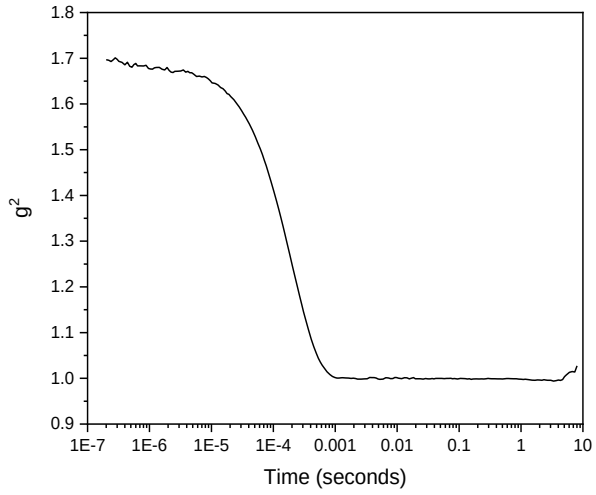

Figure A4.26 DLS correlogram for **P(MM2-Sty)$_{80}$**

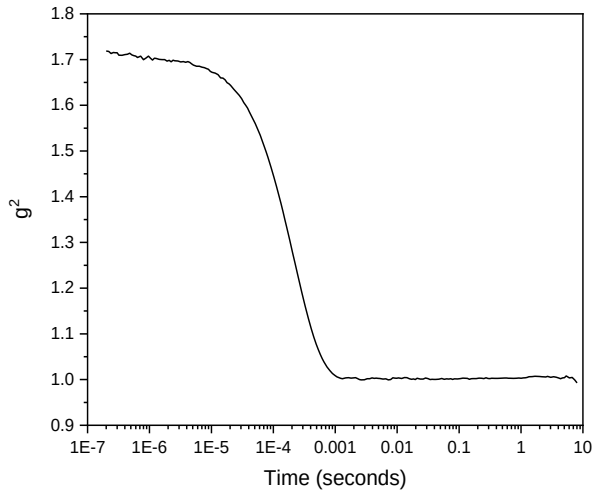

Figure A4.27 Correlogram for **P(MM2-Sty)$_{100}$**

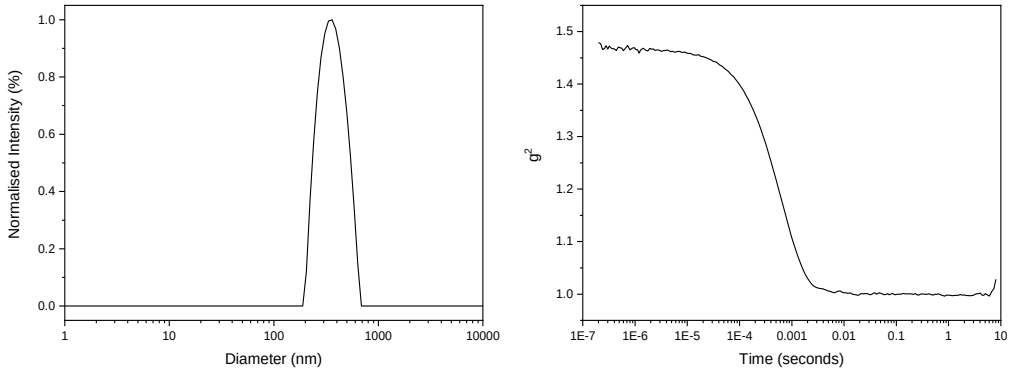

Figure A4.28 Normalised DLS intensity distribution and correlogram for **P(BA)**.

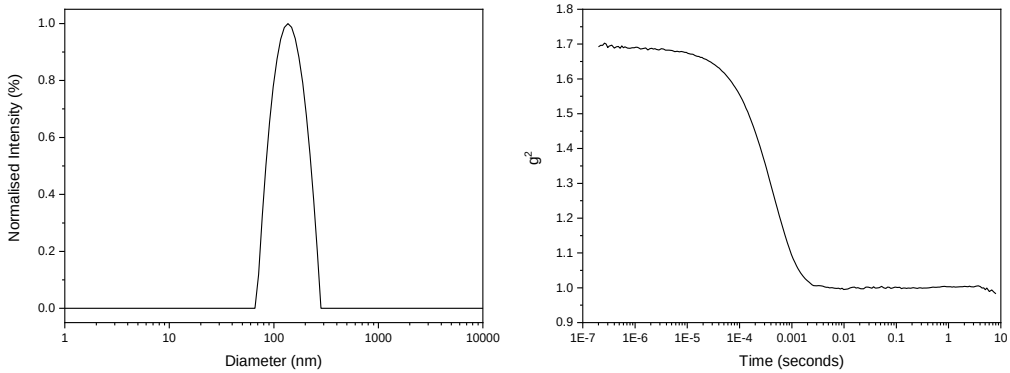

Figure A4.29 Normalised DLS intensity distribution and correlogram for **P(MM1-BA)$_{20}$.**

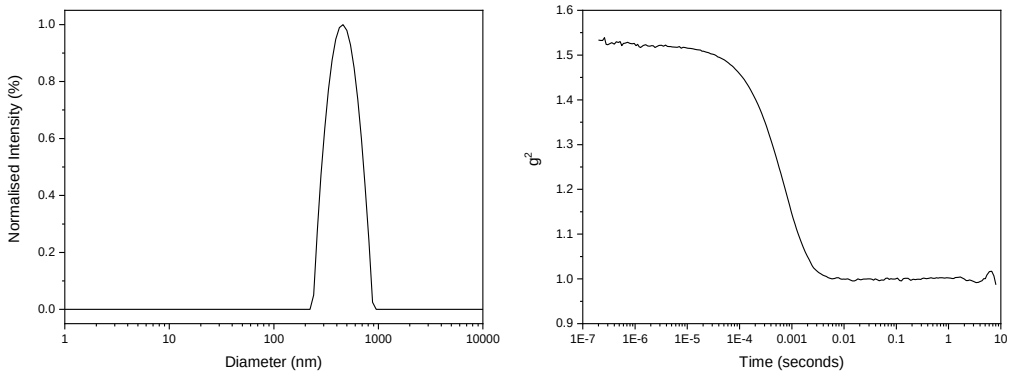

Figure A4.30 Normalised DLS intensity distribution and correlogram for **P(BMA)**.

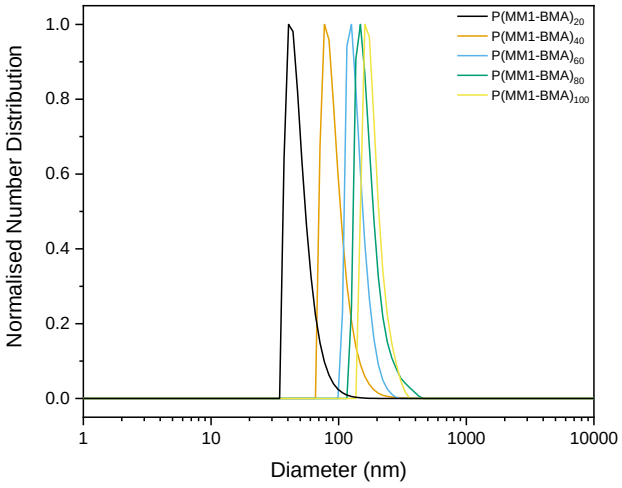

Figure A4.31 Overlay of DLS number traces for particles synthesised by the copolymerisation of **MM1** and BMA.

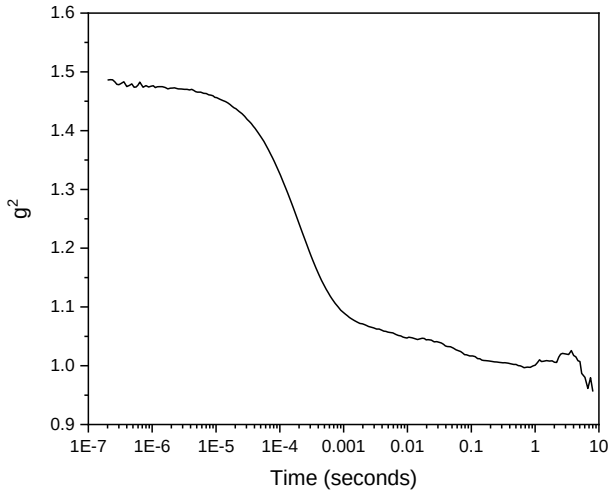

Figure A4.32 DLS correlogram for **P(MM1-BMA)$_{20}$**

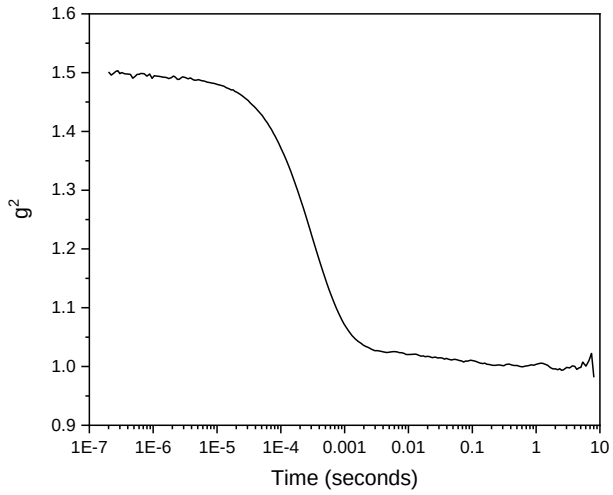

Figure A4.33 DLS correlogram for **P(MM1-BMA)$_{40}$**

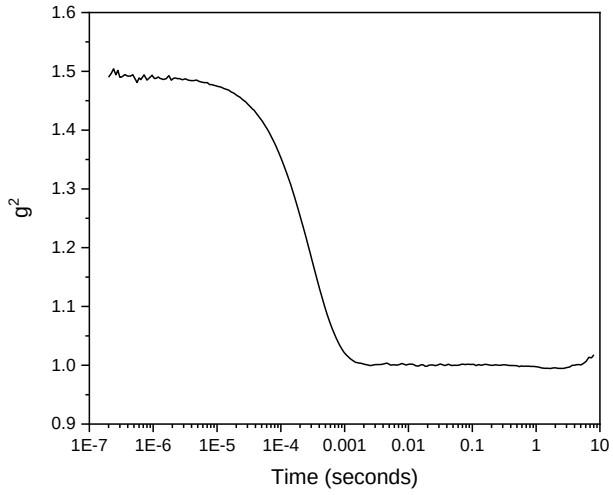

Figure A4.34 DLS correlogram for **P(MM1-BMA)$_{60}$**

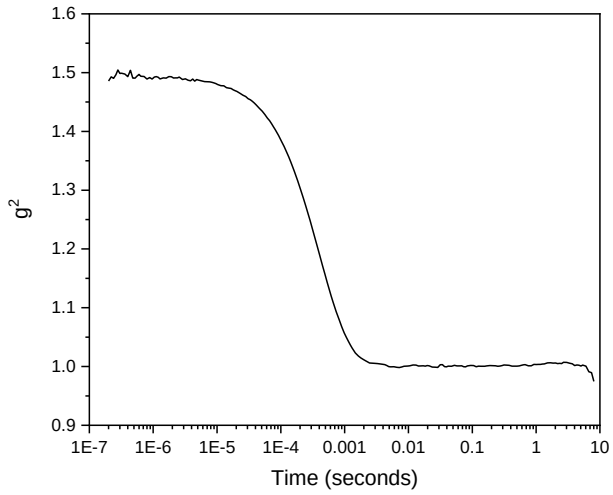

Figure A4.35 DLS correlogram for **P(MM1-BMA)$_{80}$**

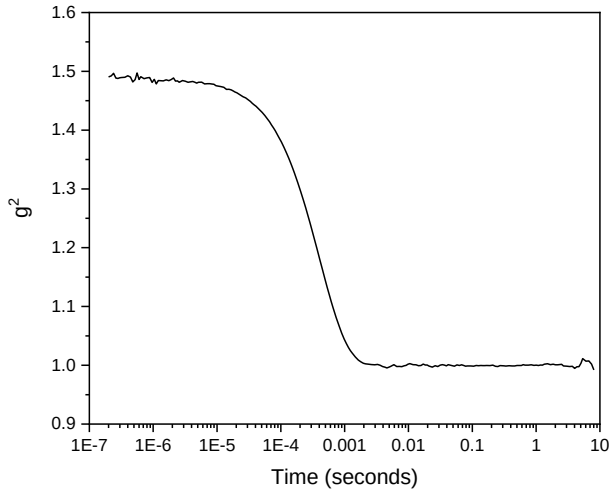

Figure A4.36 DLS correlogram for **P(MM1-BMA)$_{100}$**

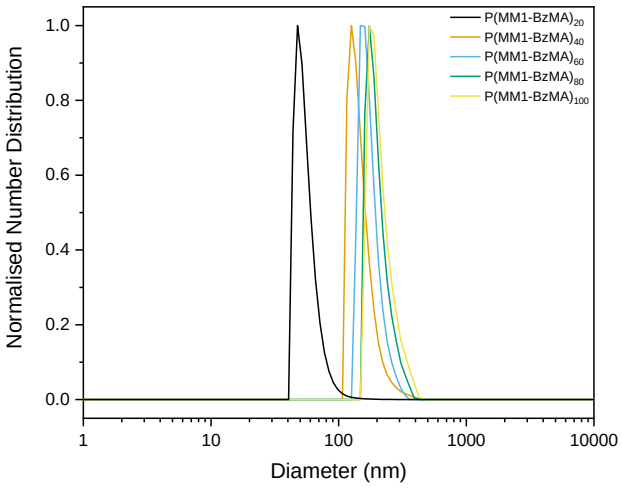

Figure A4.37 Overlay of DLS number traces for particles synthesised by the copolymerisation of **MM1** and BzMA.

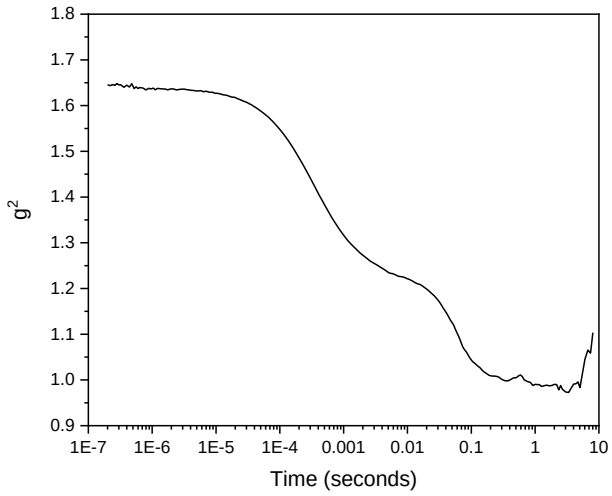

Figure A4.38 DLS correlogram for **P(MM1-BzMA)$_{20}$**

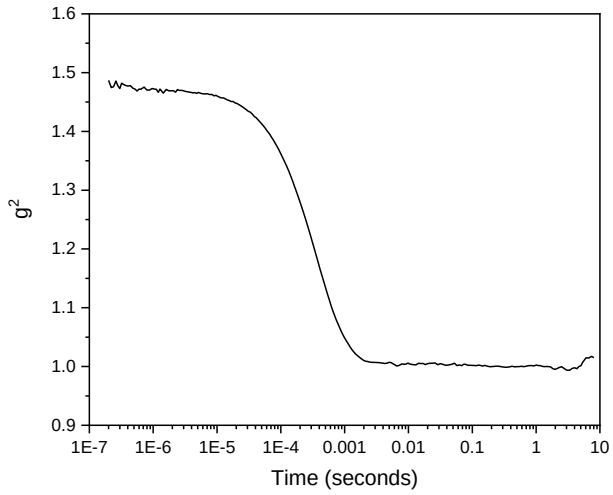

Figure A4.39 DLS correlogram for **P(MM1-BzMA)$_{40}$**

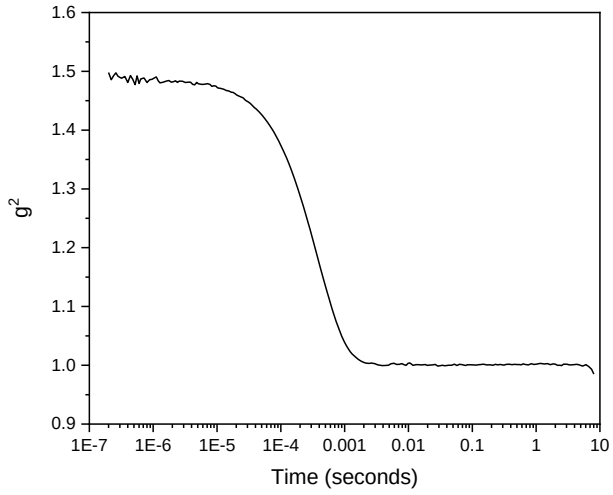

Figure A4.40 DLS correlogram for **P(MM1-BzMA)$_{60}$**

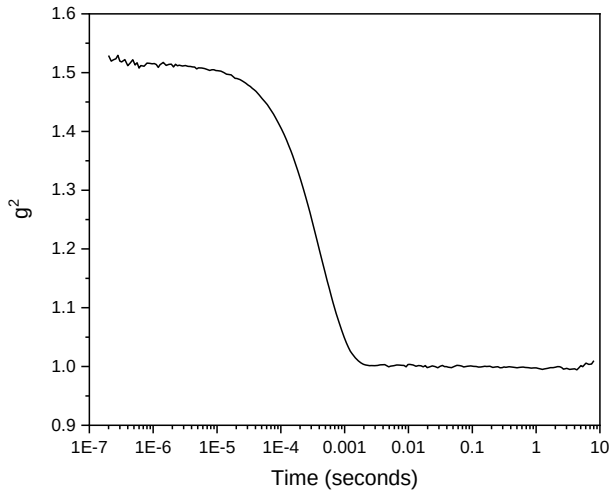

Figure A4.41 DLS correlogram for **P(MM1-BzMA)$_{80}$**

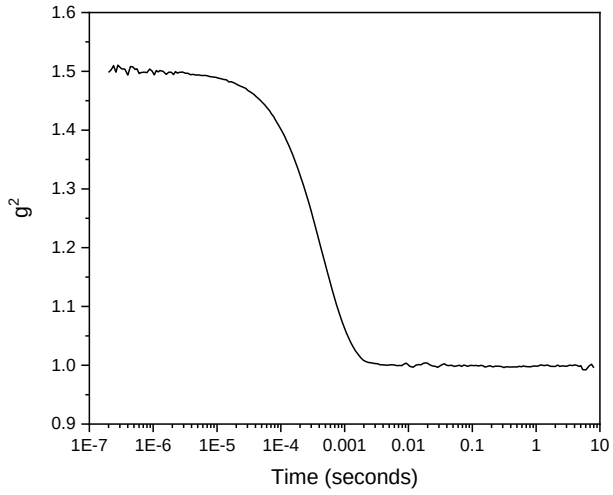

Figure A4.42 DLS correlogram for **P(MM1-BzMA)$_{100}$**

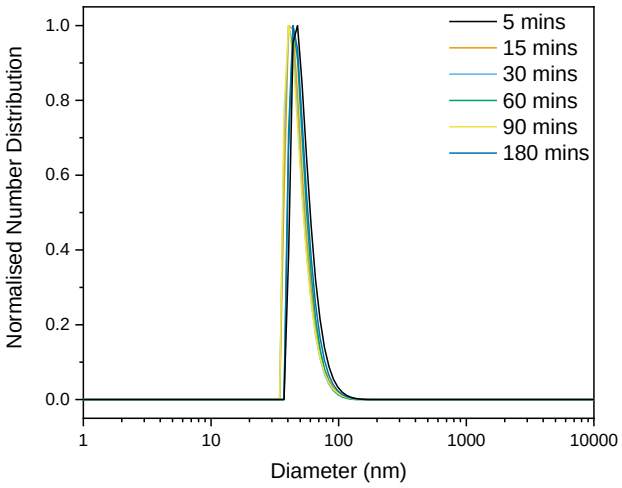

Figure A4.43 Overlay of DLS number traces for particles synthesised by the hydrolysis of **P(MM1-Sty)$_{20}$A**.

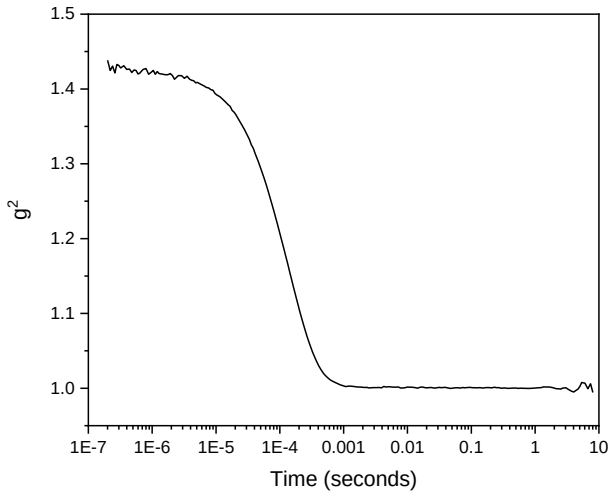

Figure A4.44 DLS correlogram for **P(MM1-BzMA)$_{20}$A** hydrolysed for 5 minutes.

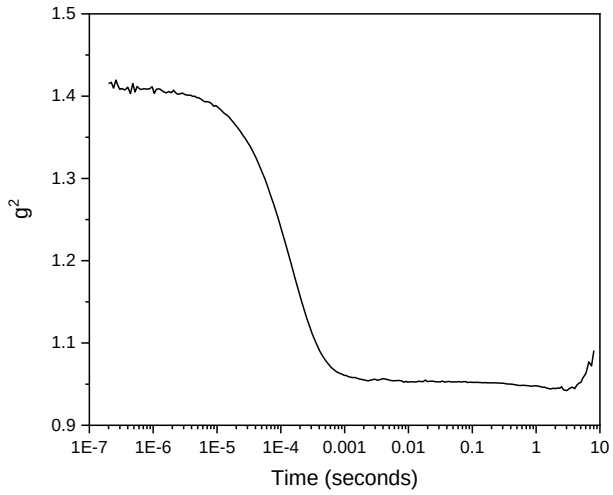

Figure A4.45 DLS correlogram for **P(MM1-BzMA)$_{20}$A** hydrolysed for 15 minutes.

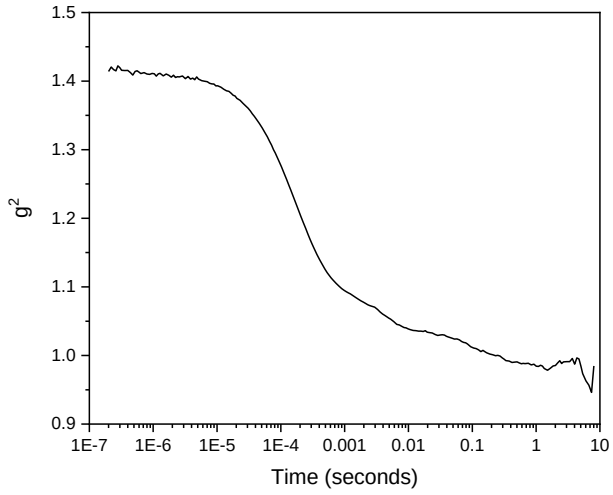

Figure A4.46 DLS correlogram for **P(MM1-BzMA)$_{20}$A** hydrolysed for 30 minutes.

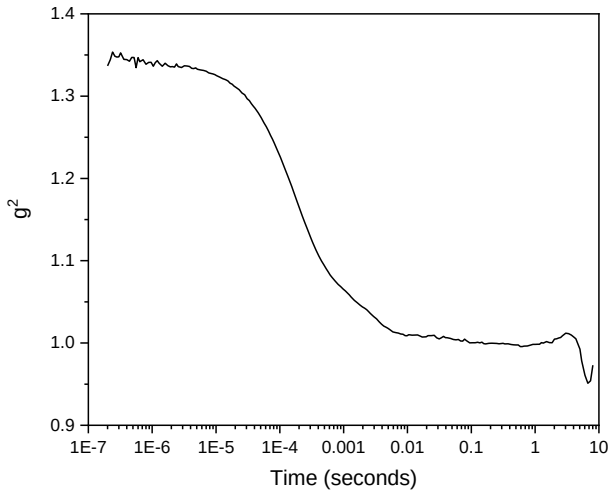

Figure A4.47 DLS correlogram for **P(MM1-BzMA)$_{20}$A** hydrolysed for 60 minutes.

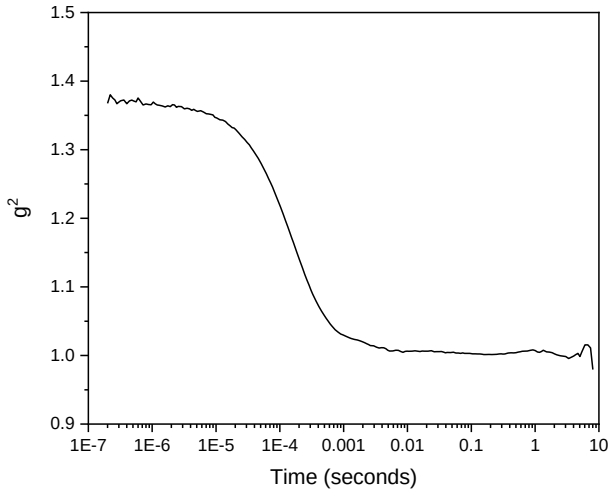

Figure A4.48 DLS correlogram for **P(MM1-BzMA)$_{20}$A** hydrolysed for 90 minutes.

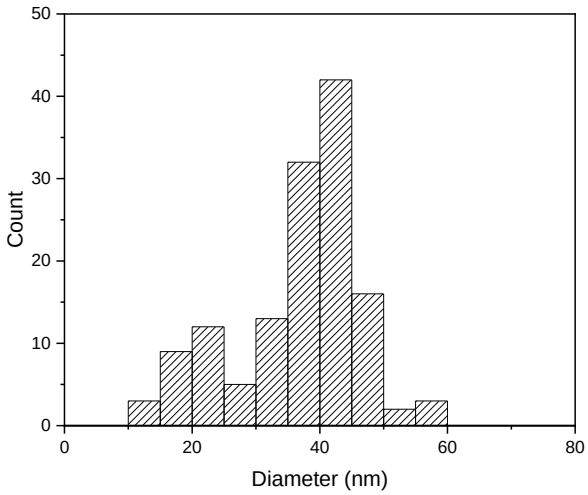

Figure A4.49 Nanoparticle size distribution determined from TEM micrographs (n = 119) of **P(MM1-Sty)$_{20}$A** hydrolysed for 90 minutes.

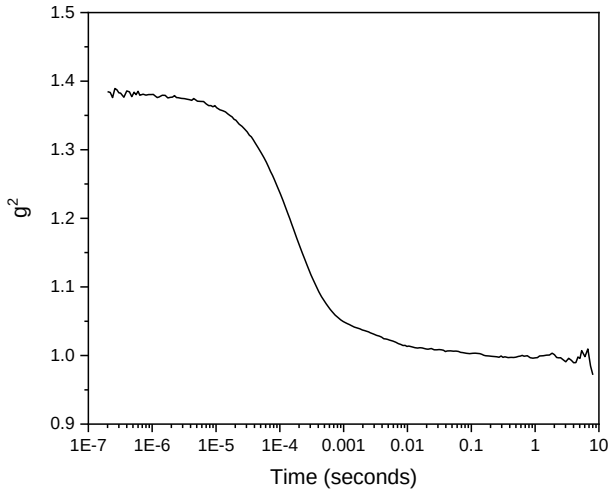

Figure A4.50 DLS correlogram for **P(MM1-BzMA)$_{20}$A** hydrolysed for 180 minutes.

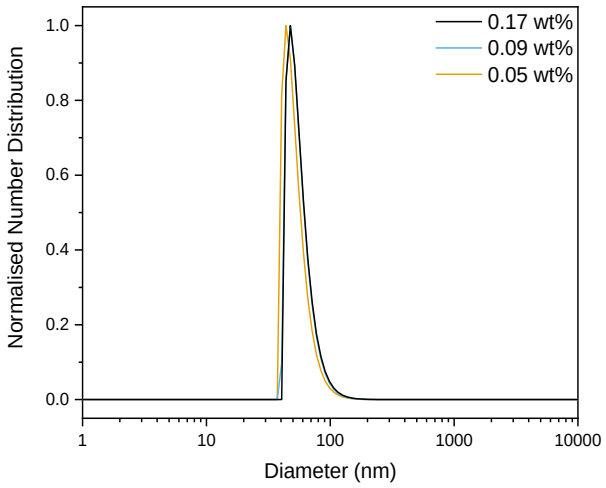

Figure A4.51 Overlay of DLS number distribution for polyplexes prepared at various wt%.

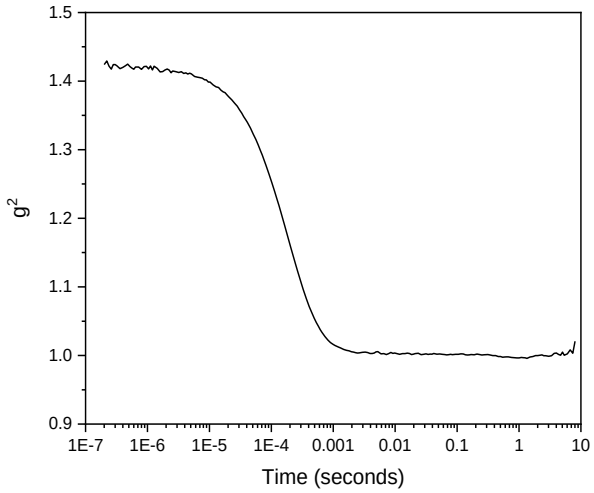

Figure A4.52 DLS correlogram for polyplexes formed at 0.17 wt% pDNA.

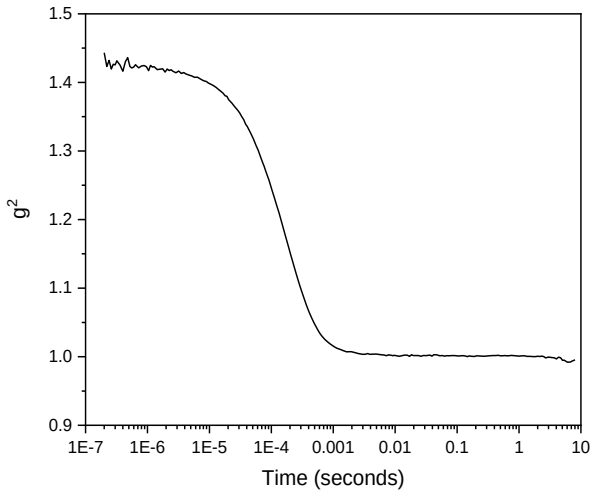

Figure A4.53 DLS correlogram for polyplexes formed at 0.09 wt% pDNA.

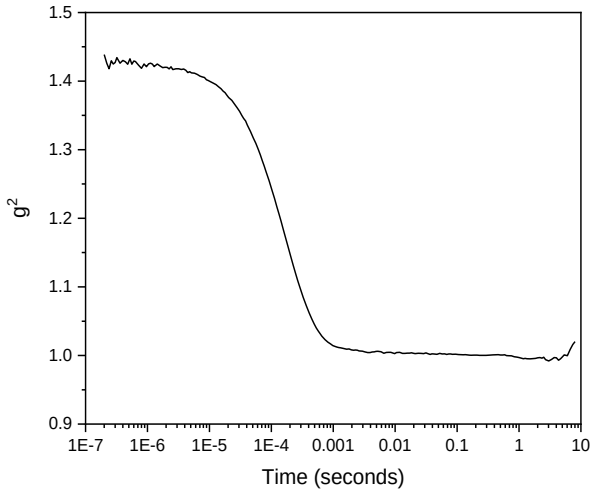

Figure A4.54 DLS correlogram for polyplexes formed at 0.05 wt% pDNA.

5 Conclusions and Outlook

It has long been a goal to develop gene transfection vectors with low associated toxicity and high transfection efficiencies. Development of non-viral vectors with these properties would allow for a simplification in the implementation of gene therapy, with reduced manufacturing cost and straightforward vector synthesis. Due to their high degree of structural variation and facile synthesis, polymers are attractive candidates for new generation vectors, however, they have long been associated with high cytotoxicity and reduced transfection efficiency compared to their viral and liposome counterparts.

In this work we set out to synthesis novel polymeric gene transfection agents possessing complex architectures with the aim of drawing structure property relationships and aiding to design the next generation of vectors.

Chapter 2 investigates the synthesis of styrenic-functionalised poly(2-ethyl-2-oxazoline)s (EtOx) which are subsequently used in grafting-through polymerisation to synthesise bottlebrush copolymers. Both the macromonomer and bottlebrush copolymers are extensively characterised, and their synthesis optimised. It was found that thorough purification of the initiators was required for successful incorporation of the styrenic moiety into the PEtOx, with end-group fidelity and molecular weight control highly dependent on their purity. Furthermore, it was found that an upper limit exists for the molecular weight of bottlebrush copolymers synthesised with narrow molecular weight distributions.

Once the bottlebrush polymers were synthesised, the PEtOx grafts were partially hydrolysed to form copolymers of EtOx and ethylenimine (EI). This allows for the random introduction of charged units into the bottlebrush copolymer grafts, enabling complexation of nucleic acids. The hydrolysed bottlebrush polymers were analysed by aqueous SEC, SANS, and AFM to assess the structural effects of hydrolysis. All bottlebrush copolymers were found to retain their morphology.

The third chapter investigated the use of the hydrolysed bottlebrush copolymers to complex pDNA and transfect mammalian cells. A series of bottlebrush copolymers were investigated with varying molecular weights and charge densities. It was found that below a charge density of 45 %, the polymers were unable to effectively condense pDNA into polyplexes. Above this threshold however, full complexation was achieved for all polymers with a lower concentration of higher charge density polymers required for complete complexation. The polyplexes formed were imaged using TEM revealing complexes with more elongated structures for bottlebrush polymers compared to the

linear controls. As expected however, the complexation process results in a wide distribution of polyplex sizes and morphologies.

Bottlebrush copolymers were then investigated for their ability to transfect mammalian cells and ascertain any toxicity. Compared to linear controls all bottlebrush polymers caused little cytotoxicity towards HEK293T cells, with cell viabilities > 80 % achieved in all cases. There was a slight molecular weight dependence, with higher molecular weight polymers exhibiting greater toxicities, however, the level of toxicity was still low enough to be considered non-toxic. Using a GFP reporter pDNA, HEK293T cells were transfected using the library of polymers. It was found that polymers with greater charge density caused the highest levels of GFP expression, with higher molecular weight bottlebrush polymers causing similar levels of transfection to the "gold standard" lPEI.

The macromonomer synthesised in chapter 2 was then applied to the synthesis of PEtOx coated nanoparticles. Using a surfactant-free emulsion polymerisation approach, copolymerisation of the macromonomer with hydrophobic monomers such as styrene and butyl methacrylate enabled the synthesis of well controlled nanoparticles, with predictable sizes based on the molar ratio between the two monomers. PEtOx coated nanoparticles were subsequently hydrolysed, with no structural perturbation to the nanoparticle structure observed by TEM or DLS. Using the cationic charges installed onto the corona of the nanoparticle complexation with pDNA was attempted. Whilst the nanoparticles were able to complex pDNA and restrict their migration in agarose gel electrophoresis, TEM revealed loose complexes with nanoparticles contained within a network of pDNA.

Building upon this thesis there are several routes of interest for future work. From the third chapter the bottlebrush architecture has shown high potential as a gene transfection vector, therefore further synthetic work should be carried out to introduce biodegradable units into the architecture or to simplify the synthetic approach. Grafting-to bottlebrush synthesis could provide a platform for degradability through either a degradable backbone or linker between the backbone and grafts. Additionally, partial modification of the ethylenimine units with targeting ligands, such as sugar moieties or peptide residues, could aid these materials when used *in vivo*.

Further understanding on why the bottlebrush polymer shows reduced toxicity and relatively high transfection efficiencies is imperative to the development of these materials. This could allow for tuning of the bottlebrush structure to further improve their

transfection efficiencies. Experiments looking at the disruption to the cellular membrane and studying the polyplex uptake are vital additions to this work. In addition, these systems should be further investigated using different forms of nucleic acids as the size of the bottlebrush may be suited to ones of different sizes.

Similar studies should be carried out with the cationic nanoparticles as improvement of the complexation may come with reduced nucleic acid size. Once efficient polyplex formation has been established these materials should be investigated for their ability to transfect cells and understand any associated toxicity. If conducted correctly, comparison with bottlebrush polymers should allow for conclusions on the length scale effect on gene transfection vectors. Alternatively, the surface associated amines could undergo modification, providing a straightforward platform for the generation of surface functionalised nanoparticles.

To conclude, this thesis highlights the importance of polymeric architecture in the complexation and delivery of nucleic acids. Whilst it is unlikely that any of these materials will become established vectors for gene transfection, the understanding gained on how the polymer parameters effect complexation and transfection are vital for the developments for the next generation of non-viral vectors.